Data analysis and scientific exploitation of the CMB B-modes experiment, POLARBEAR

Julien Peloton

UNIVERSITÉ SORBONNE PARIS CITÉ

Thèse préparée
à l'UNIVERSITÉ PARIS DIDEROT
École doctorale STEP'UP – ED N°560
Laboratoire AstroParticule & Cosmologie

Data analysis and scientific exploitation of the CMB B-modes experiment, POLARBEAR

par
Julien PELOTON

présentée et soutenue publiquement le
11 Septembre 2015

Thèse de doctorat de Sciences de l'Univers
dirigée par Radek STOMPOR

Devant un jury composé de :

Directeur de Thèse :	Dr. Radek STOMPOR	-	APC
President :	Prof. Stavros KATSANEVAS	-	APC
Rapporteurs :	Prof. Carlo BACCIGALUPI	-	SISSA
	Dr. François COUCHOT	-	LAL
Membres :	Dr. Antony LEWIS	-	University of Sussex
	Dr. Juan Francisco MACÍAS-PÉREZ	-	LPSC
	Prof. Benjamin D. WANDELT	-	IAP

À ma mère et mon père

Abstract

Over the last two decades cosmology has been transformed from a data-starved to a data-driven, high precision science. This transformation happened thanks to improved observational techniques, allowing to collect progressively bigger and more powerful data sets. Studies of the Cosmic Microwave Background (CMB) anisotropies have played, and continue on doing so, a particularly important and impactful role in this process. The huge data sets produced by recent CMB experiments pose new challenges for the field due to their volumes and complexity. Its successful resolution requires combining mathematical, statistical and computational methods all of which form a keystone of the modern CMB data analysis.

In this thesis, I describe data analysis of the first data set produced by one of the most advanced, current CMB experiments, POLARBEAR and the major results it produced. The POLARBEAR experiment is a leading CMB B-mode polarization experiment aiming at detection and characterization of the so-called B-mode signature of the CMB polarization. This is one of the most exciting topics in the current CMB research, which only just has started yielding new insights onto cosmology in part thanks to the results discussed hereafter.

In this thesis I describe first the modern cosmological model, focusing on the physics of the CMB, and in particular its polarization properties, and providing an overview of the past experiments and results. Subsequently, I present the POLARBEAR instrument, data analysis of its first year data set and the scientific results drawn from it, emphasizing my major contributions to the overall effort. In the last chapter, and in the context of the next generation CMB B-mode experiments, I present a more systematic study of the impact of the presence of the so-called E-to-B leakage on the performance forecasts of CMB B-mode experiments, by comparing several methods including the pure pseudospectrum method and the minimum variance quadratic estimator. In particular, I detail how the minimum variance quadratic estimator in the case of azimuthally symmetric patches can be used to estimate efficiently parameters, and I present an efficient implementation based on existing parallel algorithms for computing Spherical Harmonic Transforms.

Résumé

L'évolution des techniques d'observation au cours des deux dernières décennies a rendu possible l'obtention de jeux de données de plus en plus précis, et a permis l'évolution de la cosmologie vers une science de haute précision. Les études menées sur les anisotropies du Fond Diffus Cosmologique n'ont jamais cessé de jouer un rôle prépondérant dans cette transformation, tant leurs impacts ont été importants. Néanmoins, les jeux de données extrêmement volumineux et complexes produits par les expériences de Fond Diffus en cours posent un nouveau défi pour le domaine, à tel point que la réussite de l'analyse moderne des données du Fond Diffus repose sur une forte interdisciplinarité combinant de la physique, des mathématiques, des méthodes statistiques ainsi que des méthodes de calcul numérique.

Dans cette thèse, j'expose l'analyse du premier jeu de données produit par POLARBEAR, l'une des expériences actuelle de premier plan sur le Fond Diffus, ainsi que les résultats majeurs obtenus. L'expérience POLARBEAR est spécifiquement dédiée à la détection et à la caractérisation de la signature des modes B de la polarisation du Fond Diffus Cosmologique. La recherche des modes B est l'un des sujets actuel les plus passionnants pour le Fond Diffus, qui a commencé à ouvrir de nouvelles perspectives sur la cosmologie, en partie grâce aux résultats présentés et discutés dans ce travail.

Dans cette thèse, je décris en premier lieu le modèle cosmologique actuel, en me concentrant sur la physique du Fond Diffus, et plus particulièrement ses propriétés de polarisation; ainsi qu'une vue d'ensemble des contributions et des résultats des expériences antérieures et en cours. Dans un deuxième temps, je présente l'instrument POLARBEAR, l'analyse des données prises lors de la première année d'observation, ainsi que les résultats scientifiques qui en ont été tirés, en soulignant principalement ma contribution au projet dans son ensemble. Dans le dernier chapitre, et dans le contexte des prochaines générations d'expérience sur les modes B, je détaille une étude plus systématique concernant l'impact de la présence des fuites des modes E dans les modes B sur les performances prévues par ces futures expériences, notamment en comparant plusieurs méthodes dont la méthode des pseudospectres pures ainsi que l'estimateur quadratique à variance minimum. En particulier, dans le cas d'observation du ciel présentant une symétrie azimutale, je détaille comment l'estimateur quadratique à variance minimum peut être utilisé pour estimer de manière efficace les paramètres cosmologiques, et je présente une implémentation performante basée sur des algorithmes parallèles existants pour le calcul des transformations en harmoniques sphériques.

Acknowledgments

I have had a wonderful experience working on the POLARBEAR project over the past three years. I am thankful to my advisor Radek Stompor, who took me on as an inexperienced undergraduate and let me work on important problems from day one. You always were here to support me, and you taught me more than just science. I could not have asked for better advisor.

I also thank Adrian Lee, without whom POLARBEAR wouldn't be such a great experiment and who always let me an important freedom in the data analysis of the experiment.

A big thanks to the *pbearapc* team members who are more than just colleagues: Davide for your criticism on everything (in a good way!) and sharing 2 years of trips/lunches/telecons, Josquin for introducing me the POLARBEAR experiment and introducing me Berkeley and California, and Maude for your extraordinary computing skills. A big special thanks to Giulio, with whom I have done a lot during my thesis: endless discussions with many ideas turned into thousands lines of code, around-the-clock debugging, many talks and posters, many trips around the world, and much more. I like to think that our duo is the most efficient one ever!

I should also thank the rest of the POLARBEAR collaboration, and in particular Bryan Steinbach, Kam Arnold, Dave Boettger, Yuji Chinone, Zigmund Kermish, Frederick Matsuda, and Haruki Nishino who were key people for the data analysis of the first season.

I thank Carlo Baccigalupi and François Couchot who accepted, during this summer, to report this thesis. I am very grateful for their efforts and the advices they have provided for the improvement of this manuscript. I thank Stavros Katsanevas for giving me the honor of being at the head of the committee. I also thank Juan Francisco Macías-Pérez and Benjamin D. Wandelt for participating to the jury as examiners of my work. Many thanks to Antony Lewis, who comes from Brighton for this defense as examiner, and who offered me a postdoctoral position in his team for the next years.

I thank the Orséens from IAS, Agnès and Julien, the masters of the pure pseudospectrum formalism. You were more than just collaborators, and I hope we will continue this working style!

I thank all the friends from APC, especially Alexis and Jibril and the buddies from the 312B, Ileyk and Matthieu.

A big thanks to all nursery/high school/prépa/University/Rock band friends I have the chance to have (in complete disorder): Cyrille, Vincent P., Aurélie, Vincent V., Nico, Sophie, Cécile, Valoute, Delphine, Elise, Simon, Pierre, Matthieu, Huy Vu, Max, Charlotte, Agnès, Mégane, Renaud, Jo... You are invaluable friends.

I also feel extremely fortunate to have a fantastic family, who always supports me in every circumstances. I wouldn't be here without you, and I could not have dreamed of a better childhood and a better education. You have an important role in all I do.

Last but not least, my wife Isalyne, for her immense love, patience and courage.

Contents

Chapter 1

Introduction to the Standard Model of Cosmology

Contents

1.1 From first observations to modern cosmology

1.1.1 That's all started with observations

On a clear night far from big cities, if you raise your eyes to the sky, you might be enough lucky to see stars. It's one of those things. For centuries all observations were made in the visible light, which is the one accessible to our eyes. There was not yet the necessary knowledge and technology to probe the full electromagnetic spectrum. But in the middle of the 20^{th} century, boosted by the second World War and the development of radars, people started turning towards the sky detectors

sensitive to different part of the electromagnetic spectrum such as infrared, radio, X-rays, etc... The sky that they thought they knew everything showed its true colors! So much to understand now. The story that I will tell you is mainly in the *radio* band, but be sure that most frequency bands will appear as well!

1.1.2 Homogeneity, isotropy

Do we have a special position in our Universe? For long time, people wondered whether this was the case or not. Due to the lack of formalism and observations, this question was debated metaphysically rather than scientifically. And for long time, a majority of scientists and philosophers had no doubt that our position had to be special, otherwise why we would be here ? Nonetheless the whole scientific community were in two minds about the matter and little by little the so-called "Cosmological Principle"[1] became viable. It states that *the most important feature of our universe* is its large scale homogeneity and isotropy[2], *e.g.* [Mukhanov 2005]. This feature ensures that observations made from our single vantage point are representative of the universe as a whole and can therefore be legitimately used to test cosmological models. Homogeneity states that the universe has the same properties at all locations, and isotropy states that it has the same appearance in all directions. At the beginning of the 20^{th}, this principle was the result of intuitive guesses in contrast to laws, which refer to experimentally established facts. We needed to wait for the end of the 20^{th} century to be able to collect data. The main observational fact in favor of the Cosmological Principle has been brought by the detection of the Cosmological Microwave Radiation Background in the early 90's [Mather *et al.* 1990], which revealed to us a uniform sky, with fluctuations of the order of 10^{-5}, whatever the observed direction!

1.1.3 The foundation of the Standard Model

The Cosmological Principle in hands, one can start elaborating a theory describing the evolution of the universe. The different fundamental interactions that we know are: the weak interaction, the strong interaction, the electromagnetic force and the gravitational interaction. The weak and strong interactions do not play a *direct* role in the evolution of the universe[3]. Only the electromagnetic and gravitational interactions have an infinite range. Due to the global neutrality of the universe, the electromagnetic force is negligible at long range (screening effect). We thus need a theory of the gravitation to build a model capable of describing the evolution

[1] There are presently several versions of this principle such as the Weak Cosmological Principle, the Strong Cosmological Principle, the Final Cosmological Principle, etc. All versions, formulated in markedly different ways, in one way or another interrelate the properties of the universe, the properties of elementary particles, and the very fact that mankind exists in this universe. There exists several variations under the denomination Copernician Principle, Anthropic Principle, etc.

[2] We really talk about *statistical* homogeneity and isotropy.

[3] Rigorously, they do not play a role in the recent evolution of the Universe. But it is worth mentioning that they certainly play a big role during the Primordial Big Bang Nucleosynthesis. In addition they are of a great importance for other probes.

and the structure of our universe. This theory is the General Relativity, initially formulated by Albert Einstein in 1916, and it is the foundation of the Standard Model in cosmology[4].

General relativity links gravity to the underlying curvature of the space-time manifold (a shape in three spatial and one time dimensions). This curvature in turn, is described by a metric, $g_{\mu\nu}$, which encodes the distances between any two points on the manifold. The invariant (under transformations, such as Poincaré, Lorentz) interval is defined by[5]

$$ds^2 = g_{\mu\nu} dx^\mu dx^\nu. \tag{1.1}$$

The Einstein's field equations are given by

$$G_{\mu\nu} = 8\pi G T_{\mu\nu}, \tag{1.2}$$

where $G_{\mu\nu}$ is called the Einstein tensor and encodes information about the geometry of the universe, and the right-hand side is the stress-energy tensor (symmetric tensor describing the content of the Universe). The 00 component of the stress-energy tensor corresponds to the energy density, the $0i$ components correspond to momenta, and the ii components correspond to the pressure. The constant of proportionality comes from the newtonian limit for weak gravitational fields (Poisson equation, $\Delta\phi = 4\pi G\rho$). From the Einstein's field equations and Bianchi identities and assuming that there is no *torsion*[6], we can show that $D_\mu G^\mu_\nu = 0$ implies

$$D_\mu T^\mu_\nu = 0. \tag{1.3}$$

The last equality is the generalization of the conservation laws for energy in a curved space-time. The simplest solution (different from zero) which satisfies the last equality in Eq. 1.3 is the metric itself. In this case, this particular solution is generally written as an additional term in Einstein's field equations, defining the so-called cosmological constant Λ such as:

$$G_{\mu\nu} + \Lambda g_{\mu\nu} = 8\pi G T_{\mu\nu}. \tag{1.4}$$

1.1.4 The expanding universe

We wish to expand this discussion to General Relativity to a cosmological context. For this we need a support from the observations. In 1929, Hubble measured the redshift of nearby galaxies [Hubble 1929]. He showed that galaxies seem to be receding from us, no matter the direction of observation. Combined with the Cosmological

[4] Despite the fact that we need the full artillery of General Relativity to fully describe modern cosmology, we many aspects of cosmology using Newtonian mechanics and gravity. I will not enter into details here.

[5] I will use the Einstein summation convention, where we summed over repeated indices.

[6] The full definition of terms and the demonstrations of statements are beyond the scope of this thesis. For an advanced discussion about the torsion see *e.g.* (in French) [Cartan 1923, Cartan 1924, Cartan 1925].

principle, the galaxies have to escape from any point. Hubble pointed out also that the bigger the redshift the faster the galaxy is escaping from us.

Expansion Continuing, let's consider first on the meaning of *expansion*. On scales corresponding to nearby galaxies, we can think of the expansion as a relative velocity between any two galaxies, increasing with time and distance. On larger scales, such that the time between the emission of light from the distant galaxy and its reception is large, speaking of velocity relative to us loses its meaning[7]. Same is true when speaking about the distance to that galaxy. There are different ways to define distances in an expanding universe, and we choose the one which expands with it. This coordinate system is called a comoving coordinate system. Objects that we observe may have small motions, called peculiar velocities, with respect to this coordinate system, but on average[8] they are at rest with respect to this coordinate system as the universe expands. A comoving observer is an (hypothetical) observer expanding along with these comoving coordinates.

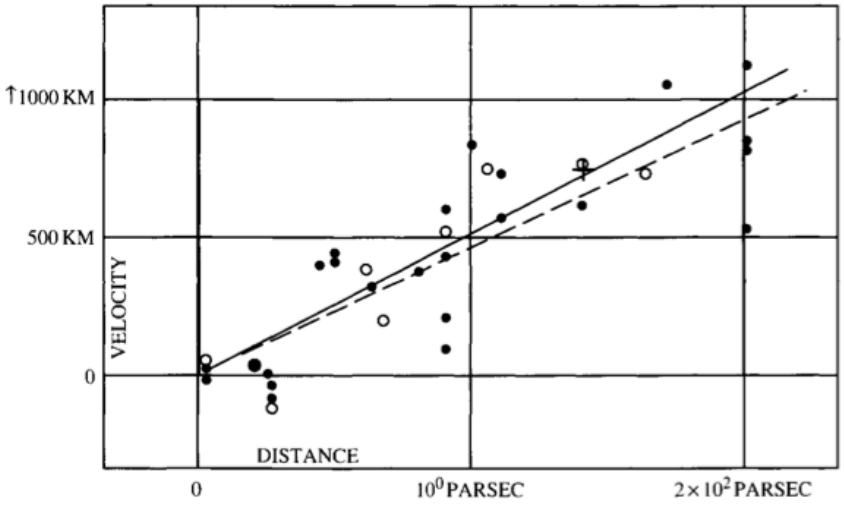

Figure 1.1: Relation between distance and radial velocity among extra-galactic nebulae. The original figure is from [Hubble 1929]. The units on the diagram are not really clear. On the one hand we have the open points and their best fit in dashed line corresponding to original measurements, and on the other hand the filled points and their best fit in solid line are the same measurements but corrected for the sun's motion.

Scale factor and Hubble's law Hubble's law is one of the pillars of the Hot Big Bang scenario that describe later in Sec. 1.2. Let's consider two points i and j at

[7] Think of very distant galaxy for which such a reasoning would give a relative velocity $v \geq c$!
[8] Due to homogeneity and isotropy of the universe, see the Cosmological Principle.

some time t_1 in the universe, and then later at some time t_2. If the universe is in expansion, the distance between i and j at a given time $r_{ij}(t) = r_i(t) - r_j(t)$ must be scaled as a function of time (but not position). That is[9]:

$$r_{ij}(t_1) = a(t_1) r_{ij}(t_0) \tag{1.5}$$
$$r_{ij}(t_2) = a(t_2) r_{ij}(t_0) \tag{1.6}$$

where t_0 is some arbitrary time, which is often taken to be the present day. The quantity $a(t)$, called the *scale factor*, describes the evolution of the universe, and for an homogeneous and isotropic universe, it tells us almost everything we need to know about the dynamics. In the 2-sphere analogy, $a(t)$ has a precise geometrical interpretation as the radius of the sphere. Here the value of the scale factor $a(t)$ itself has no geometrical meaning and its normalization can be chosen arbitrarily. Once the normalization is fixed, the scale factor $a(t)$ describes the coordinate distance between observers as a function of time. We can easily combine both equations, and noticing that at a general time t we have:

$$a^{-1}(t) r_{ij}(t) = \text{const.} \tag{1.7}$$

Taking the derivative with respect to time of the previous equation, and rearranging terms, we end up with:

$$\frac{\dot{a}}{a} = \frac{\dot{r}_{ij}}{r_{ij}}, \tag{1.8}$$

where time dependency has been dropped for more clarity. Interestingly enough, the right-hand side of Eq. 1.8 does depend on i and j but not the left-hand side. Therefore, the scaling between two points is just a function of time and can be written more generally:

$$\frac{\dot{a}}{a} = \frac{\dot{r}}{r}, \tag{1.9}$$

for an arbitrary distance r. The left-hand side of Eq. 1.9 is often called the *expansion rate* or *Hubble parameter*:

$$H(t) = \frac{\dot{a}}{a}\Big|_t \tag{1.10}$$

and more specifically today at time $t = t_0$:

$$H_0 = H(t_0) = \frac{\dot{a}}{a}\Big|_{t=t_0} \tag{1.11}$$

is the expansion rate today, one of the most important quantities in cosmology, and still difficult to measure precisely [Planck Collaboration 2015d]. The most common form of the Hubble's law used today is under the form:

[9] Eq. 1.5 & 1.6 makes use of $a(t)$ without units, but I could have chosen $a(t)$ units of length, and so to have a factor $a(t)/a_0$ instead of $a(t)$ only. a_0 is a normalization that is often set to the value of a today.

$$v = H_0 d \tag{1.12}$$

where v is the velocity of the object that we are observing relative to us, and d is its coordinate distance. See the Fig. 1.1 for the first measurements from Hubble.

Robertson-Walker metric What would be the metrics which would satisfy the geometry of the universe, meaning what would be the metrics satisfying at least the symmetries on large scales imposed by the Cosmological Principle and expansion ? There are several, but they can all be reduced to the Robertson-Walker metric. In a spherical coordinate system, choosing the signature to be $(-+++)$, this metric is given by

$$ds^2 = -dt^2 + a^2(t)\Big[\frac{dr^2}{1-\kappa r^2} + r^2\big(d\theta^2 + \sin^2\theta d\phi^2\big)\Big], \tag{1.13}$$

where $a(t)$ is the scale factor, which encodes the expansion of the Universe. To try to understand what sort of manifolds are behind this metric, let's start in two spatial dimensions, much easier to picture for our brain. What two-dimension shapes satisfy the requirements of homogeneity and isotropy ? So does the sphere, so does the infinite plan and not so obviously does the hyperbolic paraboloid (also known as Lobachevski space). it turns out that in 3+1 dimensions, we have the same set of homogeneous and isotropic manifolds but promoted to higher dimensionality: the three-sphere, the flat space in 3 dimensions and the three-hyperboloid.

The term κ in the Eq. 1.13 is a real number with dimension $[\text{length}]^{-2}$. The sign of κ sets the possible manifolds described above, and so it sets the *curvature* of our space. The choice $k > 0$ corresponds to the three-sphere, the choice $k = 0$ corresponds to the flat space (Minkowski plus expansion), and the choice $k < 0$ corresponds to the three-hyperboloid. Although, we should mention that General Relativity itself places no restrictions upon the topology of the Universe [De Sitter 1917], and many searches are done to assess the properties of anisotropic geometries and non-trivial topologies, as in [Planck Collaboration 2014f, Planck Collaboration 2015f] and references therein.

Friedmann-Lemaître equations The Robertson-Walker metric describes the universe at a given time, but we need now to discuss how the universe evolves with time. The equations of Friedmann-Lemaître do so, and they come from the Einstein's field equations by inserting the Robertson-Walker metric. All computations done, it reads:

$$H^2(t) = \Big(\frac{\dot{a}}{a}\Big)^2 = \frac{8\pi G\rho}{3} - \frac{\kappa}{a^2} + \frac{\Lambda}{3}, \tag{1.14}$$

$$\frac{\ddot{a}}{a} = -\frac{4\pi G}{3}(\rho + 3P) + \frac{\Lambda}{3} \tag{1.15}$$

where a, ρ (energy density) and P (pressure) are all functions of time. From those two equations (or from the conservation of the stress-energy tensor Eq. 1.3), one has the continuity equation

$$\dot{\rho} + 3H(\rho + P) = 0 \tag{1.16}$$

which can also be viewed from the first law of thermodynamics ($dE = -pdV$). However in Eq. 1.16, the quantities ρ and P are not independent quantities and are linked via the equation of state

$$P = w\rho, \tag{1.17}$$

with w being a real constant. In order to gain in intuition, let's rewrite the Friedmann equations in terms of *densities*

$$\left(\frac{\dot{a}}{a}\right)^2 = \frac{8\pi G}{3}\Big(\rho - \rho_\kappa + \rho_\Lambda\Big). \tag{1.18}$$

$\rho = \rho_m + \rho_r$ is the sum of matter density (non-relativistic) and radiation (relativistic), $\rho_\kappa = 3\kappa/(8\pi G a^2)$ is the energy density associated with the curvature, and $\rho_\Lambda = \Lambda/(8\pi G)$ is the energy density related to the cosmological constant. Consider today now a flat universe ($\kappa = 0$) with no cosmological constant ($\Lambda = 0$), in which case we say that the density today is the *critical density*, ρ_c[10]. The first Friedmann equation gives:

$$\rho_c = \frac{3H_0^2}{8\pi G}. \tag{1.19}$$

Then define the *density parameter* Ω_i as:

$$\Omega_i = \frac{\rho_i}{\rho_c} \tag{1.20}$$

such that

$$\left(\frac{\dot{a}}{a}\right)^2 = H^2\Big(\Omega_m + \Omega_r - \Omega_\kappa + \Omega_\Lambda\Big). \tag{1.21}$$

The Ω_i are functions of time through ρ_i, and therefore are functions of redshift[11], and one can define the density parameters today $\Omega_{0,i}$ such as[12]:

$$\Omega_r = \Omega_{0,r}(1+z)^4 \tag{1.22}$$
$$\Omega_m = \Omega_{0,m}(1+z)^3 \tag{1.23}$$
$$\Omega_\kappa = \Omega_{0,\kappa}(1+z)^2 \tag{1.24}$$
$$\Omega_\Lambda = \Omega_{0,\Lambda}(1+z)^0 = \Omega_{0,\Lambda}. \tag{1.25}$$

[10] The critical density changes with time. However, it is common to define ρ_c to be a constant, the critical density today.

[11] Remember that $a(t) = 1/(1+z)$.

[12] Notice that Eqs. 1.22 & 1.23 are exact only if there is no conversion between components due to particle decays for instance.

Let's rewrite the first Friedmann equation one more time:

$$H(t) = \frac{\dot{a}}{a} = H_0 E(z) = H_0 \sqrt{\Omega_{0,m}(1+z)^3 + \Omega_{0,r}(1+z)^4 + \Omega_{0,\kappa}(1+z)^2 + \Omega_\Lambda}. \tag{1.26}$$

The function $E(z)$, first popularized by J. Peebles in his books and papers is sometimes called the *Hubble Function*. In particular, at $z = 0$ (today), $E(0) = 1$ so $1 = \Omega_{0,m} + \Omega_{0,r} + \Omega_{0,\kappa} + \Omega_\Lambda$. Because all Ω_i, but Ω_κ, are physical densities, we define the total density parameter as:

$$\Omega_{tot} = \Omega_{0,m} + \Omega_{0,r} + \Omega_\Lambda = 1 - \Omega_{0,\kappa} \tag{1.27}$$

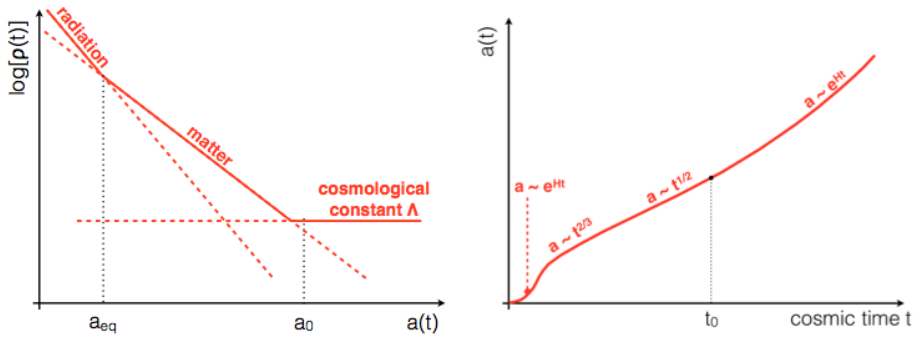

Figure 1.2: *Left panel:* energy density ρ as a function of the scale factor a. *Right panel:* Scale factor a versus time t, in our universe. In the early times, the Universe is in an inflation epoch. As time increase, the dominant component is first the radiation ($a \propto t^{2/3}$), and then the matter ($a \propto t^{1/2}$). We are today in a cosmological constant domination era ($a \propto e^{Ht}$). Figure taken from [Errard 2012].

Evolution of the scale factor By combining the equation of state and the continuity equation to get $\rho_i(a)$, and using the first Friedmann equation, we get the time dependency of the scale factor:

- Radiation domination era: $p_r = (1/3)\rho_r \xrightarrow{Eq.1.16} \rho_r \propto a^{-4} \xrightarrow{Eq.1.26} a(t) \propto t^{1/2}$
- Matter domination era: $p_m = 0 \times \rho_m \xrightarrow{Eq.1.16} \rho_m \propto a^{-3} \xrightarrow{Eq.1.26} a(t) \propto t^{2/3}$
- Cosmological constant domination era: $p_\Lambda = -\rho_\Lambda \xrightarrow{Eq.1.16} \rho_\Lambda \propto a^0 \xrightarrow{Eq.1.26} a(t) \propto e^{Ht}$

The case where the curvature dominates is a bit different, since there exists a physical solution to the first Friedmann equation only if in an open Universe ($\kappa < 0$), which gives:

$$\left(\frac{\dot{a}}{a}\right)^2 = -\frac{\kappa}{a^2} \quad \overset{Eq.1.26}{\longrightarrow} \quad a(t) \propto t. \tag{1.28}$$

We can see that each density of component does not depend on the scale factor the same way. If we go back in time sufficiently far, the early universe was dominated by the radiation. However, the energy density of the radiation being proportional to a^{-4}, it drops quicker than the non-relativistic matter component which is cubic in the inverse scale factor. So starting from a radiation dominated era, if we let the time to go forward there is a moment when matter and radiation energy densities are equal, and then a matter domination era. Finally, the energy density associated with the cosmological constant is constant with respect to the scale factor. So given that all other components have an energy density which decreases as a function of the scale factor a, they will have an energy density lower than the one of the cosmological constant at some point. This is the cosmological constant domination era that we experience nowadays. As of now, we interpret this era as the domination of a new form of energy, of unknown fundamental nature, called the dark energy. Those behaviors are summarized in Fig. 1.2.

Recent observations revealed that the curvature is negligible [de Bernardis *et al.* 2000, Balbi *et al.* 2000] (we live in a nearly perfectly flat universe), and the universe seems to be currently in a cosmological constant domination era [Riess *et al.* 1998, Perlmutter *et al.* 1999]. The latest measurements from the satellite Planck unveiled a universe with roughly: $\Omega_{0,k} = 0$, $\Omega_{0,m} \approx 0.3$, $\Omega_{0,r} \approx 10^{-5}$ and $\Omega_\Lambda = 1 - (\Omega_{0,m} + \Omega_r) \approx 0.7$ (Planck temperature, polarization and lensing [Planck Collaboration 2015d]).

1.1.5 Dark energy

If we sum up matter and radiation components and consider that the curvature is negligible (critical Universe), we quickly find a huge budgetary shortfall. Around 70% of the energy density of the Universe is missing. This missing energy seems not to interact with ordinary matter, and is in an unclustered form. It has been called the dark energy. While it remained of theoretical interest for long time, in 1998 two independent groups observing supernovae reported direct evidence for the dark energy [Riess *et al.* 1998, Perlmutter *et al.* 1999]. To study models of dark energy, we sometimes parametrize the relation between pressure and energy density as $P = w\rho$ (equation of state), and try to constrain the value of w. Applied to the cosmological constant we have $w = -1$. From supernovae measurements, values of w greater than ~ -0.5 are disfavored, and a cosmological constant is consistent with the data. However, one should keep in mind that the cosmological constant is by no means the only possible explanation, and on the theoretical grounds, it is indeed not the preferred solution.

1.2 Thermodynamics and the Hot Big Bang scenario

In the previous sections, we focused on the geometrical description of our universe. We would like to have now a microscopical picture of the universe and in particular the evolution of its different components and fundamental interactions. From what we derived previously, on all epochs (era), the scale factor grows with time, and so approaches zero as expansion is extrapolated back in time up to the theoretical $t = 0$. This would formally give an infinite energy density, which gave rise to the popular name *Big Bang* to refer to the singularity in our model of space-time.

1.2.1 Thermal history of the universe

The universe is considered as adiabatically expanding. In an FRLW expanding universe the energy density of photons decreases as a^{-4}. For most of the Universe history the photons are in thermal equilibrium, therefore the spectrum shape is a Planckian distribution[13] and thus is preserved all along the universe history. Therefore, it is possible to define a temperature of the Universe, related to the thermal distribution of the photons. The distribution is only governed by the dilution due to the expansion, and as we go further back in time the universe gets hotter as

$$T(t) = \frac{1}{a(t)} T_0, \tag{1.29}$$

where T_0 is the equivalent temperature now. This increase of temperature gave rise to the name *Hot* Big Bang scenario.

The Big Bang nucleosynthesis If the universe is in expansion, there should exists a moment in its past when it is sufficiently hot and dense such as there are no neutral atoms or even bound nuclei. The vast amounts of radiation in such a hot environment ensures that any atom produced would be immediately destroyed by a high energy photon. As the universe cooled (expanded) well below the binding energies of typical nuclei, light elements begin to form. Nowadays, our universe is made of 90% of Hydrogen, a bit less than 10% of Helium, and the rest in heavy elements (heavier than Helium). In 1946, Gamov published a theory in which he claimed that *almost all* matter in the universe was created in the first 3 minutes [Gamov 1946]. It is now known under the name Big Bang primordial nucleosynthesis [Gamov 1946], and it is a remarkable combination of Cosmology and Nuclear Physics. The Big Bang primordial nucleosynthesis gives us a way of constraining the baryon density in the universe. Combining the knowledge from the Standard Model in Particle Physics and the production rates as measured in colliders for instance or issued from numerical model of nuclear reactions, we can predict the relative abundances of each species [Kolb & Turner 1990], [Burles *et al.* 2001a], [Burles *et al.* 2001b] as a function of the ratio baryon over photon η (supposed constant over time). Since we know how those densities scale as the universe evolves

[13] Bose-Einstein distribution with zero chemical potential.

(see Eq. 1.23), we can also turn the measurements of light element abundances into estimates of the baryon density today. The figure 1.3 shows the constraint on the baryon density from Big Bang Nucleosynthesis (from [Nollett & Burles 2000]). The colored curves (green, red, blue, purple) are predictions from the primordial nucleosynthesis and their width corresponds to the 95% confidence level from cross-sections. The rectangles are different observations from [Bonifacio & Molaro 1997], [Izotov & Thuan 1998], [Olive *et al.* 1997]. The light blue vertical band is the η value estimated by [Burles & Tytler 1998].

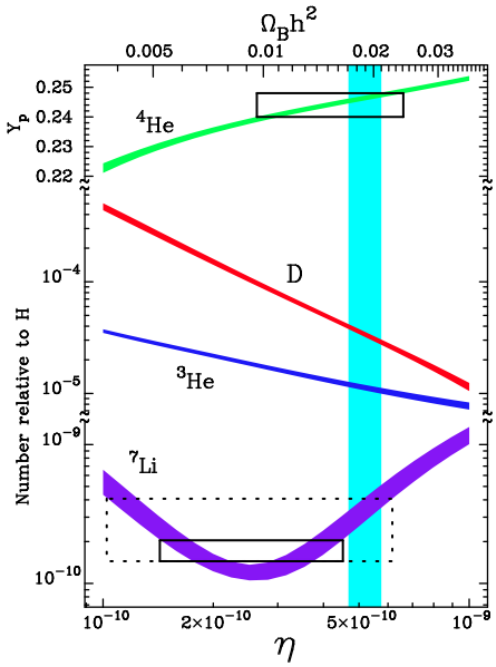

Figure 1.3: Constraint on the baryon density from Big Bang Nucleosynthesis. See text for more explanations. Figure adapted from [Nollett & Burles 2000].

The radiation/matter decoupling In the primordial plasma, the photons are coupled to electrons via Compton scattering: $e^- + \gamma \rightarrow e^- + \gamma$, with a rate Γ given by:

$$\Gamma = \sigma n v, \tag{1.30}$$

where σ is the cross-section of the interaction, n is the number density of electrons and v their relative velocity. Photons and electrons remain in thermodynamics equilibrium only if their mean time Γ^{-1} between two interactions is less than the *Hubble time* H^{-1}. Given that the cross-section decreases with the temperature, the mean time increases. That means that there exists a moment when photons and electrons stop interacting. In other words, if the universe expands away more rapidly

than the particles can interact, most particles do not experience the interaction, and hence fall out of equilibrium. We call this departure from equilibrium *freeze-out*, and this special moment is called the matter/radiation *decoupling*. Since this moment, the photons propagate freely through the universe (their comoving abundance is frozen). However, radiation/matter decoupling does not mean that matter and radiation lose all thermal contact. We can show that the interaction of a small number of photons with matter keeps the temperatures of matter and radiation equal down to redshifts $z \sim 100$. Only after that does the temperature of baryonic matter begin to decrease faster than that of radiation [Mukhanov 2005]. We can predict that the photons from the decoupling should have a equivalent temperature brightness of the order of 3 K today (see Sec. 1.2.2).

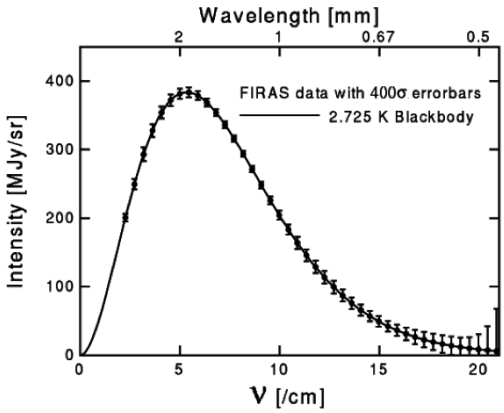

Figure 1.4: Frequency spectrum of the Cosmic Microwave Background radiation measured by the FIRAS instrument on the COBE satellite [Mather *et al.* 1990].

The whole thermal history in few steps At higher temperature, more interactions take place because the average energy of particles increases. By extrapolation, at the earliest times, all possible particles were relativistic and if interactions were strong enough, they remained in thermal equilibrium. Doing the reverse pass, as the universe cools the particles become non-relativistic and some of them fall out of equilibrium, leaving around relics that we see today and making departures from thermal equilibrium what makes life interesting. Non-equilibrium dynamics allows massive particles to acquire cosmological abundances. In addition, deviations from equilibrium are also crucial for understanding the origin of the Cosmic Microwave Background and the formation of the light elements. In Table 1.1, we show some of the most important steps in the history of the universe according to the approximate temperature of the universe and the approximative moment it happened.

1.2.2 The Cosmic Microwave Background

The first predictions of the Cosmic Microwave Background have been made in the late 40's [Gamow 1948, Alpher & Herman 1948]. It was the consequence of a model of universe in expansion with an early phase hot and dense. As we have seen previously, the thermal distribution of the photons should have a blackbody (Planckian) distribution. The photons in the Cosmic Microwave Background last scattered off electrons and then traveled freely trough space. That's why the CMB is the oldest accessible light in the Universe, and one of the most powerful probe of the early Universe. But the physicists thought at first that the detection of such a weak signal (attenuated by the expansion the Universe) would be impossible, and the prediction remained of theoretical interest for couples of decades. However, by a lucky coincidence, two engineers from Bell's laboratories Penzias and Wilson, found in 1964 an excess of noise while calibrating their antenna [Penzias & Wilson 1965]. This signal was consistent with a value in temperature units of the order of 3.5 K on several separated positions on the sky[14]. The Cosmic Microwave Background was discovered [Dicke *et al.* 1965]! However Penzias and Wilson made a measurement at a single wavelength, and the Planck form of the radiation frequency distribution was still to be verified. Other measurements consistent with the expected equivalent blackbody temperature of the CMB were even done earlier, by using absorption of light by molecules in interstellar space [McKellar 1941], but due to a lack of clear conclusion at that time they were not considered as strongly as the measurement of Penzias and Wilson. In the 90's, the FIRAS instrument embarked on the COBE satellite ([Mather *et al.* 1990], [Mather *et al.* 1994]) made the most precise measurement of the frequency spectrum of the Cosmic Microwave Background radiation observed today, as shown in the Fig. 1.4. This spectrum is consistent with a black body spectrum with temperature at 2.725 K. We will see later (see Chap. 2) that in addition to this remarkable agreement with an isotropic radiation, the CMB has small anisotropies which can be understood by going beyond the Standard Model.

1.2.3 Interaction rates and the Boltzmann equation in a expanding universe

If we look around us, we find only matter. That means that there is no or *very very* little anti-matter. The most recent estimation gives a present-day asymmetry between matter and anti-matter of the order of one-in-a-billion or so. We could ask the question why such an asymmetry.This question was investigated by Andrei Sakharov, and he defines three necessary conditions for such asymmetry [Sakharov 1967]. Let X and $\bar{Y}$ be some particle and some antiparticle respectively:

- Baryon number violation. Particle physics must allow interactions which change the number of baryons, including $X + \bar{Y} \rightarrow B$, where B represents some state of particles with net baryon number different from zero.

[14] The temperature nowadays of the CMB is very small because it has been redshifted by roughly a factor 1,000 since its emission.

Table 1.1: The history of the universe in few facts.

T (K)	t (s)	
10^{32}	10^{-43}	The Planck era: Classical GR breaks down
10^{29-27}	$10^{-(35-38)}$	Thermal Equilibrium established. GUT transition ?
10^{15}	10^{-11}	Electroweak phase transition
$1-5\times10^{12}$	$10^{-(5-6)}$	Quark confinement ("chiral symmetry breaking")
10^{11}	10^{-4}	$\mu^+\mu^-$ annihilation (and freeze out)
10^{10}	1	ν decoupling
5×10^{9}	$3-4$	e^+e^- annihilation, leaves mainly γ,
		$(\nu\bar{\nu})$ separately in equilibrium
10^{11-9}	180	Primordial nucleosynthesis $\rightarrow$ ^{4}He, D, T, Li
10^{5-3}	10^{10-11}	Matter domination (matter/radiation equality $\sim$ 65,000 K)
10^{3-2}	10^{11-13}	H recombination ($e+p\rightarrow H+\gamma$),
		Universe becomes neutral and transparent
10^{1}	-	Structure formation
2.725	10^{17}	today

Note. — Temperature and time values are approximative.

- CP violation. If CP is not violated, then in quantum field theory for any interaction, the related interaction with all particles replaced by antiparticles and vice versa will have exactly the same rate.
- Departure from equilibrium. In thermal equilibrium, the rate of a reaction going forward ($X+\bar{Y}\rightarrow B$) will be the same as the rate of the reaction going backward ($B\rightarrow X+\bar{Y}$), again canceling out any change in baryon number.

They are the Sakharov conditions.But even if they are all satisfied, in order to calculate the abundance of some particle species in more generalities, we need to consider its interactions in detail.

The Eq. 1.29 implicitly assumes that the universe is in thermal equilibrium [15] , but we saw that there have been several departures from thermal equilibrium. If the mean time Γ^{-1} of the interaction becomes bigger than the Hubble time H^{-1}, then

[15]The dominant interaction in the primordial plasma (before recombination) is the Compton interaction between photons and electrons (protons are off due to the ratio $(m_e/m_p)^2 << 1$). This interaction does not allow the plasma to have a black body distribution, that is the distribution in frequency of the photons is a Bose-Einstein distribution S_μ:

$$S_\mu(\nu;T,\mu)=\frac{2hc^2\nu^3}{e^{x+\mu}-1} \tag{1.31}$$

where $x=hc\nu/(kT)$. Double Compton interaction is needed to reach the thermal equilibrium ([Danese & De Zotti 1982], [Bartlett 2001]) because it allows the number of photons to change, and set to zero the chemical potential.

we should expect departure from thermal equilibrium, a freeze-out[16]. A particle that freezes out when its $kT >> mc^2$ is called a hot relic, and one that freezes out when $kT << mc^2$ is a cold relic. These deviations from equilibrium have led to some relics such as light elements (H, He, ... - cold relics), a neutrino and photon backgrounds (hot relics), etc. and quite possibly in production of dark matter in the early universe.

For phenomena that are the result of nonequilibrium physics, the appropriate formalism is here the *Boltzmann equation*. In its general form, the Boltzmann equation tells us for species i that only the interactions can change the distribution function form:

$$L\Big[f_i\Big] = C\Big[f_i\Big] \tag{1.32}$$

where f_i f is the phase space density (the time-dependent density of particles in position and momentum for non-relativistic species) and L is the Liouville operator, just the total time derivative of the distribution function for particle species i:

$$L = p^\alpha \partial_\alpha - \Gamma^\alpha_{\beta\gamma} p^\beta p^\gamma \frac{\partial}{\partial p^\alpha}. \tag{1.33}$$

The quantity $C\Big[f_i\Big]$[17] represents the effect of interactions, which unfortunately can possibly depend on the distribution function of all other species j. Naturally, we want to perform computation in a FLRW universe, homogeneous and isotropic, so we must take into account the expansion of the universe. The easiest case is when there are no interactions, and the *comoving* number density of particles is conserved (a fact that was known from the continuity equation 1.16)

$$\frac{dn}{dt} + 3\frac{\dot{a}}{a} n = 0, \tag{1.34}$$

where n is the number density. In this context, the Liouville operator is simply $L = d/dt + 3\dot{a}/a$. We shall now write explicitly the collision operator C, which depends on the interactions we are considering. In thermal equilibrium, we know that the number density n should obey the equilibrium distributions (Bose-Einstein or Fermi-Dirac, not discussed here). Consider interactions such as annihilation or recombination (two-particle to two-particle interaction). In equilibrium, the number of forward interactions is the same as inverse interactions. The forward rate is $\sigma|v|n^2$, where σ is the cross-section, and $|v|$ the relative velocity of the particles. The inverse rate must be such that the collision term is zero when $n = n_{eq}$, the number density in equilibrium. That is, we can re-write Eq. 1.32 as:

$$\frac{dn}{dt} + 3\frac{\dot{a}}{a} n = - < \sigma|v| > \left(n^2 - n_{eq}^2\right) \tag{1.35}$$

[16] The comparison between the rate of interactions Γ and the rate of expansion H is the key to understanding the thermal history of the Universe.

[17] C is sometimes called the collision operator.

where $< \sigma|v| >$ is the thermally-averaged product of the cross section and the relative velocity. The second factor on the left-hand side accounts for the dilution effect due to the expansion of the universe and the right-hand side term accounts for the interactions that change the number of particles. We can rewrite the equation one more time to get:

$$\frac{\dot{n}}{n_{eq}} = -\Gamma\Big(\frac{n^2}{n_{eq}^2} - 1\Big) - 3\frac{\dot{a}}{a}\frac{n}{n_{eq}} \tag{1.36}$$

where $\Gamma =< \sigma|v| > n_{eq}$ is the interaction rate. The solution of this equation is usually solved numerically, and we show such a solution in Fig. 1.5. The dashed line shows the solution at the equilibrium, and the solid line corresponds to freeze-out. Notice that in general higher Γ results in latter departure from equilibrium (plateau appears for higher value of redshift).

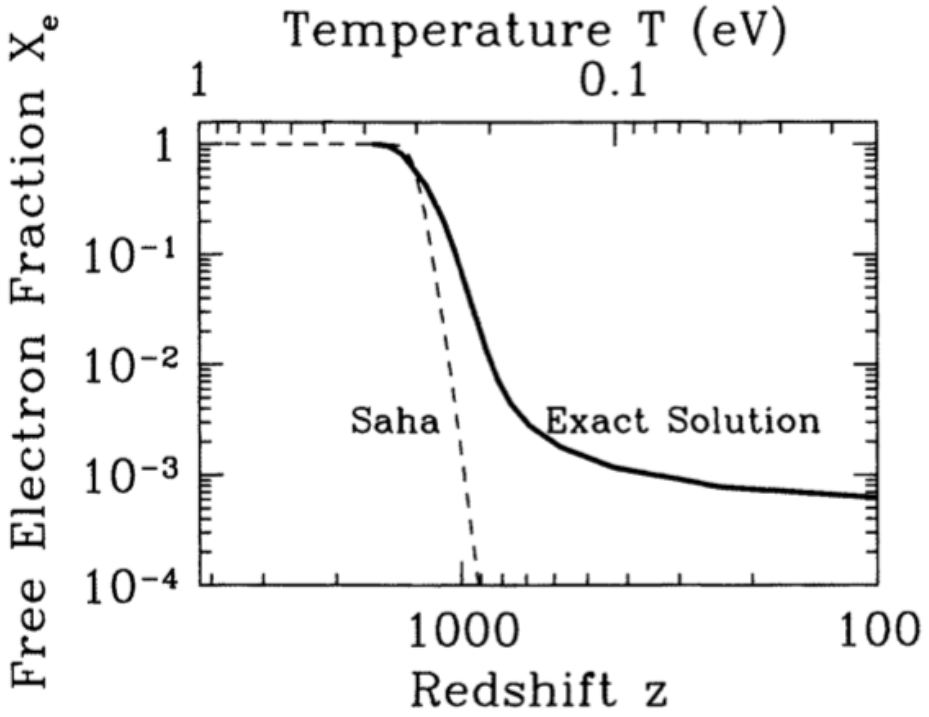

Figure 1.5: Free electron fraction as a function of redshift. The dashed line shows the solution at the equilibrium (called Saha approximation), and the solid line corresponds to freeze-out. Recombination takes place almost suddenly at $z \sim 1000$ corresponding to $T \sim 1/4$ eV. The fact that the decoupling happened in an interval Δz and not instantaneously has important observational consequences as we will see later. Figure adapted from [Mukhanov 2005].

1.2.4 Limits of the model

The Hot Big Bang scenario that we outlined in the previous sections is a remarkably simple model describing the expansion of the universe, the Big Bang primordial nucleosynthesis and the Cosmic Microwave Background. However, there are some observables that cannot be explained by the model, and require further extensions[18]. I briefly mention four of them here:

The problem of (in)homogeneities or origins of structures. We built our cosmological model based on the Cosmological Principle which states statistical homogeneity and isotropy at large scales. However, we do observe structures today (think of the galaxies, the clusters of galaxies and so on). Those structures could come from the gravitational collapse of small inhomogeneities. To account for the structures that we see in the Universe, we therefore need a model to explain the seeds of inhomogeneities.

Flatness. Going back to the Friedmann equation:

$$\Omega_{tot} - 1 = \frac{\kappa}{a^2 H^2}, \tag{1.37}$$

and noticing that $a(t)$ is only an increasing function of the time t, the term $|\Omega_{tot} - 1|$ diverges while t tends towards zero. That means that to observe today a flat universe we would need at Planck's time (10^{-43} s):

$$\Omega_{tot} - 1 \sim 10^{-60}. \tag{1.38}$$

A priori, nothing prevents such a value, but we are facing a very special *initial condition*. We often find the term *fine tuning* in the literature to illustrate the fact that Ω_{tot} is set optimally in the early universe to give a nearly perfectly flat universe today.

Horizon. We call (particle) horizon the maximum distance that a light ray can travelled from a given time t_i to a time t. Let $dr = a(t)dt$ be the radial trajectory of the light ($ds^2 = 0$), that is the horizon $d_H t$ can be expressed as:

$$d_H(t) = a(t) \int_{t_i}^{t} \frac{dt'}{a(t')} = a(t) \frac{t^{1-p} - t_i^{1-p}}{1-p}, \tag{1.39}$$

assuming $a(t) \propto t^p$. In the standard cosmology ($p < 1$), the integral does converge in the limit $t_i \to 0$ and the horizon has a finite size, of the order of the Hubble radius:

$$d_H(t) = \frac{p}{1-p} H^{-1}. \tag{1.40}$$

[18] The problem of dark energy is treated elsewhere (see Secs. 1.1.5 & 3.6).

From the measure of H_0 today and considering its evolution in a matter dominated era, one can compute the the size of the horizon at the moment of the matter/radiation decoupling. However, Cosmic Microwave Background observations show that the universe at that time was extremely homogeneous (of the order of 10^{-5}) over much bigger distances. So we need a mechanism to explain that the universe be homogeneous over scales bigger than the horizon scale[19].

The monopoles. We do not observe monopole relics which would be nonetheless expected by the Theory of Grand Unification (GUT) due the transition phases in the early universe.

In the early 80's, while the Hot Big Bang scenario was in a strong bargaining position thanks to more and more observational facts, it couldn't answer those questions. As of now, only the paradigm of inflation seems to give the most comprehensive answer to all of those problems.

1.3 Inflation as tentative answer to the limitation of the HBB scenario

The inflation epoch is defined as a period of accelerating expansion of the universe and was first introduced by Starobinski (1979) and Guth (1981). The inflation scenario was proposed to solve the horizon and monopole problems as discussed in the previous section over the Standard Model of Big Bang[20].

Inflation, by supposing that the expansion of the universe undergoes an accelerated phase before the radiation domination era solves *all* the problems mentioned earlier[21]. According to it, the matter fluctuations would be the results of quantum fluctuations of a given field which would have experienced a quantum-classical transition during the inflation era. The generic consequences of these models are the following: gaussian initial fluctuations with a scale-invariant spectrum of perturbations, and a nearly zero-curvature universe (flat). Those three consequences are consistent with all the recent data.

I will neither give an exhaustive presentation of inflation theories[22], nor describe all the *zoology* of inflationary models. For a comprehensive review of inflation and inflationary models, see for instance [Martin *et al.* 2014]. Instead, I will briefly describe a simple toy model of inflation to provide the intuition on the Physics of inflation and the consequences of such a model in the early Universe, loosely following [Baumann 2009].

[19] Of course, one assumes a finite speed of light and finite age for the universe.

[20] The fact that inflation deals with fluctuations was not initially thought.

[21] Although there are models of early Universe which do not require accelerated phase, see for example the varying speed of light model [Albrecht & Magueijo 1999].

[22] There are several, inflation being a generic name which postulated an accelerated phase in the early universe

1.3.1 Scalar fields dynamics

As a simple toy model for inflation we consider a single scalar field. In the context of Inflation, this scalar field is called the inflaton[23] $\phi(t, \mathbf{x})$. The value of the field can depend on time t and the position in space $\mathbf{x}$. Associated with each field value is a potential energy density $V(\phi)$. If the field changes with time (*i.e.* is dynamical) then it also carries kinetic energy density and if the stress-energy associated with the scalar field dominates the universe, it sources the evolution of the FRW background. Starting from the action of a scalar field, one can express its stress-energy tensor $T_{\mu\nu}$:

$$T_{\mu\nu} = \partial_\mu\phi\partial_\nu\phi - g_{\mu\nu}\Big(\frac{1}{2}g^{\alpha\beta}\partial_\alpha\phi\partial_\beta\phi - V(\phi)\Big). \tag{1.41}$$

Following symmetries defined in Sec. 1.1.2, we require that the background value of the inflaton only depends on time t (homogeneity). Relating the 00 component of the stress-energy tensor to the energy density of the field ρ_ϕ, and the ii component (space-space component, $T^i_j = -P_\phi\delta^i_j$) to the pressure P_ϕ of the field we have:

$$\rho_\phi = \frac{1}{2}\dot{\phi}^2 + V(\phi) \tag{1.42}$$

$$P_\phi = \frac{1}{2}\dot{\phi}^2 - V(\phi), \tag{1.43}$$

where $\dot{\phi} = \partial_t\phi$. One can immediately see that if the potential energy dominates over the kinetic energy, a configuration leading to inflation corresponds to $P_\phi < -1/3\rho_\phi$. From the Friedmann equations defined earlier, one can write the evolution equation for the field, or also named the Klein-Gordon equation of the field:

$$\ddot{\phi} + 3H\dot{\phi} + V' = 0. \tag{1.44}$$

In the language of mechanics, it is interesting to notice that the potential acts like a force ($V' = dV/d\phi$), while the expansion of the Universe play the role of friction ($H\dot{\phi}$). Finally, the Friedmann equations in a flat Universe would lead to:

$$H^2 = \frac{8\pi G}{3}\Big(\frac{1}{2}\dot{\phi}^2 + V(\phi)\Big) \tag{1.45}$$

$$\dot{H} + H^2 = -\frac{4\pi G}{3}\Big(\rho_\phi + 3P_\phi\Big) \tag{1.46}$$

1.3.2 Physics of Inflation

In this section, we want to determine under which conditions we end up with an accelerated expansion. In order to have an inflationary period[24], the simplest condition is to have:

[23] We will not discuss here the physical nature of this field, but simply use it as an order parameter to parametrize the time evolution of the inflationary density.

[24] that is a decrease of the *comoving* Hubble radius.

$$\frac{d}{dt}\Big(\frac{1}{aH}\Big) < 0, \tag{1.47}$$

or equivalently $\ddot{a} > 0$. In the literature, the inequality above is often re-written in term of the parameter ε:

$$\frac{d}{dt}\Big(\frac{1}{aH}\Big) = -\frac{1}{a}(1 + \frac{\dot{H}}{H^2}) = -\frac{1}{a}(1 - \varepsilon) < 0. \tag{1.48}$$

The shrinking comoving Hubble sphere therefore also corresponds to:

$$\varepsilon = -\frac{\dot{H}}{H^2} < 1. \tag{1.49}$$

The first Friedmann equation and the continuity equation together imply that inflation requires negative pressure or a violation of the strong energy condition:

$$\varepsilon = -\frac{\dot{H}}{H^2} = \frac{3}{2}\Big(1 + \frac{P_\phi}{\rho_\phi}\Big) < 1. \tag{1.50}$$

How much "inflation" do we need to solve the horizon problem that is how long should last inflation? The length of inflation can be in general expressed as a number of the so-called e-fold. Let's rewrite the inequality 1.49 in a slightly different fashion:

$$\varepsilon = -\frac{\dot{H}}{H^2} = -\frac{d\ln H}{dN} < 1, \tag{1.51}$$

where dN is defined as $dN = d\ln a = Hdt$, and measure the number of e-folds N of inflationary expansion. Typically, in order for inflation to solve the problem of horizon, $N \sim 40 - 60$ e-folds is required. In addition, Eq. 1.51 tells us that the fractional change of the Hubble parameter per e-fold is small. That is ε should remain small for time periods much longer than the Hubble times. In order to quantify this statement, let's define a second parameter, called η, such as:

$$\eta = \frac{d\ln\varepsilon}{dN} = \frac{\dot{\varepsilon}}{H\varepsilon}, \tag{1.52}$$

and require that $|\eta| < 1$ together with $\varepsilon < 1$. ε can also be written in terms of the kinetic energy of the field and the total energy density of the field:

$$\varepsilon = -4\pi G\frac{\dot{\phi}^2}{H^2} = -3\frac{\frac{1}{2}\dot{\phi}^2}{\rho_\phi}. \tag{1.53}$$

Therefore, the inequality 1.49 is satisfied only if the kinetic energy makes a small contribution to the total energy density ρ_ϕ. This situation is called slow-roll inflation. It is noteworthy that we didn't use any approximations so far. We just noted that in the regime $\{\varepsilon, \eta\} << 1$, inflation occurs and its duration to be sufficient to solve the different problems of the Standard Model of Cosmology. Let's now use this approximation ($\{\varepsilon, \eta\} << 1$) to simplify the first Friedmann equation 1.45 and the Klein-Gordon equation 1.44 respectively:

$$H^2 \approx \frac{8\pi G}{3} V \tag{1.54}$$

$$3H\dot{\phi} \approx -V'. \tag{1.55}$$

Finally, a convenient way to assess whether a given potential $V(\phi)$ can lead to slow-roll inflation is to compute the potential slow-roll parameters:

$$\varepsilon_v = \frac{1}{16\pi G}\left(\frac{V'}{V}\right)^2 \tag{1.56}$$

$$|\eta_v| = \frac{1}{8\pi G}\frac{|V''|}{V}. \tag{1.57}$$

Successful slow-roll inflation occurs when these parameters are small together, $\{\varepsilon_v, |\eta_v|\} << 1$

Under some assumptions, the latest derived constraints for the first two slow-roll potential parameters from the Planck satellite [Planck Collaboration 2015g] are[25]:

$$\varepsilon_v < 0.0068 \qquad \text{(95\% CL, Planck TT + LowP)} \tag{1.58}$$

$$\eta_v = -0.010^{+0.005}_{-0.009} \qquad \text{(68\% CL, Planck TT + LowP)} \tag{1.59}$$

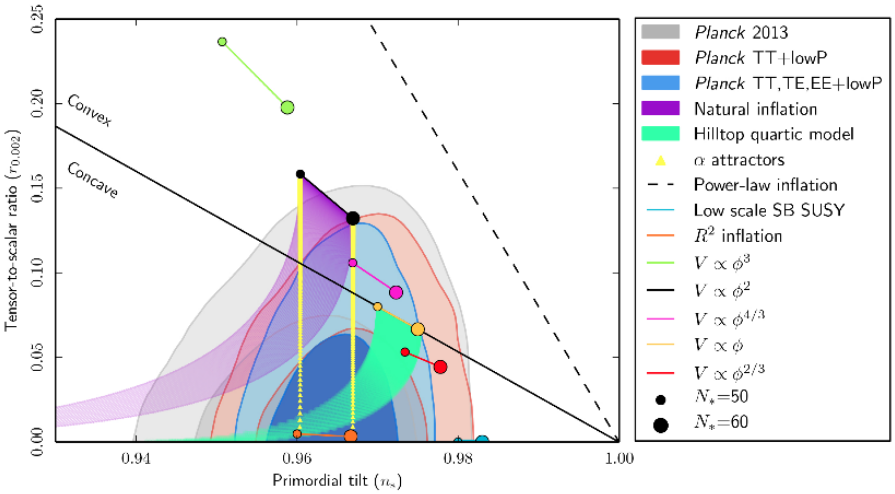

Figure 1.6: Marginalized joint 68% and 95% CL regions for n_s and $r_{0.002}$ from Planck in combination with other data sets, compared to the theoretical predictions of selected inflationary models. R^2 inflation seems favor, but the constraints are on overall not very tight. Figure adapted from [Planck Collaboration 2015g].

[25] Assuming standard slow-roll single-field inflationary models, and using the Planck intensity power spectrum (TT) and polarized spectra (LowP).

1.3.3 Reheating

During inflation most of the energy density in the universe is in the form of the inflaton potential energy $V(\phi)$. Inflation ends when the potential steepens (for most classes of inflation) and the inflaton field picks up kinetic energy. But the question is how the energy in the inflaton sector has been transferred to the particles of the Standard Model, and how did such a transition take place from an universe which had an equation of state with negative pressure to a universe with a more natural equation of state? A process called reheating is largely evoked within the literature and this is when the Hot Big Bang phase starts.

After inflation, the inflaton field ϕ undergoes a phase of oscillation. It begins to oscillate at the bottom of the potential, and the expansion time scale soon becomes much longer than the oscillation period that is $H^{-1} >> m^{-1}$ (assuming a potential $V(\phi) = 1/2m^2\phi^2$). From the continuity equation, one can notice that the oscillating field therefore behaves like pressure-less matter, and the fall in the energy density is reflected in a decrease of the oscillation amplitude. Then to avoid that the universe ends up empty, the inflaton has to couple to the fields of the Standard Model. The energy stored in the inflaton field is then be transferred into ordinary particles. The particles produced by the decay of the inflaton interact, create other particles through particle reactions, and the resulting particle soup eventually reaches thermal equilibrium.

1.3.4 Generation of cosmological fluctuations

So far, we discussed the classical evolution of a scalar field called the inflaton field on top of a homogeneous and isotropic universe. One can show that if we consider quantum fluctuations of the inflaton, accelerated inflation provides an elegant mechanism for converting initial vacuum quantum fluctuations into macroscopic cosmological perturbations. In other words, quantum fluctuations during the accelerated inflation are the source of the primordial power spectra of scalar and tensor fluctuations. We should also keep in mind that even if we used a quantum description for the scalar field, the cosmological perturbations that we are seeing are usually described classically. Roughly speaking, the transition between the quantum and classical (although stochastic) descriptions takes place when the perturbations exit the Hubble radius (quantum-classical transition) [Langlois 2005]. Perturbations are pushed outside the radius of causal contact (Hubble radius) by the rapid expansion, and they only re-enter the horizon again at some point during the radiation or matter dominated eras, as shown in Fig. 1.7. A complete treatment of the problem is beyond the scope of this introduction, so I will highlight the main results of interest for us for the scalar and tensor cases. This part follows closely the treatment done by [Langlois 2005].

Perturbed inflaton in a perturbed metric - the scalar case The treatment of fluctuations in the early universe, either classical or quantum, must thus involve

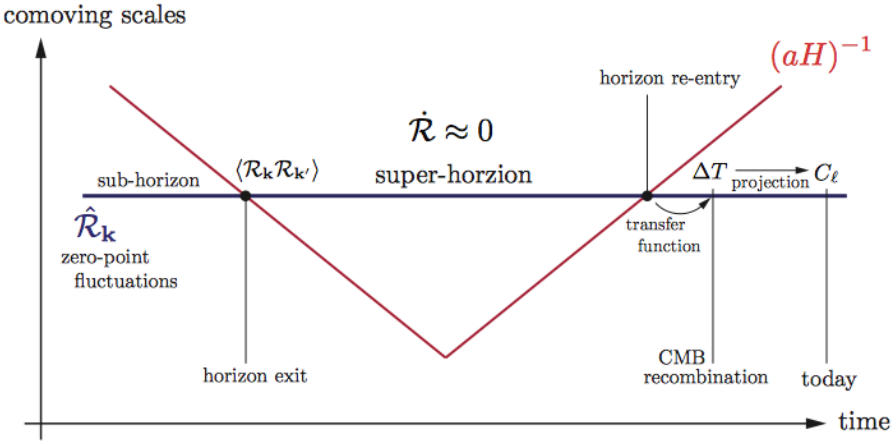

Figure 1.7: Evolution of perturbations during and after the inflationary period. The comoving scales k^{-1} (blue) remain constant, but the comoving Hubble radius during inflation, $(aH)^{-1}$, shrinks and the perturbations exit the horizon and freeze until horizon re-entry at late times. After that the fluctuations re-enter the horizon, they give rise to anisotropies in the CMB and perturbations in the large-scale structure. Figure taken from [Baumann 2009].

both the scalar field perturbations and metric perturbations. The homogeneities grow because of the gravity is attractive, and so inhomogeneities were much smaller in the past. For most of their evolution, inhomogeneities can be treated as linear perturbations, and the linear treatment only starts to be no more valid in our recent past. However, the linear assumption is quite accurate when describing perturbations at the moment of the recombination. Therefore that's why the CMB is currently the best observational probe of those primordial perturbations. So starting from a metric in a de Sitter space, we need also to take into account the linear perturbations. In its most general form, one can write:

$$ds^2 = a^2\Big\{ -(1+2A)d\tau^2 + 2B_i dx^i d\tau + (\delta_{ij} + h_{ij}) dx^i dx^j \Big\}, \tag{1.60}$$

where A and B_i are a scalar field and a vector field respectively, and δ_{ij} and h_{ij} are the spatial metric and a symmetric tensor field respectively. Those quantities are related to the so-called scalar, vector and tensor modes. Note that we assume a spatially flat metric. The full action for the inflaton (scalar field) and for gravity is given by:

$$S = S_\phi + S_{EH} = \int d^4x\sqrt{-g}\Big(-\frac{1}{4}\partial_\mu\phi\partial^\mu\phi - V(\phi)\Big) + \frac{M_p^2}{2}\int d^4x\sqrt{-g}R. \tag{1.61}$$

In order to study the linear perturbations about the FLRW background (homogeneous and isotropic), we restrict ourself to the flat gauge corresponding to the choice

$h_{ij} = a^2(t)\delta_{ij}$. So the scalar fields on the corresponding (flat) hypersurfaces can be decomposed into a spatially homogeneous background $\bar{\phi}$ and its perturbation $\delta\phi$ as:

$$\phi = \bar{\phi} + \delta\phi. \tag{1.62}$$

Expanding to quadratic order the action in Eq. 1.61, one can show that the scalar part can be expressed as[26]:

$$S^{(2)}_{sca} = \frac{1}{2}\int d\tau d^3x a^2 \Big[\delta\dot{\phi}^2 - \frac{1}{a^2}\partial_i\delta\phi\partial^i\delta\phi - \mathcal{M}^2\delta\phi^2\Big], \tag{1.63}$$

with $\mathcal{M}$ being an effective mass, given by:

$$\mathcal{M}^2 = V'' - \frac{1}{a^3}\frac{d}{dt}\Big(\frac{a^3}{H}\dot{\phi}^2\Big). \tag{1.64}$$

One can define the canonical perturbation v such as

$$v = a\delta\phi \tag{1.65}$$

leading to the action

$$S^{(2)}_{sca} = \frac{1}{2}\int d\tau d^3x \Big[(v')^2 + \partial_i v\partial^i v + \frac{z''}{z}v^2\Big], \tag{1.66}$$

This leads to a power spectrum $P_v(k)$ such that

$$\mathcal{P}_v(k) = k^3\frac{|v_k|^2}{2\pi^2} \tag{1.67}$$

However in the literature, instead of v, we often see the comoving curvature perturbation $\mathcal{R}$, related to v by

$$v = z\mathcal{R} \tag{1.68}$$

with corresponding power spectrum

$$\mathcal{P}_\mathcal{R}(k) = k^3\frac{|v_k|^2}{2\pi^2 z^2}. \tag{1.69}$$

We can even go further by assuming the slow roll approximation, leading to $z''/z \approx a''/a$ and

$$\mathcal{P}_\mathcal{R}(k) \approx \frac{\hbar}{4\pi^2}\Big(\frac{H^4}{\dot{\phi}^2}\Big)_{k=aH} = \frac{\hbar}{2M_p^2\varepsilon_*}\Big(\frac{H_*}{2\pi}\Big)^2 \tag{1.70}$$

where quantities with stars are evaluated at Hubble crossing (k=aH). This power spectrum is the so-called spectrum of scalar cosmological perturbations generated from vacuum fluctuations during a slow roll inflation phase.

[26]The zeroth order of the development of the action contains only the homogeneous part, the first order contains all terms linear in the perturbations, but only the second order contains the terms quadratic in the linear perturbations.

Perturbed inflaton in a perturbed metric - the tensor case As seen in the Eq. 1.60, tensor fluctuations are transverse-traceless perturbations to the metric, which can be viewed as gravitational waves. In the inflationary scenario primordial gravitational waves are generated from vacuum fluctuations as the scalar perturbations. Expanding to quadratic order the action in Eq. 1.61, one can show this time that the tensor part can be expressed as:

$$S^{(2)}_{tens} = \frac{M_p^2}{8}\int d\tau d^3x a^2 \eta^{\mu\nu}\partial_\mu \bar{E}^i_j \partial_\nu \bar{E}^j_i \tag{1.71}$$

where $\eta^{\mu\nu}$ is the Minkowski metric and E^i_j a symmetric tensor depending on h_{ij} and derivatives of the lapse function. One can show that the gravitational waves can be viewed as two massless scalar fields - one for each polarization - and so the power spectrum of tensor cosmological perturbations generated from vacuum fluctuations is given by

$$\mathcal{P}_{\mathcal{T}}(k) = 2 \times \frac{2\hbar}{M_p^2}\left(\frac{H}{2\pi}\right)^2 \overset{\text{slow roll}}{=} \frac{8\hbar}{M_p^2}\left(\frac{H_*}{2\pi}\right)^2. \tag{1.72}$$

It is interesting to note that the power spectrum of tensor depends only on H_*, while the power spectrum of scalar depends on both H_* and the slow roll parameter ε_*. Thus a measurement of the tensor amplitude would direction probe energy scales during inflation. In addition, one can define the so-called tensor-to-scalar ratio r as

$$r = \frac{\mathcal{P}_{\mathcal{T}}}{\mathcal{P}_{\mathcal{R}}} \tag{1.73}$$

given at a certain scale k. For example, the best constraints from B-modes is from the joint analysis Planck x BICEP2. They quoted an upper limit on r at scale $k = 0.05$ Mpc^{-1}, $r_{0.05} < 0.12$ at 95% confidence level [Ade *et al.* 2015].

1.3.5 Implication from inflation

The theoretical aspects of inflation described above are interesting because they can be tested experimentally using present and future cosmological data sets. To compare different inflationary predictions, the primordial spectra of scalar and tensor perturbations in Eq. 1.69 and 1.72 are often parametrized by an amplitude A and a spectral index n such as[27]

$$\mathcal{P}_{\mathcal{R}}(k) = A_s\left(\frac{k}{k_*}\right)^{n_s-1} \tag{1.74}$$

$$\mathcal{P}_{\mathcal{T}}(k) = A_t\left(\frac{k}{k_*}\right)^{n_t}, \tag{1.75}$$

where k_* is a scale of reference (arbitrarily chosen). The scalar spectral index n_s equal to one corresponds to a scale-invariant spectrum of perturbations. So a measurement of n_s different than one would mean a departure from the scale invariance.

[27] No running is considered here.

Recently, PLANCK in combination with other experiments measured a value of n_s slightly different from one, with $n_s = 0.9673 \pm 0.0045$ (see also Fig. 1.6). Another robust and model-independent prediction of inflationary models is the production of a stochastic background of gravitational waves. In addition, the amplitude of the primordial spectrum of tensor perturbations is only dependent of the Hubble crossing scale H_* (k=aH). Those two spectra (scalar and tensor) are connected through the tensor-to-scalar ratio r, which is is a valuable source of information for the physics of the primordial universe since it directly sets the energy scale for inflation

$$V^{1/4} \approx \left(\frac{r}{0.01}\right)^{1/4} 10^{16} \text{ GeV} \tag{1.76}$$

where we supposed that the spectrum of scalar perturbations is fixed and the one for tensor is proportional to the potential $V(\phi)$. This prediction means that any measurement of a primordial gravitational waves signature would give information about energy scale of inflation and distinguish between models of inflation. This also means that a measured value of $r \geq 0.01$ corresponds to test a physical regime in the playground of Grand Unified Theories. In addition, the tensor-to-scalar ratio is directly related to the number of e-folds, N_{inf}, and the excursion of the scalar field, $\Delta\phi$, from the instant when cosmological fluctuations observed in the CMB are created during inflation to the end of inflation [Lyth 1997]:

$$N_{\text{inf}} = \sqrt{\frac{8}{r}} \times \frac{\Delta\phi}{M_p}, \tag{1.77}$$

with $M_p = 1/\sqrt{8\pi G}$ the reduced Planck mass. Single field inflationary models can be roughly classified between large fields models and small fields models, whether the excursion of the scalar field is transplanckian or subplanckian, respectively. Though the value $\Delta\phi/M_p = 1$ should not be considered as a sharp and univocally defined frontier between small fields and large fields models, a precise measure of r then allows for discriminating between this two classes of models. For $N_{\text{inf}} \sim 30$, a value of r greater than ~ 0.01 would correspond to a large fields model of inflation (see however Ref. [Chatterjee & Mazumdar 2015] and references therein for examples of small fields models evading the Lyth bound). As we will see in the next chapter, the B-modes power spectrum is the main source of information on r, as its amplitude is directly proportional to r, therefore the most dramatic confirmation of inflation would come from a detection of primordial B-mode polarization.

Chapter 2

CMB anisotropies

Contents

2.1 From primordial fluctuations to anisotropies in the CMB

The inflationary phase left density fluctuations as we have seen previously, and the amplitude of those fluctuations remains constant as long as they are larger than the size of the horizon. Depending on their comoving size (k^{-1}), the modes re-enter the horizon at a different time, see Fig. 1.7. For large-scale perturbations (with wavelength greater than the horizon size), the perturbations is frozen into its initial conditions and it does not evolve much. For smaller perturbations, the re-entry is done earlier and the evolution of the modes becomes more complex. As the Universe expands and the temperature decreases, the matter starts little by little to dominate over the radiation, and the overdense region starts to collapse under the action of the gravity (the perturbations grow). The density in those overdense regions increases, and so does the radiation pressure. However, the baryons are still strongly coupled to radiation at that time, and so the amplitude of the overdense regions decreases, leading to a decrease of the temperature and the radiation pressure becomes so large that it can withstand the tendency towards collapse. When the radiation pressure

is too low, the gravity (matter) wins again, and there is a new collapse. This scheme repeats again and resulting in what we call the acoustic oscillation, which is a phase of oscillation of densities[1]. Physically these density oscillations represent the heating and cooling of a fluid (photon-baryon fluid) that is compressed and rarefied by a standing sound or acoustic wave.

Given that the re-entry of the horizon depends only on the comoving size of the fluctuations, the smallest fluctuations start to oscillate first, and all the fluctuations with the same comoving size start to oscillate at the same time. This mechanism of oscillation stops the moment the coupling photon-baryon becomes negligible.This moment is called the recombination (or decoupling). From that moment, the baryon can freely collapse in the potential wells of a non-baryonic matter, called dark matter, and which doesn't oscillate because it has no coupling with the radiation (dark matter needs to be non-baryonic so that the primordial potential in which baryons fall into can already be in place). As a result of those collapses the structures that we observe today form later: large-scale structures, cluster of galaxies and galaxies. The only overdensities that can grow with time has size greater than the Jeans length [Peebles & Dicke 1968]. On the other hand, the photons can escape from the potential wells, and freely travel in the Universe. We observe today those Cosmic Microwave Background photons *via* a quasi isotropic radiation with small fluctuations related to the density fluctuations of the baryons at the moment of recombination.

So if our comprehension of the structure formation via gravitational instability and collapse is correct, density fluctuations should also exist at the moment of the recombination. We should be able to detect those density fluctuations, that is the temperature variations of the Cosmic Microwave Background radiation. We know today that those fluctuations $\Delta T/T_0$ are of the order of 10^{-5}, that's why it took 20 years to build an instrument sensitive enough to detect them[2]. And the first evidence of *anisotropies* in the Cosmic Microwave Background was brought by the data taken by the instrument DMR embarked on the satellite COBE (COsmic Background Explorer) [Smoot *et al.* 1992].

In addition the standing sound waves[3] that propagated in the hot plasma of tightly coupled photons and baryons in the early Universe should leave a faint imprint in the clustering of galaxies and matter today, see for instance [Peebles & Yu 1970, Bond & Efstathiou 1984]. The signature is a small excess in number of pairs of galaxies separated by a certain scale, corresponding to roughly 150 Mpc in radius at recombination. These features are often referred to as the baryon acoustic oscillations (BAO), and the first measurement has been done *via* the large-scale correlation function of SDSS luminous red galaxies [Eisenstein *et al.* 2005].

[1] Those oscillations naturally gives rise to peaks that we see in the power spectrum of the anisotropies, described later.

[2] Before the first measurements, models predicted fluctuations of the order of 10^{-5} and even smaller in a large number of scenarios.

[3] The same sound waves that revealed as the acoustic oscillations in the anisotropies of the Cosmic Microwave Background.

2.2 CMB anisotropies: temperature

2.2.1 The angular power-spectrum

Models of structure formation which describe the origin of the anisotropies predict only their statistical properties. Accordingly, the first statistical quantity on which we focus on is the two-point correlation functions[4]. Notice that our universe is *one* realization of those initial stochastic processes. Since the CMB spectrum is an extremely good blackbody [Mather *et al.* 1994] with a nearly constant temperature across the sky T, we generally describe this observable in terms of a temperature fluctuation $\Delta T/T$. The temperature field in the universe is given by:

$$T(\mathbf{x}, \hat{p}, t) = T(t)\left[1 + \frac{\Delta T}{T}(\mathbf{x}, \hat{p}, t)\right], \tag{2.1}$$

where $\mathbf{x}$ is our position in the universe, $\hat{p}$ is the direction of the incoming photons (three-dimensional vector), and t is the conformal time (sometimes noted η). We do not need to define this field at every point in space and time, since we can observe it only here and now. From this information, observers typically make maps of the sky, displaying a pattern of hot and cold spots. Usually, we work with spherical coordinates (θ, ϕ). But how do the anisotropies of the Cosmic Microwave Background look like projected on our sky? We can answer this question by going back to the properties of the initial fluctuations: most of the inflationary models predict gaussian temperature anisotropies, with preferred angular sizes set by the physics at the moment of recombination. In Fig. 2.1, three all-sky maps delivered by the three satellites COBE [Bennett *et al.* 1996], WMAP [Bennett *et al.* 2013] and Planck [Planck Collaboration 2014a] are shown. Those are supposedly cleaned maps of the anisotropies of the Cosmic Microwave Background, at different sensitivities, pixelization sizes and beams. But they all give a picture of our universe back in time at the moment of recombination. A more complete description of the mapmaking process is done later in this manuscript (see Sec. 8).

Let's now project the fluctuations of our scalar field T on the basis of the spherical harmonic[5], well suited for functions defined on the sphere:

$$\frac{\Delta T}{T}(\mathbf{x}, t, \theta, \phi) = \sum_{\ell=1}^{\infty} \sum_{m=-\ell}^{\ell} a_{\ell m}(\mathbf{x}, t) Y_{\ell,m}(\theta, \phi). \tag{2.2}$$

The subscripts ℓ and m are conjugate to the real space unit vector (θ, ϕ). Notice that there is no loss of information at this point, all the information contained in the temperature field T is also contained in the space-time dependent amplitudes $a_{\ell m}$ (but the monopole). Instrumental setup will further put some constraints on the

[4] The mean - or monopole - is left on aside.

[5] We are all familiar with one-dimensional Fourier transforms, so it is useful to think of the expansion in terms of spherical harmonics as a kind of generalized Fourier transform. A detailed work on the harmonic analysis and spectral estimation on the sphere with application to CMB can be found for instance in [Guilloux 2008]. More generally there exists now an ample literature about spherical harmonic transforms applied for CMB purposes.

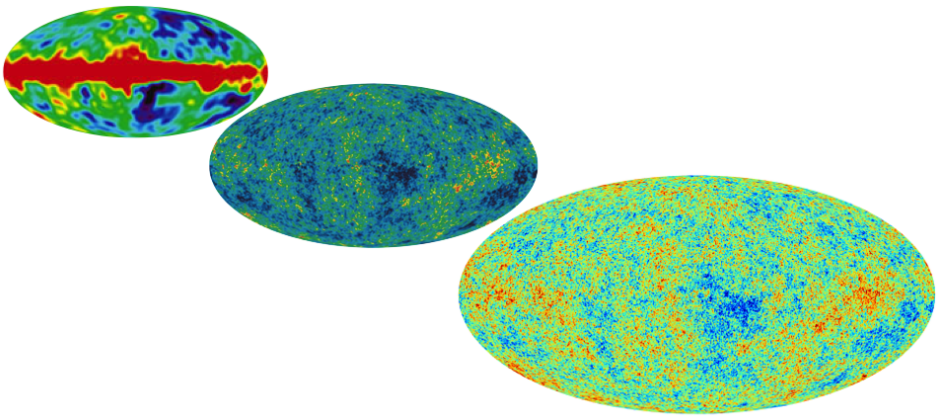

Figure 2.1: Maps of the anisotropies of the Cosmic Microwave Background. Maps taken from the results of the satellites: COBE (left), WMAP (middle) and Planck (right). The color scale, the pixelization size, the sensitivity, the beam and the treatment to get a cleaned map are not the same for all three pictures but we can see the resemblance between them and the progress achieved over the last two decades.

maximum multipole ℓ that we can probe. Ultimately, we would also be interested in the inverse transform, that is find the relation between the coefficients $a_{\ell m}$ and the temperature field. To do so, one needs to invoke the orthogonality properties of spherical harmonics:

$$\int d\Omega Y_{\ell m}(\theta,\phi) Y^*_{\ell' m'}(\theta,\phi) = \delta_{\ell\ell'}\delta_{mm'}, \tag{2.3}$$

where Ω is the solid angle spanned by (θ,ϕ). Using this inverse transform, one has:

$$a_{\ell m}(\mathbf{x},t) = \int d\Omega Y^*_{\ell m}(\theta,\phi)\frac{\Delta T}{T}(\mathbf{x},t,\theta,\phi). \tag{2.4}$$

This equation is sometimes written with the Fourier transform of $\Delta T/T(\mathbf{x},t,\theta,\phi)$, since this is the object that we usually get from earlier computations. In practice with real data, the integral is replaced by finite sums by means of (exact or approximate) quadrature formulae, which are implemented in standard packages for CMB data analysis such as HEALPix [Gorski *et al.* 2005], GLESP [Doroshkevich *et al.* 2005], ECP [Crittenden & Turok 1998], or S^{2}HAT [Szydlarski *et al.* 2014]. From what we previously discussed about the randomness of the density perturbations, we cannot make predictions about any particular $a_{\ell m}$ coefficient. Different theories cannot predict where precisely perturbations arise. But we know about the distribution from which they are drawn, a distribution which has its origin to the quantum fluctuations first laid down during inflation. That is the mean value of all the $a_{\ell m}$ is zero, with a non-zero variance. The variance of the $a_{\ell m}$ is called the *power-spectrum*, noted C_ℓ:

$$< a_{\ell m} >= 0 \qquad \text{and} \qquad < a_{\ell m} a^*_{\ell' m'} >= \delta_{\ell\ell'}\delta_{mm'} C_\ell \tag{2.5}$$

Note that, for a given multipole ℓ, each corresponding harmonic coefficient $a_{\ell m}$ has the same variance, because they are all drawn from the same distribution. However, Eq. 2.5 is not the one we usually use in the analysis. Indeed, this equation implies that we are able to average the $a_{\ell m}$ over all sets of realization of those perturbations, or strictly speaking on an infinite set of Universe. So instead we build an estimator of C_ℓ, denoted $\hat{C}_\ell$ by replacing the mean on an infinite set of Universe by the mean on $2\ell + 1$ m modes for each ℓ. The consequence of this replacement is represented through the Cosmic Variance. Loosely speaking it states that parameters, including the value of the estimator itself, are inevitably affected by an intrinsic uncertainty which cannot be canceled (the variability due to the peculiar realization of the random field that we are able to observe). This effect is more pronounced at low ℓ and is smaller for higher multipoles. When ℓ is large, we are effectively sampling the distribution, but not for lower ℓ ($2\ell + 1$ m modes are available for each ℓ). This estimator is given by:

$$\hat{C}_\ell =< |a_{\ell m}|^2 >= \frac{1}{2\ell + 1} \sum_{m=-\ell}^{\ell} |a_{\ell m}|^2, \tag{2.6}$$

and its variance (mode-by-mode) is given by:

$$\Delta\hat{C}_\ell = \frac{2}{2\ell + 1}\hat{C}_\ell^2. \tag{2.7}$$

2.2.2 Primordial anisotropies

The primordial anisotropies of the Cosmic Microwave Background are the anisotropies generated at or before the *last scattering surface*. By understanding the evolution of the photon perturbations, we can make predictions about the expected anisotropy spectrum today. However, there are more subtleties involved when passing from acoustic oscillations to anisotropies. The previous discussion in Sec. 2.1 helps to get a qualitative understanding of the acoustic peaks in the power spectra of the temperature, but we must consider more carefully the sources of anisotropies and their projection into multipole moments [Hu & Dodelson 2002]. The observed anisotropy today $\Theta = \Delta T/T$ is

$$\Theta(\hat{\mathbf{n}} = (\theta, \phi), \eta_0) = \sum_{\ell m} Y_{\ell m}(\hat{\mathbf{n}}) \Big[(-i)^\ell \int \frac{d^3k}{(2\pi)^3} a_\ell(k) Y^*_{\ell m}(\hat{\mathbf{k}}) \Big] \tag{2.8}$$

where the projected source[6] $a_\ell(k) = [\Theta + \Psi](\mathbf{k}, \eta_*) j_\ell(kD_*)$, with j_ℓ the spherical Bessel function and $D_* = \eta_0 - \eta_*$. Notice that the one-to-one relation between k

[6] Note that since it is the effective temperature $\Theta + \Psi$ that oscillates, acoustic oscillations occur even if the temperature fluctuation Θ is zero. The quantity $\Theta + \Psi$ can be thought of as an effective temperature which is the observed temperature fluctuation.

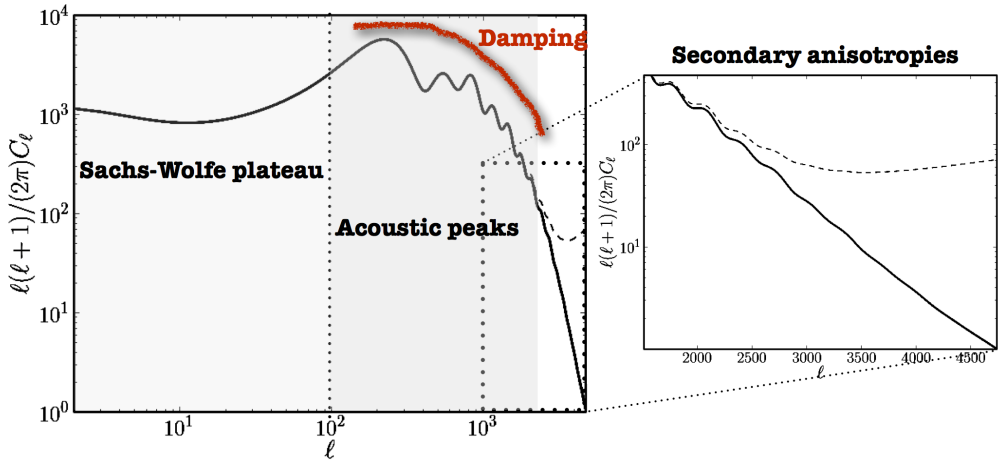

Figure 2.2: Temperature angular power spectrum C_ℓ^{TT}: power on the sky as a function of the multipole ℓ. The three effects discussed in the previous section, that is Sachs-Wolfe effect, acoustic peaks and the damping are labeled on the figure. Notice that $C_\ell^{TT}\ell(\ell+1)/(2\pi)$ is plotted on the y-axis rather than C_ℓ^{TT}. The insert on the right is a zoom over the region of damping. If there were only primordial anisotropies (solid line), the power-spectrum would fall abruptly. However, secondary anisotropies (dashed line) are dominant at the high multipoles end, which makes even more difficult the characterization of the primordial anisotropies in this region of the spectrum.

and ℓ is related to the presence of the spherical Bessel function, although it is only approximately true (Bessel functions are peaked at $kD_* \approx \ell$). Eq. 2.4 implies that $a_{\ell m}$ today is given by the integral in square brackets today in Eq. 2.8 (orthogonality properties of spherical harmonics).

In the previous discussion, we have not mentioned the fact that the acoustic motion of the photon-baryon fluid also produces a Doppler shift in the radiation that appears to the observer as a temperature anisotropy as well. Doppler peaks are out of phase with the acoustic ones because the velocity is out of phase of 90° with respect to the variations of potential. However, the Doppler effect has a directional dependence as well since it is only the line-of-sight velocity that produces the effect. Formally, it is a dipole source of temperature anisotropies and hence has an $\ell = 1$ structure (dipole). The coupling of the dipole and plane wave angular momenta implies that in the projection of the Doppler effect involves a combination of $j_{\ell\pm1}$ that may be rewritten as the derivative of $j_\ell(x)$ over x. The structure of $j_\ell^{'}$ lacks a strong peak at $x = \ell$ which corresponds to the fact that the velocity v_b is irrotational and hence has no component in the direction orthogonal to the wavevector (unlike the acoustic peaks which correspond to contributions in the direction orthogonal to the wavevector where the correspondence between ℓ and k is almost one-to-one). Correspondingly, the Doppler effect cannot produce strong peak structures, and the observed peaks must be acoustic peaks in the effective temperature not "Doppler peaks" [Stompor 1994]. Put differently, the baryons while increasing the effective mass of the oscillating system, decrease the velocity such that this Doppler effect becomes subdominant.

We also saw that radiation leads to decay of the gravitational potentials. Residual radiation after decoupling therefore implies that the effective temperature is not precisely $[\Theta + \Psi](\mathbf{k}, \eta_*)$. The photons actually have slightly shallower potentials to climb out of and lose the perturbative analogue of the cosmological redshift, so the $[\Theta + \Psi](\mathbf{k}, \eta_*)$ overestimates the difference between the true photon temperature and the observed temperature.

From all those effects, the source term a_ℓ in Eq. 2.8 gets generalized to [Hu & Dodelson 2002]

$$a_\ell(k) \approx [\Theta + \Psi](\eta_*) j_\ell(kD_*) + v_b(k, \eta_*) j_\ell^{'}(kD_*) + \int_{\eta_*}^{\eta_0} d\eta (\dot{\Psi} - \dot{\Phi}) j_\ell(kD). \quad (2.9)$$

This equation shows that the fluctuations of the CMB temperature, propagated until the present epoch, can be affected by the evolution of the gravitational potential Ψ in time (referred to as Sachs-Wolfe effect [Sachs & Wolfe 1967]), and Doppler effects due to the baryon peculiar velocity v_b between the last scattering surface and the observers.Note that residual radiation driving is particularly important because it adds in phase with the monopole: the potentials vary in time only near recombination, so the Bessel function can be set to its value at recombination and removed from the integral in Eq. 2.9. This complication has the effect of decreasing the multipole value of the first peak as the matter-radiation ratio at recombination

decreases [Hu & Sugiyama 1995]. Finally, we mention that time varying potentials can also play a role at very late times due to non-linearities or the importance of a cosmological constant for example. Those contributions, to be discussed more in the next section, are sometimes referred to as late Integrated Sachs-Wolfe effects, and do not add coherently with the effective temperature $[\Theta + \Psi](\mathbf{k}, \eta_*)$. See [Stompor 1994] for the first estimate of the contribution of each terms to the total spectrum. Nowadays, popular codes like CMBFAST [Seljak & Zaldarriaga 1996] and CAMB [Lewis *et al.* 2000] exploit these properties to calculate the anisotropies in linear perturbation efficiently (in addition they adopt a line of sight approach).

In addition, the photon-baryon fluid has slight imperfections mainly due to two physical processes corresponding to bulk viscosity and heat conduction in the fluid. These imperfections damp acoustic oscillations. The source of damping comes from the free streams of those photons in this transition phase. The free stream damps all perturbations with characteristic length smaller than the diffusion length of photons at that moment. This effect is called the Silk Damping [Silk 1968]. In addition, the decoupling is not instantaneous as seen in Fig. 1.5, but there is a given width in redshift. All the modes with a (temporal) period lower than this window of decoupling have contributions from different moments of the decoupling phase. The sum of those contributions are incoherent and so the total contribution of those modes is damped. Note that even if recombination had occurred instantaneously, the anisotropies on smallest angular scales would have been damped. This is because the Universe before recombination would not have been infinitely optically thick and photons would still stream between scatterings, hence damping fluctuations on the smallest scales given by the mean free path (the width of the last scattering surface), given thus rise to a different pattern of the peaks.

Once we multipoles of the distribution are known, we obtain the power spectrum of the acoustic oscillations as a projection

$$C_\ell = \frac{2}{\pi} \int dk k^2 a_\ell^2(k, \eta_0). \tag{2.10}$$

We shall also emphasize the link between the size of perturbations at recombination to the scale of anisotropies we observe today. Photons from over and under densities separated by a typical distance k^{-1} travel to us coming from an angular distance $\theta \approx k^{-1}/(\eta_0 - \eta_*)$, where η is the conformal time and $\eta_0 - \eta_*$ is the comoving distance between us and the last scattering surface (assuming that the Universe is flat). Using a decomposition of the temperature field into multipole moments $\ell \sim 1/\theta$, we have $\ell \approx k\eta_0$, using $\eta_0 >> \eta_*$. Modes which have their maxima or minima of oscillation at the moment of recombination correspond respectively to odd and even peaks according to the relation $k_n = n\pi/s_*$, where s_* is the distance sound has travelled inside the horizon at recombination. In the harmonic domain, this relation implies a series of peaks located at $\ell_n = n\pi\eta_0/s_*$.

2.2.3 Secondary anisotropies

Once the recombination takes place, the mean free path of the photons becomes so big that we can consider the photons as essentially free. But this is only partially true. Even if subdominant with respect to primordial anisotropies, there are other physical process involving photon[7]-matter interactions between the last scattering surface and us. We call them the *secondary anisotropies*, and by convention, they do not include foregrounds or weak gravitational lensing which are treated separately later (see Sec. 3 and 4). Several factors came into play but the origins of the secondary anisotropies are either gravitational or linked to a period of reionization[8].

Integrated Sachs-Wolfe effect (gravitational). The integrated Sachs-Wolfe effect (ISW) is another aspect of the Sachs-Wolfe effect. It takes into account the variation of the potential between the moment when the photon enters and leaves this potential. Photons gain energy if the depth of the potential is shallower and they lose energy otherwise. We can distinguished between two integrated Sachs-Wolfe effect: the late and the early. On the one hand, the late ISW effect is due to the growth rate of the fluctuations just after the decoupling, and does not contribute for short potential fluctuations, because the number of over- and under-densities should be equal and thus their effects compensate. However, the bigger the size of the potential, the more significative this effect is, and it is even dominant at the largest scales. We can think of the late ISW in the light of a universe in a cosmological constant domination era, which freezes the evolution of some modes of the gravitational potential. On the other hand, the early ISW finds its origin in the fact that the radiation density tends to damp the fluctuations of the potential which are entering the horizon. So all the potential modes entering the horizon between the decoupling and the matter domination era can give rise to an important early ISW. This effect starting at the moment of decoupling, it could be categorized into the primordial anisotropies. The ISW effect is especially important in that it is sensitive to the dark energy: its amount, equation of state and clustering properties, see *e.g.* [Stompor & Efstathiou 1999]. Unfortunately, it is severely limited by cosmic variance near $w = -1$.

Rees-Sciama effect (gravitational). The Rees-Sciama effect [Rees & Sciama 1968] arises if the modes of the potential start to have a non-linear evolution (and so a fast evolution). In a bottom-up model (from small scales to large scales), small fluctuations become non-linear first, so this effect should be mainly seen at small scales. However, this is a small effect on overall, leading to variation of the order of $\Delta T/T \sim 10^{-7}$ at degree scales [Hu *et al.* 1997], and $\Delta T/T \sim 10^{-(5-6)}$ at arcminute scales [Seljak & Zaldarriaga 1997].

[7] from CMB

[8] Interactions through Compton effect, with the electrons in the ionized medium.

Period of reionization Recombination led to a neutral universe.However, the Gunn-Peterson test [Gunn & Peterson 1965] showed that the universe has been reionized somewhere between $5 \leq z \leq 20$[9]. The exact cause of this reionization period is not known, but it might be related to the first population of free stars[10]. During this phase, the free electrons interact once again with photons through the Compton diffusion (first order effect, involving the monopole). The effect on the Cosmic Microwave Background photons is seen both locally around the galaxy clusters (decrease of power) but also more globally at large scales. Due to diffusion of these photons, all primordial anisotropies smaller than the size of the horizon at the moment of the reionization is damped. Also, inhomogeneities at the moment of the reionization could imprint signature which would be difficult to disentangle from the primordial anisotropies. Hopefully, for a reionization around $z \sim 6$ (from recent data), the size of the horizon θ_r at the moment of reionization is somehow similar to the damping length at recombination, θ_D.

Ostriker-Vishniac effect (reionization). The Ostriker-Vishniac effect is a non-linear effect which is due to correlations between density perturbations and velocity perturbations (of the electrons which diffuse the photons) along the line of sight. The amplitude of the effect depends on the precise history of the reionization, but it is commonly accepted that this effect starts to contribute for multipoles $\ell > 2000$.

Sunyaev-Zel'dovich effect The Sunyaev-Zel'dovich effect ([Zeldovich & Sunyaev 1969], [Sunyaev & Zeldovich 1970]) is an inverse Compton effect which involves Cosmic Microwave Background photons and free electrons from the inter-cluster hot gas. This thermal effect modifies locally the angular spectrum of the Cosmic Microwave Background photons, hence is more visible at small angular scales. In addition, if the cluster has a motion, a kinetic effect created by Doppler effect has to be taken into account. In addition, both thermal and kinetic effects have a specific effect of the frequency spectrum, and their amplitudes inform us on the thermal history of the cosmic gas. Fig. 2.3 shows the predictions of these effects as well as observational results. On top, the diffusion on free electrons of the Local cluster produced a large scale effect. The produced anisotropies can reach $\Delta T/T \sim 10^{-4}$ for scales between the degree and the arcminute. It is by far the most dominant secondary effect on the Cosmic Microwave Background, and very recently, the satellite Planck delivered full-sky maps of the Sunyaev-Zel'dovich emission [Planck Collaboration 2015h]. The study of the Sunyaev-Zel'dovich effect allows to put constraints on the moment of reionization as well as its duration [Zahn *et al.* 2005], [Zahn *et al.* 2012], [Planck Collaboration 2015i].

All those anisotropies - primordial and secondary - contribute to the observed power spectrum of the anisotropies of the Cosmic Microwave Background. Our

[9] In fact, analyzing the spectra of the most distant quasars, one can conclude that most of the intergalactic hydrogen is ionized at $z \sim 5$.

[10] Or more speculatively the disintegration of exotic particles.

comprehension of the Standard Cosmological Model depends on the knowledge of all of them.

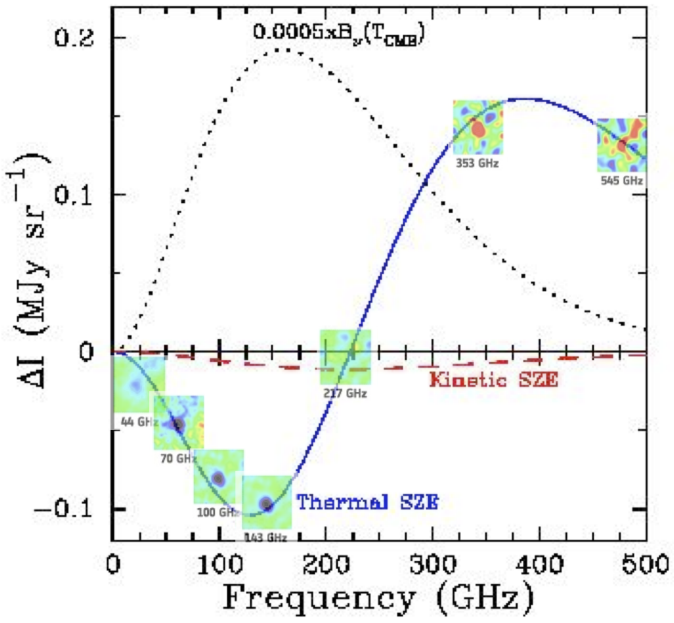

Figure 2.3: Expected spectra of the thermal (blue) and kinetic (red) Sunyaev-Zel'dovich effect. Notice the different scales. The thermal effect, multi-band observations of the galaxy cluster Abell 2319 from the satellite Planck is over plotted, bringing a remarkable confirmation of the predictions.

2.3 CMB anisotropies: polarization

Whereas anisotropies in the temperature of the CMB and inhomogeneities in the density field were studied and discovered back in the 20th century, the radiation of the Cosmic Microwave Background - which is an *electromagnetic* radiation - is also expected to be polarized because of Compton scattering at the time of decoupling. Up to now, we have focused on the temperature fluctuations in the Cosmic Microwave Background, because the two-point function for temperature provides the single, most powerful test for distinguishing cosmological models and determining cosmological parameters. However, there is more information to be gained by measuring the polarization and its correlation with the temperature fluctuations[11]. In

[11] Moreover, in the Standard Cosmological Model, the polarization peaks and correlation are precise predictions of the temperature peaks as they depend on the same physics. As such their detection would represent a sharp test on the implicit assumptions of the working model, especially its initial conditions and ionization history. Recently, and before their polarization release, Planck delivered a very precise power-spectrum of E-modes and temperature-polarization correlation

particular, polarization provides the cleanest and most sensitive method of probing the primordial spectrum of gravitational waves predicted by models of inflation, one of the most challenging predictions to verify - or reject. The scientific community just started to observe polarization of the background radiation [Kovac *et al.* 2002], [QUaD Collaboration 2008], [Chiang *et al.* 2010], [Quiet Collaboration 2011], [POLARBEAR Collaboration 2014c], [Hanson *et al.* 2013], [Naess *et al.* 2014] [Planck Collaboration 2015a], so it is a true 21st century observational challenge and it promises to deliver much cosmological information in the nearly future.

2.3.1 Electromagnetic wave and Stokes formalism

Electromagnetic wave and experimental context. Let's first recall the formalism of the polarization of the light. In order to make things easier, we work with plane waves, and more precisely harmonic plane waves. For a harmonic plane wave $\mathbf{E}$(M=(x,y,z),t) we can write in a cartesian basis :

$$\mathbf{E}(M,t) = E_{0x}\cos(\omega t - \mathbf{k}.\mathbf{r} + \phi_x)\mathbf{u}_x + E_{0y}\cos(\omega t - \mathbf{k}.\mathbf{r} + \phi_y)\mathbf{u}_y + E_{0z}\cos(\omega t - \mathbf{k}.\mathbf{r} + \phi_z)\mathbf{u}_z, \tag{2.11}$$

where E_{0i} and $\phi_i(t)$ are constant amplitudes and time dependent phases of each components of the wave. Written in a complex way :

$$\mathbf{E}(M,t) = \mathbf{E}_0(t)e^{i(\omega t - \mathbf{k}.\mathbf{r})}. \tag{2.12}$$

We are interested to define the polarization of these waves. Let $\mathbf{E}(M,t)$ be an electromagnetic harmonic plane wave which is monochromatic, *ie* the frequency content is around an average value ω. Let us propagate this wave along the z axis in a cartesian basis. The nonzero components of $\mathbf{E}$ are :

$$E_x(z,t) = E_{0x}e^{i(\omega t - k.z + \phi_x(t))} \tag{2.13}$$

$$E_y(z,t) = E_{0y}e^{i(\omega t - k.z + \phi_y(t))}. \tag{2.14}$$

By definition, the wave is assumed polarized if there is a dependence between the time evolution of E_x and E_y. We are interested by the sinusoidal evolution of the wave in a wavefront, *i.e.* we study the curve describes by the extremity of the vector $\mathbf{E}$ in a wavefront in such a way that the observer sees the wave arriving toward him. Moreover, as all wavefronts are equivalent to describe polarization, we do not take into account the spatial part in the wave, and so set $z = 0$. From one wavefront to another, there is only a constant phase, which does not affect results. So we end up with waves of the form

power-spectrum based on their temperature power-spectrum only [Planck Collaboration 2014b]. Impressive!

$$E_x(t) = E_{0x}e^{i\omega t} \tag{2.15}$$

$$E_y(t) = E_{0y}e^{i(\omega t+\phi(t))} \tag{2.16}$$

where $\phi(t)$ is the relative phase between the two components. In the general case of polarization, the two parameters describe an ellipse. We have two particular cases: $\phi = 0$ - the wave is said linearly polarized - and $\phi = \pi/2$ with $E_{0x} = E_{0y}$ - the wave is said circularly polarized. Notice that there exists no choice of these parameters corresponding to unpolarized light. Instead, unpolarized light can be represented as a linear combination of plane waves with different phases and polarization angles. This results in light with polarization changing rapidly over short time scales, adding up to a zero net polarization. So the knowledge on the polarization state of an electromagnetic wave is equivalent to determine the parameters E_{0x}, E_{0y} and $\phi(t)$ of Eqs. 2.16. Let's imagine that we dispose of an instrument capable of disentangling the two projections E_x and E_y of the electrical field[12]. We do not have easily access to $E_x(t)$ or $E_y(t)$ just from the basic fact that the light we are trying to measure have a frequency of the order of the Giga-Hertz, and no instrument is up to now capable to record such a high frequency signal. So instead, we only have access to intensities (averaged quantities) as $<|\ E_x|^2>$ or $<|\ E_y|^2>$, where the average is done over the integration time of the detector supposed to be big compared to the period of the wave. Finally, to disentangle the parameters of Eqs. 2.16, meaning to find the value of the semi-axis of the ellipse and its orientation, we have perform several measures of intensity with different orientations of the instrument. This is not very far from what we do with POLARBEAR on a daily basis in Chile!

Stokes parameters: definition. A useful way of characterizing the electromagnetic waves is in terms of the Stokes parameters. There are 4 parameters, labelled I, Q, U and V. Following our notation defined previously, the intensity I is just the sum of the intensities measured by the detector:

$$I =< |E_x|^2 > + < |E_y|^2 >= I_x + I_y \tag{2.17}$$

In our context, I is just the temperature of the photons from the Cosmic Microwave Background that we described earlier. Then, the second quantity to characterize the parameters of the ellipse is Q. the Stokes parameter Q is the difference between the intensity along x-axis and y-axis:

$$Q = I_x - I_y \tag{2.18}$$

If the sign of Q is positive, then the major axis of the ellipse is more along the x-axis, and if Q is positive the major axis is more along the y-axis, as shown in Fig. 2.4. We say that Q represents the linear polarization along the x (positive) and y (negative) axes, However, this is not sufficient to describe the polarization state

[12] Just use two orthogonal polarizers for instance.

given that there exists several ellipse configurations with the same Q. So the idea is to construct another quantity, called U. The coordinate system used to construct U is at 45° of the one of Q, and we define U as:

$$U = 2\mathrm{Re}(E_x E_y^*) = I_x^{45} - I_y^{45} = \frac{1}{\sqrt{2}} < \left| E_x + E_y \right|^2 > + \frac{1}{\sqrt{2}} < \left| -E_x + E_y \right|^2 > \quad (2.19)$$

So U represents the linear polarization along the $x+y$ (positive) and $x-y$ (negative) axes. In this new basis (at 45°), U is the equivalent of Q in the old basis. There exists a fourth Stokes parameter called V and given by:

$$V = 2\mathrm{Im}(E_x E_y^*), \quad (2.20)$$

and which probes the right-handed (positive) and left-handed (negative) circular polarization. The Stokes parameters describe not only completely polarized light but unpolarized and partially polarized light as well. A useful quantity for the rest of this manuscript is the degree of polarization p, defined as:

$$p = \frac{\sqrt{Q^2 + U^2 + V^2}}{I} \quad (2.21)$$

However, as far as the physics of the Cosmic Microwave Background is concerned, V polarization is not generated, and so the sign of the phase is not known[13]. And for the rest of the manuscript, we only refer to the *linear* degree of polarization (unless specified):

$$p = \frac{\sqrt{Q^2 + U^2}}{I}. \quad (2.22)$$

p is consequently ranging from 0 for an unpolarized light to 1 for a totally polarized light. A partially polarized light has its polarization degree such as $0 < p < 1$.

Finally, if we operate a rotation of the coordinate system, I and V are unchanged, while (Q, U) rotates as a spin-2 quantity. That is, under a rotation ψ around the z-axis of the local coordinate system,

$$\begin{pmatrix} Q \\ U \end{pmatrix} \rightarrow \begin{pmatrix} Q' \\ U' \end{pmatrix} = \begin{pmatrix} Q\cos 2\psi - U \sin 2\psi \\ U \cos 2\psi + Q \sin 2\psi \end{pmatrix} \quad (2.23)$$

This transformation defines a rotation invariant quantity $Q^2 + U^2$ and the angle

$$\alpha = \frac{1}{2} \tan^{-1} \frac{U}{Q}, \quad (2.24)$$

which transforms under rotation as $\alpha - \psi$. Compared to a description in terms of polarization fraction and polarization angles, the Stokes parameters are useful because they add linearly when combining radiation from multiple sources. And the physical observable connected to polarization is defined as a *headless* vector P whose components are Q and U. P is orthogonal to the direction of propagation, with magnitude $\sqrt{Q^2 + U^2}$ and polar angle α.

[13] For a nice discussion about the Stokes parameter V, see [Fabbian 2013].

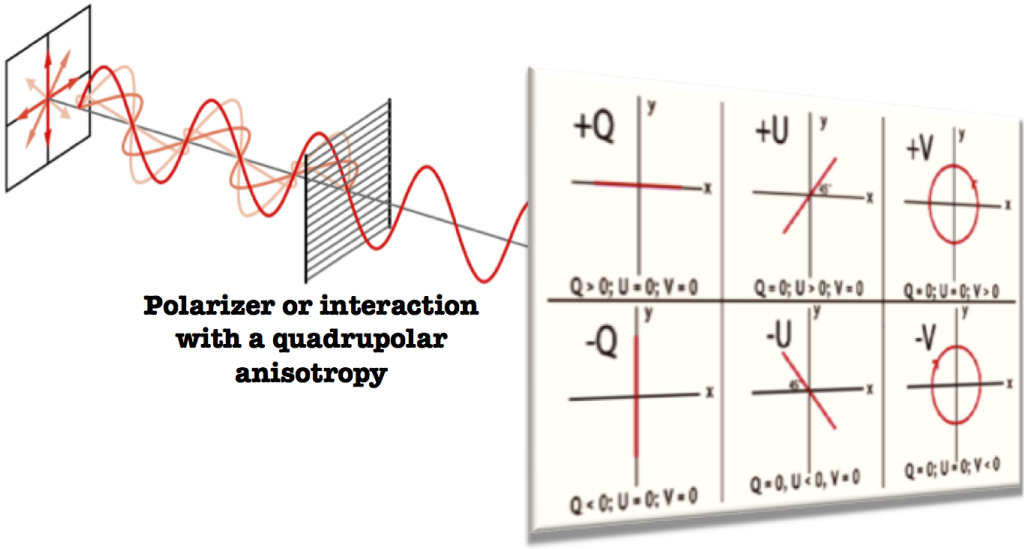

Figure 2.4: On the left, it is shown the effect of a linear polarizer or an interaction (Compton scattering for instance) pictured as a grid on an incident unpolarized light: the scattered light is linearly polarized. Then, the panel on the right is an illustration of the linear polarization Stokes parameters Q, U, and the circular polarization parameter V (not present in the CMB). Stokes parameters are useful due to their linearity when combining light from multiple sources and the ease of measuring them, but they are arbitrary in the sense that they depend on the orientation of the coordinate system.

2.3.2 Sources of polarized radiation

The previous section was somewhat general in the sense that it describes the polarization in general.Concerning the physics at the moment of recombination, the Thomson scattering is a perfect mechanism for producing polarized radiation. It allows all transverse radiations to pass through, while any radiation parallel to the outgoing direction is completely stopped. However, every electron is heat up by many photons, and a priori the total outgoing polarization would be most likely zero (incident polarizations all cancel out each other). But there should be a way...

Thomson scattering, quadrupole and... polarization! Thomson scattering is the low energy limit of Compton scattering, and we find both denomination in the literature. This paragraph follows loosely[14] the treatment done by [Kosowsky 1996]. So let's consider the Thomson scattering off of photons with electrons in the primordial plasma. Let $\hat{\varepsilon}$ ($\hat{\varepsilon}'$) be the incident (scattered) polarization directions. The differential cross-section of the reaction could be expressed as :

$$\frac{d\sigma}{d\Omega} = \frac{3\sigma_T}{8\pi}|\hat{\varepsilon}_{sca}.\hat{\varepsilon}_{inc}|^2 \tag{2.25}$$

Where σ_T is the Thomson cross section, $\hat{\varepsilon}_{sca}$ and $\hat{\varepsilon}_{inc}$ are the unit vectors labeling the linear polarization of the scattered and incident photons respectively, and $d\Omega$ is the surface element. Let us consider unpolarized photons scattering of a single electron from the point of view of an observer. The diffusion plan makes an angle ϕ with respect to the plan of the observer (x,z). If in addition the incident intensity varies with the direction, that is it has a direction dependent intensity $I_{inc}(\theta,\phi)$, one can derived the scattered intensity and polarization using the previous equation:

$$I_{sca} = \frac{3\sigma_T}{16\pi\sigma_b} I_{inc}(1+\cos\theta) \tag{2.26}$$

$$Q_{sca} = \frac{3\sigma_T}{16\pi\sigma_b} I_{inc}\cos\theta^2\cos 2\phi \tag{2.27}$$

$$U_{sca} = -\frac{3\sigma_T}{16\pi\sigma_b} I_{inc}\cos\theta^2\sin 2\phi \tag{2.28}$$

where σ_b is the surface of interaction. Thomson scattering cannot create circular polarization as it does not modify the phases but only the amplitudes of each component of the electrical field. Then by summing over all possible incident directions we obtain the scattered Stokes parameters (in the rest frame of the electron):

[14] For a more detailed treatment of it, see the results obtained from generalized Boltzmann equation including polarization source functions by [Kamionkowski *et al.* 1997b] and [Zaldarriaga & Seljak 1997].

$$I_{sca} = \frac{3\sigma_T}{16\pi\sigma_b}\int d\Omega I_{inc}(1+\cos\theta) \tag{2.29}$$

$$Q_{sca} = \frac{3\sigma_T}{16\pi\sigma_b}\int d\Omega I_{inc}\cos\theta^2\cos 2\phi \tag{2.30}$$

$$U_{sca} = -\frac{3\sigma_T}{16\pi\sigma_b}\int d\Omega I_{inc}\cos\theta^2\sin 2\phi \tag{2.31}$$

Using the decomposition in spherical harmonic of the incident intensity[15],

$$I_{inc}(\theta,\phi) = \sum_{\ell=0}^{\infty}\sum_{m=-\ell}^{\ell} a_{\ell m}(\mathbf{x},t)Y_{\ell,m}(\theta,\phi) \tag{2.32}$$

one can show that:

$$I_{sca} = \frac{3\sigma_T}{16\pi\sigma_b}\left[\frac{8}{3}\sqrt{\pi}a_{00} + \frac{4}{3}\sqrt{\frac{\pi}{5}}a_{20}\right] \tag{2.33}$$

$$Q_{sca} = \frac{3\sigma_T}{8\pi\sigma_b}\sqrt{\frac{2\pi}{15}}\mathrm{Re}(a_{22}) \tag{2.34}$$

$$U_{sca} = -\frac{3\sigma_T}{8\pi\sigma_b}\sqrt{\frac{2\pi}{15}}\mathrm{Im}(a_{22}) \tag{2.35}$$

From the last set of equations, we can clearly see that Thomson scattering generates polarization from an unpolarized radiation if the incident radiation at a given point as a function of direction has a non-zero a_{22} quadrupole moment. More generally, starting from an unpolarized light, only quadrupole patterns of the incident radiation can create polarization from the observer point of view. However, if we have many scatterings, the total net polarization is most likely zero (polarization is erased, rather than accumulate). Therefore the polarization that is detected by a distant observer comes from the very last period of decoupling.

Sources of quadrupole. In this paragraph, instead of the Stokes parameter Q and U, we talk in terms of *transformed Stokes Parameters* Q_r and U_r, first introduced by [Kosowsky 1996], [Kamionkowski *et al.* 1997a]. These transformed Stokes parameters are defined with respect to the new coordinate system that is rotated by ϕ, and thus they are defined with respect to the line connecting the temperature spot and the polarization at an angular distance θ from the center of this spot [Komatsu *et al.* 2011]. We will see later that Q_r and U_r are easier to relate to E and B modes than Q and U while interpreting the data.

There are three types of perturbations, related to three different physical sources, that give rise to quadrupole anisotropies and thus can induce Cosmic Microwave Background polarization. These are:

[15] In the general case, when the direction of observation $\hat{n}$ is not aligned with the direction of propagation $\hat{z}$ (implicitly assumed here), one needs to introduce the rotation R which transforms $\hat{z}$ into $\hat{n}$.

- Scalar, from density fluctuations (compressional). Electrons fall into potential wells, corresponding to matter over-densities, and do so as more rapidly as they are close the center. Considering an electron, other plasma particles aligned on the same radius go away whereas those which belong to the same iso-contour of density come closer. The same reasoning applies for electron escaping matter under-densities. At recombination, a quadrupole is produced as photons started to free-stream. A that moment every electron see more and more anisotropic incoming radiation. The resulting quadrupole is proportional to the velocity field. Moreover an acoustic wave perturbation is $\pi/2$ out of phase with respect to the velocity, so we expect the peaks of the polarized power-spectra to be out of phase with respect to the temperature ones. Scalar perturbations are invariant by parity, thus it only produces Q_r polarization field.

- Vector, due to the motion of vortices (vortical). They are not related to density fluctuations at first order. Vector perturbations create both Q_r and U_r. Vector perturbations are however suppressed in pre-decoupling period -as most of the non-gravitational effects - and are typically negligible compare to other contributions in inflationary models. Cosmic strings could however produce a non-negligible fraction of vector perturbations [Durrer *et al.* 2002], which could generate B modes (see *e.g.* [Moss & Pogosian 2014] for a recent study).

- Tensor, related to the passage of gravitational waves as first mentioned by [Polnarev 1985]. Tensor fluctuations are transverse-traceless perturbations to the metric, which can be viewed as gravitational waves. A plane gravitational wave perturbation represents a quadrupole "stretching" of space in the plane of the perturbation. A gravitational wave passing through a density fluctuation changes the shape of he potential well. Density contours are no longer circular but become elliptical, thus forming quadrupole perturbations and losing their symmetry properties. Tensor perturbations create both Q_r and U_r.

2.3.3 E and B fields

As we just saw, the CMB linear polarization is completely described by the Q and U Stokes parameters. They can be combined into two spin-2 and spin-(-2) fields defined as:

$$ {}_{\pm 2}P = Q \pm iU. \tag{2.36} $$

If we restrict ourself to an all-sky problem[16], the spin fields can be expressed in the harmonic space making use of the spin-weighted (2 and -2) spherical harmonic basis

[16]The case of cut-sky is an entire field of development for polarization, since it introduces unwanted artifact , [Lewis *et al.* 2001], [Bunn 2002], [Bunn *et al.* 2003], [Grain *et al.* 2009]. See also Sec. 9.

[17]:

$$ {}_{\pm2}P(\theta,\phi) = \sum_{\ell m} {}_{\pm2}a_{\ell m}\,{}_{\pm2}Y_{\ell m}(\theta,\phi) \tag{2.37} $$

The ${}_{\pm2}Y_{\ell}^{m}$ are the spin-2 spherical harmonics, complex-valued functions on the sphere that are related to the usual spherical harmonics Y_l^m by derivative operators. They constitute a complete, orthonormal basis for spin-2 fields, i.e., fields of headless vectors, defined on a sphere [Newman & Penrose 1962]. Going further, and following [Grain *et al.* 2009], any complex, spin-±2 field[18], with ${}_{\pm2}P^{\dagger} = {}_{\mp2}P$ is completely characterized by its projection on the spin-2 spherical harmonics, defining its (scalar) harmonic representation,

$$ {}_{\pm2}a_{\ell m} = \int d\Omega\, {}_{\pm2}P\, {}_{\pm2}Y^{\dagger}_{\ell m} \tag{2.38} $$

However, Q and U are not the most natural description of a statistically isotropic radiation field, as the definition of the linear polarization parameters Q and U depends on the arbitrary choice of a preferred direction, which results in Q rotating into U and vice versa during a rotation of the coordinate system. Instead we introduce two new quantities called E and B. E is a scalar field and B is a pseudo-scalar field[19] that are rotationally invariant alternatives to Q and U. E and B are respectively curl-free and gradient- free, and the names of these quantities come from analogy with mathematical properties the electromagnetic field. The value of E and B in a given point can be defined as radially-weighted averages of Q_r and U_r, the transformed Stokes parameters defined in the previous section.

In the harmonic space, these two approaches are related via the relation:

$$ \begin{aligned} a^{E}_{\ell m} &= -\frac{1}{2}({}_{2}a_{\ell m} + {}_{-2}a_{\ell m}) \\ a^{B}_{\ell m} &= \frac{i}{2}({}_{2}a_{\ell m} - {}_{-2}a_{\ell m}). \end{aligned} \tag{2.39} $$

This decomposition allows to distinguish physical causes generating those geometrical patterns. Density or scalar perturbations only generate parallel polarization (E-modes polarization, about 100 times lower in overall amplitude than the temperature anisotropies or T-modes) whereas gravitational waves generate both E-modes and B-modes and so therefore create a nonzero B-modes polarization (about 10 times weaker than the E-modes). These latter, named hereafter primordial B-modes, to avoid confusion with lensed B-modes, generated by the gravitational lensing of the E-mode polarization, and are treated in a specific section Sec. 3.

Continuing in this decomposition, we can define the E and B spherical harmonic basis for a spin-s field as

[17] Notice that we could expand the polarization field P in terms of scalar harmonics, but in this case the harmonic coefficients would be spin-±2 and therefore depend on the choice of coordinate.

[18] More generally any spin-s field.

[19] That is E-modes have $(-1)^{\ell}$ parity while B-modes have $(-1)^{\ell+1}$ parity.

$$
\begin{aligned}
{}_s\mathbf{Y}^E_{\ell m} &= {}_s\mathbf{D}^E Y_{\ell m} = \frac{1}{2}\sqrt{\frac{(\ell-s)!}{(\ell+s)!}}\begin{pmatrix}\partial^s + (-1)^s\bar{\partial}^s \\ -i(\partial^s - (-1)^s\bar{\partial}^s)\end{pmatrix} Y_{\ell m} \\
{}_s\mathbf{Y}^B_{\ell m} &= {}_s\mathbf{D}^B Y_{\ell m} = \frac{1}{2}\sqrt{\frac{(\ell-s)!}{(\ell+s)!}}\begin{pmatrix}i(\partial^s - (-1)^s\bar{\partial}^s) \\ \partial^s + (-1)^s\bar{\partial}^s\end{pmatrix} Y_{\ell m}
\end{aligned}
\tag{2.40}
$$

where we have defined two differential operators $\mathbf{D}^E$ and $\mathbf{D}^B$ which generalizes to arbitrary spin the operators used in [Bunn *et al.* 2003]. The harmonic representation of the field $\mathbf{P}$ (polarization signal as measured on the sky) in the E and B subspaces then reads,

$$
\begin{aligned}
a^E_{\ell m} &= \int d\Omega\ \mathbf{P} \cdot {}_2\mathbf{Y}^{E\dagger}_{\ell m} \\
a^B_{\ell m} &= \int d\Omega\ \mathbf{P} \cdot {}_2\mathbf{Y}^{B\dagger}_{\ell m}.
\end{aligned}
\tag{2.41}
$$

The E and B subspaces defined previously are orthogonal, thus for any complex spin-±2 field, ${}_{\pm2}\mathbf{D}^{E\dagger}.{}_{\pm2}\mathbf{D}^B = 0$. If the fields are defined over the all-sky (more generally a over a surface without boundary) this decomposition into E and B is unique. However, if we introduce boundaries to our surface, the decomposition is more complicated as we shall see later in this manuscript.

2.3.4 Polarized angular power spectra

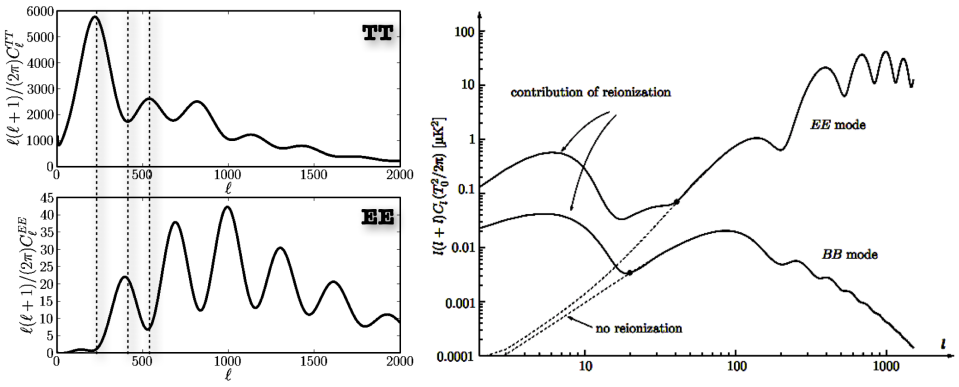

Figure 2.5: *Left:* Power spectra for temperature (top left), and E modes (bottom left). *Right*: E-modes and primordial B-modes power spectra with (solid line) and without (dotted line) reionization assumed. Figure taken from [Mukhanov 2005].

The polarization signal is very weak: it is expected to be only 10% of the total temperature fluctuations on small angular scales, decreasing to much less than 1%

on large angular scales. This is due to the fact that the CMB is only partially polarized because of two facts: Thomson scattering is not so efficient in converting unpolarized light to polarized light, and the process of recombination is somehow too short to expect all the photons from the Cosmic Microwave Background to be polarized. To be even more specific, degree of polarization is proportional to the duration of recombination and vanishes if recombination is instantaneous. But we know that recombination was not instantaneous, so we are left now with three observables: the temperature T, and the polarization via E and B. Just as with the temperature fluctuations, a useful quantity to compute is the two-point correlation function for polarization, and so we can form up to 6 two-point functions including temperature and polarization information[20]. Although the tensor harmonics are technically more complicated than the scalar harmonics, the point is that, given the orthogonality relations, the analysis of the polarization correlation functions is exactly parallel to that of the correlation function for the temperature fluctuations introduced in Sec. 2.2.1.

$$< a^T_{\ell m} a^{T*}_{\ell' m'} > = \delta_{\ell\ell'}\delta_{mm'} C^{TT}_\ell \tag{2.42}$$
$$< a^E_{\ell m} a^{E*}_{\ell' m'} > = \delta_{\ell\ell'}\delta_{mm'} C^{EE}_\ell \tag{2.43}$$
$$< a^B_{\ell m} a^{B*}_{\ell' m'} > = \delta_{\ell\ell'}\delta_{mm'} C^{BB}_\ell \tag{2.44}$$
$$< a^T_{\ell m} a^{E*}_{\ell' m'} > = < a^E_{\ell m} a^{T*}_{\ell' m'} > = \delta_{\ell\ell'}\delta_{mm'} C^{TE}_\ell \tag{2.45}$$
$$< a^T_{\ell m} a^{B*}_{\ell' m'} > = < a^B_{\ell m} a^{T*}_{\ell' m'} > = \delta_{\ell\ell'}\delta_{mm'} C^{TB}_\ell \tag{2.46}$$
$$< a^E_{\ell m} a^{B*}_{\ell' m'} > = < a^B_{\ell m} a^{E*}_{\ell' m'} > = \delta_{\ell\ell'}\delta_{mm'} C^{EB}_\ell \tag{2.47}$$

From parity consideration, T and E being *even* quantities and B being an *odd* quantity, the last two cross-correlations vanish in the Standard Cosmology:

$$C^{TB}_\ell = 0 \tag{2.48}$$
$$C^{EB}_\ell = 0. \tag{2.49}$$

This prediction is true assuming the Standard Cosmological Model, but there exists alternative models which predict non-vanishing TB and EB power spectra, *e.g.* [Contaldi *et al.* 2008, Magueijo & Benincasa 2011, Ferte & Grain 2014, Ferté 2014]. A detection of non-zero EB or TB spectra would signify a deviation from the Standard Cosmological Model, and thus open a window on to new physics[21]. In the following, we will assume the Standard Cosmological Model, and we are left with 4 non-zero estimators:

[20] Theoretically, up to 9, but the cross-correlation terms are symmetrical.

[21] However, as we will see later on section 10, there are several ways to generate non-zero EB and TB not related with the physics of the universe, but due to instrumental systematic errors, which are as of now order of magnitudes higher than any predictions from those alternative models.

$$\hat{C}_\ell^{TT} = \frac{1}{2\ell+1}\sum_{m=-\ell}^{\ell} |a_{\ell m}^T|^2 \tag{2.50}$$

$$\hat{C}_\ell^{EE} = \frac{1}{2\ell+1}\sum_{m=-\ell}^{\ell} |a_{\ell m}^E|^2 \tag{2.51}$$

$$\hat{C}_\ell^{BB} = \frac{1}{2\ell+1}\sum_{m=-\ell}^{\ell} |a_{\ell m}^B|^2 \tag{2.52}$$

$$\hat{C}_\ell^{TE} = \frac{1}{2\ell+1}\sum_{m=-\ell}^{\ell} a_{\ell m}^T a_{\ell m}^{*E}. \tag{2.53}$$

Fig. 2.5 shows the power-spectra of temperature (top left), E modes (bottom left). Also is shown on the right panel, the power spectra for E modes (scalar + tensor) and B modes (tensor), with or without reionization assumed, and one can see that the power spectrum is a invaluable information to disentangle between two different models.

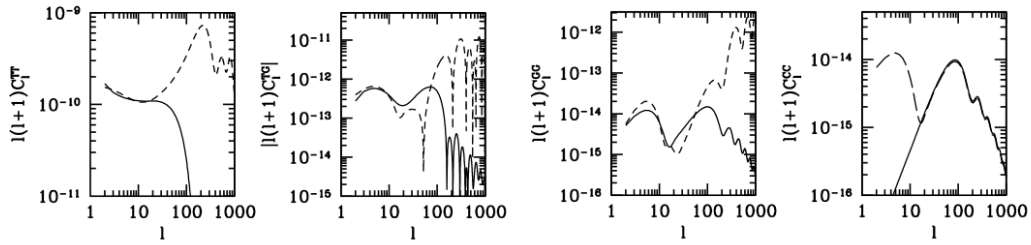

Figure 2.6: Power spectra for temperature (left), E modes (middle right), temperature-polarization cross spectrum (TE, middle left) and B modes (right). The dashed lines represent the power spectra of the scalar perturbations, while the solid lines represent the power spectra of perturbations due to gravitational waves. However, since the B modes do not have a scalar counterpart, the dashed line stands instead for a power spectrum of perturbations due to gravitational waves but generated using a reionized model with optical depth $\tau = 0.166$ to the surface of last scattering. In the figure, G and C stand for *gradient* and *curl* respectively, alternative names to talk about E and B modes. We notice easily that contributions from gravitational waves are mainly at low multipoles (large angular scales) while scalar perturbations exhibit more power at intermediate scales (degree to arcminute). In the Standard Model of Cosmology, the cross correlation TB and EB are vanishing. Figure adapted from [Cabella & Kamionkowski 2004].

Scalar and tensor contributions. As we discussed previously, there are scalar contributions and tensor contributions in the primordial Universe. While in reality

we measure the sum of both, let's see individually what is their contribution in the harmonic domain. We argued that a scalar perturbation can generate temperature, and polarization of type E only, while the tensorial perturbations can generate all components, that is T, E and B. As shown in figure 2.6, scalar and tensor contributions are very different. The tensor contributions are more pronounced at low multipoles (large angular scales), whereas the scalar contribution, via the acoustic peaks, have a typical signature at intermediate scales (degree to arcminute scales). The B modes polarization is an especially important object of Cosmic Microwave Background measurement, since in the Standard Cosmological Model, the presence of primordial B mode is then related to the presence of gravitational waves in the early Universe. Moreover as of now it is the most decisive and probably the only realistic way of detecting the nearly scale-invariant spectrum of gravitational waves predicted by inflation. Therefore a discovery of the B-mode of the CMB polarization, which is related to tensor metric perturbations, would be a strong argument in favor of the simplest versions of chaotic inflation, whereas the absence of the B-mode would rule out the simplest versions of chaotic inflation without helping much in distinguishing between many other versions of inflationary theory [Linde *et al.* 2005]. While we can predict the shape of this spectrum, its amplitude is related to the amount of gravitational waves in the early universe, which is not predictable. This makes the search for primordial tensor modes difficult, and in the same time what makes it so exciting. One way to see this problem is to wonder what is the contribution of tensor perturbations with respect to scalar ones. One way to answer this question is to define the *tensor-to-scalar* ratio, called r, defined by the amplitude of the tensor power spectrum relative to the amplitude of the scalar spectrum[22]. The primordial power spectrum of B modes then have a fixed shape and its amplitude is proportional to r.

Pattern in maps and power-spectra. In the same way as for temperature, the polarization spectra exhibit oscillations for sub-degree scales, but those oscillations are more peaked because they come from the velocity gradient of the photon-baryon fluid at the moment of decoupling (Doppler) (temperature gets in addition the dragging from baryons). Moreover as mentioned earlier, the acoustic wave perturbations are $\pi/2$ out of phase with respect to the velocity, so the peaks of the polarized power-spectra are out of phase with respect to the temperature one, as clearly seen in Fig. 2.5. In addition, another feature of this temperature-polarization correlation is the non-zero TE correlation which bring additional informations, at least from the fact that it is supposedly noiseless (noise of T and E are at zeroth order uncorrelated.). And last but not the least, due to the fact that the process of polarization is partial at the moment of recombination, the amplitude of the polarized spectra is a fraction of the amplitude of the temperature power spectrum plus the fact that we cannot predict the amplitude of primordial B modes (current bound at $r < 0.11$ from [Ade *et al.* 2015]).

[22] For more details on the definition of r, see Sec. 1.3.4.

Following and complementing the very comprehensive article [Cabella & Kamionkowski 2004], here are some interesting features on both temperature and polarization spectra :

- **Acoustic peaks (TT, EE):** as said earlier the acoustic wave perturbations are $\pi/2$ out of phase with respect to the velocity, so the peaks of the polarized power-spectra are out of phase with respect to the temperature one, as seen in Fig. 2.5.

- **Acoustic peaks (TE):** the maxima and minima of temperature and polarization respectively correspond to the zeros of the TE cross-correlation.

- **Highest acoustic peak (TT, EE):** the temperature power spectrum has its highest peak at $\ell \sim 200$ whereas the one for E modes peaks around $\ell \sim 1000$ pointing out that polarization contains more power at smaller scales than temperature. That can be explained by noticing that polarization induced by a particular harmonic mode of the primordial density field depends on the gradient of that density field (as velocity).

- **Reionization bump (TE, EE, BB):** reionization induces an excess of power in all spectra at very large scales ($\ell \leq 10$), as shown in Fig. 2.6. This is simply due to scattering of the quadrupole by reionized gas at the moment of the reionization. Notice that the position of this peak gives an information on the moment of reionization: $\ell_{reio} \propto \sqrt{z_{reio}}$.

- **Drop, scalar (TT, EE, TE):** as mentioned earlier in section 2.2.2, the damping of anisotropies is due to the fact that decoupling is not instantaneous plus the free-streaming of photons. The damping can be seen as the envelope of the power spectra, with a typical cut-off at $\ell \sim 1500$.

- **Drop, tensor (TT, EE, TE, BB):** The power spectra due to gravitational waves drop precipitously for $\ell \geq 100$, as seen on Fig. 2.6. This is because on smaller scales, the gravitational waves have entered the horizon and their amplitudes were redshifted away by the time of recombination.

- **Tensor contributions (TT, EE, BB, TE):** Gravitational waves spectrum exhibits a plateau at low ℓ, just like density perturbations. However, the cosmic variance removes our ability to detect an excess of a tenth over the density perturbation contribution to temperature, even if we could predict theoretically the density-perturbation amplitude. For E modes and TE cross correlation, in addition to the cosmic variance, there is the reionization bump which, if too big, can completely masked the tensor contribution, both effects acting at low multipoles. No, really our major hope is low-ℓ B modes!

Let's also give a description of the polarization patterns in the real domain, that is in maps of the sky. As discussed earlier, E and B quantities have specific

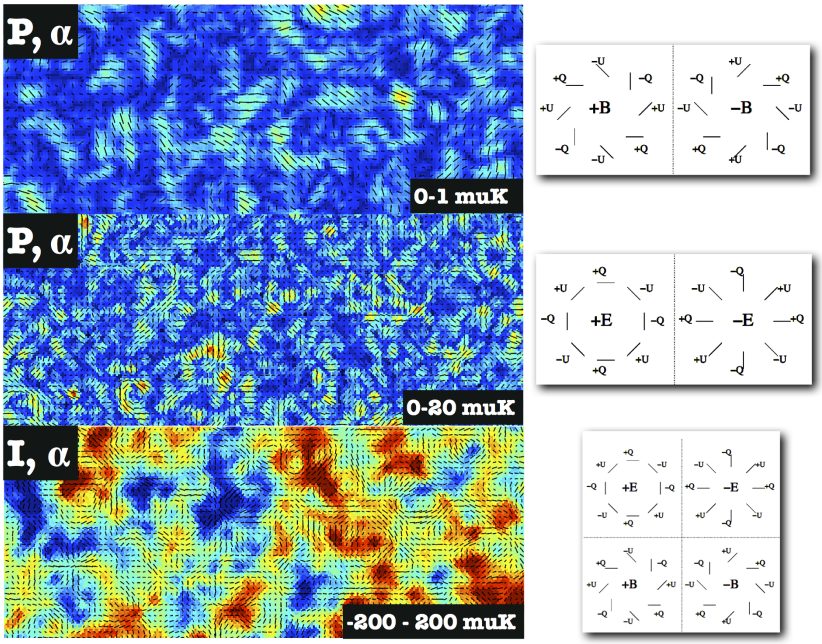

Figure 2.7: Polarization patterns in the real domain. *Top:* The norm of the polarization vector, defined by $P = \sqrt{Q^2 + U^2}$, is plotted in color, while the arrows are the polarization angle α, defined in Eq. 2.24. For this panel, a map from primordial B modes only ($r = 0.5$) has been generated, to highlight its curly pattern. Notice the large scale structures (one pixel has a size of $15'$.) *Middle:* Same but for E modes only (pixels have a size of $1.5'$). Notice that the scale is not the same as top panel: E modes are expected to have more power at sub-degree scales while primordial B modes have a peak around the degree scale. *Bottom:* The temperature anisotropies are in color instead of the polarization vector, and both B modes and E modes are used to compute the polarization angle. Notice that the major contribution comes from E modes. We can also see that polarization patterns follow the temperature patterns, from the fact that scalar perturbations are directly linked to density perturbations. Units in the figure are given in μK_{CMB}.

properties, the main being that E is even-parity and B is odd-parity. As for power spectra, the difference of power between E and B makes the E pattern majority. The norm of the polarization vector $P = \sqrt{Q^2 + U^2}$, with arrows overlaid representing the polarization angle α defined in Eq. 2.24, is often displayed. In some context, we also find the map of temperature anisotropies instead of the polarization vector, to highlight the correlation between temperature and polarization. I show an example of such a patterns for three different cases in Fig. 2.7: polarization vector + α in a case with only primordial B modes, polarization vector + α in a case with only E modes, and temperature + α in a case with both E and B modes. The pixel size is different between the case with B modes only and the other, to highlight the large scale structures inherent to primordial B modes.

Note that if we replace (Q,U) by $(U,-Q)$, then $E \to B$ and $B \to -E$ (on $a_{\ell m}$, power spectra being squared quantities, this effect is only positive). This tells us therefore, that a pure-E polarization pattern becomes a pure-B pattern if we rotate each polarization vector by 45°, and vice versa. It has a lot of consequences, discussed in the next section on weak gravitational lensing[23].

2.4 Cosmological parameters

Going back to the section 1.1.4, we would like to extract informations from our observables (the angular power spectra of the anisotropies, the lensing, etc.) to constrain our cosmological model. To do so, we usually described cosmological models by a set of parameters. Different cosmological models predict different observables and thus, extracting cosmological information means constraining the parameters of a model given the data, including confidence intervals. More specifically, cosmology is a stochastic theory which requires observation of statistical quantities (think of homogeneity, isotropy for instance), and a given set of parameters produces prediction for these statistical quantities. Therefore, one needs to know how to infer the value of the parameters given the data. This problem is known as inverse problem, that is having a set of data $\mathbf{x}$, how to interpret it in terms of a model. But this is not the only need for parameter estimation. Assuming a particular model we would like for instance to be able to forecast the performance of future experiments for experimental design.

World is often in two minds when speaking about parameter estimation: Frequentists or Bayesians. Roughly speaking, Frequentists only consider probability distributions of events (occurence) while Bayesians consider hypothesis as events (degree of belief). Obviously for both, the rules of probability apply. We do not follow only strictly one or the other throughout this manuscript, but rather use one or the other approach depending on the context. One of the pillar of the parameter estimation is the Bayes theorem, which states that the probability of the hypothesis H given the data D is given by:

[23] But also for E/B leakage due to cut-sky or filtering, or instrumental systematics unfortunately... This is also discussed later.

$$\mathcal{P}(H|D) = \frac{\mathcal{P}(D|H)\mathcal{P}(H)}{\mathcal{P}(D)}, \tag{2.54}$$

where $\mathcal{P}(H|D)$ is also called the posterior, $\mathcal{P}(D|H)$ is the likelihood meaning the probability of the data given the hypothesis, $\mathcal{P}(H)$ is called the prior, and $\mathcal{P}(D)$ is called the evidence. Although we may have the full probability distribution for the parameters and using marginalizations, often one simply uses the peak of the distribution as the estimate of the parameters, making the maximum likelihood often used as a method of parameter estimation to determine the best-fit model. Given a class of models and an observed data set, the probability distribution of the data (sometimes multiplied by prior functions) is maximized as a function of the parameters. Note that if the priors are not flat, the peak in the posterior is not necessarily the maximum likelihood estimate. Then the goodness-of-fit must be constructed in order to decide if the best-fit model is indeed a good description of the data. If it is, one has to determine confidence intervals on the parameters estimation. One strength of this formalism is that we can naturally update the probability distribution for a parameter by including new constraints from other data sets than the initial one. The literature on the subject is broad, see for instance the reviews [Verde 2010, Heavens 2009].

The predominant use of Bayesian methodology in cosmology is partly motivated by the fact that one observes a single realization of the Universe, and has been boosted by the introduction of Markov chain Monte Carlo (MCMC) techniques [Christensen *et al.* 2001]. Indeed, finding the maximum of the likelihood surface in a multi-dimensional space can be very computationally heavy. At first, solvers discretized the space in order to estimate the cosmological parameters. For each set of parameters in a predetermined grid, they can store either all statistical information or only the likelihood value, $\mathcal{L}$, before marginalizing or minimizing. Nowadays, popular sophisticated softwares using fast MCMC exploration of cosmological parameter space[24] are publicly available, regularly updated and widely used such as COSMOMC [Lewis & Bridle 2002] and MONTE PYTHON [Audren *et al.* 2013]. They are often interfaced to Boltzmann codes such as CAMB [Lewis *et al.* 2000] or CLASS [Blas *et al.* 2011] which are called to give the theoretical prediction for the data being tested. In the frequentist framework, profile likelihoods [Wilks 1938] are instead built for individual variables and, by construction, the individual parameter estimates match (up to numerical accuracy) the maximum likelihood estimator values [Planck Collaboration 2014c].

The base ΛCDM model recently released by the satellite Planck is made of 6 cosmological parameters[25]: the Cold dark matter density (today) $\Omega_{DM}h^2$, the Baryon density (today) $\Omega_b h^2$, 100 times the ratio of the Comoving size of the sound horizon over the angular distance at the moment of recombination $100\theta_{MC}$,

[24] While the methods using grids scale exponentially with the number of parameters, the MCMC method scales at its best linearly.

[25] This is remarkably simple.

the Thomson scattering optical depth due to reionization τ, the log power of the primordial curvature perturbations $\ln(10^{10}A_s)$ (at $k_0 = 0.05$ Mpc^{-1}), the Scalar spectrum power-law index n_s (at $k_0 = 0.05$ Mpc^{-1}). The most recent constraints on the base ΛCDM cosmology from the Planck CMB power spectra [Planck Collaboration 2015d] (temperature, polarization, lensing) are shown in Fig. 2.8. Other standard parameters can be derived from the base set, such as the age of the universe for instance. Usually, the likelihood function is not a linear function of the cosmological parameters since the parameters enter through the covariance matrix in a non-linear way. Moreover, the complexity of the problem is increased by the size of the data set. On the one hand, if we work directly with maps, the size of the problem is given by the number of pixel (can reach easily $o(10^6)$ pixels), and becomes quickly too big for the current computer speed. On the other hand, if we work with the angular power spectrum, the size of the problem is given by the number of bandpowers (up to $o(10^3)$). Thus, the angular power spectrum is preferred, as it reduces significantly the size of the data set without any loss of information, for the case of Gaussian fluctuations. It has to be noticed also that couple of these parameters are degenerated and those are generally broken using other observations such as galaxy surveys, supernovae surveys, or the abundance of light elements as predicted by the Big Bang primordial Nucleosynthesis.

2.5 Overview of the field as of 2013

CMB investigations have been and continue to be a very active and exciting area of research, which has excellent potential to impact profoundly our understanding of cosmology and fundamental physics in its broadest sense, providing a new and unique window on the physics of both the early Universe and the growth of its large-scale structure.

The observational results about CMB started in 1965 by the discovery of the CMB radiation by radio astronomers Arno Penzias and Robert Wilson [Penzias & Wilson 1965], leading to the Nobel prize in 1978. The first accurate measurements of both the CMB radiation and anisotropies were made between 1989 and 1996, with the instruments FIRAS and DMR embarked in the satellite COBE [Mather *et al.* 1990, Smoot *et al.* 1992], also leading to Nobel prizes! On the one hand, their measure of the CMB frequency spectrum confirmed it as being a black body with temperature of 2.725 K to within experimental limits, making the CMB spectrum the most precisely measured black body spectrum in nature. On the other hand, the existence of fluctuations in the CMB temperature, of the order of 10^{-5}, was put forward observationally. Several ground-based and balloon-borne experiments took over the measurements of anisotropies at intermediate angular scales during the 90's, for instance [Cheng *et al.* 1993, De Bernardis *et al.* 1994, Devlin *et al.* 1994, Dragovan *et al.* 1994, Gutierrez de La Cruz *et al.* 1995, Piccirillo & Calisse 1993, Netterfield *et al.* 1997]. A small revolution has been performed at the end of the 90's, by the balloon-borne BOOMERanG [de Bernardis *et al.* 2000], and MAX-

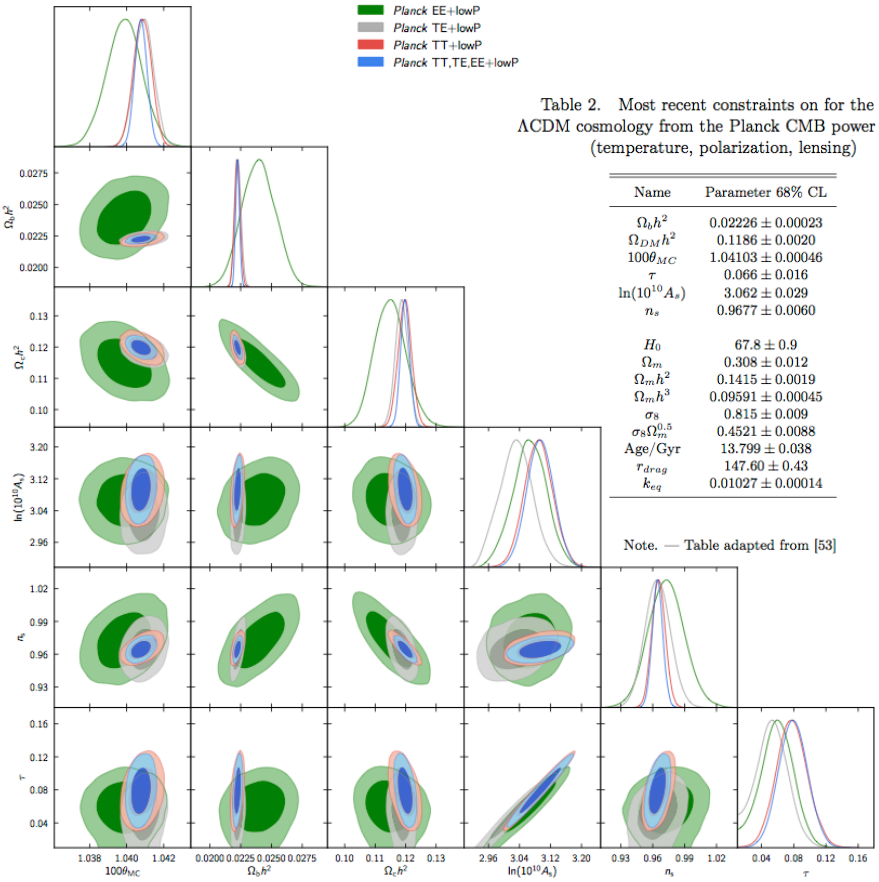

Table 2. Most recent constraints on for the base ΛCDM cosmology from the Planck CMB power spectra (temperature, polarization, lensing)

Name	Parameter 68% CL
$\Omega_b h^2$	0.02226 ± 0.00023
$\Omega_{DM} h^2$	0.1186 ± 0.0020
$100\theta_{MC}$	1.04103 ± 0.00046
τ	0.066 ± 0.016
$\ln(10^{10} A_s)$	3.062 ± 0.029
n_s	0.9677 ± 0.0060
H_0	67.8 ± 0.9
Ω_m	0.308 ± 0.012
$\Omega_m h^2$	0.1415 ± 0.0019
$\Omega_m h^3$	0.09591 ± 0.00045
σ_8	0.815 ± 0.009
$\sigma_8 \Omega_m^{0.5}$	0.4521 ± 0.0088
Age/Gyr	13.799 ± 0.038
r_{drag}	147.60 ± 0.43
k_{eq}	0.01027 ± 0.00014

Note. — Table adapted from [53]

Figure 2.8: Most recent constraints on the base ΛCDM cosmology from the Planck CMB power spectra (temperature, polarization, lensing). The tabular shows the latest constraints (68% C.L.) from Planck angular power spectra in combination with the CMB lensing likekihood on the 6 base parameters plus 9 derived parameters. Figure adapted from [Planck Collaboration 2015d].

IMA [Hanany *et al.* 2000] which provided accurate constraints on the first acoustic peak in temperature, and revealed the flatness of the Universe ($\Omega_K \approx 0$). They have been followed by the ground-based experiment DASI [Halverson *et al.* 2002] and the balloon-borne ARCHEOPS [Benoit *et al.* 2003]. In the 2000's, the satellite WMAP[26] was launched, and quickly provided very tight constraints on the first acoustic peaks (from degree scale down to few tens of arcminute). It successfully delivered unprecedented constraints on CMB temperature and polarization but also astrophysical results for almost 10 years. Its successor, the satellite Planck[27] has been launched in 2009, and mapped the sky during almost 2 years. Planck delivered the ultimate constraints on CMB temperature, together with very high constraints on polarization and astrophysics from arcminute scales to largest scales. In the meantime, ground-based experiments with very high resolution mapped out the sky from few tens arcminute scales down to arcminute scales, probing the damping tail of the CMB and the secondary anisotropies with high precision, such as ACT [Fowler *et al.* 2010] and SPT [Lueker *et al.* 2010].

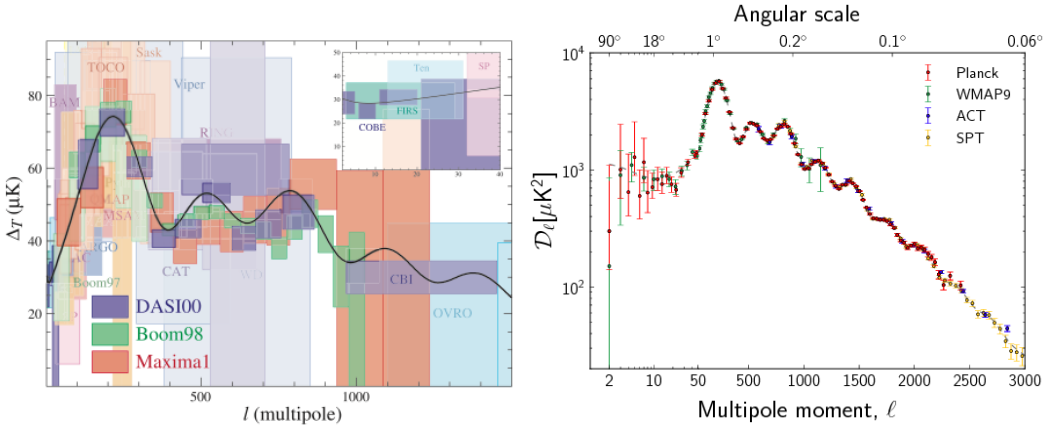

Figure 2.9: Measurements of the angular temperature power-spectrum early 2000 (left, [Hu & Dodelson 2002]) and after Planck release in 2013 (right, [Planck Collaboration 2014a]). The improvement in terms of error bars and scale coverage is impressive.

Concerning polarization, the first successful measurements were done early 2000 by the experiment DASI [Kovac *et al.* 2002], with the detection of E-modes. Then, a number of experiments delivered better characterization on E-modes and temperature-polarization correlation (TE) in the following years: WMAP, QUIET [Quiet Collaboration 2011], BICEP [Chiang *et al.* 2010], QUaD [QUaD Collaboration 2008]. Since 2012-2013, there has been a complete change of the landscape, with the start of operation of large arrays of powerful detectors enabling to reach very low instrumental noise levels such as Polarbear, ACT-

[26] http://map.gsfc.nasa.gov
[27] http://www.cosmos.esa.int/web/planck

POL, SPTPOL, and BICEP2, in addition to the satellite PLANCK launched in 2009. Their first results are discussed in Chap. 11, along with the results of this thesis.

2.6 Other cosmological probes

The observation of the Cosmic Microwave Background provides a unique window onto the physics of the very early universe and an exceptional probe of the laws governing at the highest energies. However the CMB is one cosmological probe among others.

While the CMB measurements are relatively insensitive to the dark energy and the epoch of cosmic acceleration, supernovae observations have recently provided evidence that the expansion of the Universe is undergoing a late time acceleration [Perlmutter *et al.* 1999], [Schmidt *et al.* 1998], [Riess *et al.* 1998]. The past years, surveys such as the Sloan Digital Sky Survey (SDSS) and the Supernova Legacy Survey (SNLS) provided tight cosmological constraints from the Hubble diagram of type Ia supernovae, and will be followed for instance by the Dark Energy Survey (DES) experiment, which has just begun its high-redshift supernovae survey.

Concerning the mapping of large-scale structure of the Universe, the next galaxy surveys such as DES, Dark Energy Spectroscopic Instrument (DESI), Large Synoptic Survey Telescope (LSST), and EUCLID will allow to probe diverse aspects of cosmology, from the distribution of dark matter and nature of dark energy, to the neutrino mass hierarchy and absolute mass scale. In particular Baryon Acoustic Oscillation (BAO) measurements form a key part of the observation program of these experiments, boosted by recent discoveries. The first measurement of the BAO signal has been done *via* the large-scale correlation function of SDSS luminous red galaxies [Eisenstein *et al.* 2005]. More recently, the BAO distance scale has been measured in the three dimensional correlation of the Ly-α forest in nearby quasar lines of sight from the BOSS survey [Busca *et al.* 2013].

The gravitational lensing is another very active topic in cosmology, see *e.g.* [Wittman *et al.* 2000] (and the particular case of CMB weak lensing is discussed later in this thesis). The ability of weak lensing to constrain the matter power spectrum makes it a potentially powerful probe of cosmological parameters, especially when combined with other observations such as the Cosmic Microwave Background, Supernovae, and galaxy surveys. Future major experiments such as LSST and EUCLID satellite, by exploiting at the same time the gravitational lensing, measurements of BAO, and measurements of galactic distances by spectroscopy should deliver unprecedented constraints on dark energy and dark matter distribution over a large range of redshifts.

Currently, a consortium of major radio astronomy institutions across the world is planning the world's next generation large radio telescope, the Square Kilometer Array (SKA). In parrallel, several ground-breaking observatories aiming at measuring and characterisation of the 21 cm signal start observing and herald a coming-of-age of a new and quickly growing area of research, which offers complementary constraints

to those expected from the CMB. The 21 cm line is of great interest in cosmology because it is the only known way to probe the Universe from the recombination to the reionization, namely the so-called "dark ages".

All those cosmological probes are complementary in many ways. Combining these probes together will not only help to break statistical degeneracies present in some of them and tighten the statistical uncertainties but also to better control and understand systematic errors specific to and different for each of them, helping thus to obtain more robust and reliable results.

Chapter 3

Weak gravitational lensing of the CMB by large-scale structure

Contents

We were interesting so far in the physics of the early Universe, that is at a redshift greater than $z \sim 1000$. At the epoch of the recombination, the Universe becomes transparent to photons. However the CMB photons and the matter continue to interact gravitationally at lower redshifts while large-scale structures form. A detailed study of the perturbed CMB allows us to probe the more recent history of the Universe, see *e.g.* the early papers [Blanchard & Schneider 1987, Cole & Efstathiou 1989, Cayon *et al.* 1993]. As we shall see later, on the one hand the lensing is probing the matter distribution at the level which is sensitive to "late-time" parameters that modify the growth of structure such as neutrino mass [Bond *et al.* 1980] or dark matter as the magnitude of the lensing effect is sensitive to the whole clustered mass [Blanchard & Schneider 1987]. On the other hand, lensing can be used to break the degeneracy of geometrical parameters that CMB measurements alone cannot, such as the curvature of the universe [Stompor & Efstathiou 1999]. What makes also unique the CMB in the context

of lensing is that CMB acts as a backlight, thought of as a single source plane, and extended across the entire sky. However, we should keep in mind two general properties while studying the lensing on fluctuations in the CMB. First, the lensing conserves surface brightness, meaning that if the primordial CMB was completely isotropic gravitational lensing would have no effect on it. Second, it is not the absolute value of the light deflection due to lensing which matters, but the relative deflection of neighbouring light rays which is of importance to capture the effect of gravitational lensing [Bartelmann & Schneider 2001]. Most importantly, the effect of the lensing on E mode introduces a B mode polarization pattern on the sky, overwhelming the primordial B mode signal on small scales. Therefore the detection of those B-modes arising from the primordial E-modes in the presence of matter perturbations is a crucial consistency check for our understanding of the gravity, the structure formation, and the physics at the moment of recombination. The four first subsections follow broadly the detailed review [Lewis & Challinor 2006] on weak lensing. We then focus on the reconstruction of the lensing potential and the observational status, and we conclude by highlighting the main challenge of the delensing.

3.1 Bending the light

The bending of the CMB photon trajectories due to gravitational lensing is at the core of this section since it enables us the reconstruction of the gravitational potential. The bending of the light by massive object is not a specific feature of General Relativity, and could be also interpreted within the Newtonian theory of gravity (although it was not made for initially).

3.1.1 Deflections

Let's consider a photon with velocity $\mathbf{v}$ passing close to a point of mass M. The idea behind the weak lensing - weak in the sense that the effect is small (small deviations, small angles) and is accurately described by first-order developments in the deviations - is that the photon has its initial trajectory deviates, due to the fact that the mass induces a transverse acceleration, proportional to the gradient of the potential Ψ:

$$\dot{\mathbf{v}}_\perp = -\boldsymbol{\nabla}_\perp \Psi. \tag{3.1}$$

However as far as General Relativity in concerned, one also has to incorporate the effect of the curvature of the space-time not taken into account in the Newtonian approach. The General Relativity predicts the *local* deflection angle $\delta\beta$ to be

$$\delta\beta = -2\delta\chi \boldsymbol{\nabla}_\perp \Psi, \tag{3.2}$$

where $\delta\chi$ is a small distance along the photon path and χ represents the comoving (conformal) distance. From the point of view of an observer observing the CMB at

comoving distance χ_* and the point of mass (M, Ψ) at comoving distance χ from the observer, the observed deflection $\delta\theta_\chi$ in the direction of $\boldsymbol{\nabla}_\perp\Psi$ is given by:

$$\delta\theta_\chi = \frac{f_K(\chi_* - \chi)}{f_K(\chi_*)}\delta\beta, \tag{3.3}$$

where f_K is the angular diameter distance and encodes the relationship between comoving distance and angle.

Let's consider now that our photon undergoes several deviations from its emission at the moment of recombination until now. Here again, assuming *weak* gravitational lensing and lowest order in the potential, the total deflection angle $\boldsymbol{\alpha}$ is the summation of the deflection angles defined in Eq. 3.3 and can be expressed as:

$$\boldsymbol{\alpha} = -2\int_0^{\chi_*} d\chi \frac{f_K(\chi_* - \chi)}{f_K(\chi_*)}\boldsymbol{\nabla}_\perp\Psi(\chi\hat{\mathbf{n}}, \eta_0 - \chi), \tag{3.4}$$

where the quantity $\eta_0 - \chi$ is the conformal time at which the photon was at position $\chi\hat{\mathbf{n}}$, and $\hat{\mathbf{n}}$ is the line of sight.

3.1.2 Born approximation

The exact calculation of Eq. 3.4 is in practice difficult as it would require to perform the integral over the perturbed path of the photon. However, since we are working to first order in Ψ (small deflections), we can evaluate the integral along the unperturbed path of the photon. More specifically, starting from the geodesic equation for the photon, one has:

$$\chi = \eta_0 - \eta - 2\int_{\eta_0}^{\eta} d\eta'\Psi(\eta'). \tag{3.5}$$

Assuming Born approximation is equivalent to set $\chi = \eta_0 - \eta$ (that is approximating the light path by the unperturbed line of sight), and makes computation much simpler without losing much in precision. Under the Born approximation, the transverse derivative in the Eq. 3.4 can be identified to derivative over the line of sight $\hat{\mathbf{n}}$:

$$\boldsymbol{\alpha} = -2\int_0^{\chi_*} d\chi \frac{f_K(\chi_* - \chi)}{f_K(\chi_*)f_K(\chi)}\boldsymbol{\nabla}_{\hat{\mathbf{n}}}\Psi(\chi\hat{\mathbf{n}}, \eta_0 - \chi). \tag{3.6}$$

This is a good approximation if the deflection angles are sufficiently small, or if all the lensing occurs in a single thin plane [Hanson *et al.* 2010]. The validity of the single lens approximation in the context of CMB has been recently investigated in [Calabrese *et al.* 2015] who tested the validity of Born approximation against more physically motivated ray tracing techniques. They found the difference between the two methods to be very small. By some intuitive order of magnitude calculations [Lewis & Challinor 2006, Hanson *et al.* 2010], one can show that taking each lens to be independent the total quadratic mean deflection is about 2" (assuming that each photon undergoes 50 deviations on average from the last scattering to us), while the typical coherence scale of the deflection field is about 2°.

3.2 The lensing potential

In the Born approximation, we define the (projected) lensing potential Ψ as

$$\psi(\hat{\mathbf{n}}) = -2\int_0^{\chi_*} d\chi \frac{f_K(\chi_* - \chi)}{f_K(\chi_*) f_K(\chi)} \Psi(\chi\hat{\mathbf{n}}, \eta_0 - \chi). \tag{3.7}$$

The deflection angle is given by the derivative over the line of sight of the lensing potential $\boldsymbol{\alpha}(\hat{\mathbf{n}}) = \boldsymbol{\nabla}\psi(\hat{\mathbf{n}})$. Although in principle, we probe projected effects between the last scattering surface ($z \sim 1100$) and us ($z = 0$), most of the constraints come from a range of redshift around $z \sim 2$ up to $z < 20$, as depicted in the figure 3.1. Indeed, after the recombination, there are no structures yet formed in the Universe, and most of the photons are not bent. One has to wait for the first large-scale structures to form to start to have significant effect. One can also notice in Eq. 3.7 that the lensing potential is an integrated measure of the mass distribution back to the moment of recombination, including geometrical effects of the background (through f_K).

As for the temperature perturbations, the lensing potential can be decomposed into multipole moments (all-sky) or Fourier moments (flat-sky):

$$\psi(\hat{\mathbf{n}}) = \sum_{\ell m} \psi_{\ell m} Y_\ell^m(\hat{\mathbf{n}}), \tag{3.8}$$

$$\psi(\hat{\mathbf{n}}) = \int \frac{d^2\mathbf{l}}{(2\pi)^2} \psi(\mathbf{l}) e^{i\mathbf{l}.\hat{\mathbf{n}}}, \tag{3.9}$$

where (ℓ,m) and $\mathbf{l}$ are conjugate to the real space unit vector $\hat{\mathbf{n}}$ in all-sky and flat-sky respectively. The assumption of linear evolution from the primordial density fluctuations and Gaussian primordial primordial fluctuations implies that the lensing potential is also Gaussian, and therefore can be completely described by its power spectrum[1]. The power spectra of the lensing potential in the all-sky and flat-sky cases can be expressed as:

$$< \psi_{\ell m} \psi^*_{\ell' m'} > = \delta_{\ell\ell'} \delta_{mm'} C_\ell^{\psi\psi}, \tag{3.10}$$

$$< \psi(\mathbf{l}) \psi^*(\mathbf{l}') > = (2\pi)^2 \delta(\mathbf{l} - \mathbf{l}') C_l^{\psi\psi}. \tag{3.11}$$

Note that one can relate the all-sky and the flat-sky limits power spectra $C_\ell^{\psi\psi}$ and $C_l^{\psi\psi}$, as shown in *e.g.* [Hu 2000].

The computation of the lensing potential depends on a given cosmology, that is the geometry of the universe and the gravitational potential along the line of sight. Following the same treatment as for CMB temperature, and also assuming linear evolution from the primordial density fluctuations, one can evaluate numerically the

[1] The gaussianity of lensing potential is just an approximation. However [Schäfer *et al.* 2012] showed non gaussianities induced by non linearities to be small analytically.

power spectrum of the lensing potential in terms of the gravitational potential power spectrum expressed in the harmonic space [Lewis & Challinor 2006]:

$$C_l^{\psi\psi} = 16\pi \int \frac{dk}{k} \mathcal{P}_{\mathcal{R}}(k) \left[\int_0^{\chi_*} d\chi T_\Psi(k; \eta_0 - \chi) j_l(k\chi) \left(\frac{f_K(\chi_* - \chi)}{f_K(\chi_*) f_K(\chi)} \right) \right]^2 \tag{3.12}$$

where $j_l(k\chi)$ is a spherical Bessel function, which can be expressed in terms of standard functions. $T_\Psi(k;\eta)$ is the transfer function in the linear theory in the Fourier space such that the gravitational potential at later epoch $\Psi(k;\eta)$ is $\Psi(k;\eta) = T_\Psi(k;\eta)\mathcal{R}(\mathbf{k})$, with $\mathcal{R}(\mathbf{k})$ being the primordial comoving curvature fluctuations (set at the inflationary time, see Sec. 1.3.4) with 3D power spectrum $\mathcal{P}_{\mathcal{R}}(\mathbf{k})$. So given some primordial power spectrum, the Eq. 3.12 can be computed numerically using Boltzmann codes such as CAMB [Lewis *et al.* 2000] or CLASS [Blas *et al.* 2011].

Since the deflection angle is the gradient of the lensing potential, its power spectrum is related *via*:

$$C_l^{\alpha\alpha} = l(l+1) C_l^{\psi\psi}. \tag{3.13}$$

Given that deflection angles are physically relevant, the last relationship explains why in the literature many authors choose to plot $l(l+1)C_l^{\psi\psi}$ rather than $C_l^{\psi\psi}$[2]. Such a power spectrum is depicted in Fig. 3.1. One can see that its maximum is reached for a multipole $l \sim 60$, and then decreases very steeply. In addition, the variance of the deflections $< \alpha >^2$ is given by:

$$\int d\ln l \frac{[l(l+1)]^2 C_l^{\psi\psi}}{2\pi} \approx < \alpha >^2, \tag{3.14}$$

and its square root is of the order of few arc minutes.

3.3 The lensed CMB temperature power spectrum

There are many ways to study the lensing effects, but we are interested in the effects on the CMB observables, namely the angular power spectra. In this section, we focus on the temperature power spectrum, and we extend the discussion to polarized power spectra in the next section. Neglecting non-Gaussianity of the anisotropies at the moment of recombination, the primordial power spectrum can be worked out accurately in linear theory. The most intuitive way of seeing the weak lensing of the CMB and of studying the properties of the lensed CMB, is to think in terms of remapping the primary anisotropies according to the deflection angle $\boldsymbol{\alpha}$. To do so, we often use a Taylor expansion of the lensing displacements on the nearest pixel center assuming flat-sky approximation:

[2] To be precise, $l(l+1)/2\pi \times l(l+1)C_l^{\psi\psi}$ is often plotted.

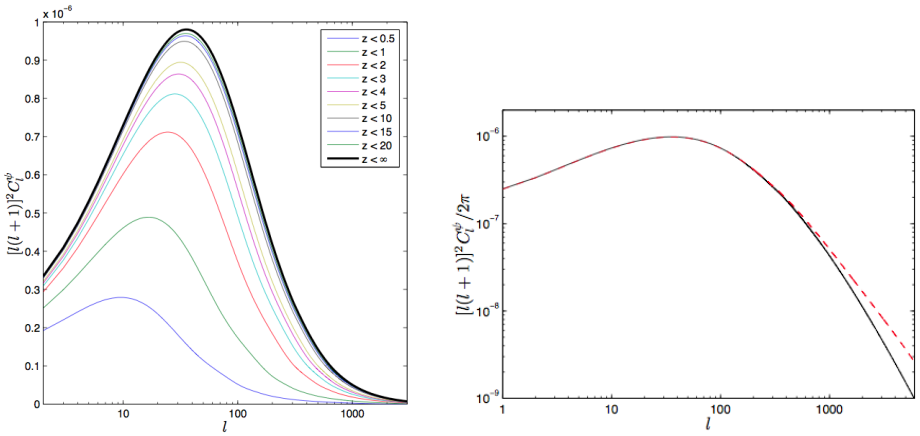

Figure 3.1: *Left:* Cumulative contribution of different redshifts to the power spectrum of the lensing potential for a concordance ΛCDM model. Note that main contribution come from the more recent history of the Universe, $z < 20$. *Right:* The power spectrum of the deflection angle for a concordance ΛCDM model. The solid black line corresponds to the linear theory spectrum and the dashed red line is the same model including non-linear corrections. Figures taken from [Lewis & Challinor 2006].

$$\begin{aligned}\tilde{T}(\hat{\mathbf{n}}) &= T(\hat{\mathbf{n}} + \boldsymbol{\alpha}) \\ &= T(\hat{\mathbf{n}} + \boldsymbol{\nabla}\psi) \\ &= T(\hat{\mathbf{n}}) + \left[\nabla^i\psi\nabla_i T\right](\hat{\mathbf{n}}) + \frac{1}{2}\left[\nabla^i\psi\nabla^j\psi\nabla_i\nabla_j T\right](\hat{\mathbf{n}}) + ... \end{aligned} \tag{3.15}$$

where we denote with a tilde a lensed quantity. Assuming flat-sky approximation for simplicity, the equation 3.15 can be expand in Fourier domain to second order in the lensing potential [Lewis & Challinor 2006, Challinor & Chon 2002, Hu 2000]:

$$\begin{aligned}\tilde{T}(\mathbf{l}) \approx T(\mathbf{l}) &- \int \frac{d^2\mathbf{l}_1}{2\pi}\mathbf{l}_1(\mathbf{l}-\mathbf{l}_1)\psi(\mathbf{l}-\mathbf{l}_1)T(\mathbf{l}_1) \\ &- \frac{1}{2}\int \frac{d^2\mathbf{l}_1}{2\pi}\int \frac{d^2\mathbf{l}_2}{2\pi}\mathbf{l}_1.[\mathbf{l}_1+\mathbf{l}_2-\mathbf{l}]\mathbf{l}_1.\mathbf{l}_2 T(\mathbf{l}_1)\psi(\mathbf{l}_2)\psi^*(\mathbf{l}_1+\mathbf{l}_2-\mathbf{l})\end{aligned} \tag{3.16}$$

It is interesting to notice that lensing affects the unlensed multipoles by coupling different scales: a mode of the lensing potential $\psi(\mathbf{l}-\mathbf{l}_1)$ with wavevector $\mathbf{l}-\mathbf{l}_1$ couples the unlensed temperature at wavevector $\mathbf{l}_1$ into the observed temperature at wavevector $\mathbf{l}$. We have a mode-coupling effect, and for a fixed realization of lenses, it introduces off-diagonal components into the covariance matrix of the observed temperature, with a characteristic spacing given by the peak of the deflection power spectrum (see Fig. 3.1). More specifically, large-wavelength modes of the lensing

potential introduce correlations between CMB modes on much smaller scales. In addition, small scales correlate also with the large ones. Particularly this is true and more evident for B-modes (see discussion in [Fabbian & Stompor 2013]). We see later how the current CMB experiments derive lensing by measuring these lensing-induced mode correlations.

3.3.1 Taylor expansion: pros and cons

On the one hand, the Taylor expansion of the lensed temperature field is often used to get simpler derivation and qualitatively correct results for the lensed temperature power spectrum. Moreover, it helps to gain intuition on the physical and geometrical effects of lensing onto the unlensed CMB. On the other hand, one can show that the Taylor expansion is not a good approximation on all scales. The Taylor expansion is not good when deflections are comparable to the scales under investigation (few arcminutes). However, it gives good results on large scale when order zero dominates, and in very small scale when order zero is negligible. In a CMB analysis, we do not focus on one lens only, and we rather work with ensemble-averaged quantities. In this case, the Taylor expansion gives reasonable results, as it is relative displacements and no more absolute displacements which are of importance to capture the effect [Bartelmann & Schneider 2001, Hanson *et al.* 2009b]. Nevertheless, the expansion is not accurate enough to reach a percent level calculation of the lensed power spectrum.

3.3.2 Lensed temperature power spectrum

In the following, we work in the flat-sky approximation. The covariance for the lensed temperature field defined in Eq. 3.16 remains diagonal due to statistical isotropy:

$$< \tilde{T}(\mathbf{l})\tilde{T}^*(\mathbf{l}') >= \delta(\mathbf{l}-\mathbf{l}')\tilde{C}_l^{TT}. \tag{3.17}$$

Working to lowest order in the lensing potential power spectrum $C_l^{\psi\psi}$, and neglecting the averaged correlations between the temperature field and the lensing potential $< T(\mathbf{l})\psi^*(\mathbf{l}) >$ (assuming that primordial small scale temperature at the moment of recombination is uncorrelated with the late time potentials responsible for the lensing, *i.e.* neglecting the ISW effect), one obtains:

$$\tilde{C}_l^{TT} \approx C_l^{TT}\Big(1 - \int \frac{d^2\mathbf{l}_1}{(2\pi)^2}(\mathbf{l}.\mathbf{l}_1)^2 C_{l_1}^{\psi\psi}\Big) + \int \frac{d^2\mathbf{l}_1}{(2\pi)^2}(\mathbf{l}-\mathbf{l}_1)^2\mathbf{l}_1^2 C_{l_1}^{TT} C_{|\mathbf{l}-\mathbf{l}_1|}^{\psi\psi} \tag{3.18}$$

The last integral in the previous equation represents a convolution of the unlensed temperature power spectrum with the lensing potential power spectrum. Intrinsic features in the unlensed temperature power spectrum with width in harmonic space less than the characteristic spacing given by the peak of the deflection power spectrum are washed out by the convolution term, that is it leaves a small blurring of

the acoustic peaks. In addition, this equation tells us that the smoothing effect - even for high multipoles where the flat-sky approximation is suitable - mainly comes from a range of wavelength from the lensing potential given by the peak of the lensing potential power spectrum, that is around $\delta l \approx 50$. The width of this peak being broad, each modes receive in fact a broader contributions from other modes, as shown in *e.g.* [Fabbian & Stompor 2013].

As we have seen before there is a damping of primordial anisotropies due to the fact that decoupling is not instantaneous plus the free-streaming of photons. The damping can be seen as the envelope of the power spectra, with a typical cut-off at multipole ≈ 1500. So at smaller scales (larger multipoles) the unlensed CMB has very little power. Therefore in Eq. 3.18, most of the contributions at large multipole l of the lensed temperature power spectrum from the unlensed temperature power spectrum are from modes l' of the unlensed power spectrum such that $l' << l$.

To summarize, the weak lensing affects the unlensed temperature power spectrum by smoothing the peaks (large scale lenses) and boosting small-scale power in the damping tail (small scales lenses on the large-scale temperature gradient). In addition, we should stress that if the weak lensing alters photon directions, it does not change the variance in any given direction. It can be seen as a reshuffling of power in space, but the total variance is conserved.

3.4 The lensed CMB polarization power spectra

We have seen previously that the CMB linear polarization is completely described by the Q and U Stokes parameters. They can be combined into two spin-2 and spin-(-2) fields defined as:

$$ {}_{\pm 2}P = Q \pm iU. \tag{3.19} $$

In the flat-sky approximation, the Fourier representation of the polarization field reads:

$$ {}_{\pm 2}P(\hat{\mathbf{n}}) = -\int \frac{d^2\mathbf{l}}{(2\pi)^2} {}_{\pm 2}P(\mathbf{l}) e^{\pm 2i\phi_l} e^{i\mathbf{l}.\hat{\mathbf{n}}} \tag{3.20} $$

$$ {}_{\pm 2}P(\mathbf{l}) = E(\mathbf{l}) \pm iB(\mathbf{l}), \tag{3.21} $$

where ϕ_l is azimuthal angle of $\mathbf{l}$ (the angle between $\mathbf{l}$ and $\mathbf{l}'$). Similarly to the definition of Sec. 2.3.4, one can define the different power spectra under the flat sky approximation:

$$ < X(\mathbf{l}) Y^*(\mathbf{l}') >= \delta(\mathbf{l} - \mathbf{l}') C_l^{XY}, \tag{3.22} $$

where X, Y denotes T, E or B. The lensing of the polarization field may be obtained by following the same steps as for the temperature field [Hu 2000]:

$$
\begin{aligned}
{}_{\pm2}\tilde{P}(\hat{\mathbf{n}}) &= {}_{\pm2}P(\hat{\mathbf{n}}+\boldsymbol{\alpha}) \\
&= {}_{\pm2}P(\hat{\mathbf{n}}+\boldsymbol{\nabla}\psi) \\
&= {}_{\pm2}P(\hat{\mathbf{n}}) + \big[\nabla^i\psi\nabla_{i\pm2}P\big](\hat{\mathbf{n}}) + \frac{1}{2}\big[\nabla^i\psi\nabla^j\psi\nabla_i\nabla_{j\pm2}P\big](\hat{\mathbf{n}}) + ... \qquad (3.23)
\end{aligned}
$$

Notice that we have to add one more complication with respect to the case of temperature, as the polarization field is a tensor field and therefore requires parallel transport along deflection vectors. We can expand in the Fourier domain the last equation:

$$
\begin{aligned}
&\tilde{E}(\mathbf{l}) \pm i\tilde{B}(\mathbf{l}) \approx [E(\mathbf{l}) \pm iB(\mathbf{l})] - \int \frac{d^2\mathbf{l}_1}{2\pi}\mathbf{l}_1(\mathbf{l}-\mathbf{l}_1)\psi(\mathbf{l}-\mathbf{l}_1)[E(\mathbf{l}_1) \pm iB(\mathbf{l}_1)]e^{\pm2i(\phi_{l_1}-\phi_l)} \\
&- \frac{1}{2}\int \frac{d^2\mathbf{l}_1}{2\pi}\int \frac{d^2\mathbf{l}_2}{2\pi}\mathbf{l}_1.[\mathbf{l}_1+\mathbf{l}_2-\mathbf{l}]\mathbf{l}_1.\mathbf{l}_2[E(\mathbf{l}_1) \pm iB(\mathbf{l}_1)]\psi(\mathbf{l}_2)\psi^*(\mathbf{l}_1+\mathbf{l}_2-\mathbf{l})e^{\pm2i(\phi_{l_1}-\phi_l)}.
\end{aligned} \qquad (3.24)
$$

Using Eq. 3.22, we can compute all combinations between lensed fields $\tilde{T}$, $\tilde{E}$ and $\tilde{B}$. Assuming that the lensing conserves the statistical parity invariance, the two cross-correlations $\tilde{T}\tilde{B}$ and $\tilde{E}\tilde{B}$ vanish. Stopping our development to the lowest order in the lensing power spectrum, we are left with:

$$
\begin{aligned}
\tilde{C}_l^{EE} &\approx C_l^{EE}\Big(1 - \int \frac{d^2\mathbf{l}_1}{(2\pi)^2}(\mathbf{l}.\mathbf{l}_1)^2 C_{l_1}^{\psi\psi}\Big) \\
&\quad + \frac{1}{2}\int \frac{d^2\mathbf{l}_1}{(2\pi)^2}(\mathbf{l}-\mathbf{l}_1)^2\mathbf{l}_1^2 C_{|\mathbf{l}-\mathbf{l}_1|}^{\psi\psi}[(C_{l_1}^{EE}+C_{l_1}^{BB}) + \cos 4\phi_{l_1}(C_{l_1}^{EE}-C_{l_1}^{BB})] \qquad (3.25) \\
\tilde{C}_l^{BB} &\approx C_l^{BB}\Big(1 - \int \frac{d^2\mathbf{l}_1}{(2\pi)^2}(\mathbf{l}.\mathbf{l}_1)^2 C_{l_1}^{\psi\psi}\Big) \\
&\quad + \frac{1}{2}\int \frac{d^2\mathbf{l}_1}{(2\pi)^2}(\mathbf{l}-\mathbf{l}_1)^2\mathbf{l}_1^2 C_{|\mathbf{l}-\mathbf{l}_1|}^{\psi\psi}[(C_{l_1}^{EE}+C_{l_1}^{BB}) - \cos 4\phi_{l_1}(C_{l_1}^{EE}-C_{l_1}^{BB})] \qquad (3.26) \\
\tilde{C}_l^{TE} &\approx C_l^{TE}\Big(1 - \int \frac{d^2\mathbf{l}_1}{(2\pi)^2}(\mathbf{l}.\mathbf{l}_1)^2 C_{l_1}^{\psi\psi}\Big) \\
&\quad + \int \frac{d^2\mathbf{l}_1}{(2\pi)^2}(\mathbf{l}-\mathbf{l}_1)^2\mathbf{l}_1^2 C_{l_1}^{TE} C_{|\mathbf{l}-\mathbf{l}_1|}^{\psi\psi}\cos 2(\phi_{l_1}-\phi_l) \qquad (3.27)
\end{aligned}
$$

Notice that even if the primordial B mode component is zero to start with, the total B modes spectrum is always non zero due to the presence of E mode and the lensing potential! It is often referred as to lensing B-modes. Such a B-mode angular power spectrum is shown on lower right panel in the Fig. 3.2.

The E-mode power spectrum peaks around $l \sim 1000$, so the lensed B-modes coming from E-modes in Eq. 3.26 (last integral term) for modes $l < 1000$ is somehow independent of the multipole considered (white noise spectrum). In terms of

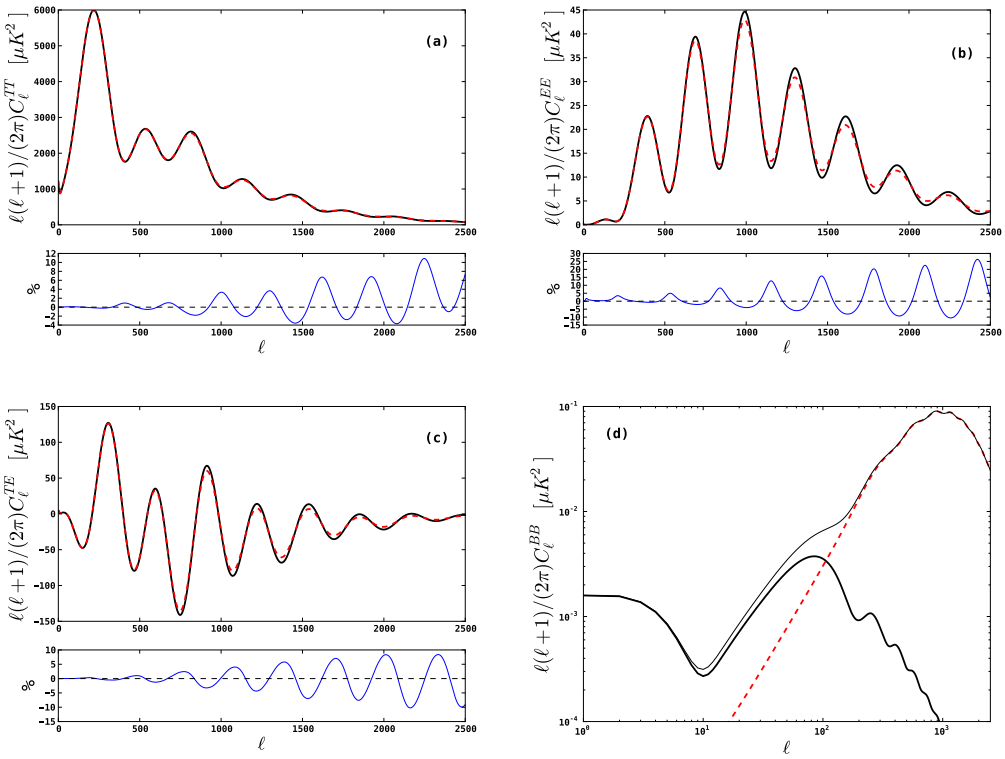

Figure 3.2: Effect of the lensing on the power spectra. (a), (b), and (c) panels show the unlensed (solid black) and lensed (dashed red) TT, EE and TE power spectra. The small panels under TT and EE show the relative difference between the lensed and unlensed spectra (in blue. The small panel under TE shows the ratio $(C_\ell^{TE,lensed} - C_\ell^{TE,unlensed})/\sqrt{C_\ell^{TT,unlensed} C_\ell^{EE,unlensed}}$. One can easily see both suppression of oscillations and enhancement of power on small scales. The panel (d) shows the B modes spectrum generated via gravitational lensing of E modes (dashed red). The B modes spectrum from tensor perturbation for $r = 0.05$ and $\tau = 0.0866$ (solid bold black line) and the total contribution (solid thick black line) is also overplotted. Spectra have been generated using CAMB.

instrumental white noise level, it would correspond to roughly 5 μK.arcmin. Depending on the value of the scalar-to-tensor ratio, the lensed B-modes may be an important contaminant in the search for primordial B-modes on large angular scales ($l < 200$).

To conclude, we shall also stress that an important effort has been done in order to model accurately the gravitational lensing effect on the primordial CMB. An important part of this effort involves simulating very accurate, high-resolution maps of the CMB total intensity and polarization, covering a large fraction of the sky and with lensing effects included [Lewis 2005, Basak *et al.* 2009, Lavaux & Wandelt 2010, Fabbian & Stompor 2013].

3.5 Reconstructing the lensing potential

We previously saw how the large-scale structure affects the primordial CMB anisotropies. However, since we don't know the primordial shape of the CMB *a priori* we need to use more statistical information to extract the lensing deflection field. One of the effect of lensing is to introduce small amounts of non-Gaussianity (when marginalized over realizations of the lenses) or statistical anisotropy (for a fixed distribution of lenses) [Lewis & Challinor 2006]. At first, people tried to use the lensing information contained in CMB maps as a probe of the projected mass density κ [Zaldarriaga & Seljak 1999, Guzik *et al.* 2000]. The projected matter distribution κ is related to the deflection field $\boldsymbol{\alpha}$ by:

$$\kappa = -\frac{1}{2}\boldsymbol{\nabla}.\boldsymbol{\alpha} \tag{3.28}$$

In order to estimate the projected mass distribution, a particular quadratic combination of derivatives of the CMB temperature field was constructed (averaged over realizations of the CMB). But quickly one of the difficulty was to build an estimator able to reach high signal-to-noise ratio. Since then, two main optimal estimators for the lensing deflection field have emerged: the first method is to use optimal quadratic estimators [Hu & Okamoto 2002, Okamoto & Hu 2003] while the second employs maximum likelihood techniques [Hirata & Seljak 2003]. In this section, we only review the optimal quadratic estimator for temperature and polarization.

3.5.1 Temperature

One important effect of the remapping due to lensing is to boost the small-scale (non-Gaussian) power in the damping tail of the CMB temperature anisotropy, as measured by the four-point function. One can show under some assumptions that there exists a quadratic estimator that maximizes the signal-to-noise ratio information available in this four-point function. On top of the fact that we assume Gaussianity and statistical isotropy for the unlensed CMB, we need to assume first that the lensing potential is a Gaussian random field, then that the noise is Gaussian and uncorrelated with the signal and that the deflections due to lensing are small.

As we discussed previously, for a given fixed lensing potential, the distribution of the observed (and so lensed) temperature $\tilde{T}$ is not isotropic. The Taylor expansion of the lensed temperature field to first order in the deflection angle shown in Eq. 3.16 reveals that the off-diagonal elements of the two-point correlation function of $\tilde{T}$ are proportional to the lensing deflection field. The simplest estimator (to lowest order in the lensing potential) should therefore be quadratic in $\tilde{T}$, and we define the quadratic estimator of the lensing potential on our specific sky by a weighted average of the off-diagonal terms [Hu & Okamoto 2002]:

$$\hat{\psi}(\mathbf{l}) = N(\mathbf{l}) \int \frac{d^2\mathbf{l}_1}{(2\pi)^2} \tilde{T}(\mathbf{l}_1)\tilde{T}^*(\mathbf{l}_1 - \mathbf{l})g(\mathbf{l}_1, \mathbf{l}), \tag{3.29}$$

where g is a function (called the filter) that is used to optimize the signal-to-noise ratio, and

$$N^{-1}(\mathbf{l}) = \int \frac{d^2\mathbf{l}_1}{(2\pi)^2} \Big((\mathbf{l} - \mathbf{l}_1).\mathbf{l} C^{TT}_{|\mathbf{l}_1 - \mathbf{l}|} + \mathbf{l}_1.\mathbf{l} C^{TT}_{l_1} \Big) g(\mathbf{l}_1, \mathbf{l}) \tag{3.30}$$

is a normalization so that the estimator is unbiased at lowest order in ψ. Note that the unlensed (and so theoretical) C_l^{TT} appears in this equation. We thus need to suppose an early cosmology to reconstruct the lensing potential. Instead of the predicted unlensed CMB power spectrum, we could use the observed lensed CMB power spectrum or any slightly incorrect assumption, and it would simply degrade the signal-to-noise ratio by a correspondingly small amount but it does not introduce spurious structures in the ensemble-averaged recovery. Indeed, assuming that there exists a parametrization in which the unlensed CMB power spectrum can be reconstructed from the lensed CMB power spectrum (what we do explicitly), using wrong assumptions appears as a calibration error [Hu 2001][3]. The optimal filter function g is then chosen in order to minimize the leading-order variance $< \hat{\psi}(\mathbf{l})\hat{\psi}^*(\mathbf{l}') >$ such that:

$$g(\mathbf{l}_1, \mathbf{l}) = \frac{(\mathbf{l} - \mathbf{l}_1).\mathbf{l} C^{TT}_{|\mathbf{l}_1 - \mathbf{l}|} + \mathbf{l}_1.\mathbf{l} C^{TT}_{l_1}}{2\tilde{C}^{tot}_{l_1} \tilde{C}^{tot}_{|\mathbf{l}_1 - \mathbf{l}|}}, \tag{3.31}$$

where $\tilde{C}_l^{tot} = \tilde{C}_l^{TT} + N_l$ and N_l is the instrumental noise power spectrum. Combining all the results, the power spectrum of the optimal quadratic estimator of the lensing potential on our specific sky is given by:

$$< \hat{\psi}(\mathbf{l})\hat{\psi}^*(\mathbf{l}') >= (2\pi)^2 \delta(\mathbf{l} - \mathbf{l}')(\hat{C}_l^{\psi\psi} + N^{(0)}(\mathbf{l})) + \mathcal{O}[(\hat{C}_l^{\psi\psi})^2] \tag{3.32}$$

Here, $N(\mathbf{l})$ is the lowest order noise on the reconstructed potential, given by the Eq. 3.30, and is often called the Gaussian bias. The four-point correlation function[4] takes advantage of the fact that gravitational lensing converts Gaussian primary anisotropy to a non-Gaussian lensed anisotropy. When calculating this non-Gaussian signal, however, there is a term N which is the disconnected part in

[3] See also [Anderes & Paul 2012] for a robust technique to mis-specification of the model.

[4] Recall that $< \psi\psi > \propto < TTTT >$.

the four-point correlation that has to be subtracted. Notice that we truncate the computation of the estimator to the lowest order in the lensing potential. In fact, the estimator is severely biased by also highest-order terms in the noise, which are significant when attempting to estimate the lensing potential power spectrum from the variance, such as the so-called $N^{(1)}$ and $N^{(2)}$ biases which matter at large and smale scales [Kesden *et al.* 2003, Hanson *et al.* 2011, Anderes 2013]. Fortunately, those biases can be estimated, and removed, in several ways, as done for instance for the Gaussian bias in [Das *et al.* 2011, van Engelen *et al.* 2012, Planck Collaboration 2014d].

3.5.2 Polarization

Although high precision polarization measurements are more difficult to obtain than temperature, the polarization measurements have greater potential to improve the lensing reconstruction in the case of low instrumental noise. The lensing effects are in general stronger in polarization, and the lens-induced B-modes arise from smaller-scale lenses than for temperature (typically $l \sim 1000$, where the E-modes peak) which makes the reconstruction of the lensing potential better in principle. Following the same steps as in temperature, one can define optimal quadratic estimator $\hat{\psi}_{XY}$:

$$\hat{\psi}_{XY}(\mathbf{l}) = N_{XY}(\mathbf{l}) \int \frac{d^2\mathbf{l}_1}{(2\pi)^2} \tilde{X}(\mathbf{l}_1)\tilde{Y}^*(\mathbf{l}_1 - \mathbf{l}) g_{XY}(\mathbf{l}_1, \mathbf{l}), \tag{3.33}$$

where X, Y are T, E or B. The signal-to-noise ratio reachable with those estimator depends on the correlation between X and Y and the effect of the lensing on them. For statistical parity invariance, the two cross-correlations TB and EB should vanish. Therefore, their estimator does not suffer from the cosmic variance from the unlensed E and B fields on small scales, unlike other correlations. For example, $\hat{\psi}_{BB}$ gives little information if there are no unlensed B-modes, while the correlation between the lens-induced B-modes with the E-modes gives a powerful estimator. In order to increase even more the signal-to-noise ratio and have a better estimate of the lensing potential, one can combine all the estimators to give a total minimum-variance estimator estimator:

$$\hat{\psi}_{MV}(\mathbf{l}) = \sum_p \hat{\psi}_p(\mathbf{l}) W_p(\mathbf{l}) \tag{3.34}$$

$$N_{MV}(\mathbf{l}) = \Big(\sum_{pq} (\mathbf{N}^{-1})_{pq} \Big)^{-1} \tag{3.35}$$

where p and q are the possible auto and cross correlations between T, E and B (without permutations). The weights W_p are given by:

$$W_p = \frac{\sum_q (\mathbf{N}^{-1})_{pq}}{\sum_{qn} (\mathbf{N}^{-1})_{qn}} \tag{3.36}$$

3.5.3 Some limitations

I highlighted the reconstruction of the lensing potential in an ideal case, where we have all-sky measurements. In general, working with a partial sky coverage makes the reconstruction more difficult, including leakage of E-modes into B-modes [Pearson *et al.* 2014]. In addition, for a nonuniform survey geometry, with perhaps foreground-contaminated regions removed, more sophisticated techniques than the Fourier transform weighting scheme employed here would have to be developed [Hu 2001, Hanson *et al.* 2009a].

3.6 Weak lensing, dark energy and cosmological neutrinos

The CMB lensing is an early dark energy probe. For instance the B modes directly feel the intensity of lensing from the Hubble expansion at high redshift [Hu 2005, Acquaviva & Baccigalupi 2006]. Concerning the background evolution, many of the dark energy models are parametrized by essentially two parameters: the present value w_0 of the equation of state and its first derivative with respect to the scale factor a, $-w_a$

$$w(a) = w_0 + w_a(1 + a). \tag{3.37}$$

In particular an accurate measurement of the lensing peak may break the degeneracy between those two parameters. As seen in Fig. 3.3, we show the effect of different values for w_0 and w_a on the lensed B modes power spectrum.

Dark energy is not the only component to modify the structure formation rate. Since the detection of neutrino oscillations has proved that neutrinos have mass, the idea that massive neutrinos could play a significant role in the history of the Universe and in the formation of structures becomes an active field of research (see [Bond *et al.* 1980] or [Lesgourgues & Pastor 2006] for a review of the field). Even if the effect of such a component is a priori small, observational cosmology reached recently such a high precision that it is unavoidable to take into account the presence of massive neutrinos, in particular in the observable matter density power spectrum [Planck Collaboration 2015d]. The latter would be for instance damped in a noticeable way by massive neutrinos as shown in Fig. 3.4. The effect on the background cosmology from the neutrinos is highly degenerate and can be compensated by changes in other cosmological parameters (such as H_0). There is, however, some sensitivity of the CMB anisotropies to neutrino masses as the neutrinos start to become less relativistic at recombination[5] (modifying the early ISW effect), and from the late-time effect of lensing on the power spectrum. The latest constraints from the satellite Planck (assuming three species of degenerate massive neutrinos), in combination with other experiment gives $\sum m_\nu < 0.17$ eV [Planck Collaboration 2015d]

[5] Neutrinos became non-relativistic after recombination.

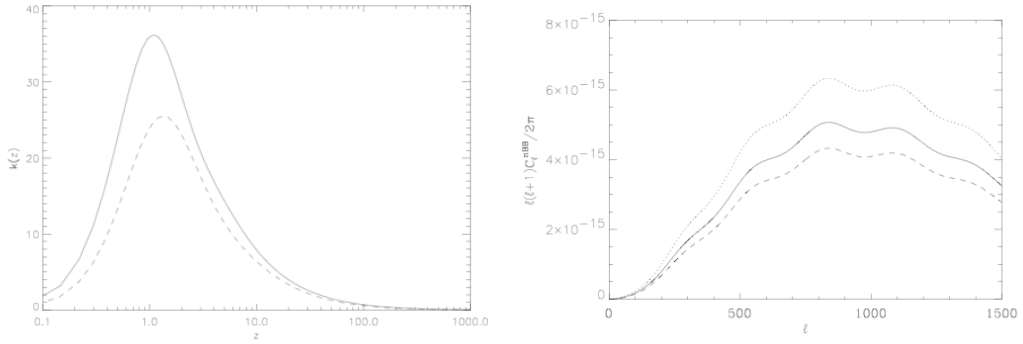

Figure 3.3: *Left panel:* Measure of the redshift distribution of the lensing effect coming from the background cosmological expansion (lensing kernel) for two different dark energy models: SUGRA (inspired by supergravity theories, dashed line) and ILP (inverse power law potentials, solid line). *Right panel:* Lensed B modes power spectrum for various possible values of the dark energy parameters: $w_0 = -0.9$ and $w_a = 0.5$ (solid line), $w_0 = -0.965$ and $w_a = 0.665$ (dashed line), $w_0 = -0.8$ and $w_a = 0.24$ (dotted line). The change in amplitude is noticeable. Figures taken from [Acquaviva & Baccigalupi 2006].

and an experiment like Simons Array in combination with galaxy surveys forecasts an error on the total sum of the neutrino masses of $\sigma(\sum m_\nu) = 0.04$ eV after foregrounds subtraction.

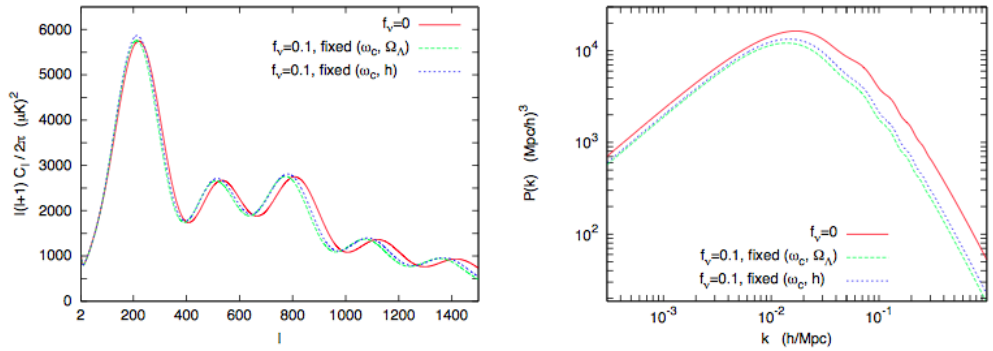

Figure 3.4: CMB temperature anisotropy spectrum and matter power spectrum for three models: ΛCDM model with three massless neutrinos (red), and two models with three massive degenerate neutrinos and a total density fraction $f_\nu = 0.1$. In the last two models, ω_b and ω_{cdm} have been kept fixed (to the value of the model with massless neutrino), and so it implies a shift either in h (dashed green) or in Ω_Λ (dotted blue). Figures taken from [Lesgourgues & Pastor 2006].

3.7 Observational status as of 2012

The first observational constraints on CMB lensing are quite recent given the fact that they require measurements of CMB power spectra at high resolution with low instrumental noise. So at first, people tried to put constraints on the gravitational lensing potential by measuring its correlation with other large-scale tracers of the gravitational lensing potential. For example, we discussed previously the Integrated Sachs-Wolfe effect which takes into account the variation of the gravitational potential between the moment when the photon enters and leaves this potential. This effect is extremely sensitive to the background properties of the dark energy [Coble *et al.* 1997] and can provide an unique probe on its clustering properties. Unfortunately, the ISW effect is difficult to capture as it is hidden by larger primordial anisotropy. But using the fact that both ISW and the deflection field of CMB lensing are large-scale tracers of the same gravitational potential, their cross correlation can be probed [Seljak & Zaldarriaga 1999, Goldberg & Spergel 1998] and can be used to isolate the ISW effect or measure the matter power spectrum. While lensing measurements from the CMB alone provide direct constraints on the evolution of gravitational potentials, cross-correlations with tracers of large-scale structure have the advantage of being less sensitive to systematic errors and have potentially larger detection significance which makes that cross correlations happened earlier than the direct detections. The first detections of CMB lensing were obtained through cross-correlation with radio and optical galaxies [Smith *et al.* 2007, Hirata *et al.* 2008]. Finally, the first detection of the CMB lensing potential power spectrum using the four-point function has been made recently by ACT using the CMB temperature lensing alone [Das *et al.* 2011]. The observational field is now extremely active, and the publications made during the period 2012-2015 (which covers my PhD study) and a more extensive account of the latest results on the subject is provided in the Chap. 11.

3.8 Delensing

The lens-induced B-modes pattern is added on top of any B-modes produced earlier, such as the primordial ones related to tensor metric perturbations and which are a key prediction of many inflationary models, see Sec. 2.3. The tensor contributions are more pronounced at low multipoles (large angular scales), whereas the lensed contribution has a typical signature at small scales (arcminute scales) as shown in the Fig. 3.2. So for a relatively high value of the tensor-to-scalar ratio r, those two effects can be loosely distinguished on the extrema of the spectrum (very low multipoles *vs* very high multipoles). Therefore if we want a precise characterization of the primordial B-modes power spectrum, the lensing contribution acts as a strong contaminant. In addition, the smaller the value of r, the more difficult is the separation of effects.

Observations from large-scale CMB B-mode polarization put already several upper limits on the value of the tensor-to-scalar ratio, reaching recently $r < 0.12$

(95% C.L.) [Ade *et al.* 2015]. For long time, experiments were in an instrumental noise-limited regime and upper limits decreased as the observation time increased. Recently, large arrays of detectors sensitive to polarization have been deployed and observe the sky for few years now. The instrumental sensitivities of those different experiments are now reaching a turning point where their "noise" levels will be soon limited by the lensing amplitude[6]. Leaving foreground contamination on aside, the limiting factor in constraining the amplitude of the primordial B-modes power spectrum will be the lensing B-modes, acting as a source of noise for scales larger than the arcminute.

So in order to get rid of the contamination of lensing, and put tighter constraints on primordial B-modes, we needs to "delens" the observations[7]. Such algorithms already exist and are based on a statistical separation of the tensor and lensing B-mode signals. Those mainly fall into two categories, internal delensing [Knox & Song 2002, Kesden *et al.* 2002, Seljak & Hirata 2004] and external delensing [Smith *et al.* 2012, Simard *et al.* 2014, Sherwin & Schmittfull 2015], but both are based on the same idea: given a noisy observation of E-modes and an estimate of the CMB lensing deflection field, one can form an estimate of the large-scale lensing B-mode and subtract it from the observed B-mode to reduce the level of lensing contamination. The definition of internal or external methods relies on the type of data sets used to estimate the CMB lensing deflection field. In the case of internal delensing, the CMB lensing deflection field is estimated from the same data sets used to estimate the CMB angular power spectra, while in the case of the case of external delensing, one tries to obtain maps of the integrated mass distribution from observations of large-scale structure which are tracers of the same underlying mass distribution.

Ideally, one would like to use internal delensing, as it requires only one data set. However, to achieve best delensing perfomance, this also requires very low noise levels and high angular resolution experiments. The latter is crucial as the large-scale lensing B-modes receive contributions from E-modes and gravitational lensing on small scales. So, for low noise experiment limited by the lensing, large and small scales become linked [Smith *et al.* 2012]. So far, major ground-based experiments focusing only on large-scale B-modes have been using large beams (degree scales) and they do not have the internal capability of delensing as they cannot determine with high fidelity the small scale polarization. In this respect, relying on an external delensing seems promising with such experiments. On the contrary, experiment with small beams (arcminute scale) like POLARBEAR and its upgrades will have the capability of using internal delensing with their upcoming data sets[8]. As of now,

[6] We recall that the lensed B-modes coming from E-modes for modes $l << 1000$ is somehow independent of the multipole considered (white noise spectrum). in terms of instrumental white noise level, it would correspond to roughly 5 μK.arcmin.

[7] Theoretically it is not actually needed if one knows the full statistical distribution of the lensed sky accurately enough by using the full true likelihood [Lewis & Challinor 2006]. However in practice, building such a likelihood is not trivial and delensing algorithms appear easier to handle at first even though limitations of such algorithms are their efficiency to actually delens.

[8] The main difficulty for those small beam experiments will be to be able to reconstruct the

the delensing algorithms are not perfect in the sense that simulations shown that we cannot completely remove the effect of the lensing, and are yet to be validated on real data. The main realistic forecasts predict an improvement on the constraints on r of a factor less than 10 [Sherwin & Schmittfull 2015].

largest modes. This requires a perfect control of systematic effects, and a long integration time. For ground-based experiments, there are also the problem of the atmosphere and the foreground removal. This is discussed later in the manuscript.

Chapter 4

Foregrounds

Contents

4.1 We live in a complex world

Observations of the CMB are conducted from the inside of our Galaxy. The photons collected by the instruments are a mixture of CMB photons and photons that come from many physical mechanisms that generate microwave emissions in the sky. In addition to contaminants from our galaxy, there are also extra-Galactic contaminants such as point sources (quasars or distant galaxies) or emission from the Sunyaev Zel'dovich effect. Those emissions make measurement of CMB temperature anisotropies difficult, and some of the effects are also believed to be polarized. The main foregrounds for intensity measurements are:

- Synchrotron radiation: Relativistic electrons which undergo an acceleration by a magnetic field produce a synchrotron radiation. The spectrum is function of the intensity of the magnetic field but also the energy of the electrons. The magnetic field of our Galaxy (few nG) is sufficient to produce a large synchrotron emission for frequency up to 100 GHz. The spectrum is often modeled by a power law ν^{β_s}, where ν is the frequency and $\beta_s \sim 3$ [De Zotti *et al.* 1999].

- Galactic dust: Cold dust within our own Galaxy can emit via thermal radiation (vibrational dust). At frequencies above 100GHz, the dominant radiation mechanism is thermal dust emission. The characteristic frequency is function of the dust grains, and therefore varies with dust population and environment. The thermal dust has been recently modeled as a modified black body with free temperature T_d and spectral index β_d per pixel [Planck Collaboration 2015c]. On average, the spectral index is around $\beta_d \sim 1.5$ and the dust temperature $T_d \sim 20$ K.

- Thermal Sunyaev-Zeldovich: Inverse Compton effect which implies Cosmic Microwave Background photons and free electrons from the inter-cluster

hot gas. This thermal effect modifies the spectrum of the Cosmic Microwave Background photons, parametrized by the Compton parameter y_{sz} [Planck Collaboration 2015h].

- Free-free emission, or bremsstrahlung: This radiation arises from electron-ion collisions, and therefore is well characterized by physical considerations [Dickinson *et al.* 2003].

- Spinning dust: Cold dust within our own Galaxy can also emit by excitation of their electrical dipolar moment (rotational dust) [Draine & Lazarian 1998]. It has been shown that simple two-parameter model can accommodate a large number of spinning dust model variations to high precision [Bennett *et al.* 2013, Planck Collaboration 2015c].

In polarization, the status is somewhat different. We do not have as many measurements as for intensity, and as of now we have often to rely only on models. On the other hand, while in intensity between 10 and 20 different diffused components for a proper model depending on the level of details required have been identified [Planck Collaboration 2015c], there are only two clearly detected foregrounds in polarization:

- Synchrotron: The exact level of polarization fraction is not really known, and vary across the sky. Several predictions and measurements reported polarization fraction between 3% and 20% (Galactic plane *vs* high Galactic latitudes) [Page *et al.* 2007], while other analyses report polarization fractions as high as 40-50% [Kogut *et al.* 2007] with a maximum of 70% [Pacholczyk 1970].

- Thermal dust: Depending on the alignment of dust grains with the magnetic fields, thermal dust radiation can be polarized. Here again, the exact level of polarization fraction is not exactly known. The balloon-borne ARCHEOPS gave the first constraints at large angular scales [Ponthieu *et al.* 2005], and recently the satellite PLANCK released higher precision measures [Planck Collaboration 2015b, Planck Collaboration 2015c]. The effect of polarized dust has been shown to be a high contaminant at large angular scales for frequency above 90GHz, thus particularly dangerous for ground-based experiments exploiting those range of frequency to observe the CMB.

4.2 Challenges for polarization measurements

"One of the main challenges facing upcoming CMB experiments will be to distinguish the cosmological signal from foreground contamination". This sentence could have been written in an article this year, but it has been written almost 20 years ago in [Tegmark *et al.* 2000]! In fact the problem of foregrounds is well known for long time [Bennett *et al.* 1992, Brandt *et al.* 1994, Dodelson & Stebbins 1994].

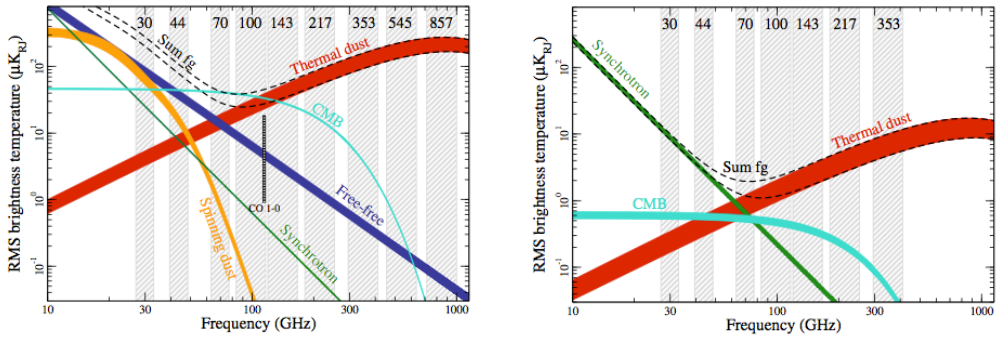

Figure 4.1: Brightness temperature rms as a function of frequency and astrophysical component for temperature (left) and polarization (right). Notice that they vary depending on location on the sky, angular resolution and sky coverage. One can clearly see the different behaviours of the component with respect to the frequency, which help in performing a component separation (cleaning) to get the CMB. Figure adapted from [Planck Collaboration 2015c].

For sure our knowledge on foregrounds is way better than 20 years ago thanks to better measurements and better models, but they still remain one of the main contaminant of CMB measurements. Concerning polarization measurements, we are entering into a era of precision measurements. In the early 2000, first measurements of E-modes were published [Kovac *et al.* 2002]. Luckily, the amplitude of E-modes on the region measured was still higher than any foreground contamination. However, during my thesis, first B-modes measurements came out along with the first trouble due to foregrounds. At first, results were focused on small scales B-mode, were the levels of polarized foregrounds are supposedly low. The experiment POLARBEAR reported its first measurement of B-modes at sub-degree scales, with a contamination of foreground much lower than the statistical uncertainties [POLARBEAR Collaboration 2014c]. But shortly after, the BICEP2 experiment claimed detection of B-mode polarization at degree angular scales [BICEP2 Collaboration 2014], consistent with a tensor contribution with tensor-to-scalar ratio $r = 0.2^{+0.07}_{-0.05}$. Right after, a detailed study by the satellite PLANCK of the polarized dust over the sky [Planck Collaboration 2014g] and latter a joint analysis PLANCK x BICEP2 revealed that the excess of power found by the BICEP2 team was mainly due to polarized dust contamination, leaving an upper limit on the tensor-to-scalar ratio $r < 0.12$ at 95% confidence [Ade *et al.* 2015].

The weakness of the BICEP2 experiment was its lack of frequency coverage. They observed mainly at one frequency, 150 GHz, and so they didn't have the capability to disentangle the different contributions. However, the satellite PLANCK has 9 frequency bands, which make it a powerful machine to separate the different sky components. Unfortunately, the sensitivity of PLANCK compared to ongoing and future experiment is not very good, and is quickly the limiting factor while

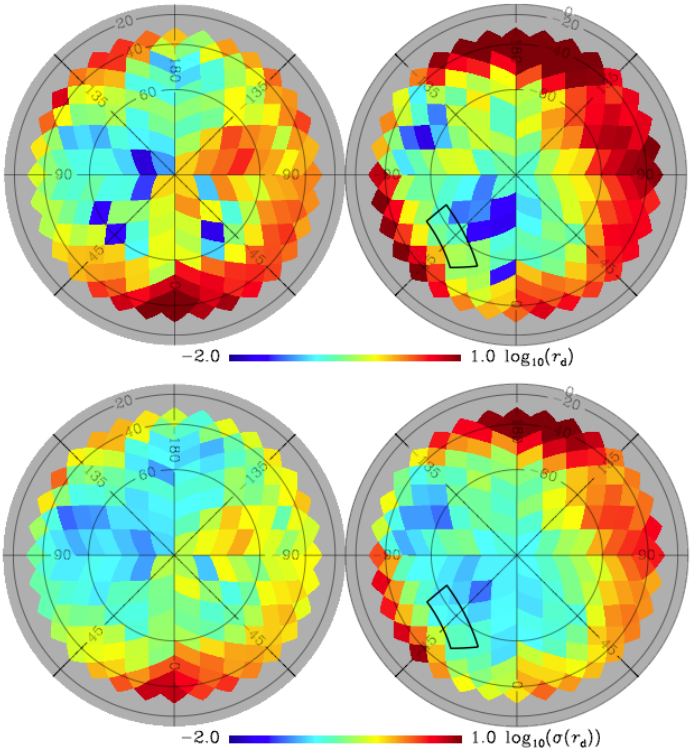

Figure 4.2: *Top:* Estimated contamination at 150 GHz at $\ell = 80$ from dust in r_d units from the Planck data (see [Planck Collaboration 2014g] for more explanations and definitions). Maps are in orthographic projection and Northern (Southern) Galactic hemisphere is on the left (right). *Bottom:* Associated uncertainty. The main message of these figures is that there exists no regions where the contamination of polarized dust can be safely neglected. Even low dust regions have a large uncertainties. Figures taken from [Planck Collaboration 2014g].

cross-correlating with others. Future ground-based experiments already plan to have multi-frequency detector arrays, with $\mathcal{O}(10^4)$ detectors, enabling an efficient component separation such as POLARBEAR-2 [Barron *et al.* 2014]. These hardware upgrades have also to be coupled to new, statistically robust and numerically efficient component separation algorithms and methodologies to enable unlocking the full scientific potential of the data[1]. In this manuscript, I will detail the analysis of POLARBEAR-1, which firstly target the part of the B modes at high multipoles ($>$500), believed to have little contribution from polarized foregrounds (at 150 GHz).

[1] Although I worked on component separation over the course of my PhD with collaborators from APC (FR), SISSA (IT) and LBNL (US), with potential application to future POLARBEAR data sets, this is not discussed later in this manuscript (not yet published and released).

Chapter 5

The Polarbear experiment

Contents

Polarbear is a new generation CMB B-mode polarization experiment. It consists of the Polarbear receiver and the Huan Tran Telescope (HTT). Since the beginning of 2012, Polarbear is located at the James Ax Observatory in the Atacama Desert in Chile. During the first half of the first campaign of observations (2012-2014), it focused on small patches on the sky (10 deg^2 each) with approximately 3.5 arcminute resolution and precise control and mitigation of systematic effects. These regions on the sky were scanned repetitively at constant elevation with the polarization of the incident radiation modulated by a cold stepped half-wave plate (HWP). The observations were performed with 1,274 bolometric detectors operating simultaneously all along the first campaign. In order to handle such a huge flow of data (about 10 times more than Planck), Polarbear instrument includes a complex detector/readout system. Its operation involved multiple modulations on different timescales to allow for discrimination of the sky signals from the instrumental or atmospheric ones. Mid-2014 to the end of 2015, we switched to the observation of a bigger patch on the sky (roughly 400 deg^2), and the cold stepped HWP was replaced by a warm (outside the receiver) and continuously rotated HWP. During observations, the instrument is observing the sky with the initial array at

Figure 5.1: POLARBEAR experiment at the James Ax Observatory in Northern Chile on Cerro Toco at West longitude 67° 47' 10.40", South latitude 22° 57' 29.03", elevation 5,200 m.

150 GHz. The future upgrades of the instrument (POLARBEAR-2 and SIMONS ARRAY) will have several frequency bands of observation to allow an efficient cleaning of the cosmological signal of interest from various astrophysical contaminations.

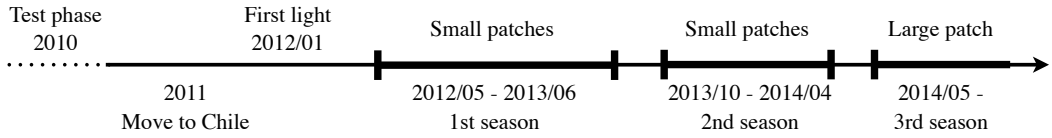

Figure 5.2: Timeline for the first campaign of the POLARBEAR experiment. I started to work on POLARBEAR in April 2012, just before the first season, and my thesis finishes at the end of 2015, at the end of the 3rd season of observation.

5.1 Science goals

POLARBEAR is dedicated to characterize the B-mode polarization of the CMB on both large and small angular scales (for more informations about B-modes science, see Chap. 1, 2, 3, 4). Its relatively small angular resolution (3.5 arcminutes) allows to probe the small scales down to $\ell \sim 2500$ while its location in Chile gives in prac-

tice access to more than half-sky coverage revealing the largest scales. In its first campaign, POLARBEAR focused on small patches on the sky, and integrated deeply to quickly achieve a very low level of noise.This strategy was devised in order to characterize first the gravitational lensing signal. This strategy has been a success, and based on one year of the data the signal has been detected using three different observables as described in three major papers [POLARBEAR Collaboration 2014a, POLARBEAR Collaboration 2014b, POLARBEAR Collaboration 2014c]. Combining all probes (galaxy cross-correlation, deflection field power spectrum, and direct B-power measurement), POLARBEAR achieved a 4.7σ rejection of the null hypothesis of no B-modes. The second season focused also on the small patches, while the third season seen a change of scanning strategy. A large portion of the sky is now under observations ($\sim$ 400 sq. degrees), in order to also probe larger scales. POLARBEAR and its successor, so-called SIMONS ARRAY, are projected to achieve a 2σ detection of $r = 0.001$ and will also continue to characterize the gravitational lensing signals in an attempt to measure properties of cosmological neutrinos and dark energy properties.

5.2 Instrument overview

The following sections describe the instrument's detectors and optics depicted also in Fig. 5.4. Informations and descriptions are taken from [Arnold *et al.* 2010, Kermish *et al.* 2012, Errard 2012].

5.2.1 Huan Tran Telescope

The Huan Tran Telescope is an off-axis Gregorian telescope with a 2.5 meter primary aperture that provides the 3.5 arcminute angular resolution necessary to characterize the gravitational lensing and leading to low edge diffraction. The telescope was designed for large optical troughput while simultaneously mitigating systematic effects such as temperature-to-polarization leakage and cross polarization.

5.2.2 Receiver

The fundamental noise limit for any CMB experiment is known as photon noise, which is set by the quantum fluctuations in the arrival rate of photons. CMB polarimeters seek to minimize all other noise sources, as phonon noise or readout noise, such that photon noise dominates. To achieve a high level of sensitivity, the POLARBEAR focal plane is cooled to 250 milliKelvin so that thermal carrier noise in the detectors is smaller than the photon noise. A closed-cycle refrigeration is used to achieve this cooling.

5.2.3 Detectors Array

Because only bolometers operated from sub-Kelvin platforms and at frequencies less than 90 GHz are sensitive enough to be photon noise limited, the Berkeley group

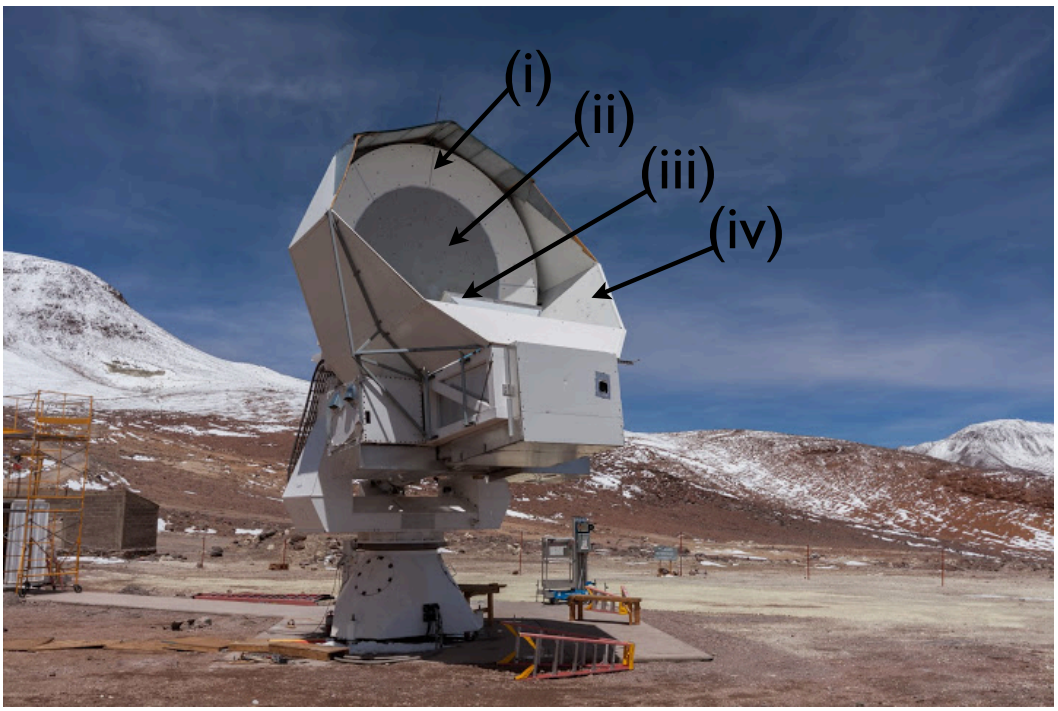

Figure 5.3: The Huan Tran telescope at the James Ax Observatory. The labels on the picture are (i) the primary guard ring, (ii) the precision primary mirror surface (2.5 meter primary aperture), (iii) the prime-focus baffle, and (iv) the co-moving shield. The secondary mirror and receiver are not visible within their respective enclosures.

created a crossed double slot dipole, TES Bolometer which can measure polarized radiation with the required sensitivity. Gains in sensitivity were made using huge number of these TES bolometers and by increasing the throughput of the telescope.

Antenna The antenna used in our detector is a double slot dipole. The antenna is used in conjunction with a silicon hyper hemi-spherical lens on which the detector chip sits on. The combination antenna/lens couples efficiently to typical telescope optics. Each antenna is also linearly polarized and a dual linearly polarized version can be used. This is convenient in our application, since the polarization of the incident light is what we want to measure.

Superconducting Microstrip The antenna is connected to a transmission line, which brings the incoming optical power to the detector. Conventional transmission line materials would be very high loss at these frequencies, which would be unacceptable for an experiment such as this where we are already looking for an extremely weak signal. However, superconducting microstrip is a very low loss transmission line that works well in our application. A convenient choice of materials is niobium,

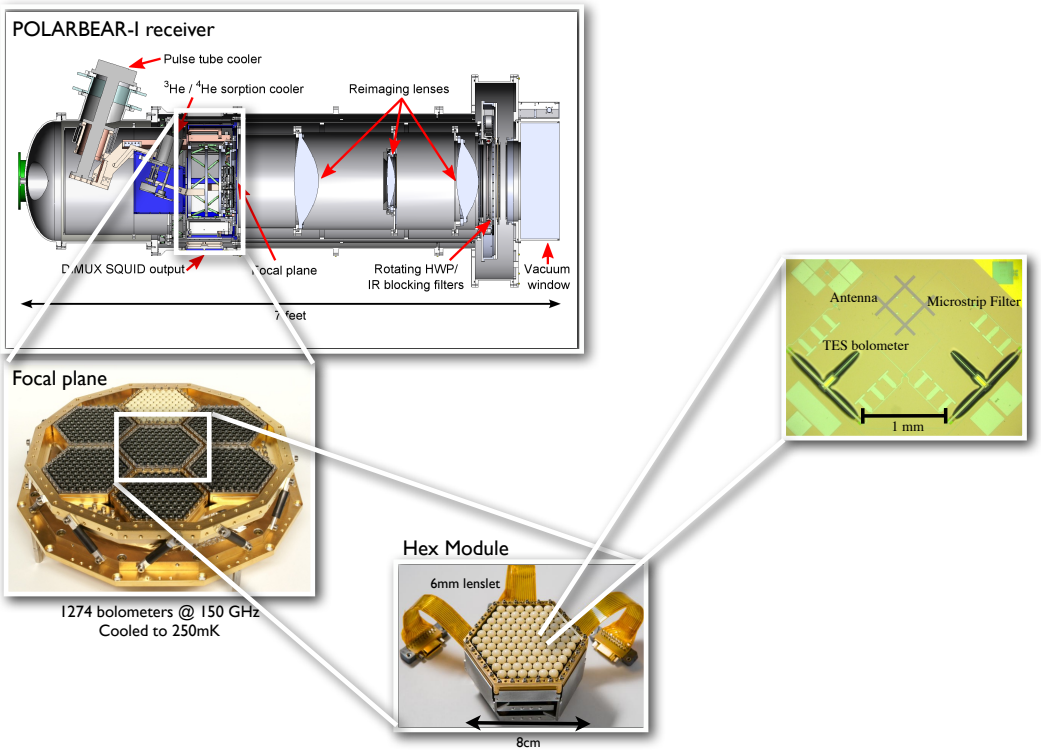

Figure 5.4: Overview of the POLARBEAR receiver. A zoom is progressively made on the focal plane which contains 7 wafers (Hex module), in which are allocated the 1,274 bolometers grouped in 637 pixels of two bolometers. The small white and black "balls" seen in focal plane and in the Hex module are the hemi-spherical lenslets. The microstrip filters and the antennas can also be seen on the last picture.

which has the highest superconducting temperature of all the elements.

Band defining microstrip filter An advantage of the use of microstrip to connect the antenna to the bolometer is that band defining microstrip filters can be integrated into the transmission line [Myers *et al.* 2008]. In a conventional millimeter wave receiver, band defining filters are metal mesh off-chip optical filters. In our detectors, the filters are integrated on the chip and different pixels can easily have different frequency sensitivities. Increasing the level of integration eases the scaling of current receivers to higher pixel counts (strategy used for POLARBEAR-2 for instance).

Bolometers The bolometers are composed of a terminating resistor and a superconducting Transition Edge Sensor (TES) located on a leg isolated silicon nitride substrate. The incoming power on the superconducting microstrip is dissipated in the load resistor as heat, and the change in temperature is measured by the TES.

The bath temperature must be below 300 mK in order to achieve the sensitivity needed, that is reducing the detector noise to below that in the incident light. TESs have many advantages over conventional semiconducting bolometers. Probably the most important one in our application is that the TES readout electronics can be multiplexed, so that the signal for more than one pixel can be brought out on each pair of wires.

5.2.4 Multiplexing

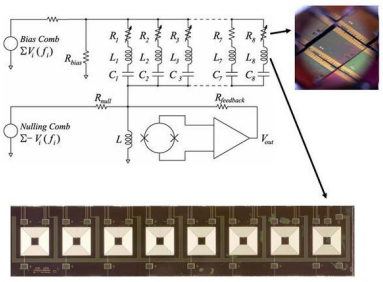

Figure 5.5: Schematic outlining the demonstration of an eight-channel readout multiplexer. Also shown is a picture of the inductor chip.

POLARBEAR focal plane hosts more than a thousand of bolometric detector, and thus they require sophisticated readout schemes. To reduce thermal loading onto the coldest stages of the experiment and to reduce the complexity of instrumenting large arrays, a readout multiplexing scheme has been developed and demonstrated at Berkeley (digital frequency domain multiplexer, or DfMux [Smecher *et al.* 2012]). Bias signals, which are sinusoidal voltage at a unique frequency, must be sent from room temperature electronics down to cryogenic focal planes and readout signals must get back out without exceeding the cryogenic budgets of feasible milliKelvin refrigerators [Kermish *et al.* 2012]. The sensor signals are thus separated in frequency space and can by summed before being readout by SQUID electronics (superconducting quantum interference device).

5.2.5 Half-wave plate

The rotated (stepped) half-wave plate is a 3.1 mm thick single crystal disk of A-plane sapphire. Because of its birefringent properties, rotation of the HWP modulates the polarization of the sky signal (and not the instrumental one), and thus allows for mitigation of instrumental systematic effects which do not have the requisite symmetry of true CMB polarization such as $1/f$ noise of scan-synchronous noise. It also ease requirements on the levels of instrumental and cross-polarization and allow such systematic errors to be better characterized and corrected later in the data analysis step. In the first season, the HWP was at the entrance of the receiver

and stepped everyday by an angle of 11.25 degrees. For the 3rd season, we stopped using this HWP, and we instead installed a warm (outside the receiver) continuously rotated HWP.

5.3 Observations

5.3.1 Different types of observation

As mentioned previously, POLARBEAR is a dedicated B-modes experiment. Our main objective is to observe the CMB, and extract the polarization information with an unprecedented precision. For the first and second season, we scanned repetitively three patches on the sky. The patch locations, reported in table 5.1, have been chosen to optimize a combination of low dust intensity, availability throughout the day, and overlap with other observations for cross-correlation studies (e.g. QUIET, HERSCHEL).

Table 5.1: The three POLARBEAR patches.

Patch	RA	Dec	Effective Area
RA23	$23^h1^m48^s$	-32°48'	8.8 deg^2
RA12	$11^h53^m0^s$	-0°30'	8.7 deg^2
LST	$4^h40^m12^s$	-45°	7.0 deg^2

Driven by our cooling system, we operate with a 36 hour observation cycle, shown in Fig. 5.6. We start the cycle by performing observations of astrophysical calibrators such as radio sources, planets and polarized sources (Tau A or Cen A). Those observations are used afterwards to model the different instrument properties, as described in Chap. 6. Then the first patch shows up above the horizon, and we start observing it. Before and after each hour long observation of CMB patch (and before/after each planet/radio sources/polarized source measurements), we perform two calibration measurements: the stimulator (gain calibration) and the elevation nods (weather). We continue to observe during 36 hours in total, and then we perform a fridge cycle, and we start again observing once the first patch or astrophysical source shows up again. The main type of scans performed are summarized in Tab. 6.1.

5.3.2 The scanning strategy for the CMB patches

Each patch is available from 6 to 8 hours per day. We break up each patch observation into approximately 15 minutes long scans, called Constant Elevation Scans (CES). During each CES, we work at constant elevation, and we scan back and forth in azimuth while the patch moves in the sky. Each sweep in azimuth is called a subscan. After approximately 15 minutes, the patch is entirely scanned and has disappeared from our field of view, and we change the elevation of the telescope

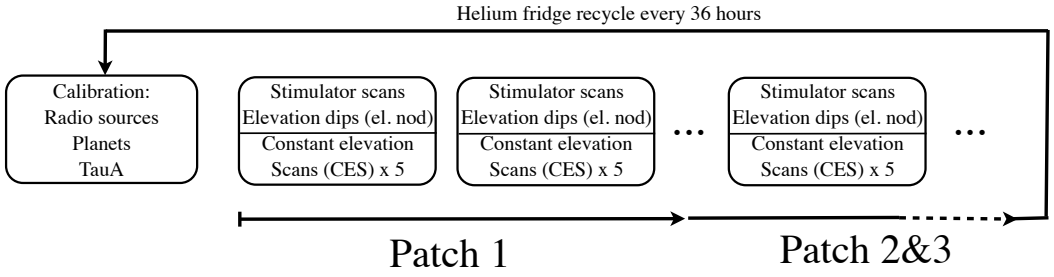

Figure 5.6: Diagram of a typical observation cycle, with observations of astrophysical sources and CMB. Ground-based calibrator measurements (stimulator) are often performed in order to latter calibrate the bolometers. The cycle last for 36 hours and then we restart again the whole cycle.

to catch up with the patch, and we start again scanning in azimuth. Per day and per patch, we have about 30 CES, and each CES consists in roughly 200 subscans. This scanning strategy has the advantage of taking benefit of the rotation of the sky in the telescope frame. Indeed for a given patch, we scan the same sky for all CES, but the "attack angle" (value of the polarization angle projected on the sky) is not the same between two different CES. This allows us to break degeneracies in polarization as we need at least two measurements with different polarization angle values to disentangle Q and U inside a pixel. It also mitigates the spurious signals which are coming from the instrument or from the ground and therefore which do not rotate with the sky. Such an illustration of the mitigation of systematic effects is shown in Fig. 5.7 and is quantified latter in Chap. 10.

5.3.3 Remote observations

I also participated to the routine operations of the telescope through remote observations. In order to improve the efficiency of the observations as well as the quality of the data, a set of tools has been created to watch the site activities at all times. Those shifts are shared between people in US, Chile, Europe and Japan so that there is always someone watching the operations and operating remotely or contacting the site team quickly. In this way we find and correct problems more quickly and minimize down time. Those shifts are usually 4 hours long, with several reports used afterwards to build statistics.

5.4 Data analysis framework

The data analysis of an experiment such as POLARBEAR is not the task of a single person. The volume of data recorded, and the complexity of the data set require a broad panel of knowledge in instrumentation, signal processing, statistics, physics, astrophysics, CMB data analysis as well as high level coding skills. Fortunately,

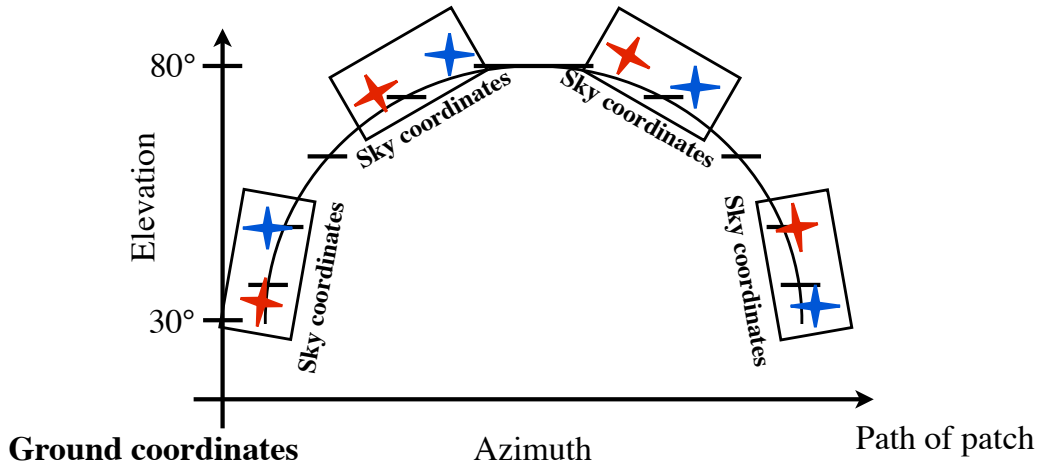

Figure 5.7: The CMB signal (red star) is fixed in sky coordinates while the leakage signal (blue star) is fixed in ground coordinates, leading to an averaging of leakage due to sky rotation when we compute sky maps.

the development over the last decades of efficient programming languages and collaborative tools made this task easier for many people with different skills to work together efficiently. At any given time, the data analysis team was constituted of about 10-15 people, distributed all over the world (US-Europe-Japan-Chile). We used a collaboration platform (Twiki[1]) to share all kind of materials and news, and regular teleconferences (1-3 per week as far as I was concerned) were done in order to report everyone's work to the collaboration. I also did several extended visits in both the US (University of California, Berkeley) and Japan (KEK, Kavli IPMU).

5.4.1 AnalysisBackend

AnalysisBackend is POLARBEAR's analysis package, designed both for in-the-field use for Chile data, as well as for analysis the data from elsewhere in the world. AnalysisBackend is a stand-alone package in the sense that we can analyze the data from row timestreams up to the power-spectrum estimation. It can also serve as an interface with already existing analysis tools, by first pre-processing the data (unpacking and calibration). Working on AnalysisBackend codes involves dealing with rapid development and changes from up to a dozen users, so we make use of GIT which is a distributed version control system[2] (free and open source). The programming language chosen was PYTHON[3]. One of the main advantage of this language is it's open source license. Also, PYTHON allows for easy interfacing with other programming language, and we sometimes make use of C to get better computational

[1] http://twiki.org
[2] http://git-scm.com
[3] https://www.python.org

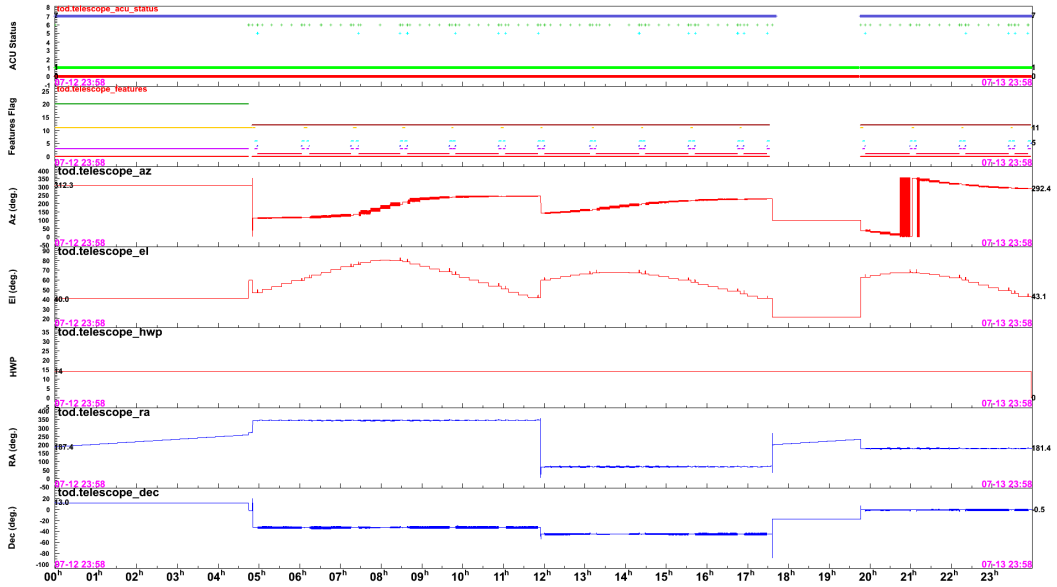

Figure 5.8: One of the page of the web interface of the *LivePB* software (Yuji Chinone). We can easily check out the azimuth, elevation, RA, Dec, the feature flags (describing operations ongoing), etc. We can see for example a typical CMB scan between 5 am and 12pm, with constant elevation period changing every 15 minutes and quick azimuth sweeping meanwhile.

performances.

5.4.2 High performance computing: the era of supercomputers

We collect the data at a rate of about few Terabytes per year. Exact analysis of the data set produced is a serious computational challenge, which cannot be done on a single laptop or simple workstation. This has to be matched by sophisticated and robust analysis performed on powerful machines, as we need to process several times the data set, or even simulate it thousands times. Most of the work done in this thesis has been performed at the National Energy Research Scientific Computing Center[4] (NERSC), which is a scientific computing facility based in California (USA). NERSC provides several of the largest computing systems of the world. All along my thesis, I mainly performed my data analysis work on three machines: Edison, Hopper and Carver. The data were mostly processed on the Edison machine, which is a Cray XC30 supercomputer with 133,824 compute cores, grouped in 5,576 computes nodes (2x12-core Intel "Ivy Bridge" processor at 2.4 GHz). Each node has 64 GB memory, and each core has 19.2 Gigaflops/sec at the peak performance. Over the course of my three years of thesis, I used about 1.5×10^6 CPUhours, with 3/4 of it devoted to the analysis of the first and second seasons of observation.

[4] https://www.nersc.gov

Chapter 6

Low level data processing

Contents

The calibration of the data is the first step, and at this early stage of the experiment, it's one of the longest in order to have the cleanest data possible. While I only had a small contribution to the calibration for the first release, mostly learning from experienced observers, I was highly involved in the calibration throughout the second release by leading the overall effort. In addition, I was leading the gain calibration

pipeline for the second release, while contributing to modeling the beams in the meantime. I completely automated and parallelized the gain calibration pipeline, so that as a result we can generate the gain model for more than 2 years of data in less than an hour. While working on the gain calibration, and motivated by a discrepancy between the two first seasons, I also extended the framework to use Saturn's observations consistently, by for instance accounting for the contribution from its rings in the analysis. I only participated indirectly to the effort to model the pointing by providing the inputs and feedback from the studies I led, and followed closely on the work related to the polarization angle calibration to ensure its coherence with other steps of the calibration pipeline. The atmosphere correction and the pixel differencing technique were already in place when I arrived, but I participated to the characterization of the performances for real observations.

6.1 Overview

The POLARBEAR instrument is a complex system, operating in a complex and changing environment. In order to do any meaningful analysis, we need to calibrate the data taken by the instrument. Calibrating the data consists in building a coherent data model in which we can compare and combine different measurements of the same quantity. This means establishing a relation between reference measurements with uncertainties and any "real life" measurements with their uncertainty used to derive the scientific results. Ideally, the reference measurements (calibrator) have smaller uncertainties than the measurements used for scientific purposes, so that the calibration should only be a small part of the total error budget in the final results. In order to maintain the quality of measurement as well as to monitor the performance of the instrument, we perform some of the calibration steps recurrently.

There are four primary instrument properties to be modeled: individual detector pointing (Sec. 6.3), thermal-response calibration (Sec. 6.5), the instrument effective beam (Sec. 6.6), and the polarization angle (Sec. 6.7). In addition, specifically to ground-based experiment, one needs to take into account the influence of the atmosphere through its transmission, the weather and the surrounding environment: POLARBEAR is set on the ground and surrounded by mountains!

The low level processing is a long and complex task. There are few and rather general recipes available in the literature given that each experiment is unique and requires a unique treatment, and so we need the in-depth knowledge of the instrument and its environment in order to clean the data at best. We often process iteratively, by refining models and testing new hypotheses. It is also illusory to try to separate the calibration work into independent pieces as they are all entangled. So despite the four several models listed above, one upgrade in one model needs to be checked and propagated into the other models. One of the main change in calibration tools between the first release and the second release was the automation of the different pipelines. In addition, calibration is a never ending process in the sense that we can always do better at the price of spending more time and effort

Table 6.1: Main types of scan performed.

Type	Comments
Science	CES/elnod/stimulator scans
Radio pointing	Track and raster for a long time over one or many sources
Optical pointing	Track and fixed
Array beam maps	Track and raster covering many pixels, with many sets of sky offsets (planets and Tau A)
Tuning performance	Run stimulator calibration at several elevations

Note. — The complete list is bigger, including more than 30 different feature flags.

on it. The real question is what are the requirements to have a sufficiently good calibration in a reasonable amount of time? This answer is not obvious. We will see later that we make use for instance of different null tests and checks for systematics to assess the quality of the data and so the calibration.

6.2 Organizing the data

6.2.1 From Chile to elsewhere

The data is backed up on several disks in Chile down the mountain at a rate of about 50 Mb/s and then sent everyday from Chile into different places around the world at a rate of 10 Mb/s (Internet) in order to perform the data analysis. The archive file indexing software constructs a table of observations. The table describes the contents and start and stop times for observations and scans. A scan is defined as a timer period where the scan name, source, and feature registers are constant. Scans are named in a human readable format according to the starting time of observation YYMMDD_HHMMSS (gregorian date). The main type of scans are summarized in Tab. 6.1.

6.2.2 Downsampling

We record the data at a rate of 190.73 Hz. The telescope azimuth and elevation encoders are queried at 95.4 Hz.The telescope pointing is reconstructed using the procedure described in Section 6.3 and linearly interpolated to the bolometer sample times. Because the analysis of the first season and the second season focused on scales $\ell < 2100$, corresponding to time domain frequencies less than 4.2 Hz (at constant velocity of 0.75 deg/s on the sky), we downsample the bolometer TOD and we reconstruct pointing by a factor of six to 31.8 Hz. The downsampling is performed in a single stage, with a single antialiasing filter. The antialiasing filter is constructed using a Kaiser window function ($\alpha = 6$) which gives a 3 dB point at the new Nyquist frequency, which means the very top end of the band takes a small aliasing penalty and have a small roll off. The band of interest of this filter goes

from 0-14Hz and has negligible ripple, so this gives plenty of margin if we want to go for even smaller scales (up to $\ell \sim 6500$ theoretically). In addition, performing a downsampling of the timestreams allows to process a smaller amount of data, and reduce the memory consumption for the next steps of the analysis. We store on disks both the fullsampled and the downsampled data.

6.2.3 Deconvolution of time constants

The bolometer optical response times, which are between 1-3 ms, are small enough that deconvolving these transfer functions is not necessary [Arnold *et al.* 2010]. The mean and maximum values of the time constants for each bolometer over the first season is shown in Fig. 6.1. The values of the time constants for the second season are similar to the first season. We checked that the bolometers with very high time constant (higher than the science band) are discarded from the analysis.

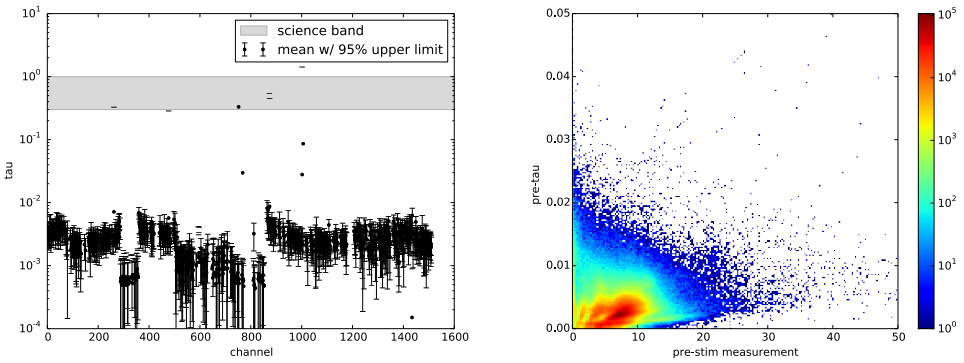

Figure 6.1: *Left panel*: Mean values of the time constants τ (in second) for each bolometer over all measurements of the first season. Most of the values are less than 10 milliseconds. For comparison, the grey shaded region corresponds to the science band (1-3 Hz). *Right panel*: Correlation between time constants (in second) and stimulator measurements (in ADC) for the first season. Most of the high values for the time constants correspond to small values of the stimulator (poor signal-to-noise).

6.3 Individual detector pointing

A five-parameter pointing model [Mangum 2001] characterizes the relationship between the telescope's encoder readings and its true boresight pointing on the sky. Of the parameters described in this reference, POLARBEAR uses IA, the azimuth encoder zero offset, IE, the elevation encoder zero offset, CA, the collimation error of the electromagnetic axis, AN, the azimuth axis offset/misalignment (north-south) and AW, the azimuth offset/misalignment (east-west). We

experimented with extending and modifying this parameter set, by adding more parameters and/or splitting the data as a functions of different criteria (distance to the Sun/Moon, weather, temperature of the ground, etc.). So far we did not find substantial improvements to the model reported above and used in [POLARBEAR Collaboration 2014c]. The pointing model is created by observing bright extended and point-like millimeter sources that were selected from known source catalogs [Wrobel *et al.* 1998, Murphy *et al.* 2010] to span a wide range in azimuth and elevation. These pointing observations occurred several times per week during observations. For the first release of data, the best-fit pointing model recovers the source positions for the sources that were used to create it with an accuracy of 25" RMS. Individual detector beam offsets are determined relative to the boresight using raster scans across Saturn and Jupiter and offsets are then combined with the boresight pointing model to determine the absolute pointing of each bolometer. In order to characterize the fluctuations, we made offset measures several times per week during observations for both seasons, and we found an RMS fluctuation of less than 6" over time. The offsets show arcsecond-level differential pointing between the two detectors in a pixel, which is shown to be a negligible contaminant in Sec. 10.3.5. I was not directly involved in the estimation of the pointing model during my thesis.

6.4 Saturn as a calibrator

6.4.1 From planet measurements to absolute calibration

Relative gain calibration using the stimulator occurs at the beginning and at the end of each hour-long CMB observation block. Ideally, we would like also to know the absolute and relative gain calibration for our CES science scans. To do so, we perform observations of planets[1] in combination with external relative measurements (stimulator, see next section on gains) to find the conversion from ADC counts to physical temperature units. This involves using our knowledge of the planet temperature, the angular size on the sky during the measurement, the atmospherical condition, and the beam of each bolometer in order to determine the gain of the bolometers mapping the planet. We have typically $\mathcal{O}(10^2)$ observations of each planet per season of observation.

Planet gain factor G When a detector is observing, the signal received is not exactly the same as the emitted one due to the diffraction-limited optics in the telescope: the input signal is convolved with the beam of the instrument. We define the planet gain factor G as the response of the detector to a signal, that is the conversion (or transfer function) from detector units to physical units. So ideally we would like to have a source filling the entire detector beam B, in order to have access to this quantity defined as

[1] We observe Jupiter, Saturn and Venus. For the gain model, we use only observations of Saturn.

$$G = \int\int d\theta d\phi B(\theta, \phi). \tag{6.1}$$

Let's now assume that we are observing a planet. For a given bolometer, we make a beam map m which is the true spatial distribution of the planet T convolved with the beam B of the bolometer such that

$$m(\theta, \phi) = (T * B)(\theta, \phi) = \int\int d\theta_1 d\phi_1 T(\theta - \theta_1, \phi - \phi_1) B(\theta_1, \phi_1). \tag{6.2}$$

In order to simplify the calibration, we approximate the planet as a point source with brightness temperature T_p. This is justified by the small angular diameter of the planets that we use to calibrate (typically 15-50 arcseconds as shown in Fig. 6.2) with respect to the beam of each bolometer (typically 3.5 arcminutes). So the Eq. 6.2 can be simplified as

$$m(\theta, \phi) \approx T_p \Omega_p B(\theta, \phi), \tag{6.3}$$

where Ω_p is the actual solid angle of the planet with angular diameter $2r_p$ ($\Omega_p = \pi r_p^2$). So finally, the planet gain factor can be expressed as a function of the measured beam map m and the planet parameters T_p and Ω_p as

$$G \approx \int\int d\theta d\phi \frac{m(\theta, \phi)}{T_p \Omega_p}. \tag{6.4}$$

Model In the actual analysis, we do not solve the Eq. 6.4 explicitly. The reason is that our scanning strategy doesn't allow us to scan entirely the planet for each bolometer at each scan. We observe planets using *raster scans* that is we track the planet as it moves across chopping around with a throw large enough so all detectors in a row see the planet. We also perform elevation steps between each azimuth scan, but they are too widely spaced (2 arcminutes) to capture all the important features of a detector beam in this direction. This scanning strategy results in individual detector beam maps having long stripes along azimuth at constant elevations. It is thus insufficient to simply integrate the map obtained from the planet scan, as it has only partial information. The technique we employ instead is to use the planet data to fit an elliptical Gaussian model to the beam core data in combination to an integral of the map residuals to that fit to account for near-sidelobes. For a given channel and a given observation, the gain planet factor $G_{ch,obs}$ is modeled as

$$G_{ch,obs} = \alpha(obs) \frac{I_1(ch, obs) + I_2(ch, obs)}{T_{\rm sat} \pi r_{\rm sat}^2(obs)}, \tag{6.5}$$

where α contains the atmosphere transmission correction (weather), $T_{\rm sat}$ is the microwave brightness temperature of Saturn, $r_{\rm sat}$ is half the average angular diameter of Saturn, and I_1 and I_2 are the integrated Saturn intensity (in ADC.steradian)

coming from the main lobe and the sidelobes respectively. The last two terms account for any dilution of intensity due to the beam of the bolometers or any intensity coming from the sidelobes.

- α(obs): The inverse of the atmospheric transparency estimated either from APEX or from POLARBEAR measurements of sky brightness at different elevations. This coefficient is computed per observation and it is the same for all bolometers. See also Sec. 6.8.1.
- $T_{\rm sat}$: the microwave brightness temperature of Saturn. See Sec. 6.4.2 for more details on the computation of the temperature.
- $r_{\rm sat}(obs)$: Half the average angular diameter of Saturn. This number is computed for each observation using ephemeris.
- $I_1(ch, obs)$: Contribution from the main lobe. Computed for each bolometer and each observation.
- $I_2(ch, obs)$: Contribution from the sidelobes. Computed for each bolometer and each observation.

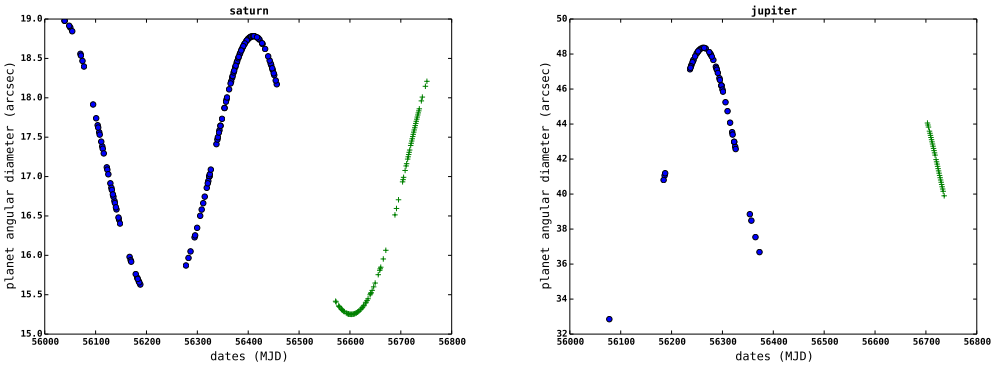

Figure 6.2: Average angular diameter (in arcsecond) for Saturn (left) and Jupiter (right) as a function of the date of observation (MJD). The angular diameter is computed for each observation using ephemeris. First season is shown with the blue circle and second season with the green cross. We do not attempt to model the change of the opening angle of Saturn's rings as viewed from Earth.

Integrated Saturn intensity from the main lobe: I_1 The Eq. 6.5 contains two contributions from the beam of each detector. The I_1 term is the contribution from the main lobe of the beam, that is the integral of the intensity map of Saturn as seen by the main lobe of the detector. In order to determine this term, we first

Table 6.2: Fitted parameters after data selection.

	Amplitude [ADC]	$\sqrt{8\log 2}\sigma_x$ [arcmin]	$\sqrt{8\log 2}\sigma_y$ [arcmin]	dx [arcsec]	dy [arcsec]
Free amplitude					
first season	222.5	3.47	3.47	0.125	-0.009
first season-p2	237.0	3.48	3.54	0.091	-0.046
second season	240.9	3.50	3.53	0.076	-0.064

Note. — Amplitudes are not normalized for the coaddition. The first season-p2 contains Saturn data from March-June 2013. The differences in amplitude are mostly due to a change of Saturn's brightness temperature.

fit (within a radius $r \sim 4$ arcmin) a 2D Gaussian $\mathcal{G}(A, \sigma_x, \sigma_y, x_c, y_c)$ to the filtered timestream of a bolometer (5th order polynomial filter) $d_{ch,obs}$ with

$$\mathcal{G}(A, \sigma_x, \sigma_y, x_c, y_c) = A \exp\Big(-\frac{1}{2}\mathbf{v}^T \mathrm{C}^{-1}\mathbf{v}\Big), \tag{6.6}$$

where $\mathbf{v}=\begin{pmatrix} x - x_c \\ y - y_c \end{pmatrix}$ and $\mathrm{C}=\begin{pmatrix} \sigma_x^2 & 0 \\ 0 & \sigma_y^2 \end{pmatrix}$. Then we estimate the I_1 term by integrating the 2D Gaussian with the fitted parameters

$$I_1 = \int\int dxdy\mathcal{G}(A, \sigma_x, \sigma_y, x_c, y_c) = 2\pi A\sigma_x\sigma_y. \tag{6.7}$$

Integrated Saturn intensity from the sidelobes: I_2 The second term in the Eq. 6.5 concerns the sidelobes. In order to determine the effect of the sidelobes, we first subtract to the filtered timestream a simulated timestream from the 2D gaussian model defined above, and then we integrate the intensity between an inner radius and an outer radius

$$I_2 = \int \int_{r_{int}}^{r_{ext}} dxdy(d_{ch,obs} - d^{sim}_{ch,obs}). \tag{6.8}$$

Typically, $r_{int} = 4$ arcmin and $r_{ext} = 15$ arcmin. The distribution of I_1 and I_2 are shown in Fig. 6.4. Typically, the near-sidelobes (I_2) contributes to 10% of the total.

6.4.2 Saturn's rings impact

So far, we didn't take into account the variation of the brightness temperature of Saturn. For the first release, we used only 4 months of data for Saturn (June-September 2012), and we assumed the temperature of Saturn to be constant, with $T_{sat} = 148$ K_{RJ}. However, when we analyzed the data for the full two seasons (May 2012 - April 2014), we saw variations up to 10% in the calibration products using Saturn as a calibrator, such as the planet gain factor defined in Eq. 6.5. The

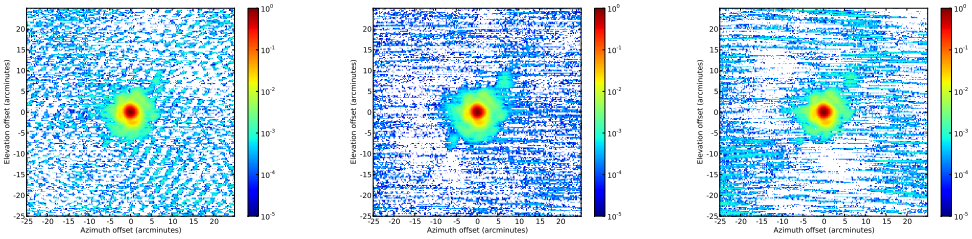

Figure 6.3: Co-added Saturn beam maps for the first release of data (left), the first season of the second release of data (middle) and the second season of the second release of data (right). This is for visualization purpose only as for gain calibration we do not use full season co-added maps, but individual observation maps to compute the planet gain factor (Eq. 6.5). The maps have been normalized to one at the peak.

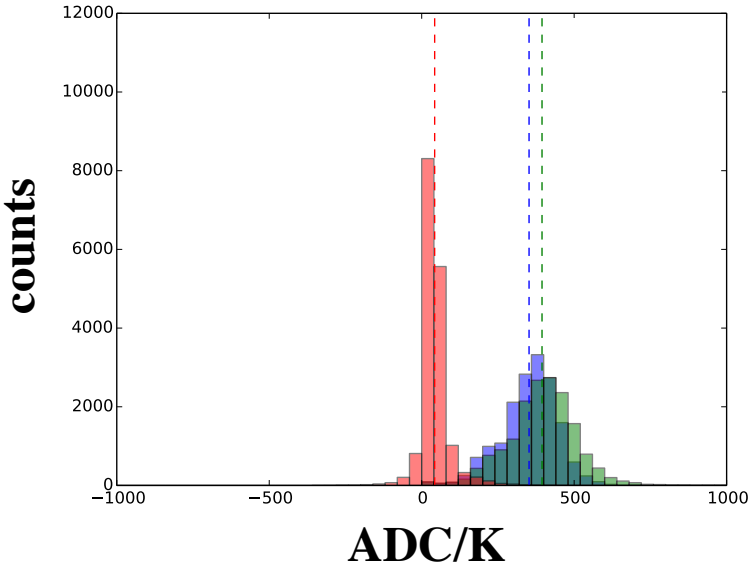

Figure 6.4: Histogram of the estimated gain planet factors for all observations, and all focal plane detectors (green) and the different contributions to the gain planet factor from the beam of each detector (Eq. 6.5): main lobe (from I_1, in blue) and sidelobes (from I_2, in red). The sidelobes contribute to ∼10% of the total.

problem with the calibration is that we have to deal with a huge parameter space, and it is difficult to isolate where the problem comes from[2]. We investigate several possibilities such as an elevation dependency or correlations with the quality of the

[2]Assuming that the problem comes from one place, which is rarely the case ;-)

weather (miscorrection of the atmosphere contribution, see Sec. 6.8.1), problem of the stimulator (see next section), change in main beam parameters, or even changes of sidelobes between seasons. But none gave a satisfactory explanation for the shift of ∼10% in between the two seasons. At some point, we wondered whether it was the right things to keep constant the brightness temperature of Saturn for such a long period of time (almost 2 years of data). Given the angular size of Saturn with respect to our beam size, we cannot resolve the details of the planet, and the variations in the atmosphere of Saturn (poles/equator differences, clouds, seasonal variations, etc.) are not under consideration. But Saturn has rings and even if we cannot resolve them, their inclination with respect to the plan of observation of an observer on Earth produces a variation in the measured microwave brightness temperature, see *e.g.* [Dunn *et al.* 2002, Weiland *et al.* 2011, Hasselfield *et al.* 2013].

Opening angle The observer's viewing angle or opening angle is the angle made by the plane of the rings and the line of sight of the observer. Our site of observation is located at the James Ax Observatory in Northern Chile on Cerro Toco at West longitude 67° 47' 10.40", South latitude 22° 57' 29.03", elevation 5,200 m. During the first two seasons of observations, the opening angle varied from $\sim 12°$ to $\sim 23°$[3]. The evolution of the opening angle is shown in Fig. 6.5. Each season has its own range of opening angles which is not shared with the other, and so we can start to guess that each season will be impacted differently.

Model The ring system is complex and rich, and has been studied by different telescopes and orbiters such as Hubble Space Telescope, Cassini, and Voyager. The contribution of the rings to the total temperature brightness of Saturn is twofold: they obscure the main disk and therefore reduce the flux coming from the main disk, but they also radiate at a lower temperature and contribute to the total signal through a mix of scattering and thermal emission of planetary emission (at 150 GHz, the thermal emission dominates over the scattering), see *e.g.* [Schloerb *et al.* 1979, Marouf *et al.* 1983, Dowling *et al.* 1987, Poulet *et al.* 2000]. The change in opening angle allows us to break the degeneracy between the contribution of the disk and that of the rings. We follow closely the empirical model proposed by WMAP in [Weiland *et al.* 2011]. The total brightness temperature of Saturn is modeled as a contribution from the disk with seven surrounding rings (A, Cassini division, Outer B, Inner B, Outer C, Middle C, Inner C)

$$T(\theta) = T_{disk}[A_{ud}(\theta) + \sum_{i=1}^{7} e^{-\tau_{0,i}|\csc\theta|} A_{od,i}(\theta)] + T_{ring} \sum_{i=1}^{7} A_{r,i}(\theta), \qquad (6.9)$$

where A_{ud} is the projected area of the unobscured disk, $A_{od,i}$ is the projected area of the ring i on the disk, and $A_{r,i}$ is the projected area of the ring i on the plane of observation. Nominal disk and rings radii have been taken from Table 2 and 10 in [Weiland *et al.* 2011], and all the projected areas depend on the opening angle at the

[3] http://new-pds-rings-2.seti.org/tools/viewer2_sat.html

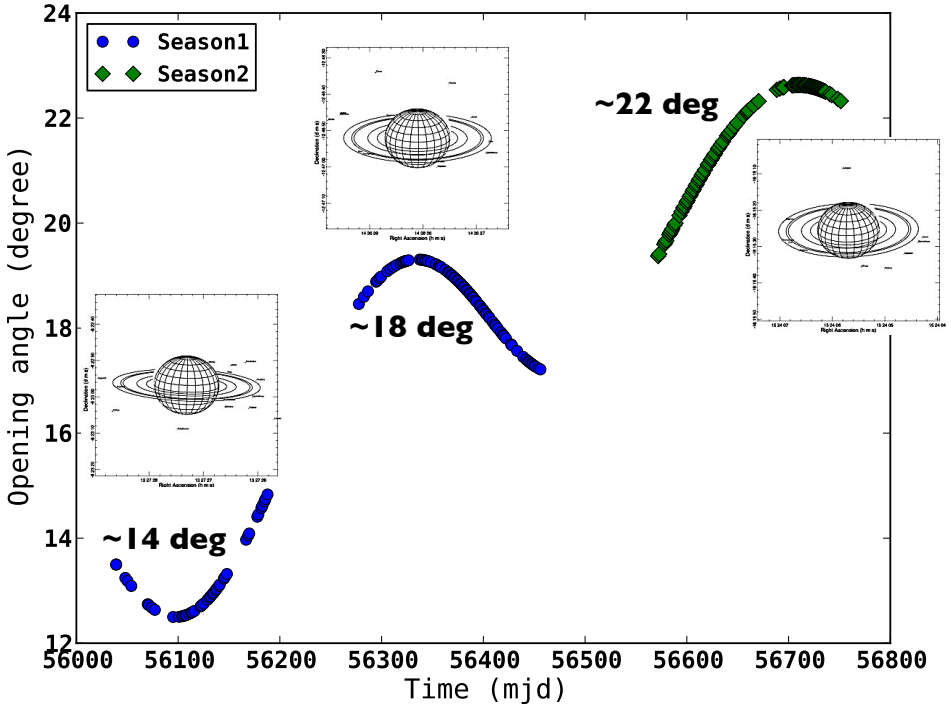

Figure 6.5: Opening angle θ of the rings of Saturn as a function of the date of observations for the first season (blue circle) and the second season (green diamond). The small cartoons represent how Saturn (body + rings) was seen by the telescope for three distinct periods: first half of the first season ($\theta \sim 14°$), second half of the first season ($\theta \sim 18°$), and second season ($\theta \sim 22°$).

moment of observation. Note that we suppose seven rings, but we only use one global temperature T_{ring} to characterize them, and both T_{disk} and T_{ring} temperatures are assumed time invariant. This is rather convenient than physical, and it could have been different. However, we suppose that each ring i has its own ring-normal optical depth $\tau_{0,i}$, whose values have been taken from [Dunn *et al.* 2002]. Concerning rings, the thermal emission dominates over the scattering at 150 GHz, so we do not correct for the part coming from the scattering while estimating the temperature of the rings (see *e.g.* Fig. 7 in [Dunn *et al.* 2002]).

Setup and results We use 132 observations of Saturn selected for their high quality of data (the data selection is the same as the gain model, see next section). The observations of Saturn are not calibrated in physical units, therefore we cannot estimate the temperature directly[4]. As an external calibrator, we use the observations

[4]This is a funny situation. We usually use planet observations to calibrate the timestreams, because we assume that we know the temperature. But in this case, we want to estimate the

Table 6.3: Rayleigh-Jeans temperature of the disk and the rings for the different wafers.

Array	number of pixels	T_{disk}	σ_{disk}	T_{ring}	σ_{ring}	χ^2 (ddof)
Wafer 10.4	19	125.9	1.2	18.5	2.5	322 (283)
Wafer 8.2.0	32	131.6	1.0	5.8	1.9	667 (478)
Wafer 10.3	40	130.7	0.9	17.6	2.2	1149 (598)
Wafer 10.2	59	123.6	0.6	22.9	1.3	946 (883)
Wafer 10.1	29	130.2	1.4	19.1	2.6	715 (433)
Wafer 10.5	49	123.7	0.8	24.7	1.6	1569 (733)
Wafer 9.4	53	130.2	0.6	21.3	1.2	805 (793)

Note. — We performed observations at 148 GHz only, so the thermodynamic brightness temperatures are obtained by adding 3.5 K to the RJ values. The uncertainties contain only statistical uncertainties. The wafer 8.2.0 is not used in the global fit.

of Jupiter, which is believed to have a stable temperature over the two seasons (at least more stable than Saturn). From Eq. 6.5 we compute an average of the gain planet factor per pixel over the whole seasons $< G_{pix}^{Jup} >$. This number is then used in combination to Eq. 6.5 for the observations of Saturn

$$\frac{G_{pix,obs}^{sat}}{< G_{pix}^{Jup} >} T_{pix,obs}^{sat} = \alpha(obs) \frac{I_1(pix,obs) + I_2(pix,obs)}{< G_{pix}^{Jup} > \pi r_{\rm sat}^2(obs)}, \tag{6.10}$$

where we combined the data of each detector within a pixel. Ideally, the ratio $G_{pix,obs}^{sat} / < G_{pix}^{Jup} >$ should be one. The two main conditions to fullfill are: the temperature of Jupiter has to be stable over the two years and the observations of Jupiter should be not too much affected by non-linearities (saturation of the bolometers because the temperature of Jupiter is too bright). So far, we found that both conditions are satisfied within our errorbars[5]. We then combine observations of Saturn per pixel into periods of 15-30 days, taking the uncertainty in each combined measurement to be the error in the mean of the contributing data. We fit the model Eq. 6.9 simultaneously to all the pixels for the temperature of the disk T_{disk} and the combined temperature of the rings T_{ring}. The binned data points, and the best-fit model for few pixels are shown in Fig. 6.6. The uncertainties include those from Jupiter measurements, those from Saturn beam measurements, and scatter in each bin. The resulting models are good fits with χ^2 per degree of freedom $\sim 1-2$ depending on the portion of the focal plane used. We show the fitted parameters in Rayleigh-Jeans units and their uncertainties per-wafer in the Table 6.3. The results are consistent except one wafer (8.2.0) which exhibits a low ring temperature. We do not understand yet this results, so we discard it from further analysis. If we use

temperature, so we need to calibrate first. Some experiments use the CMB to calibrate, see for instance [Hasselfield *et al.* 2013].

[5] Although non-linearities are still under investigation at the time of writing.

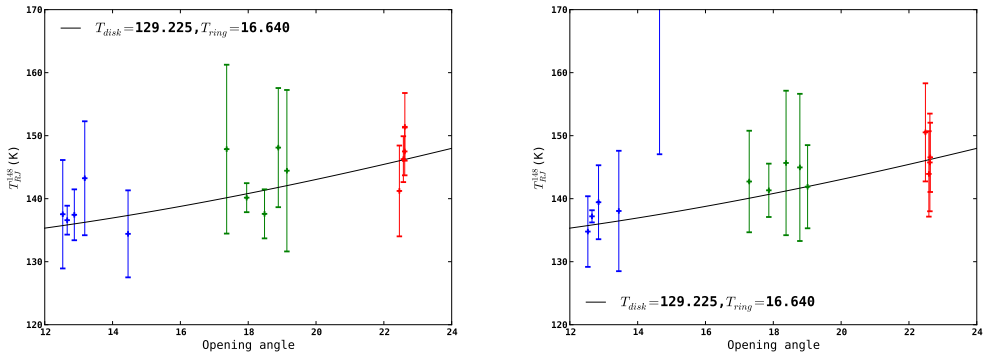

Figure 6.6: Binned data points, and the best-fit model of effective Saturn brightness as a function of the opening angle for two focal plane pixels. In the range of opening angles spanned (12° to 23°), the total temperature brightness is only increasing. The total uncertainties include those from Jupiter measurements, those from Saturn beam measurements, and the scatter in each bin. The data for the first season (May 2012 - September 2012) are in blue, the data from the first season (October 2012 - June 2013) are in green, and the data for the second season (December 2013 - April 2014) are in red. The fit is done simultaneously on all the data of all the pixel.

the full focal plane (excluding the wafer 8.2.0), we found the model fit parameters and uncertainties (χ^2 per degree of freedom ~ 2)

$$T_{disk} = 129.2 \pm 0.4(stat) \pm 2.4(syst)\ K \tag{6.11}$$

$$T_{ring} = 16.6 \pm 0.9(stat) \pm 5.2(syst)\ K, \tag{6.12}$$

where the temperatures are in Kelvin Rayleigh-Jeans (add 3.5 K to the temperature at 150 GHz to obtain the thermodynamic brightness temperatures). The systematic uncertainty has been estimated from the wafer-by-wafer variations. Notice that in the range of opening angles spanned (12° to 23°), the total temperature brightness is only increasing. ACT's team reported complementary measurements at 148 GHz from -2° to 12° in [Hasselfield *et al.* 2013]. They found $T_{disk} = 133.8 \pm 3.2\ K$ and $T_{ring} = 17.7 \pm 2.2\ K$, which is consistent with our values. A compilation of several measurements at various frequencies around 148 GHz is shown in Fig. 6.7. The features of the power spectrum are complex to explain, and a complete explanations would be beyond the scope of this thesis. In [Weiland *et al.* 2011], it is argued that the rings primarily scatter rather than absorb CMB radiation and so temperature of the rings must not be corrected to absolute brightness as for the disk. We did not follow this approach in our measurements, and both temperatures for POLARBEAR in Fig. 6.7 have been corrected to absolute brightness temperature (+3.5 K).

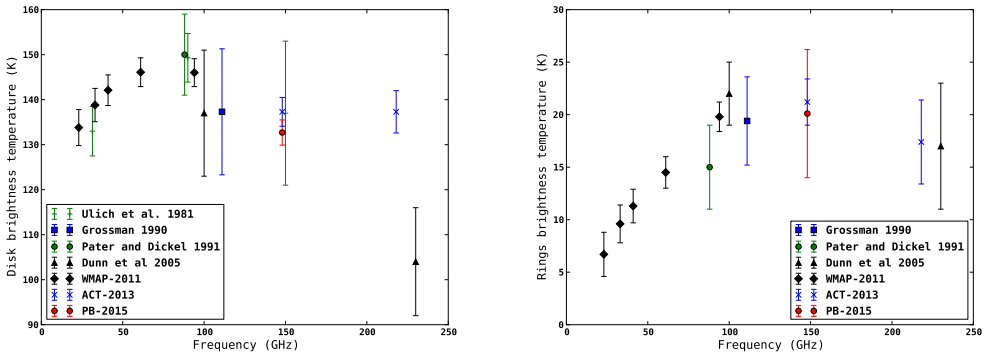

Figure 6.7: Measurements of brightness temperature of Saturn's disk (left) and of Saturn's combined rings (right) from: [Ulich 1981] (green plus), [Grossman 1990] (blue box), [de Pater & Dickel 1991] (green circle), [Dunn *et al.* 2005] (black triangle), [Weiland *et al.* 2011] (black diamond), [Hasselfield *et al.* 2013] (blue cross) and POLARBEAR (red circle).

6.5 Thermal-response calibration

While performing observations, we register the bolometer Time-Ordered Data (TOD), which are the electrical current in the detector. However we would like to convert this current into temperature units. There are two issues : the absolute gain calibration and the relative gain calibration between detectors. To perform the gain calibration, we used different relative calibrators such as astrophysical and ground-based calibrators. The determination of the gain for each bolometer is done in two ways: from observations of planets (main method) or from observations of the atmosphere (cross-check method). This section describes how we use observations of planets in combination with measurements from the *stimulator* to derive the gain model (bootstrapping). The stimulator is a thermal calibration source of known temperature of 700°C located behind the secondary mirror of the telescope. The light runs from the stimulator to the focal plane *via* a small hole in the secondary mirror, and the effective intensity of the source varies across the focal plane from about 35-85 mK.

Once we have made measurements from the stimulator, the gain pipeline proceeds in three steps to do the gain calibration. The first step is to determine the intensity template used to perform an absolute calibration. The intensity template is computed individually for each channel from stimulator measurements without accounting for stimulator polarization (Sec. 6.5.1). So in a second step we characterize the polarization of the thermal source by computing a polarization template(s) using measurements of different astrophysical sources at different HWP rotation angles (Sec. 6.5.2). The last step consists in gathering those two informations - intensity and polarization - and generate the effective temperature template which is

used to recover the absolute gain in ADC/K$_{RJ}$ of each pixel for all the observations (Sec. 6.5.3). In addition to those 3 steps, we have a two iteration process to take into account the impact of the atmosphere on the detectors.

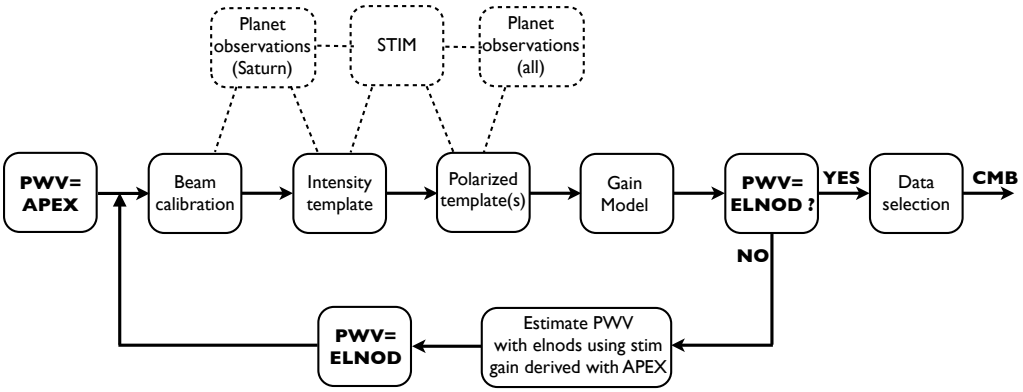

Figure 6.8: Schematic view of the computation of the gain model. The first iteration is made using atmosphere correction from APEX. Then from the first gain model, we estimate the PWV correction from the elnod measurements - believed to be more accurate than the one from APEX-, and we re-estimate the model of gain. At the end, we apply the data selection to remove data of bad quality, and we use the gain model to calibrate the CMB observations. Notice that only Saturn data are used to compute the beam calibration and the intensity template, while all planet observations (Saturn, Jupiter, Venus) are used to constrain the polarized templates.

6.5.1 Intensity template

6.5.1.1 Algebra to compute the intensity template

We use the stimulator measurements taken before and after the planet scan to compare the stimulator amplitude to the gain determined from the planet scan. For each channel *ch* and each planet observation *obs*, we first take the mean $A_{ch,obs}$ of pre- and post- amplitudes from the stimulator for a planet observation (in ADC units)

$$A_{ch,obs} = \frac{A^{pre}_{ch,obs} + A^{post}_{ch,obs}}{2} \tag{6.13}$$

$$\Delta A_{ch,obs} = \left| \frac{(A^{pre}_{ch,obs} + \Delta A^{pre}_{ch,obs}) - (A^{post}_{ch,obs} - \Delta A^{post}_{ch,obs})}{2} \right|. \tag{6.14}$$

Using the planet gain factor $G_{ch,obs}$ (from Eq. 6.5, in ADC/K$_{RJ}$ units) determined from the planet observations, we can convert the stimulator measurements into per-channel stimulator effective temperatures $T^{eff}_{ch,obs}$ such as

$$T^{eff}_{ch,obs} = \frac{A_{ch,obs}}{G_{ch,obs}} \tag{6.15}$$

$$\frac{\Delta T^{eff}_{ch,obs}}{T^{eff}_{ch,obs}} = \sqrt{\left(\frac{\Delta A_{ch,obs}}{A_{ch,obs}}\right)^2 + \left(\frac{\Delta A}{A}\right)^2 + \left(\frac{\Delta \sigma_x}{\sigma_x}\right)^2 + \left(\frac{\Delta \sigma_y}{\sigma_y}\right)^2}, \tag{6.16}$$

where A, σ_x and σ_y are beam parameters coming from the determination of the planet gain factor (see Sec. 6.4.1). For each observation we then combine the per-channel stimulator effective temperature between the two channels in a pair to form the per-pixel intensity $T^{eff}_{p,obs}$

$$T^{eff}_{p,obs} = \frac{T^{eff}_{top,obs} + T^{eff}_{bottom,obs}}{2} \tag{6.17}$$

$$\Delta T^{eff}_{p,obs} = \sqrt{\frac{\left(\Delta T^{eff}_{top,obs}\right)^2 + \left(\Delta T^{eff}_{bottom,obs}\right)^2}{4}}. \tag{6.18}$$

If the stimulator source temperature is stable enough then this quantity should be independent of the gain of the bolometers on a given day. So we average the different per-pixel intensity for all the planet observations to form the intensity template I^{eff}_p

$$I^{eff}_p = \frac{\sum_{obs} T^{eff}_{p,obs} w_{p,obs}}{\sum_{obs} w_{p,obs}} \tag{6.19}$$

$$\Delta I^{eff}_p = \sqrt{\frac{\sum_{obs} \left(I^{eff}_p - T^{eff}_{p,obs}\right)^2 w_{p,obs}}{\sum_{obs} w_{p,obs}}}, \tag{6.20}$$

where $w_{p,obs} = 1/(\Delta T^{eff}_{p,obs})^2$ is the pixel inverse variance estimate for each per-pixel intensity (assuming uncorrelated errors between two measurements).

6.5.1.2 Results for first and second seasons

The current calculation of the intensity template I^{eff}_p is done using observations of Saturn only. Saturn has been shown to give better performance than other planets as far as gains are concerned. Jupiter is boderline for the gain calibration, as bolometers can be saturated and therefore move into a non-linear regime[6], and we have too few observations of Venus to calibrate correctly the gains with it.

Dates of observations We do not use all the data from Saturn to compute the intensity template. We discard data based on some data selection criteria such as a too low number of channels available (typically the observation is rejected if the

[6] We are still investigating better this effect, to see whether we should worry about it.

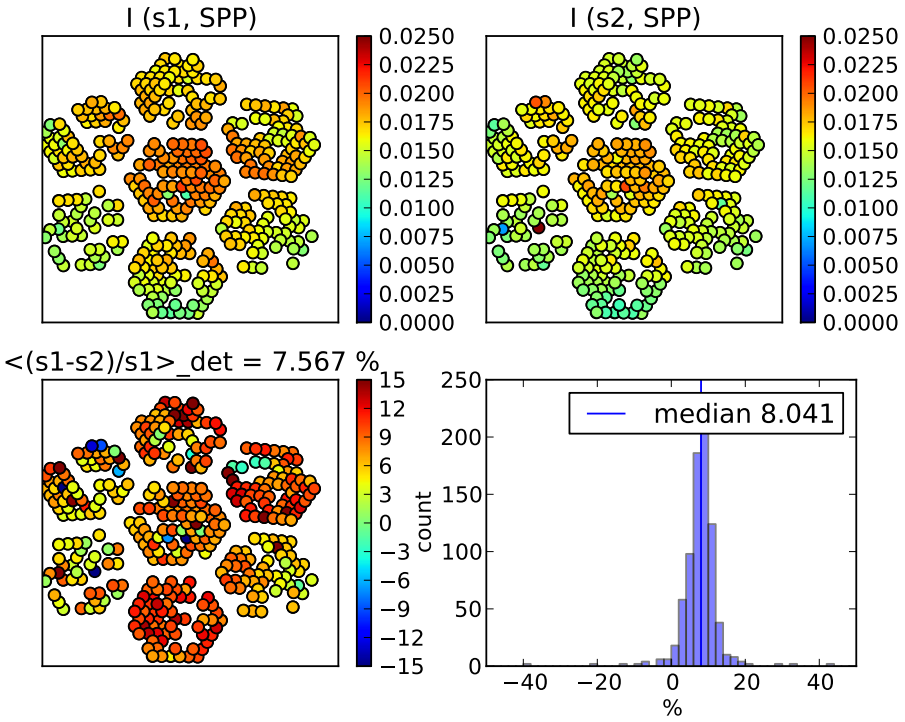

Figure 6.9: Intensity template I_p^{eff} in K_{RJ} for first season (top left) and second season (top right) without temperature correction. The bottom row shows the fractional variation between first and second seasons (s1-s2)/s1, in a focal plan view (bottom left) or as an histogram (bottom right). The mean (bottom left) and the median (bottom right) are quoted. For all pairs, there is roughly 10% difference between both seasons.

number of channel is < 300) or a too high number of negative planet gain factor (>20) for a given observation. Having a negative gain indicates problem during the observation for the channel. For the first release (first season), we restricted the data from June 2012 to September 2012, leading to 21 observations. For the second release, we took all the data available within the two years of observations. After data selection, we are left with $\sim$132 observations. However, we found a discrepancy of an order 10% for all bolometers between the template values of the first and the second season. After several investigations, we found out that the difference was coming from the change in brightness temperature of Saturn, due to a change of the opening angle of its rings with respect to the date of the observation. Thus, for the second release we implemented a temperature correction as described in Sec. 6.4.2.

Intensity templates and fractional errors The figures 6.9 and 6.10 show the intensity templates for first season and second season and their fractional variation.

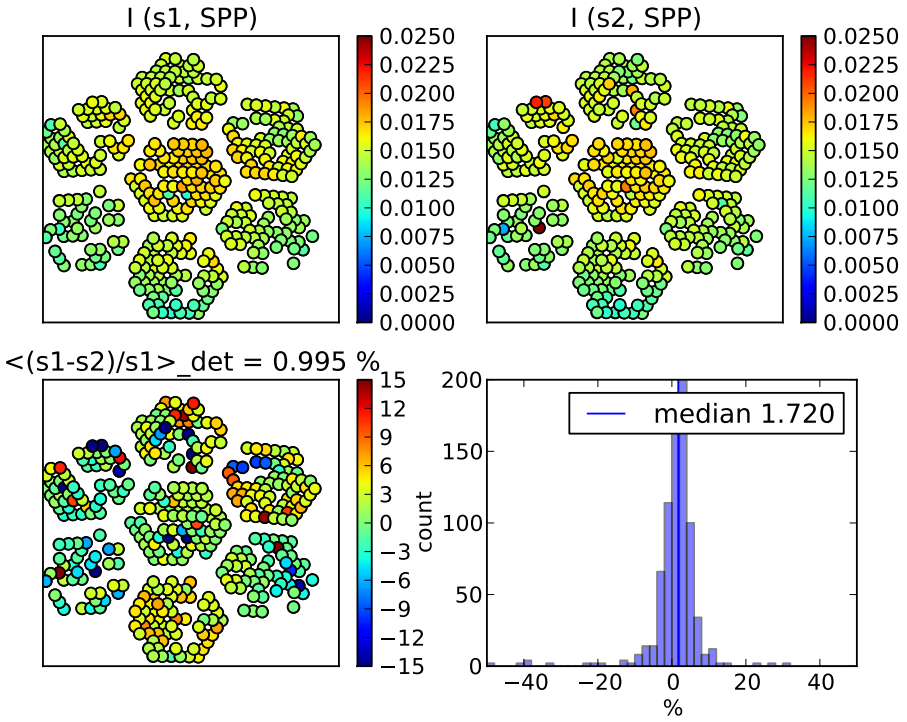

Figure 6.10: Intensity template I_p^{eff} in K_{RJ} for first season (top left) and second season (top right) using the temperature correction. The bottom row shows the fractional variation between first and second seasons (s1-s2)/s1, in a focal plan view (bottom left) or as an histogram (bottom right). The mean (bottom left) and the median (bottom right) are quoted. The difference between both seasons is much smaller than in Fig. 6.9 (and smaller than the uncertainites, not shown here).

The Fig. 6.9 shows the templates without the temperature correction whereas the Fig. 6.10 displays the templates with the temperature correction. Using the new template for the first season, the model contains 908/1274 working bolometers for first season and 812/1274 working bolometers for the second season. Bolometers not registered in a template are not used for the rest of the analysis.

6.5.2 Polarization template(s)

6.5.2.1 Algebra to compute the polarization template

The effective intensity template is unfortunately not sufficient to calibrate the pairs of bolometers. The problem is that individual detectors may have polarized response to the stimulator, which depends on several factors : elevation, time (long-term dependence) and HWP position. Because the elevation at which the measurements is taken is highly correlated with the time of the year, it is difficult to isolate these

effects which are gathered. For that, we define different epochs of the year, and we compute one polarization template per epoch. The dependence of the individual top and bottom bolometer effective temperatures on HWP angle has also to be accounted for. To compute the polarization template, we start from Eq. 6.15, but we introduce explicitly the HWP angle dependency θ_{HWP}

$$T^{eff}_{ch,obs}(\theta_{HWP}) = \frac{A_{ch,obs}}{G_{ch,obs}}(\theta_{HWP}). \tag{6.21}$$

Then for a given θ_{HWP}, we compute per observation the per-pixel per-observation fractional stimulator polarization

$$P_{frac,p,obs}(\theta_{HWP}) = \frac{T^{eff}_{top,obs}(\theta_{HWP}) - T^{eff}_{bottom,obs}(\theta_{HWP})}{T^{eff}_{top,obs}(\theta_{HWP}) + T^{eff}_{bottom,obs}(\theta_{HWP})}, \tag{6.22}$$

and we take the median value of all corresponding observations to compute the per-pixel fractional stimulator polarization

$$P_{frac,p}(\theta_{HWP}) = \text{Median}(\{P_{frac,p,obs}(\theta_{HWP})\}). \tag{6.23}$$

In practice, the planet measurements are sorted by HWP angle θ_{HWP}, and we use only measurements for which the HWP table reports no confusion about the position. All the measurements are fit simultaneously to the model

$$P^{model}_{frac,p}(\theta_{HWP}) = O_{NR} + P_a \cos(4\theta_{HWP} - 2\alpha), \tag{6.24}$$

where O_{NR} represents any offset polarization that is not rotated by the HWP (such as mismatched bandpass spectra), P_a the fractional amplitude of rotated polarization, and α the phase. The model is fit to the three parameters O_{NR}, P_a and α. If we don't have at least three measurements for a given θ_{HWP}, we replace this measurement with the model, even though we used this point to fit the model.

6.5.2.2 Results for first and second seasons

Epochs For the first season, we used four different epochs

- 20110101_000000 - 20120923_142400 : 49 observations
- 20120923_213600 - 20121003_120000 : 8 observations
- 20121003_213600 - 20130128_000000 : 63 observations
- 20130130_000000 - 20130901_000000 : 66 observations.

The HWP was stepped almost every day of an angle 11.25°, from 0° to 168.75°. The current calculation of the polarization templates is done using observations of Saturn, Jupiter and Venus. For the first season, we took all the data from May 2012 to June 2013, leading to a total of 233 planet observations. After cuts, each

epoch has respectively 49, 8, 63 and 66 observations left for the analysis. For the second season we have a total of 131 observations. The HWP was not stepped, therefore there is only one angle position which is at 45°. The stimulator pipe has been rotated February 22 2014, so we have two epochs

- 20130904_000000 - 20140222_000000 : 56 observations
- 20140222_000000 - 20140407_000000 : 48 observations.

The per-pixel per-observation fractional stimulator polarization measured $P_{frac,p}$ is small but not negligible as shown in Fig. 6.11 for the different epochs of the first season ($|P_{frac,p}| < 10\%$). The distributions are rather broad, and we performed several systematic checks in order to probe the influence of the polarized contribution in the gain model.

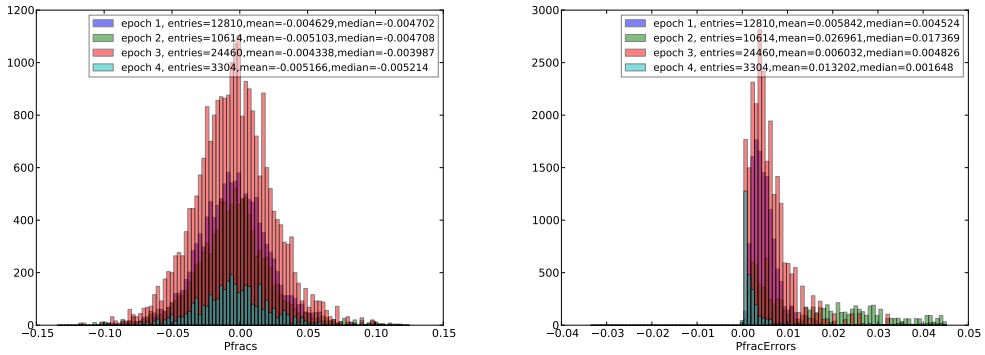

Figure 6.11: Histograms for the per-pixel per-observation fractional stimulator polarization measured $P_{frac,p}$ (left) and errors (right) for the four epochs of the first season.

6.5.3 Effective temperature

6.5.3.1 Definition

For the top and the bottom bolometers of a given pair, we model the effect of the polarization of the thermal source on the intensity template I_p^{eff} at a given HWP angle as

$$I_{p,top}^{eff}(\theta_{HWP}) = I_p^{eff}(1 + P_{frac,p}(\theta_{HWP})) \tag{6.25}$$

$$I_{p,bottom}^{eff}(\theta_{HWP}) = I_p^{eff}(1 - P_{frac,p}(\theta_{HWP})) \tag{6.26}$$

where I_p^{eff} is the intensity template computed on the previous step, using Eq. 6.19, and P_{frac} the per-pixel fractional stimulator polarization computed via Eq.

6.23. Then for a given observation *obs* and a given pixel d_p, a summed/differenced timestream is formed from top $d_{top,obs}$ and bottom $d_{bottom,obs}$ bolometer timestreams as

$$d^{\pm}_{p,obs} = \frac{I^{eff}_{p,top}(\theta_{HWP})}{A_{top,obs}} d_{top,obs} \pm \frac{I^{eff}_{p,bottom}(\theta_{HWP})}{A_{bottom,obs}} d_{bottom,obs}. \tag{6.27}$$

6.5.3.2 Results for first and second seasons

For each observation, we generate the gain calibration files using the coefficients of the Eq. 6.27. Those coefficients imply a measure of the light from the stimulator by the detectors. While for planet observations the stimulator amplitudes $A_{channel,obs}$ are measured right before and right after the observation, for CES the stimulator measurements are taken at the beginning and at the end of a group of 5 CES. Those two measurements are called the pre- and the post-stimulator measurement respectively. For the first release of papers, we rejected the group of CES which had not both the pre- and post-stimulator measurements. Those CES were never used elsewhere for the first release of data. For the remaining groups of CES, we decided to linearly interpolate the pre- and post-stimulator values in order to give to each CES inside a group, its pre- and post-stimulator amplitudes, and account for possible drifts in the gains. The Fig. 6.12 displays the number of gain files - one gain file being a CES or a planet observations - generated using the interpolation of the stimulator. However, for the second release of data, we decided also to keep in the analysis the group of CES having only a pre-stimulator measurement only (but not post-stimulator measurement only). Although having only one stimulator measurement may be a sign of a problem, we rather prefer to include them in the analysis and rely on the cuts applied to the data in the next steps of the analysis. This single measurement is used for all the observations until the next two stimulator measurements. For the first data release, we also restricted our dates from late June 2012 to early June 2013. No data from May and early June 2012 were used, even if available. However, in the second release, we decided to include those data relying on later data cuts, and the dates range from May 2012 to April 2014. The total number of files for the second season (2013-2014) is smaller than in the first season (2012-2013), reaching 7,731 observations with interpolation of the stimulator measurements, 291 observations with only a pre-stimulator measurement, and 5 files with only a post-stimulator measurement.

Since we have stimulator measurements before and after a group of several CMB observations, we can study the variation of the measures for each channel. In principle, we would like the measured amplitudes to be constant or to have a small variation in between the two stimulator runs. Most of the relative variations are below 1%, and a non-negligible fraction of all measurements is even below 0.1%. Estimates of the uncertainties for each stimulator runs (relative) are equal or higher in general than the variation in between the two stimulator runs. Similarly to the first season, the estimates of the uncertainties for each stimulator run (relative) for

the second season are low (≤ 10 %) and equal or higher in general than the variation in between the two stimulator runs.

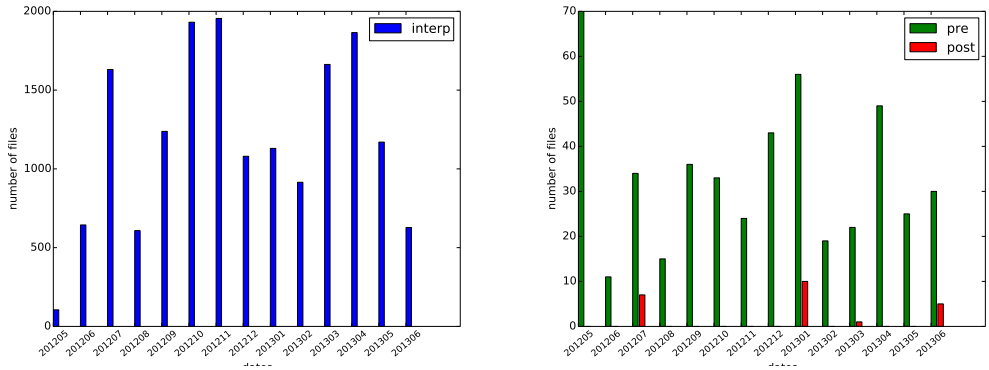

Figure 6.12: *Left* : Distribution of gain files per month generated using interpolation between pre- and post-stimulator measurements for the first season. Months such as October or November 2012 contain almost 2,000 observations each (CMB or planet observations), and the total number of gain files generated using interpolation for the first season is 16,563. *Right* : Distribution of gain files per month generated with only a pre-stimulator measurement (green, 496 observations) or only a post-stimulator measurement (red, 23 observations). This single measurement is used for all the observations until the next two stimulator measurements.

6.5.4 Automation of the pipeline

Automation of tasks is highly recommended from a data analysis point of view as it avoids mistakes, forgetfulnesses, and difficulty to keep track on all the details which went through a particular run. We are using pipelet[7] to perform the automation of the pipeline. One of the main change in terms of data analysis tools from the first release to the second was to build automated pipelines.

6.6 Instrument effective beam

As mentioned previously, when a detector is observing, the signal received is not exactly the same as the one sent due to the diffraction-limited optics in the telescope. As a consequence, all the scales undergo a suppression of signal, and the smaller the scales the bigger is the suppression. The effect start to be non-negligible at the level of the beam size, that is at scales equal to the effective Full Width Half Maximum (FHWM) if the beam would have been represented by a circular 2D Gaussian. On the observed map level m, the effect of the beam can be represented by a convolution with the sky signal S

[7] http://www.apc.univ-paris7.fr/~lejeune/pipelet/html/index.html

$$m(\theta,\phi) = (S * B)(\theta,\phi) = \int\int d\theta_1 d\phi_1 S(\theta-\theta_1,\phi-\phi_1)B(\theta_1,\phi_1), \tag{6.28}$$

where B is the effective beam of the instrument. The Fig. 6.13 represents a simulated map convolved with a beam of FWHM of 3.5' and 30'. On the second figure, the map seems blurred, and the smallest structures are no more visible.

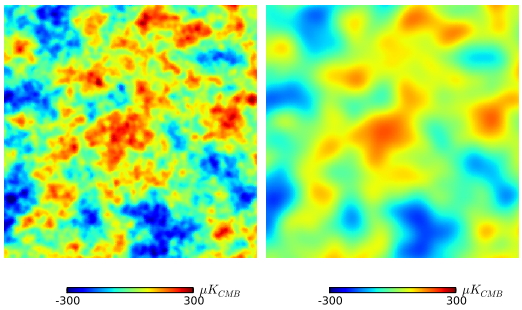

Figure 6.13: Simulated intensity map convolved with a circular gaussian beam of FWHM of 3.5' (left) and 30' (right). The level of details is clearly different in both figures. If we want to be able to measure small scales, the detector beams have to be sufficiently small with respect to the desired CMB fluctuations.

Currently, the estimation of each detector beam is made in two steps. We first make use of observations of Jupiter to determine the beam profile, and then we modify the beam profile to account for blurring in the maps due to pointing model inaccuracies, evaluated using point sources in the patches. I was not involved directly in the estimation of beams for the first release, but I participated to the characterization of it for the second release.

6.6.1 Beam profile from Jupiter measurements

We use Jupiter to fill the entire detector beam B. In order to simplify the calibration, we saw that we approximate a planet as a point source with brightness temperature T_p. This is justified by the small angular diameter of the planet that we use to calibrate (see Fig. 6.2) with respect to the effective FWHM of each bolometer (typically 3.5 arcminutes). So the Eq. 6.28 can be re-written as the Eq. 6.3 and the beam profile is given by

$$B(\theta,\phi) = \frac{m(\theta,\phi)}{T_p \Omega_p}. \tag{6.29}$$

Individual detector maps are made from timestreams that are filtered to reduce the effect of atmospheric fluctuations. This filtering is accomplished with a masked

polynomial: a first-order polynomial that is fit to the timestream everywhere outside of a 50' radius around the planet. The individual detector maps are combined to create a single-observation map with adequate coverage (see Fig. 6.14 for the full season coadded map and Fig. 6.15 for the per-wafer beam maps). The weighting used to combine individual detector maps is a noise weighting calculated from the RMS of the map outside of the mask radius.

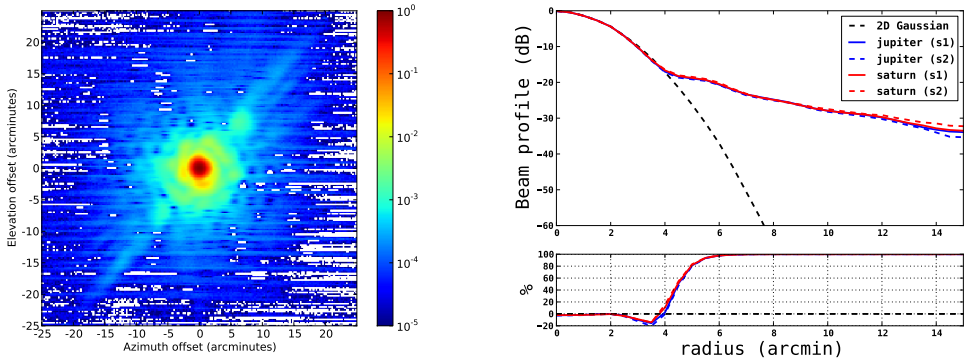

Figure 6.14: Coadded beam map from measurements of Jupiter during the first season (left), and beam profile (right) for Jupiter (blue) and Saturn (red). The stripes parallel to the azimuth axis seen in the map on the left are typical from the planet scanning strategy: the telescope tracks the planet as it moves across the sky and relative to that tracking performs azimuth scans with elevation steps (raster scans). Similar patterns are seen in Fig. 6.3. To get the beam profile from the map, we bin radially. We can clearly see the transition between the main lobe and the sidelobes around 4 arcmin. We overplot the radial profile from a 2D Gaussian with FWHM of 3.5 arcmin for comparison (dashed black line). I also included the fractional variation (planet-gaussian)/planet on the right panel.

We do not deconvolve the beam of each detector from timestreams in the map space. The convolution is a heavy operation, and if the beam is sufficiently azimuthally symmetric it is much simpler to work in the harmonic domain. Indeed, the convolution product in the real domain is simply a multiplication in the harmonic domain. In addition, the beam can be approximated as azimuthally symmetric in intensity because of the rotation of the instrument beams as projected on the CMB patch due to changes in patch parallactic angle over the course of the day from our mid-latitude site. The azimuthally averaged Fourier components[8] are then found for each single-observation map (daily map) and the multipole components of the detector-combined beam for each single-observation is expressed as

$$B_\ell = \frac{M_\ell}{T_\ell W_\ell}, \tag{6.30}$$

[8]Given the relatively small patch size for beam, we work in the flat-sky approximation.

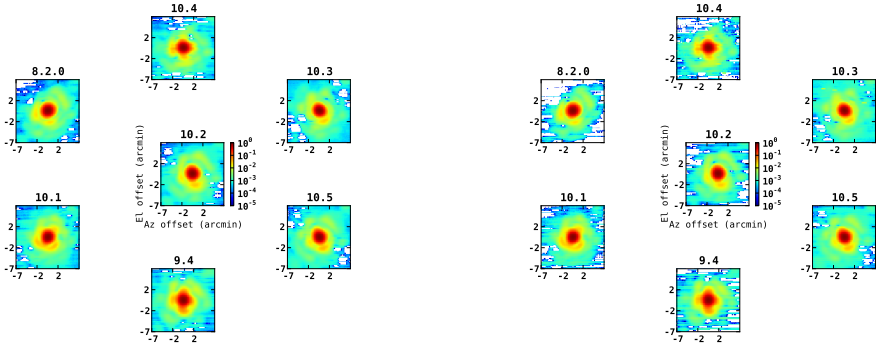

Figure 6.15: Per-wafer beam maps from all Jupiter observations for the first season (left) and the second season (right). Notice that the colorscale is the same as Fig. 6.14 but there is a zoom on the main lobes (±7.5 arcmin). The results for the two seasons are consistent as far as the main lobes are concerned.

where M_ℓ is the average over ϕ_ℓ of the two-dimensional Fourier transform $M(\ell, \phi_\ell)$ of the temperature-calibrated map $m(\theta, \phi)$, T_ℓ is the angular Fourier response function for a finite planetary disk, and W_ℓ is the pixel window function which takes into account the effect of the pixelization of the map. The multipole components and covariance matrix of the beam are estimated by the inverse-noise-weighted mean values and covariance matrix of the power spectra of many planet observations. The resulting B_ℓ and its uncertainty in each multipole bin from observations of Jupiter of the first season are shown in Fig. 6.16. The POLARBEAR beam can be approximate by a circular 2D Gaussian with FWHM of about 3.5 arcmin. The degree of ellipticity has been found to be much less than 5%.

6.6.2 Effective beams from point sources in the CMB patches

While co-adding the data of the CMB maps, there is a blurring effect due to inaccuracies in our pointing model. To take into account that effect we model the effect of an RMS pointing error in map space, σ_p, as

$$B_\ell^{\rm eff} = B_\ell \times \ e^{-\ell(\ell+1)\sigma_p^2/2}, \tag{6.31}$$

where $B_\ell^{\rm eff}$ is called the effective beam and where σ_p for each field is estimated by fitting each point source with the Jupiter beam profile convolved with a Gaussian smoothing kernel. We estimate a σ_p likelihood function for each individual point source in each map. We then combine the sources within each patch to find a joint likelihood for the RMS pointing error on that patch. The results are shown in Tab. 6.4 and the patch-specific beam functions are displayed in Fig. 6.16.

One can clearly see that the uncertainty in $B_\ell^{\rm eff}$ has increased to account for discrepancies in the measurements of σ_p. The measurements of σ_p from the ten point

Table 6.4: Pointing error for POLARBEAR observing fields

Field	RMS pointing error ["]	Number of sources
RA23	64.5 ± 20.9	4
RA12	26.7 ± 18.2	5
RA4.5	31.5 ± 15.3	10

Note. — The amount of blurring is much bigger in the RA23 than in the other field. We do not understand fully the effect (is that still true), but we think that the difference on the amount of sources and their locations within each patch play some role.

sources in RA4.5 exhibited statistically significant differences with one another, implying that the amount of blurring is not constant throughout the map, or that the model for the blurring is not capturing the entire effect; we do not understand the origin of this effect yet. One possibility would be the difference in signal-to-noise ratio between each patch. For RA23, we have only few point sources and all of them are located at the edge of the patch where the noise is very high, while for RA4.5 we get 10 point sources located everywhere in the patch.

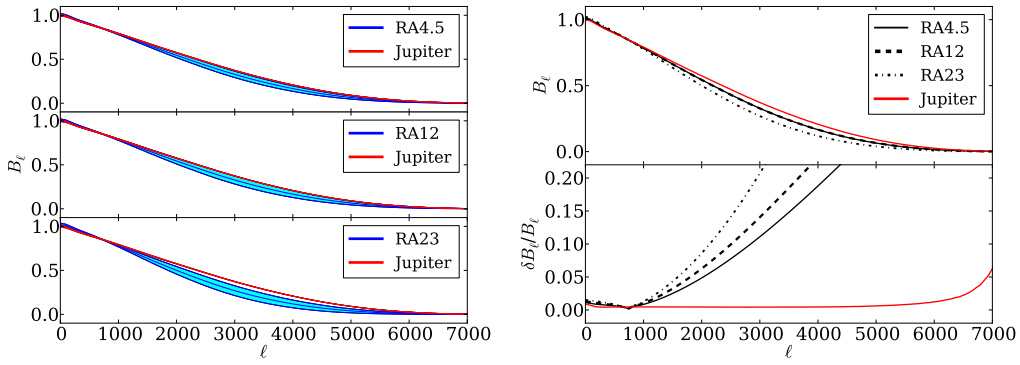

Figure 6.16: *Left:* Beam profile in the harmonic domain measured from Jupiter (red) or from fitting point sources with a Gaussian-smoothed Jupiter beam (blue solid line) with 1σ uncertainty (blue region) for each patch. (Courtesy: D. Schenck and Z. Kermish) *Right:* Same but the beam uncertainties are shown separately for more clarity. From [POLARBEAR Collaboration 2014c].

Given that the beam profile and the absolute gain calibration are partially degenerated, the beam uncertainty also increases the uncertainty of our absolute gain calibration by a factor of 1.5, from 2.8% to 4.1%. Fortunately, due to the fact that the blurring is a sub-arcminute effect, the differences and uncertainties in the patch-specific beam functions primarily affect the ℓ-range at the high end of our reported band powers and beyond ($\ell > 1500$), having little effect on the constraint of the lensing amplitude, where most of the significance comes from the low end of the reported

ℓ-range. For the first season, an analysis using simply the Jupiter beams, calibrated using the CMB temperature power spectrum, results in a lensing amplitude that differs by 0.3% from the reported result [POLARBEAR Collaboration 2014c].

6.7 Polarization angle calibration

Each of the POLARBEAR detectors' response to polarized signal, including its polarization angle, polarization efficiency, and leakage due to relative-gain miscalibration, is modeled. Also modeled are non-idealities in the HWP, which may vary for different detectors across the focal plane. This section describes the polarization model as developed using two astrophysical calibrators: Tau A and Cen A. We first describe the procedure to calibrate the individual pixel polarization angles with their uncertainties, and the global angle calibration. In the end, we propose an alternative method to estimate the individual pixel polarization angles. I'm not directly involved in the polarization angle calibration. Most of the work described in sections 6.7.1 to 6.7.3 are from discussion with H. Nishino during my stay in Nov. 2014 at Kavli IPMU, and it is primarily based on his work. However, Sec. 6.7.4 is based on my idea, but it has never been applied to the data yet.

6.7.1 Individual pixel angle calibration

Tau A and Cen A data Taurus A (Tau A) is a supernova remnant that emits a polarized signal, mainly from the synchrotron emission of the central pulsar, and its interaction with the surrounding gas. Tau A was first used for polarization angle calibration by COMPASS [Farese *et al.* 2004] and was later characterized by WMAP between 23 and 94 GHz [Weiland *et al.* 2011], and by the IRAM 30 m telescope at 90 GHz [Aumont *et al.* 2010]. The frequency dependence of the flux can be well described by a simple power law. The index of the power law has been measured by *e.g.* WMAP in combination with other experiments, giving an index value around -0.3 [Weiland *et al.* 2011]. Centaurus A (Cen A) is a fainter polarized radio-bright galaxy that has been characterized in the millimeter range by QUAD [Zemcov *et al.* 2010]. It is used as a consistency check. The polarization angle of each detector relative to the instrumental reference frame is found from observations of Tau A (and Cen A) while section 9.3.2 describes calibration of the overall instrument polarization angle using the CMB itself.

During the first season, POLARBEAR observed Tau A several times per week, leading to 125 observations[9]. After data cuts, almost 70 observations were used for the final analysis. The timestreams are calibrated using either the processed stimulator measurements (see Sec. 6.5) or gains derived from the elnods measurements (only relative calibration). The first low-level processing consists in an operation of filtering to reduce the effect of atmospheric fluctuations. First for each observation

[9]Notice that we do not use data when Tau A is within 30° of the Sun, which means May-September from Chile.

and each focal plane pixel we construct the intensity and polarization timestreams $s_p^{\pm}$ by summing and differencing the individual bolometers $s_{/\!//\perp}$ within each pair

$$s_p^+(t) = \frac{s_{/\!/}(t) + s_\perp(t)}{2} \tag{6.32}$$

$$s_p^-(t) = \frac{s_{/\!/}(t) - s_\perp(t)}{2}. \tag{6.33}$$

Then, we mask time samples lying within 5 arcminute from the center of the source, and we fit a 5th-order polynomial for both intensity and polarization timestreams. The templates are then subtracted from the whole timestreams. Detector differencing and polynomial baseline subtraction both act to remove atmospheric signals.

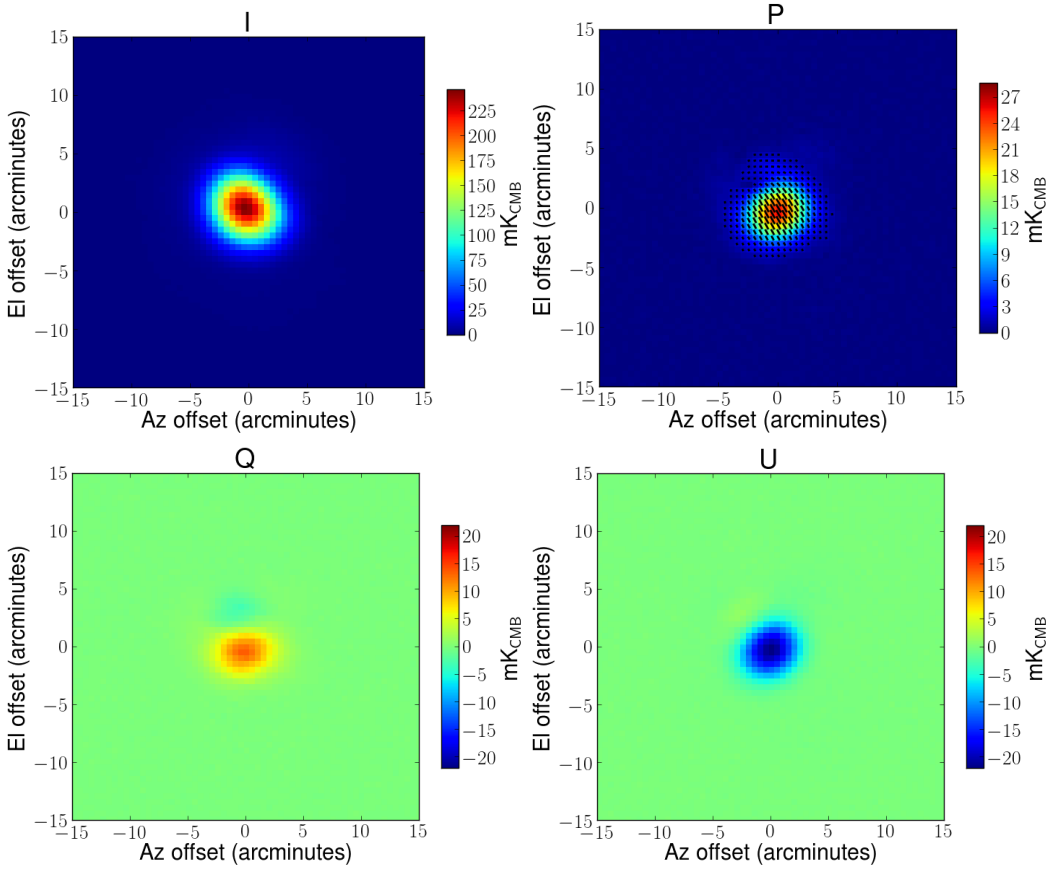

Figure 6.17: First season co-added maps of Tau A observed by POLARBEAR: intensity (top left), Stokes Q parameter (bottom left) and Stokes U parameter (bottom right). I also show the (linear) polarization intensity map, defined as $P = \sqrt{Q^2 + U^2}$. The orientations of bars in map pixels represent polarization angles at each map pixel.

Beam convolution and simulated timestreams We use the observations of Tau A from the IRAM experiment [Aumont *et al.* 2010] to calibrate the polarization angles. To do so, we first convolve the intensity and polarization maps X of IRAM with the bolometer beam map B for each POLARBEAR bolometer belonging to a focal plane pixel p[10][11]

$$X_{/\!//\perp}(\mathbf{q}) = (B_{/\!//\perp} * X)(\mathbf{q}) = \int \mathrm{d}\Omega_{\mathbf{q}'} B_{/\!//\perp}(\mathbf{q}, \mathbf{q}') X(\mathbf{q}') \tag{6.35}$$

where $/\!/$ and $\perp$ stand for top and bottom bolometers respectively and $\mathbf{q}$ is the pointing direction at time t: $\mathbf{q}(\mathrm{t})$=$[\theta(t), \phi(t)]$. The fact that we convolve the input Tau A maps from IRAM with different beam maps makes $X_\perp$ and $X_{/\!/}$ different. The bolometer beam maps are generated using an elliptical model, whose parameters are obtained using observations of planets (see Sec. 6.6). We then project out those maps in time domain using the real pointing of POLARBEAR observations to form for each focal plane pixel the top and bottom timestreams $X_{/\!//\perp}$

$$X_{/\!//\perp}(t) = \sum_q A_{tq} X_{/\!//\perp}(\mathbf{q}), \tag{6.36}$$

where A_{tq} is the pointing for sky pixel q and time t.

Data model The POLARBEAR data model in this context for a focal plane pixel p at a time t for the two bolometers can be written as

$$d_{/\!/}(t) = (1 + \Delta g(p)) I_{/\!/}(t) + \varepsilon(p)[\, Q_{/\!/}(t) \cos 2\Theta_{/\!/}(t) + U_{/\!/}(t) \sin 2\Theta_{/\!/}(t) \,] \tag{6.37}$$

$$d_\perp(t) = (1 - \Delta g(p)) I_\perp(t) + \varepsilon(p)[\, Q_\perp(t) \cos 2\Theta_\perp(t) + U_\perp(t) \sin 2\Theta_\perp(t) \,], \tag{6.38}$$

where Δg is the pixel relative-gain error and ε is the pixel polarization efficiency. A priori, both parameters depend on time, but we assume that they are constant over the full season. It only depends on the considered focal plane pixel. Notice that Δg is equivalent to O_{NR} defined in Sec. 6.5.2, so we have at least two independent methods to estimate it. This redundant information is used later to estimate the systematic uncertainty (see Sec. 10.3.6). Two bolometers in a pixel are orthogonally oriented, so for two orthogonal detectors of a focal plane pixel p, the detector polarization angle projected on the sky in equatorial coordinates $\Theta_{/\!//\perp}$ can be expressed as

[10] In principle, we should first deconvolve the IRAM beam map and then convolve with POLARBEAR beam maps. However, the IRAM beam size is approximately 27", much smaller than the POLARBEAR beam size ($\sim$ 3.5 arcminutes).

[11] Maps are here in in RA and DEC coordinate, otherwise if they are in azimuth and elevation coordinates we have to include the polarization rotation operator P with parallactic angle and R a vector rotation operator to convert from az/el to RA/DEC :

$$X_{/\!//\perp}(\mathbf{q}) = \int \mathrm{d}\Omega_{\mathbf{q}'} B_{/\!//\perp}(\mathbf{q}, \mathbf{q}') P X(R\mathbf{q}') \tag{6.34}$$

$$\Theta_{\perp}(t) = (\pi/2 - \theta_{/\!/\perp}) + 2\theta_{HWP} + \theta_{PA}(t) = \Theta_{/\!/}(t) + \pi/2, \tag{6.39}$$

where $\theta_{/\!/\perp}$ is the detector polarization angle (not projected), θ_{HWP} is the HWP angle, and θ_{PA} is the parallactic angle. We are here interested in polarized timestreams, so we differentiate the two orthogonally oriented bolometers inside a pixel p

$$d_p^-(t) = \frac{d_{/\!/}(t) - d_{\perp}(t)}{2} \tag{6.40}$$

$$= \frac{I_{/\!/}(t) - I_{\perp}(t)}{2} + \Delta g(p)\frac{I_{/\!/}(t) + I_{\perp}(t)}{2} + \varepsilon(p)\Big[\frac{Q_{/\!/}(t) + Q_{\perp}(t)}{2}\cos 2\Theta_{/\!/}(t) + \frac{U_{/\!/}(t) + U_{\perp}(t)}{2}\sin 2\Theta_{/\!/}(t)\Big].. \tag{6.41}$$

The difference of the intensity from the bolometers contains for instance the differential beam effects. However in this part of the analysis, we do not include the HWP angle dependent differential beam effects in the beam parameters used to generate beam maps, and we believe this effect to be negligible. We also need to apply the absolute gain correction to IRAM data with respect to POLARBEAR ones. We sum the POLARBEAR timestreams and we compare it to summed timestreams generated using convolved IRAM maps for each pixel, and we estimate the normalization

$$\text{IRAM}: \quad d_p^+(t) = \frac{d_{/\!/}(t) + d_{\perp}(t)}{2} \approx \frac{[I_{/\!/}(t) + I_{\perp}(t)]}{2} \tag{6.42}$$

$$\text{POLARBEAR}: \quad s_p^+(t) = \frac{s_{/\!/}(t) + s_{\perp}(t)}{2} \approx I_{p,PB}(t) + n_{p,PB}^+(t) \tag{6.43}$$

Here all the terms are negligible with respect to the sum of intensity terms. $n_{p,PB}^+$ is the intensity noise for the pixel p. The POLARBEAR data are fit to the model using a linear model

$$s_{p,model}^+(t) = \alpha_p \frac{[I_{/\!/}(t) + I_{\perp}(t)]}{2} + \beta_p. \tag{6.44}$$

Note that the "noise" term β_p is here just a global offset per focal plane pixel. We then use α_p to normalize the IRAM timestreams.

Fitting The 3 parameters which are unknown in the simulated timestreams given by Eq. 6.41 are : Δg, ε and $\theta_{/\!/\perp}$. The best-fit parameters for a focal plane pixel p are obtained by minimizing the following χ^2

$$\chi^2(p) = \sum_n \frac{\Big[s_p^-(t_n) - \alpha_p d_p^-(t_n)\Big]^2}{\sigma_{p,n}^2}, \tag{6.45}$$

where the sum is performed over the different observations of Tau A. s_p^- is the polarized timestream for the pixel p for POLARBEAR and $\sigma_{p,n}^2$ is the standard deviation

of s_p^- for the n^{th} observation. Notice that the HWP was stepped for the first season, so there are several values of the HWP angle θ_{HWP} corresponding to different observations, allowing us to determine the detector polarization angle. After subtracting the mean-wafer polarization angle, we discard the pixels being more than 3σ away.

Results Unfortunately, while writing this thesis, I cannot put out the full results of this analysis as it will be included in a later publication dedicated to the analysis of Tau A.

Some limitations The data model used in Eq. 6.41 assumes an ideal HWP, meaning that the HWP just rotates the incident polarization by $2\theta_{HWP}$. However the HWP has some non-idealities such as differential reflection and non optimal retardance for frequencies which are far from its optimized frequency at 150 GHz. Those effects can be described by using the Mueller matrix model for the HWP.

6.7.2 Estimation of uncertainties

The polarization model is based on a hierarchical understanding of our polarization calibration, consisting of a global reference polarization angle, the wafer-averaged polarization angles relative to that global angle, and the individual pixel angles relative to the wafer-averaged angle. We consider uncertainty in each of these. The systematic uncertainty in the global reference angle and wafer-averaged angle are shown in Table 6.5. These are dominated by uncertainties in the pixel-pair relative gain and in the non-axisymmetric beam model and the substructure of Tau A at 148 GHz. Non-idealities in the HWP over the finite POLARBEAR spectral bandwidth are also an important source of uncertainty, both in rotation angle of linear polarization and in the mixing of circular polarization into linear polarization. Using the upper limit on Tau A's circular polarization fraction of 0.2% [Wiesemeyer *et al.* 2011], the systematic error from the circular polarization of Tau A is estimated to be 0.09°. The individual pixel polarization angle uncertainty in each wafer is estimated to be 1.0° from the spread of the pixel polarization angle distribution from the Tau A measurement. The other systematic effects we evaluated, listed in Table 6.5, are all negligible. The impact of all these uncertainties on the BB and EB power spectra are addressed in Chap. 10.

6.7.3 Global polarization angle using Tau A

Once the timestreams are calibrated (gains and individual pixel angle), we coadd the data from every pixel for each observation : I_n, Q_n and U_n. Due to noise residuals outside Tau A, and due to the fact that Tau A is slightly extended, we have a variation of the angle of polarization. To minimize this, we restrict the fit to sky pixels q lying within 10 arcminute from the center of the source. This angle is computed for each observation as

Table 6.5: Systematic uncertainties in global reference and wafer-averaged polarization angle, as measured using Tau A. Table from [POLARBEAR Collaboration 2014c].

Angle Uncertainty	Global Reference	Wafer-Averaged
Absolute pointing uncertainties	0.12°	-
Beam uncertainties	0.21°	0.23°
Relative gain uncertainties	0.22°	0.42°
Non-ideality of HWP	0.21°	0.64°
Circular polarization of Tau A	0.09°	$\ll 0.1°$
HWP angle uncertainties	0.15°	0.13°
Pixel pointing uncertainties	$\ll 0.1°$	0.18°
Bolometer time constant	$\ll 0.1°$	$\ll 0.1°$
Filtering effect	$\ll 0.1°$	$\ll 0.1°$
Polarized dust	$\ll 0.1°$	$\ll 0.1°$
Total	0.43°	0.83°

Note. — Uncertainty in the global reference angle as measured using EB power spectra is addressed in Sec. 9.3.2.

$$\alpha_{\mathrm{TauA}} = \frac{1}{2}\arctan\left(\frac{\sum_q U_n(q)}{\sum_q Q_n(q)}\right) \tag{6.46}$$

The variation of this angle over the first season is 1.2° (RMS). The second season data exhibit some contradiction in the value and dispersion for the angle of Tau A. This is currently investigated (HWP not in a quantized position?). The final absolute value of the angle has not been published, because it will be the purpose of a calibration paper.

6.7.4 Extending the model

The Eq. 6.45 compares two quantities which haven't been processed the same way[12]. The POLARBEAR data have been filtered, whereas the timestreams from IRAM data are just maps projected on the time domain. Given the structure of Tau A (quasi point-like for POLARBEAR) and the relatively low order of polynomial (5^{th}), one could argue that the signal from Tau A is not affected by the filtering, and only atmospheric effects are effectively suppressed. However this hypothesis has not been tested so far. The data model for the difference timestream in the time domain for a given observation n and a given focal plane pixel p can be written as

$$\mathbf{d} = \mathbf{A}\mathbf{s} + \mathbf{L}\mathbf{l} + \mathbf{n}. \tag{6.47}$$

[12]Which is wrongly reported in the first release.

l is the amplitudes of the Legendre modes we want to remove from the data. The rectangular matrix **L** has size $[n_t \times n_{poly}]$ and contains the coefficients of the Legendre polynomials, and the columns of it are orthonormalized, that is $\mathbf{L}^t\mathbf{L} = \mathbb{1}$. **n** is the noise vector of the pixel p for the n^{th} observation, with size n_t. **A** is a rectangular matrix whose the number of rows is the number of time samples n_t and number of columns is the number of sky pixels n_q multiplied by the number of parameters n_{param} to recover. **A** can be seen as a pointing matrix (see Sec. 8), which relates time t and position on the sky $\mathbf{q}(t) = (\theta(t), \phi(t))$. For a given observation n and a given focal plane pixel p, it has n_{param} non-zero entries for each row corresponding to time t

$$\mathbf{As} = \begin{bmatrix} A_{t_0 q_0} & \dots & A_{t_0 q_{n_q-1}} \\ \vdots & \vdots & \vdots \\ \vdots & \vdots & \vdots \\ A_{t_{n_t-1} q_0} & \dots & A_{t_{n_t-1} q_{n_q-1}} \end{bmatrix} \times \begin{bmatrix} s(q_0) \\ \vdots \\ s(q_{n_q-1}) \end{bmatrix} \tag{6.48}$$

where $A_{t_i q_i}$ is a $[1 \times 4]$ matrix with values

$$A_{t_i q_i} = \begin{cases} [1/2, \Delta g(p)/2, \dfrac{\varepsilon(p)}{2} \cos 2\Theta_{/\!/}(t), \dfrac{\varepsilon(p)}{2} \sin 2\Theta_{/\!/}(t)]; & \text{if } (\theta(t_i), \phi(t_i)) \in q_i \\ [0,\ 0,\ 0,\ 0,\ 0]; & \text{otherwise,} \end{cases} \tag{6.49}$$

and $s(q_i)$ is a $[4 \times 1]$ matrix which contains the combination of beam-smoothed Stokes parameters in pixel q_i from IRAM re-observed maps

$$s(q_i) = \begin{bmatrix} I_{/\!/}(q_i) - I_{\perp}(q_i) \\ I_{/\!/}(q_i) + I_{\perp}(q_i) \\ Q_{/\!/}(q_i) + Q_{\perp}(q_i) \\ U_{/\!/}(q_i) + U_{\perp}(q_i) \end{bmatrix}. \tag{6.50}$$

We want to estimate the pixel parameters from all observations of Tau A, so we concatenate the data for each observations[13]. For convenience, we re-write the Eq. 6.47 as

$$\mathbf{d} = \mathbf{As} + \mathbf{Ll} + \mathbf{n} = [\mathbf{A}\ \mathbf{L}] \begin{bmatrix} \mathbf{s} \\ \mathbf{l} \end{bmatrix} + \mathbf{n} = \tilde{\mathbf{A}}\tilde{\mathbf{s}} + \mathbf{n} \tag{6.51}$$

The elements of the vector **s** are known (from IRAM maps), and we want to constrain the elements of **A** and **P**. The single-pixel multi-observations log-likelihood is given by

$$-2 \ln \mathcal{L}_{\text{data}} = \text{const} - \left(\mathbf{d} - \tilde{\mathbf{A}}\tilde{\mathbf{s}}\right)^T \mathbf{N}^{-1} \left(\mathbf{d} - \tilde{\mathbf{A}}\tilde{\mathbf{s}}\right) \tag{6.52}$$

were **N** is the time domain noise correlation matrix of pixel p for all observations. At the maximum of the likelihood, we have an estimate of $\tilde{\mathbf{s}}$, so we can eliminate

[13] Notice that the matrices **L** are uncorrelated between observations. Idem for **A**.

it from Eq. 6.52 to obtain the spectral likelihood which allows us to determine the maximum likelihood estimates of the parameters

$$-2\ln\mathcal{L}_{\rm spec} = \text{const} - \left(\tilde{\mathbf{A}}^T\mathbf{N}^{-1}\mathbf{d}\right)^T\left(\tilde{\mathbf{A}}^T\mathbf{N}^{-1}\tilde{\mathbf{A}}\right)^{-1}\left(\tilde{\mathbf{A}}^T\mathbf{N}^{-1}\mathbf{d}\right) \tag{6.53}$$

$$\tilde{\mathbf{A}}^T\mathbf{N}^{-1}\tilde{\mathbf{A}} = \begin{bmatrix}\mathbf{A}^T\mathbf{N}^{-1}\mathbf{A} & \mathbf{A}^T\mathbf{N}^{-1}\mathbf{L}\\ \mathbf{L}^T\mathbf{N}^{-1}\mathbf{A} & \mathbf{L}^T\mathbf{N}^{-1}\mathbf{L}\end{bmatrix} \tag{6.54}$$

The typical numbers per focal plane pixel for POLARBEAR data of the two seasons are : $n_{obs} \sim 10^2$, $n_t \sim 10^5$, $n_{pix} \sim 10^3$, $n_{poly} = 6$, $n_{param} = 4$. Further symmetries could be exploited[14].

6.8 Environment

6.8.1 Atmosphere correction

While looking at planet, we need to correct for the absorption due to the change in optical depth of the atmosphere and the variable amount of precipitable water vapor in the atmosphere (PWV). The PWV values are either read and interpolated from APEX weather station[15] (first iteration of the calibration) or derived from sky brightness measurements at several zenith angles (*elnods*, second iteration of the calibration). Concerning the transmission of the atmosphere, we rely on atmospheric opacity simulations. We pre-computed transmission templates with the ATM software [Pardo *et al.* 2001] for various values of PWV. Such templates[16] are shown in Fig. 6.18.

The atmospheric transparency, or transmission T_x is simply modeled as

$$T_x(z, PWV) = e^{-\tau(PWV)A(z)}, \tag{6.55}$$

where τ is the atmospheric optical depth and $A = \sec(z)$ is the airmass at zenith angle z[17]. Assuming that the form of the water vapor distribution above the site does not change, the transmission models compute, for each frequency requested, the atmospheric optical depth as [M.A. Holdaway 1997]

$$\tau(\nu, PWV) = \tau_w(\nu) \times PWV + \tau_d(\nu) \tag{6.56}$$

where τ_d represents the dry opacity terms due to atmospheric constituents which do not change with time, and τ_w represents wet opacity terms, which scale with the amount of precipitable water vapor (PWV) in the atmosphere (depending on

[14] In Eq. 6.45, we used one single number per observation and per pixel for the noise (the standard deviation of the timestream). We could assume the same which will make the structure of the noise covariance matrix easier to exploit.

[15] http://www.apex-telescope.org/weather/

[16] https://almascience.eso.org/about-alma/weather/atmosphere-model

[17] The zenith angle z is related to the elevation angle el by $z = \frac{\pi}{2} - el$.

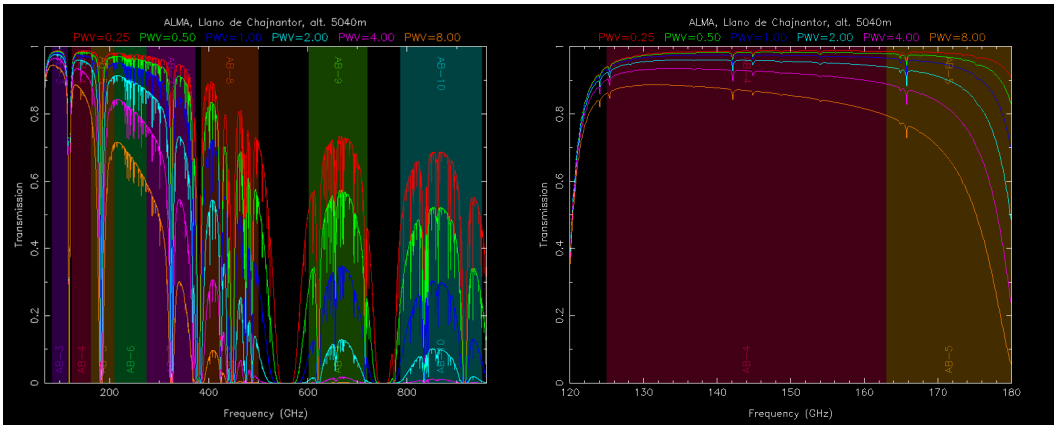

Figure 6.18: Atmospheric transmission between 70 and 960 GHz for a range of common PWV values at the site (left panel) based on ATM software [Pardo *et al.* 2001], and a zoom over the frequency range of interest for POLARBEAR, between 120 and 180 GHz (right panel). We can see that the transmission depends strongly on the amount of precipitable water vapor in the atmosphere, and so we need to have an accurate estimation of it to correct the observations.

the time of observation, highly variable). In the case of POLARBEAR we measure the sky brightness at a single frequency $\nu = 150$ GHz, and all those corrections are incorporated into the coefficient α in Eq. 6.5, computed for each observation

$$\alpha(obs) = \frac{1}{T_x(obs)}. \tag{6.57}$$

The Fig. 6.19 shows the histogram of the PWV values estimated for each observation for the first season.

6.8.2 Pixel differencing and atmospheric/ground rejection

The bolometers of the focal plane are grouped per pair. Each pixel in a POLARBEAR module contains detectors for two orthogonal polarizations. Assuming the simplest model, the POLARBEAR data model in this context for the two bolometers within a focal plane pixel can be written as

$$d_{/\!/}(t) = I(t) + Q(t)\cos 2\Theta(t) + U(t)\sin 2\Theta(t) \tag{6.58}$$
$$d_{\perp}(t) = I(t) - Q(t)\cos 2\Theta(t) - U(t)\sin 2\Theta(t), \tag{6.59}$$

where I, Q and U are the Stokes parameters and Θ is the detector polarization angle projected on the sky. From this simple model, one can immediately see that one can have I by summing the two bolometer timestreams, and Q and U by differencing the two timestreams. This is the strategy used for the first and second seasons of the first campaign (small patches). This approach has several pros and cons.

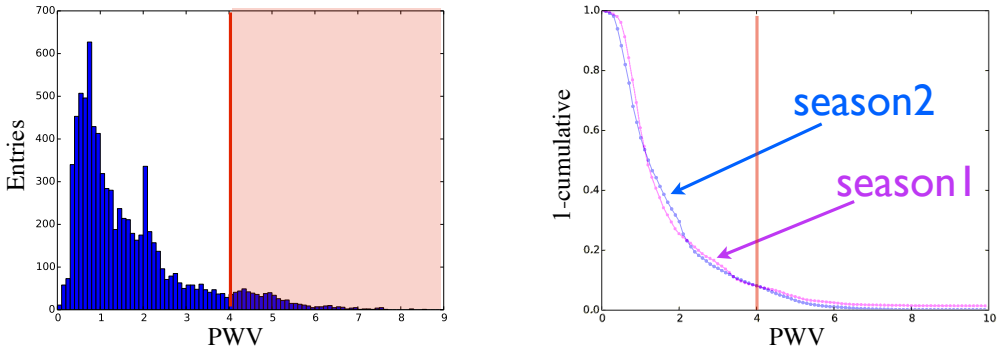

Figure 6.19: Histogram of the PWV values estimated for each observation for the first season (left panel) and complementary cumulative distribution for PWV values for first and second season (right panel). We discard from the analysis the observations taken with a PWV value higher than 4 mm ($\sim 7\%$).

The main advantage of this technique, is that any spurious signal coming from the ground or from the atmosphere behaves like I and so is not modulate by Θ. In this respect, differencing the two timestreams allows to get rid of a large amount of those spurious signals. Fourier transforming this differential timestream allows us to see how well the unpolarized atmosphere is suppressed at atmospheric frequencies (low frequencies). The cutoff of this low frequency noise informs our scan strategy to measure the large angular scale polarization signals. The sum and difference amplitude spectral densities for one focal plane pixel and observation of one of our CMB patches during 15 minutes are shown in Fig. 6.20. Pixel differencing with this simple calibration method effectively suppresses by several order of magnitudes the atmospheric fluctuations over a large bandwidth. Concerning intensity, since we sum the two bolometer timestreams, the resulting timestream data are affected by the atmospherical signal or the signal coming from the ground at low and intermediate frequencies (< 5 Hz). We will see later how to get rid of most of those signal by using appropriate filters (see Sec. 8.4).

Although this differencing method has the advantage of suppressing intensity-like signal common to both bolometers inside a pixel, it is likely dangerous if each bolometer see a different signal at a given time. In this case, differencing the timestreams of the bolometers generates a spurious polarization term coming from two unpolarized intensity terms. Especially effects such as pixel-pair differential gains, or differential pointing should be carefully controlled. We will see later how to address those issues, and what are the methods used to set up upper limits or constraints on those effects (see Chap. 10).

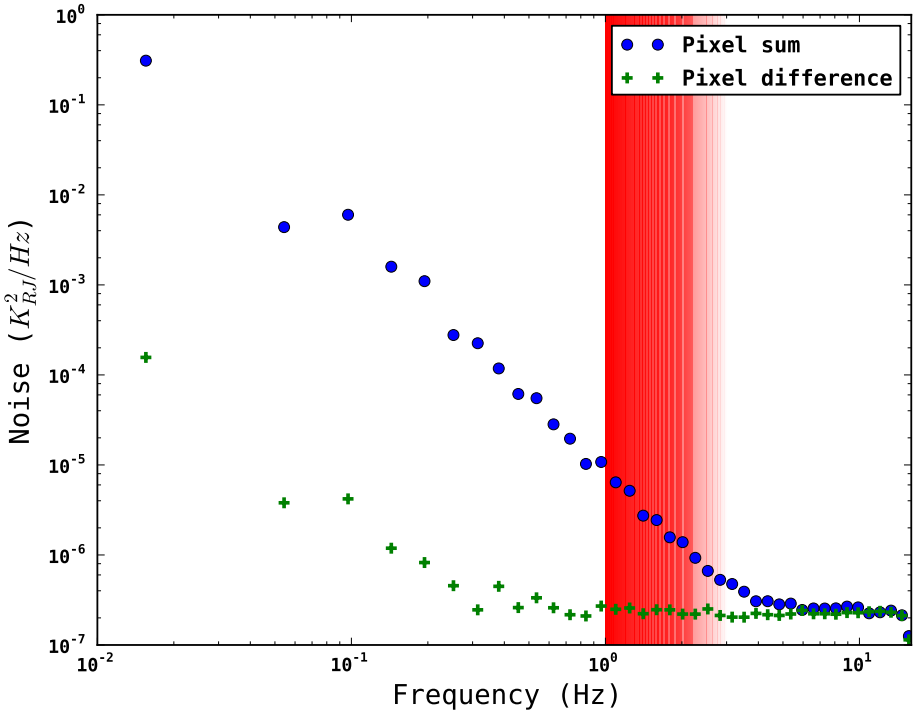

Figure 6.20: Binned intensity (blue circle) and polarization (green cross) timestream noise spectral densities for one focal plane pixel and observation of one of our CMB patches during 15 minutes. The red shaded region corresponds to our science band for the first two seasons (1.04-3.13 Hz). Pixel differencing with this simple calibration method effectively suppresses by several order of magnitudes the atmospheric fluctuations over a large bandwidth, and the noise is almost white over the region of interest. For more informations about the noise estimation, see Sec. 8.2.

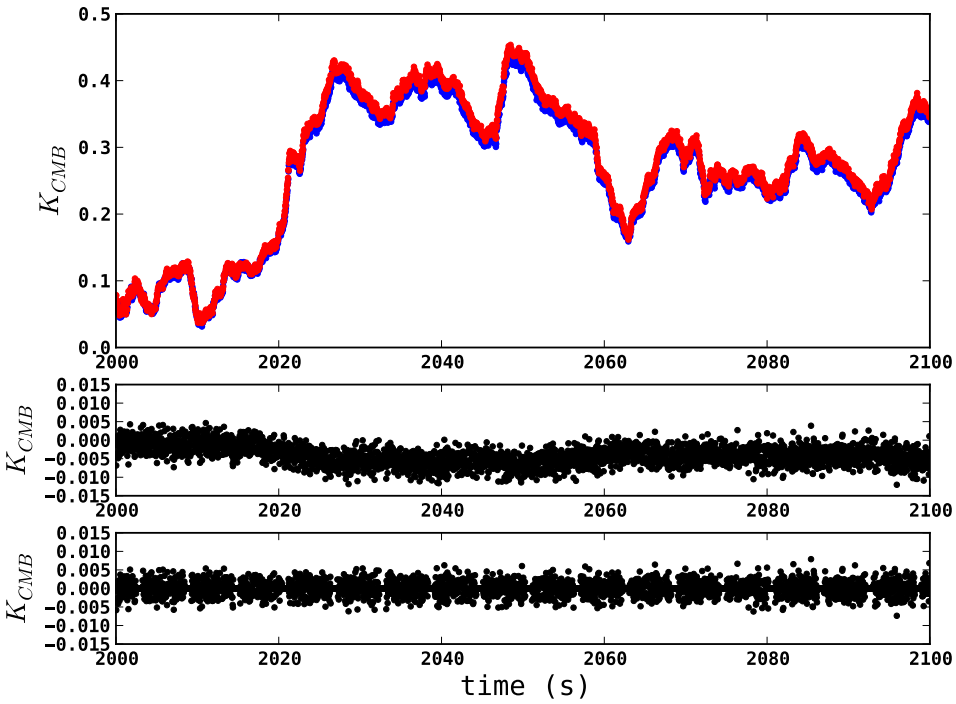

Figure 6.21: *Top panel*: Calibrated (relatively) timestreams data for two bolometers of the same pair (top in blue, bottom in red) during 100 seconds. The atmospheric fluctuations are clearly seen as large scales, and the two bolometers almost see the same amount of atmospheric signal at each given time. *Middle panel*: Difference timestream between the two bolometers of the top panel (divided by two). Most of the atmospheric fluctuations vanished, but we can see some long trends left. *Bottom panel*: Difference timestream between the two bolometers of the top panel (divided by two) and after the filtering step. We apply a mask in between subscans (sample discarded) and remove linear trends in polarization (see Sec. 8). The resulting difference timestream is almost perfectly white (noise dominated).

Chapter 7

Data selection

Contents

Once the timestreams are calibrated, we need to clean them from any instrumental or environmental contamination. This section is a description of the data cuts and the data selection used in POLARBEAR. There exists no recipes in the literature, and so it requires an understanding of the data properties and particularities of all possible pathologies. Another requirements is to be able to generate the minimum set of tests that can detect those pathologies, producing fast and reliable results at the same time. I was highly involved in the data selection process for POLARBEAR. While I mostly learned from more experienced collaborators during the first season, I took over the leadership for the second season. Based on my experience and general feedbacks gained during the first season, I redefined the data selection criteria for the second release. I also improved the analysis used for the first release (especially concerning the non-Gaussianity of the noise). I finally developed automated pipelines to speed-up this step and to back up all the details which go through each particular run. This step is highly connected to the calibration, and so we need to have a good overview of both.

7.1 First season statistics

We started observing on May 2012 and ended on June 2013. We define the first season to begin and end with the first science observations that are actually included

Table 7.1: Different steps of the data selection for the first release of the data.

Steps	Section	Comments
All seasons	7.1	Total time in the field (8,420 hours)
+ Patch hours	7.1	Availability of the patches
+ CMB hours	7.1	Time observing CMB
+ Gain avail. (raw)	7.2.1	Gain files generated
+ Gain & PSD avail. (raw)	7.2.1	Gain and noise files generated
+ Turnaround data cut	7.2.2	Accelerated data discarded
+ Data quality (observation)	7.2.3	Discard contaminated CES
+ Optical response	7.3.2	Discard broken detector
+ Data quality (detectors)	7.3.3	Discard contaminated detector
+ Centroids & Pol. angle	7.3.4	Systematic requirements
+ Non-gaussianities of the noise	7.3.5	Skewness & Kurtosis tests
+ Subscans masking	7.3.6	Mainly deglitching

Note. — In reality, the data selection is not such a linear process that is the cuts are often entangled.

in the analysis reducing the dates from June 27th, 2012 to June 13th, 2013. Between these two dates we have a total time of 8,420 hours available. However, the 3 patches observed by POLARBEAR are not always available and their presence represent only 86% of the total time. Within this science time, the CMB observations represent 3,045 hours. Given that POLARBEAR has a total number of bolometers of 1,274 we defined the bolometers hours being the product between the hours of observation and the number of bolometers considered. In total the time spent observing the CMB represents 36% of the total first season time. The remaining time was spent in calibration (planets, elnods, stimulator), re-pointing, fridge cycles and shutdowns of the telescope.

7.2 Cuts removing CES

There are two types of data selection criteria which filter out entire CES. The first one is based on the availability of the gain and noise files for a CES. The second one is based on data quality arguments.

7.2.1 Gain and PSD files generation

There are different ways to generate the gain files as seen in Sec. 6.5. We just check all the gain files generated in our gain model (planet observations). In addition, we retain only CES with both gain file and noise file (PSD) generated.

7.2.2 Accelerated portion of scans

For the first release, we immediately discarded all data obtained while the telescope was accelerating, which removed 36% of our observation time. The constant velocity portions are based on a GCP binary register which tells us when the telescope is scanning at constant velocity. However, for the second release of data (including a re-processing of the first season of data), we decided to include part of the data inside the turnarounds (portion of scans while the telescope is accelerating). Therefore, in addition to the data taken at the constant velocity portion on the sky of $0.75^\circ/\mathrm{s}$, we decided to keep data taken from this velocity down to $0.50^\circ/\mathrm{s}$ on the sky. This is how we define our subscans for the second release of data.

7.2.3 Data quality

Gains and PSD files have been generated for individual CES on a previous step. Once a CES has both a gain and a PSD for at least one pair of bolometers (pixel) it becomes part of the statistics described here. This is the first intentionally imposed cuts therefore the cuts are enforced by generating a new set of gain files excluding entire CES or individual pixels that we want to cut. For the first release of data, we had 21 imposed cuts. For the second release of data, we decided to keep only 17 of those cuts, and some of the kept tests were less conservative. This data selection drops entire CES because of *e.g.* bad weather (PWV $\geq$ 4mm), being too close to the Sun ($\leq 30^\circ$) or Moon ($\leq 20^\circ$), the remaining yield being too low (less than 50 bolometers for the observation), problematic scan length (less than 1 min and more than 15 min), bad encoder data (see Fig. 7.1), etc. An example of such cuts for one of our CMB patch is shown in Tab. 7.2.

7.3 Cuts removing channels

The next step is to loop over the remaining CESes, and identifying pathological behavior of individual bolometers[1]. In this section we assume the full length of each bolometer[2].

7.3.1 Dark bolometers

A dark a bolometer is a bolometer which shares the same readout circuit as the normal bolometers, but are not coupled to the optical signal. The focal plane of POLARBEAR has 70 dark bolometers (10 per wafer). For the first releases, they haven't been used for the final analysis, but we should definitely use them to probe systematic effects or to remove from the live bolometers any spurious signal from

[1] During observations, readout channels that show anomalously high noise properties are turned off so that pathological noise effects are not induced in other detectors. Those channels are already off when we start the data selection.

[2] The tests are done using data from the first subscan to the last subscan of the bolometer, including non-constant velocity portion of the timestream.

Table 7.2: Typical fraction of data cut by each criterion and the cumulative fraction for one patch (RA23)

Name of the cut	First release	Second release (s1)	Second release (s2)
Bad weather†	-	6.98 (6.98)	7.86 (7.86)
Too close from the Moon†	-	4.02 (10.9)	5.13 (12.6)
Too close from the Sun†	-	2.31 (12.6)	1.62 (14.2)
Bad encoder record†	-	2.54 (14.6)	11.2 (24.9)
Bad days†	-	2.80 (15.9)	4.83 (26.4)
Array median slope too high	-	2.81 (17.4)	3.26 (28.0)
Differential gain outlier	-	0.80 (17.5)	0.79 (28.1)
Differential gain variance	-	0.18 (17.7)	0.14 (28.2)
Differential gain median	-	1.19 (18.7)	1.56 (29.3)
Bad pairs	-	1.03 (19.6)	0.84 (29.9)
Differential gain slope	-	1.50 (19.8)	2.13 (30.3)
Difference PSD Lower Bound	-	0.86 (20.4)	0.66 (30.7)
Mean Gain	-	0.14 (20.4)	0.21 (30.8)
Channel slope deviation from median	-	3.66 (21.2)	5.46 (32.1)
Pair noise deviation from median	-	5.65 (26.0)	4.89 (36.0)
Scan length†	-	0.11 (26.1)	0.12 (36.0)
Ground Signal	-	18.4 (32.9)	21.4 (42.0)
Yield†	-	18.0 (33.0)	29.4 (42.2)
Total cut (in %)	-	33.0	42.2
Number of CES	8,354	10,239	4,326
Number of pixel-hours	479,998	631,116	231,447

Note. — Fraction of the entire data set (in %) removed by each data quality cut. Since cuts can overlap, the cumulative fraction is shown in parenthesis. Cuts with a † discard entire CES, while the others discard pixels inside each CES. Notice that the total is expressed in pixel-hours rather than bolometer-hours (boloh = 2 × pixelh).

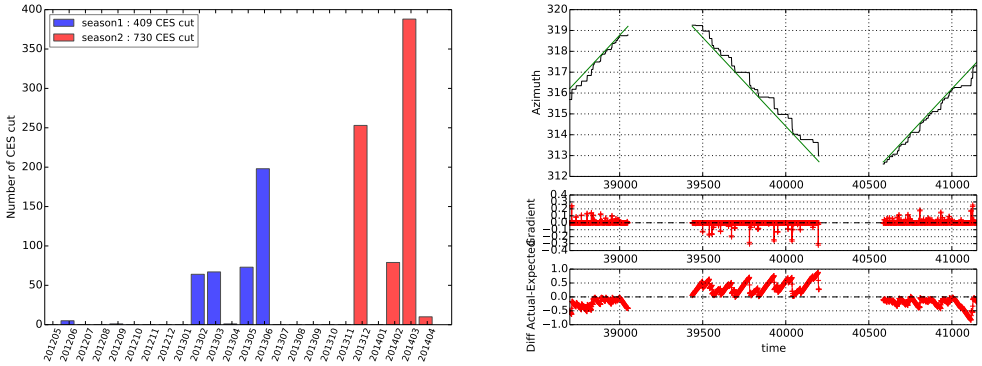

Figure 7.1: *Left panel*: Number of CES cuts due to an azimuth/elevation encoder misbehavior. The first season in labelled in blue and the second season in red. We can see that there was a lot of CES cut due to a problem with our encoder in March 2014. We had to change some part of it because it was not working properly. *Right panel*: Example of an encoder problem concerning the recording of the azimuth. The green crosses are the expected azimuth and the black crosses are the measured azimuth from the encoder. The small sub panels under the main panel are respectively the gradient of the recorded azimuth and the difference between expected and measured azimuth. We apply a maximum tolerance of 0.5° between the expected and the measured azimuth and we drop CES with over 1 zero-motion point per subscan.

the telescope such as thermal drifts. We have also 168 'demodulator' bolometers not used for the science but for the calibration of the focal plane only. The repartition of detectors is shown in Tab. 7.3.

7.3.2 Bolometers with optical response

In addition to dark and demodulator bolometers, we have broken bolometers which are defective bolometers and cannot be used in the analysis. Individual pixels are permanently excluded when they show no optical response in either one or two of the bolometers. There are typically 933 detectors out of the 1,512 showing an optical response.

7.3.3 Data quality

We follow the cuts defined in Sec. 7.2.3, but this time we are interested by the number of bolometers discarded. So in addition to the fact that entire CES can be removed, for each remaining CES, pixels are excluded from a single scan for having an outlier gain or differential gain value or if either of these quantities changes too rapidly over the course of the scan (gFrac). The number of channel cut on average is 377 ± 129, 383 ± 143 and 365 ± 124 for RA23, RA12 and LST respectively (out

Table 7.3: Typical number of detectors cut by each criterion and effective number of detectors per CES for the 3 patches for the 1st season.

		RA23	RA12	LST
Number of detectors				
Detectors w/ optical response	933			
Dark detectors	70			
Demod detectors	168			
Broken detectors	341			
Total	1512			
*Cuts applied to live detectors**				
Gain available		-377 ± 129	-383 ± 143	-365 ± 124
Centroids and pol. angle		-27 ± 8	-28 ± 9	-30 ± 8
Skewness		-12 ± 9	-12 ± 11	-13 ± 11
Kurtosis		-14 ± 10	-13 ± 11	-15 ± 11
Effective number of detectors		503 ± 118	497 ± 130	510 ± 115

Note. — * The cuts are applied consecutively. Errors are the standard deviation of the number of detectors.

of 933 live detectors). To get the number of bolometer hours, we use the time of all the subscans from each included CES and multiply it by the number of channels alive after cuts.

7.3.4 Centroids and polarization angle

We check whether the centroid is too far from the center of the pixel for a given detector pair. For that we know the position in the focal plane of the bolometers for each pair x_{pos} and y_{pos} and we compute

$$dr = \sqrt{(x^t_{pos} - x^b_{pos})^2 + (y^t_{pos} - y^b_{pos})^2} \tag{7.1}$$

where t and b stand for top and bottom bolometer. If dr is greater than 1 arcminute, we reject the pair from the analysis. In addition, we check whether there is an estimate of the polarization angle for this pair. If not, the pair is discarded. This cut discards on average 30 pairs per observation, after all other cuts.

7.3.5 Non-Gaussianity of the noise

To address pathologies related to noise properties, we put limits on the skewness and the kurtosis of the signal. We form polarized timestream by differentiating bolometer timestreams for each pair and we remove linear trends which could generate non-gaussianity. Then, to avoid the influence from low frequency signals dominated by

atmospheric signal, the data are high-pass filtered above 1 Hz[3]. Given the typical length of a CES (around 15 minutes), we expect the timestreams to be dominated by detector noise, expected to be gaussian. We put constraints such that the skewness should be between -0.5 and 0.5, and the kurtosis should lie between -1 and 1. This data selection rejects around 30 pairs per observation after all other cuts mentioned previously.

7.3.6 Cuts removing subscans

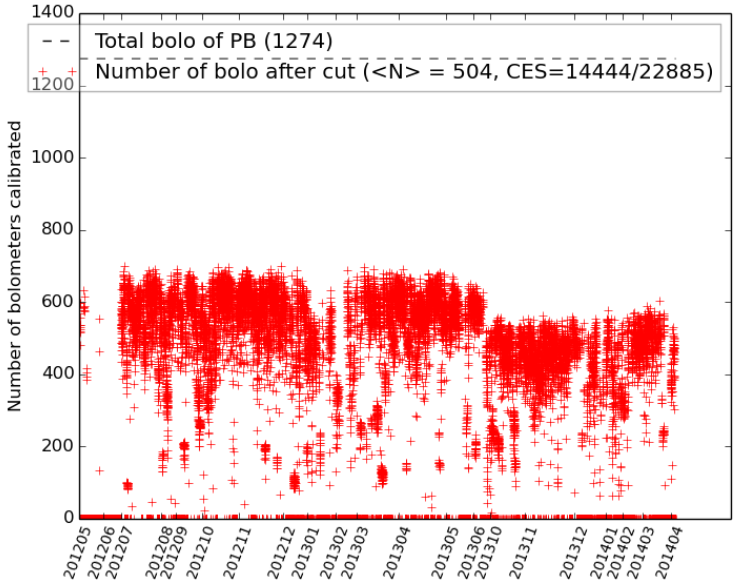

Figure 7.2: Preliminary number of bolometers on average per observation after data cuts. The second season has a lower yield, due to several problems (partly due to encoder fault).

The last step consists to take the remaining CES and their bolometers alive after all previous cuts, and to loop over the timestreams to identify bad subscans of data. Typically this is the moment where the deglitching is done. Subscans that show these glitches are simply removed from the data set. To flag subscans containing glitches, we convolve differenced timestreams with a set of Lorentzian-based kernels and remove subscans which exceed eight times the median absolute deviation of the convolved timestream. There are other flagging criteria imposed on subscans where there were problems with the bolometer or telescope pointing data acquisition systems.

[3]this procedure was not implemented for the first release.

Chapter 8

Mapmaking

Contents

This section focuses on the mapmaking step, that is the estimation of the sky maps from the cleaned and calibrated Time Ordered Data (TOD). I was highly involved in the mapmaking stage for Polarbear all along my thesis. I was an active contributor of the primary mapmaker, and a co-leader of the PCG mapmaker, by optimizing the performances, implementing routines, testing and using the pipelines almost daily. Part of my time was also devoted to check the consistency of both pipelines, by running regularly test cases and implementing new features from one pipeline to the other when needed. The PCG mapmaker has been entirely implemented by the APC team during my thesis. I also worked actively on the noise estimation and characterization. A special attention is made in this chapter to the correlated noise (from atmosphere and scan-synchronous signals) and its removal: time-domain visualization tools, jackknives, time-domain filtering, specific model of data (IGQU).

8.1 Introduction to Mapmaking and challenges for POLARBEAR

POLARBEAR scans the sky with roughly a thousand detectors at a rate of 190 Hz, and for the first two years of data we downsampled the data down to 30 Hz (see Sec. 6.2.2). Observations are performed every day, and after cleaning and performing the data selection, the data set collected is of the order of few Terabytes per year (time samples), and we want to make sky maps with $\mathcal{O}(10^5)$ pixels. Exact analysis of the data set produced is a serious computational challenge, since most of the numerical method scales as the number of time sample or pixels squared or cube[1]. Such a data set cannot be handled on a single laptop, and we always rely on the latest supercomputers in order to analyze efficiently the data. This growth of data and the use of supercomputers was predicted long time ago [Borrill 1999] and many efforts have been conducted to design robust data analysis algorithms and their implementations such as in [Stompor *et al.* 2001].

8.1.1 Data model

While recording the sky signal, we also record the pointing information of the telescope which is the position on the sky $p(t) = (\theta(t), \phi(t))$ as a function of the time. From the pointing, we associate each time sample value d to a pixel s on the sky. In addition to be sensitive to the intensity of the CMB, the detectors of POLARBEAR are polarization sensitive (linearly), that is any time sample value contains information from the three Stokes parameters of interest (I, Q, and U) convolved with the instrumental beam of the instrument. We can model such a detector as a (partial) polarizer followed by a total power detector, and the timestream data d for *one detector* may be expressed in its simplest form as a linear combination of the Stokes parameter maps

$$d(t) = I(p(t)) + Q(p(t)) \cos 2\Theta(t) + U(p(t)) \sin 2\Theta(t) + n(t), \tag{8.1}$$

where $n(t)$ represents usually the instrumental noise, and the polarization angle Θ is defined in Eq. 6.39. The projection from a time t to a sky pixel p can be encoded in a matrix which is called the pointing matrix $\mathbf{A}$ whose number of rows is the number of time samples n_t and number of columns is the number of sky pixels n_p multiplied by the number of Stokes parameters to recover[2]. The matrix $\mathbf{A}$ is in general very sparse as it contains only three non-zero values (intensity and 2 polarizations) in each row, as each sample is sensitive to only one pixel of the convolved sky. The scanning strategy of POLARBEAR is such that we come back to the same pixel

[1] As an example, multiplying an $[m \times n]$ matrix and an $[n \times p]$ matrix involves $2 \times m \times n \times p$ operations, and inverting brute force a matrix of size n involves n^3 operations.

[2] Strictly speaking, $\mathbf{A}^T$ is the pointing matrix, meaning going from time to pixel domain, while applying $\mathbf{A}$ is the transformation from pixel to time domain. Notice also that $\mathbf{A}^T\mathbf{A}$ is a diagonal matrix whose diagonal coefficients corresponding to intensity in $\mathbf{A}$ are the number of times a pixel has been seen.

very frequently to have a lot of redundancy. So still for one detector, but several measurements, the equation 8.1 can be rewritten as

$$\begin{bmatrix} d(t_0) \\ \vdots \\ \vdots \\ d(t_{n_t-1}) \end{bmatrix} = \begin{bmatrix} A_{t_0 p_0} & \dots & A_{t_0 p_{n_p-1}} \\ \vdots & \vdots & \vdots \\ \vdots & \vdots & \vdots \\ A_{t_{n_t-1} p_0} & \dots & A_{t_{n_t-1} p_{n_p-1}} \end{bmatrix} \times \begin{bmatrix} s(p_0) \\ \vdots \\ s(p_{n_p-1}) \end{bmatrix} + \begin{bmatrix} n(t_0) \\ \vdots \\ \vdots \\ n(t_{n_t-1}) \end{bmatrix}, \quad (8.2)$$

where $A_{t_i p_i}$ is a $[1 \times 3]$ matrix with values

$$A_{t_i p_i} = \begin{cases} [1, \cos 2\Theta, \sin 2\Theta]; & \text{if } (\theta(t_i), \phi(t_i)) \in p_i \\ [0,\ 0,\ 0]; & \text{otherwise,} \end{cases} \quad (8.3)$$

and $s(p_i)$ is a $[3 \times 1]$ matrix which contains the beam-smoothed Stokes parameters in pixel p_i

$$\mathbf{s}(p_i) = \begin{bmatrix} I(p_i) \\ Q(p_i) \\ U(p_i) \end{bmatrix}. \quad (8.4)$$

For many detectors, the generalization of the Eq. 8.2 is quite simple. We just have to stack vertically the timestreams from different detectors as well as for the other components of the equation. For convenience, we rewrite the Eq. 8.2 for multiple detectors and multiple measurements as

$$\mathbf{d} = \mathbf{A}\mathbf{s} + \mathbf{n}, \quad (8.5)$$

where each component of the equation is a multi-detector version the one defined in 8.2.

8.1.2 Map solution

The mapmaking method is the method to estimate $\mathbf{s}$ from Eq. 8.5. There exists many methods to estimate $\mathbf{s}$, and in POLARBEAR we decided to use the maximum likelihood method. Under the assumption of Gaussianity, the noise probability distribution is

$$\mathcal{P}(\mathbf{n}) = (2\pi)^{n_t/2} \exp\Big[-\frac{1}{2}(\mathbf{n}^T \mathbf{N}^{-1} \mathbf{n} + \mathrm{Tr}(\ln \mathbf{N}))\Big], \quad (8.6)$$

where $\mathbf{N}$ is the time-time noise correlation matrix given by

$$\mathbf{N} = < \mathbf{n}\mathbf{n}^T > . \quad (8.7)$$

Ideally, we would like the noise to be white. However, the instrumental noise is sometimes not white and contains some low frequency components. In addition, the noise coming from the atmosphere is mostly not white and dominates at low

frequencies. The treatment of the low frequency modes from the atmosphere will be the subject of a particular treatment later in this chapter. Using Eq. 8.5 to eliminate the noise vector, we can recast the Eq. 8.6 as the probability of the data for a particular sky signal

$$\mathcal{P}(\mathbf{d}|\mathbf{s}) = (2\pi)^{n_t/2} \exp\Big[-\frac{1}{2}((\mathbf{d}-\mathbf{A}\mathbf{s})^T\mathbf{N}^{-1}(\mathbf{d}-\mathbf{A}\mathbf{s}) + \mathrm{Tr}(\ln \mathbf{N}))\Big]. \tag{8.8}$$

Assuming flat map prior P($\mathbf{s}$) (*i.e.* all sky maps are a priori equally likely), this probability distribution is proportional to the likelihood of a particular sky signal given the data (see Eq. 2.54). The optimal solution for the map is given by the maximum-likelihood estimate $\hat{\mathbf{s}}$ which is obtained by solving the generalized least-squares (GLS) equation

$$\hat{\mathbf{s}} = \left(\mathbf{A}^T\mathbf{N}^{-1}\mathbf{A}\right)^{-1}\mathbf{A}^T\mathbf{N}^{-1}\mathbf{d} \tag{8.9}$$

However, since we are basically now solving for the model of a sky that is constant in time for every pixel in the map, the estimate $\hat{\mathbf{s}}$ is not a simple projection from time to pixel domain but a map solution[3]. The form of the maximum likelihood solution suggests the two main considerations: removing correlated noise components ($\mathbf{N}^{-1}\mathbf{d}$) and undoing the transfer function of those filters, $\left(\mathbf{A}^T\mathbf{N}^{-1}\mathbf{A}\right)^{-1}$. However, in experiments with a large number of detectors and long time-scale correlations in the timestream data, it is computationally intensive, and even impossible in practice, to invert or even build the $[n_p n_{Stokes} \times n_p n_{Stokes}]$ full $\mathbf{A}^T\mathbf{N}^{-1}\mathbf{A}$ matrix (the inverse of the pixel-pixel covariance matrix of the resulting map). The goal is then to find some filters or models that optimally capture noise and correlations between detectors. In practice, we also filter the timestreams in order to get rid of the correlated component of the noise, that is the data model and the mapmaking equation read

$$\mathbf{d} = \mathbf{A}\mathbf{s} + \mathbf{Z}\mathbf{z} + \mathbf{n} \tag{8.10}$$

$$\left(\mathbf{A}^T\mathbf{F}\mathbf{A}\right)\hat{\mathbf{s}} = \mathbf{A}^T\mathbf{F}\mathbf{d}. \tag{8.11}$$

$\mathbf{z}$ is the amplitudes of the modes we want to remove from the data, and $\mathbf{Z}$ is the corresponding pointing matrix which defines where we have to filter the data. The matrix $\mathbf{F}$ contains the effect of the time-domain filters and the noise weights ($\mathbf{N}^{-1}$):

$$\mathbf{F} = \mathbf{N}^{-1} - \mathbf{N}^{-1}\mathbf{Z}\Big(\mathbf{Z}^T\mathbf{N}^{-1}\mathbf{Z}\Big)^{-1}\mathbf{Z}^T\mathbf{N}^{-1}. \tag{8.12}$$

The different mapmakers developed to analyze the data of POLARBEAR make use of different assumption to solve Eq. 8.11.

[3]Note that a maximum likelihood map is not only a good visual representation of the data, but it is also a lossless way to compress CMB information. The power spectra derived from the map and directly from the timestream data will have the same uncertainty [Tegmark 1997a, Ferreira & Jaffe 2000].

8.1.3 Implementation for POLARBEAR: primary mapmaker

In an experiment such as POLARBEAR, the mapmaking is a necessary step, which has to be performed several times. Therefore, the mapmaking method has to be robust and reliable while taking a reasonable amount of time.

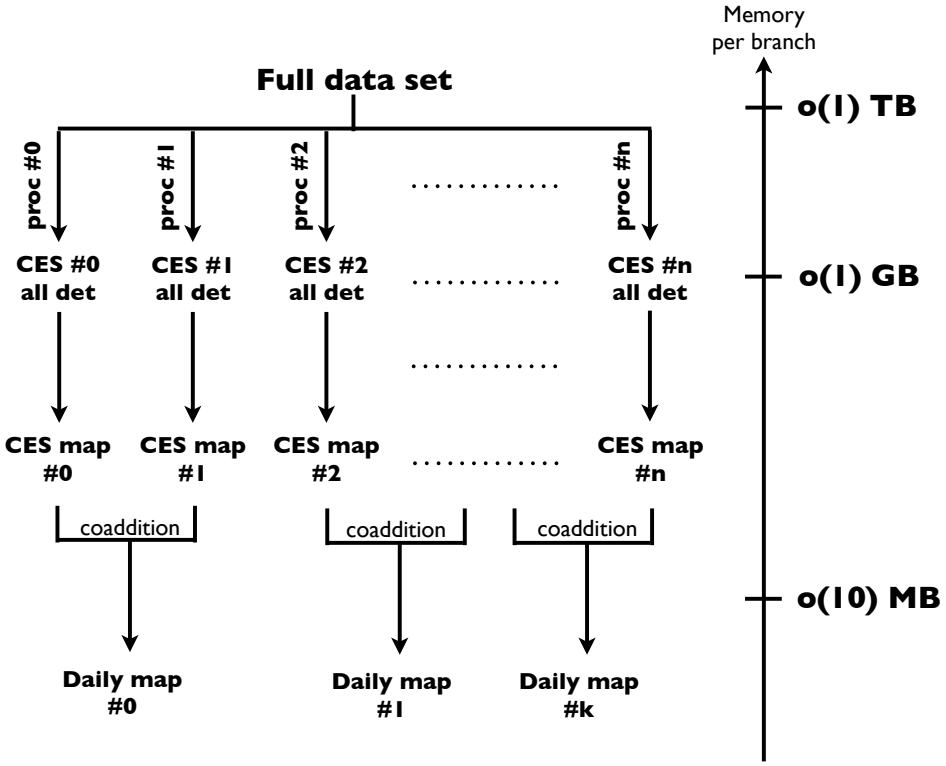

Figure 8.1: Schematic diagram of the primary mapmaking. The full data set is split between different processors. Each processor processes the data corresponding to one CES. Then the CES maps of each day are coadded into a single daily map. Notice that we started from a data set of the order of few TB, and we end up with few hundred maps, each of size few MB. This scheme has to be repeated for each sky patch separately.

The primary pipeline of POLARBEAR implements the simplest and fastest resolution of the mapmaking equation, widely used in the data analysis of CMB data sets (SPT, QUAD, BICEP, QUIET, etc.). It starts from the mapmaking equation 8.11 and makes the following assumptions

- Noise is assumed white, meaning $\mathbf{N}$ is a diagonal matrix.
- The time-domain filters are not taken into account in the pixel-pixel covariance matrix. Therefore it becomes $\left(\mathbf{A}^T\mathbf{N}^{-1}\mathbf{A}\right)$, which is a block diagonal matrix. Each block is a full 3x3 matrix corresponding to a sky pixel (I, Q, and U).

We construct an estimate $\hat{\mathbf{s}}$ of the sky signal $\mathbf{s}$ from the detector timestreams $\mathbf{d}$, the diagonal detector variance estimates $\mathbf{N}$, a set of filters $\mathbf{F}$ (noise and time-domain filters), and the pointing matrix $\mathbf{A}$, using

$$\left(\mathbf{A}^T\mathbf{N}^{-1}\mathbf{A}\right)\hat{\mathbf{s}} = \mathbf{A}^T\mathbf{F}\mathbf{d}. \tag{8.13}$$

This is a noise-weighted, biased estimate of the sky signal. The full noise covariance matrix is in general unknown, so we use an approximation of it. For a each sky pixel p, the $[3 \times 3]$ inverse covariance matrix $\left(\mathbf{A}^T\mathbf{N}^{-1}\mathbf{A}\right)_p$ is given by

$$(\mathbf{A}^T\mathbf{N}^{-1}\mathbf{A})_p = \begin{pmatrix} \sum_{t\in p}\sigma_+^{-2}(t) & 0 & 0 \\ 0 & \sum_{t\in p}\sigma_-^{-2}(t)\cos^2 2\Theta(t) & \sum_{t\in p}\sigma_-^{-2}(t)\cos 2\Theta(t)\sin 2\Theta(t) \\ 0 & \sum_{t\in p}\sigma_-^{-2}(t)\cos 2\Theta(t)\sin 2\Theta(t) & \sum_{t\in p}\sigma_-^{-2}(t)\sin^2 2\Theta(t) \end{pmatrix}_p \tag{8.14}$$

with $\sigma_\pm^{-2}(t)$ being the inverse pixel sum/difference timestream noise at time t which are assumed to be constant over a scan and are estimated from the Power Spectra Densities (see Sec. 8.2.1). Under this assumption, the noise weighting for each CES is taken as if the noise was white *i.e.* $\sigma_\pm^{-2}(t) = \sigma_\pm^{-2}$. Given that we assume no pixel-pixel correlations, we solve the mapmaking equation for each pixel separately.

Processing of the data Given the large amount of data, one needs to rely on the latest supercomputer to process the data set. The data set is divided into small chunks of data, each corresponding to roughly 15 minutes observation (one CES). According to the fact that we estimate the noise weights from the detector timestreams, the chunk boundaries are chosen to maximize the accuracy of the noise, while processing a sufficiently long timestreams to be able to have enough constraints on each pixel. The data for one CES (timestreams, pointing information, filters, noise weights etc.) is either read from the disk or computed on-the-fly and stored in the memory of one processor. Different processors do not interact each others, meaning that there is no need for communication between processors in this simple scheme and therefore the process of all the data is trivially scalable to many processors.

Once the data are sent to processors, we noise weight the timestreams to project out three types of low signal-to-noise-ratio modes: i) high frequencies, ii) low-order polynomials per subscan, and iii) scan synchronous signals. The high frequencies i) mainly come from the aliasing from the pixelization. Those modes are removed by applying a convolutional low-pass filter to the timestreams, where the 3 dB frequency of the filter is $f_{lpf} = 6.3$ Hz ($\ell \sim 3500$). Low-order polynomials ii) are used to remove excess low-frequency noise, mainly coming from atmosphere. Linear polynomials

are used for difference (polarization) timestreams, and cubic polynomials for sum (temperature) timestreams. For each detector we subtract a polynomial per CES subscan (one subscan is about 4 seconds). The scan synchronous signals iii) are more difficult to subtract from the data. Those signals mainly come from emissions of light from the ground and the mountains around the telescope which fall into the focal plane (far sidelobe scanning the ground). Fortunately, our scan strategy is designed to concentrate scan-synchronous signals (see Sec. 5.3.2), into a small number of modes which can be easily filtered. During a CES, scan-synchronous signals repeat in azimuth for the duration of the scan. Therefore, we project out scan-synchronous signals by averaging the timestreams in 0.08° azimuth bins for each bolometer to build a scan-synchronous signal template during a Constant Elevation Scan (CES). One major issue for the first season was that the telescope had over-primary sidelobe which can see the mountain nearby (TOCO) in a certain azimuth range (150° $\leq$ az $\leq$ 250°, el$\geq$ 70°). Let's denote $\mathbf{G}$ and $\mathbf{P}$ the pointing matrices for the ground template and the polynomial filters respectively. The data model reads[4]

$$\mathbf{d} = \mathbf{A}\mathbf{s} + \mathbf{G}\mathbf{g} + \mathbf{P}\mathbf{p} + \mathbf{n}, \tag{8.15}$$

where $\mathbf{g}$ and $\mathbf{p}$ are a binned ground signal and the amplitudes of the Legendre modes we want to remove from the data respectively. The general form of the filter defined in Eq. 8.12 would then be

$$\mathbf{F} = \mathbf{N}^{-1} - \mathbf{N}^{-1}[\mathbf{G},\mathbf{P}]\Big(\begin{bmatrix}\mathbf{G}^T\\ \mathbf{P}^T\end{bmatrix}\mathbf{N}^{-1}[\mathbf{G},\mathbf{P}]\Big)^{-1}\begin{bmatrix}\mathbf{G}^T\\ \mathbf{P}^T\end{bmatrix}\mathbf{N}^{-1}. \tag{8.16}$$

Given that we filter CES independently, and within a CES the noise is assumed to be white (diagonal $\mathbf{N}$), we factorize the noise term and perform the noise weighting only once (after the filtering). In addition, we do not implement the orthogonalization of the filters. Therefore, the filter operator reduces to

$$\mathbf{F} = \mathbf{N}^{-1}\Big(\mathbf{1} - [\mathbf{G},\mathbf{P}]\begin{bmatrix}\mathbf{G}^T\\ \mathbf{P}^T\end{bmatrix}\Big). \tag{8.17}$$

We can see the effect of the time-domain filters on the timestream data (polarization) in the Fig. 6.21. Most of the large scale fluctuations are removed.

Co-addition The timestream data being filtered, we use the transpose of the pointing matrix $\mathbf{A}^T$ to map the time-domain vector into the map domain. We co-add the single-CES, all-detector maps into a set of single-day I, Q, and U maps using the covariance matrix of each map. The coaddition is done pixel per pixel as

$$\hat{\mathbf{s}}_d(p) = \frac{\sum_{c\in d}\left(\mathbf{A}^T\mathbf{N}^{-1}\mathbf{A}\right)_{p,c}\hat{\mathbf{s}}_c(p)}{\sum_{c}\left(\mathbf{A}^T\mathbf{N}^{-1}\mathbf{A}\right)_{p,c}}, \tag{8.18}$$

[4]The high-pass filter is put on aside.

where d is the day of interest, and c represents the CES belonging to that day. Concerning the first season, the sky patches LST, RA12, and RA23 have 148, 139, and 189 daily maps respectively. We project the data onto a flat map using the cylindrical equal area projection centered at the nominal patch center. The map pixels have a width of 2'.

8.1.4 Implementation for POLARBEAR: PCG mapmaker

Parallel to the development of the main pipeline described above, we developed specifically at APC a second mapmaking pipeline with a different approach to the data. The primary mapmaker is able to produce fast sky maps, but those maps are biased renditions of the sky since they still contain the effect of the time-domain filters. Therefore, we wanted to go beyond, and be able to produce *unbiased* sky maps.

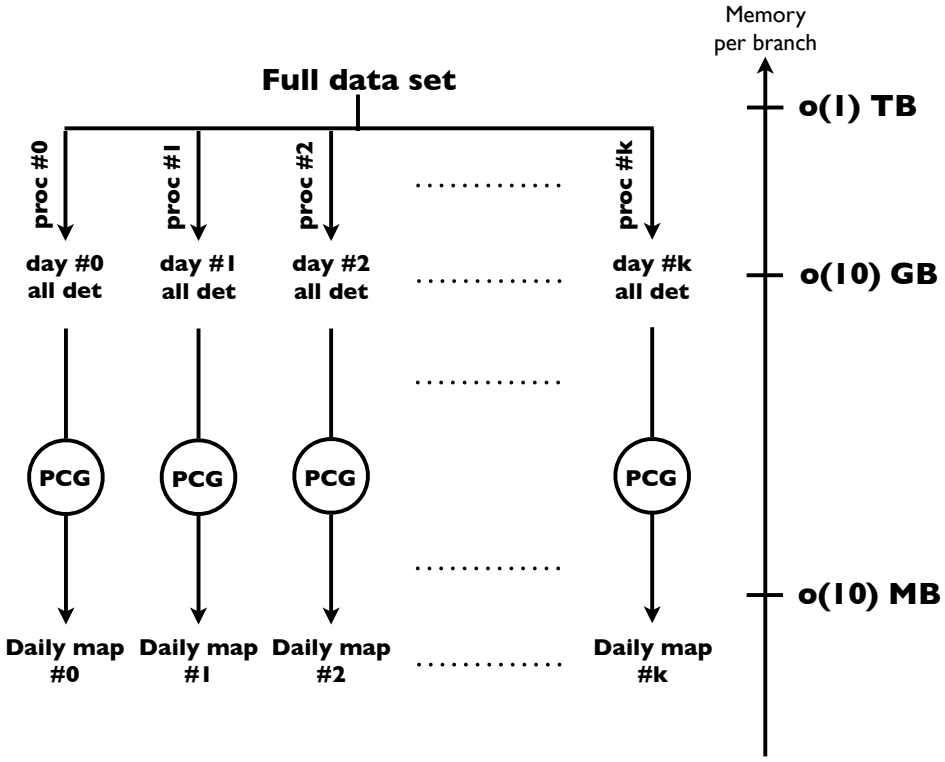

Figure 8.2: Schematic diagram of the PCG mapmaking. The full data set is split between different processors. Each processor processes the data corresponding to one day. There are typically 20-30 CES per day that are concatenated. Each processor then produces a daily map using an iterative method (PCG). The runtime depends on the number of iterations required. Notice that we started from a data set of the order of few TB, and we end up we few hundred maps, each of size few MB. This scheme has to be repeated for each sky patch separately.

Table 8.1: Comparison between the primary and the PCG mapmaker with default configuration to produce the full season map of one patch.

Mapmaker	Runtime (CPUh)	Memory/task (GB)	Output
Primary	$\mathcal{O}(10^2)$	$\mathcal{O}(1)$	Biased map
PCG	$\mathcal{O}(10^3)$	$\mathcal{O}(10)$	Unbiased map

Note. — The increase in memory for the PCG mapmaker is due to the fact that each task processes all the data for one day (∼30 CES) while the primary mapmaking processes one CES data per task. We report performances for 100 iterations of the PCG.

Starting from the mapmaking equation 8.11 we make the following assumption

- Noise is assumed white, meaning $\mathbf{N}$ is a diagonal matrix.

Note that unlike the primary pipeline, the effect of filters are kept in the pixel-pixel covariance matrix. Unfortunately, constructing and inverting explicitly $\mathbf{A}^T\mathbf{F}\mathbf{A}$ given the size of the POLARBEAR data set is extremely difficult and costly in terms of memory and number of operations. So we decided to solve the Eq. 8.11 by using an iterative numerical method called Preconditioned Conjugate Gradient (PCG) method, which will be detailed in Sec. 8.3. Given that each iteration of the PCG corresponds roughly to the primary mapmaking, the total runtime is that of the primary mapmaker multiplied by the number of steps for the PCG.

Processing of the data The data set is still divided into CES (15 minutes long observation), but we process all the CES of one day at once. By using all the CES of a day in the same time, we increase the cross-linking per pixel and we benefit from a large modulation of the polarization angle, which minimizes the risk of singularity for $\mathbf{A}^T\mathbf{F}\mathbf{A}$ in each pixel. However, the data for one day usually don't fit into the memory of one single core of a computer, and we have to use the memory of several cores for one job to have access to a larger memory (up to 30 Gb per processed day). The comparison of performances between the two pipelines is shown in Tab. 8.1.

The filtering of the timestream data is very close to the primary mapmaker described above. We first subtract a linear polynomial for polarization and cubic polynomial for temperature per CES subscan. Then we bin the timestreams in azimuth to form the ground template that we subtract to the data in order to project out scan-synchronous signals. The only difference is that we do not apply the low-pass filter to the timestreams. It was motivated by the fact that we didn't see any change by applying it or not, so we decided to not use it, to make the filtering step simpler.

Map solution Unlike the primary mapmaker, we project the data onto curve sky maps by using the HEALPIX pixelization scheme [Gorski *et al.* 2005], with a res-

olution of about 1.7' (nside=2048)[5]. This point was crucial since the HEALPix package is widely used in the community, and having maps with this pixelization scheme allows to use existing tools and libraries which are very efficient. It also allows easily cross-correlations with maps from other experiments using this pixelization scheme (*e.g.* Planck). In addition, having already maps in curve sky doesn't require any change of the pipeline once larger fraction of the sky will be scanned while the flat sky approximation will not hold.

8.2 Noise estimation and characterization

The optimal estimation of maps relies crucially on the ability to accurately model the noise properties of the instrument [Stompor *et al.* 2001, Hivon *et al.* 2002]. The raw sensitivity of the instrument determines the signal-to-noise ratio of the TOD, which is modulated by the distribution of integration time once projected on the sky maps. A good estimation of both is required to determine with fidelity the recovered sky maps.

8.2.1 Power spectral density

How to estimate the noise weights to have a map solution sufficiently close to the optimal solution? The answer is not totally trivial. In our case, if we take a sufficiently small chunk of data, the timestream data are noise dominated, and we are able to extract the noise information. But there are several different noise contributions at all frequencies, and we would like to pick up only the needed contributions (the frequency range of interest) while keeping the method simple and fast. For the first release, we decided to use the time-domain Power Spectral Density (PSD) which is the distribution of the strength of a signal in the frequency domain[6].

The procedure is the following. For each observation (CES), we load and calibrate the data of each pair. We sum and differentiate the timestream data inside each pair to form the intensity and polarization timestreams. We subtract a first order polynomial to both intensity and polarization timestreams to avoid drifts and we subtract the mean of each timestream. We then compute the PSD for each. Finally, the intensity and polarization noise weights for this CES are the average of the corresponding PSD inside the science band, that is between 1.04 Hz and 3.13 Hz. Since we estimate the noise weights from the same data that we use to make maps, we introduce a small non-linearity in the analysis[7]. But given that there are so many samples used to estimate the weights (roughly $\mathcal{O}(10^4)$ per CES), this effect should be negligible. Such PSD are shown in Fig. 6.20. Since we produce one PSD

[5] Let's also acknowledge the Python wrapper, Healpy, intensively used throughout this thesis: https://github.com/healpy.

[6] At the very beginning of the analysis, we started to weight the timestream by using their variance. But this overestimated the real noise contribution as the noises at all frequencies - and not just the science band - were picked up.

[7] Which is not taken into account in simulations because we use the same weights.

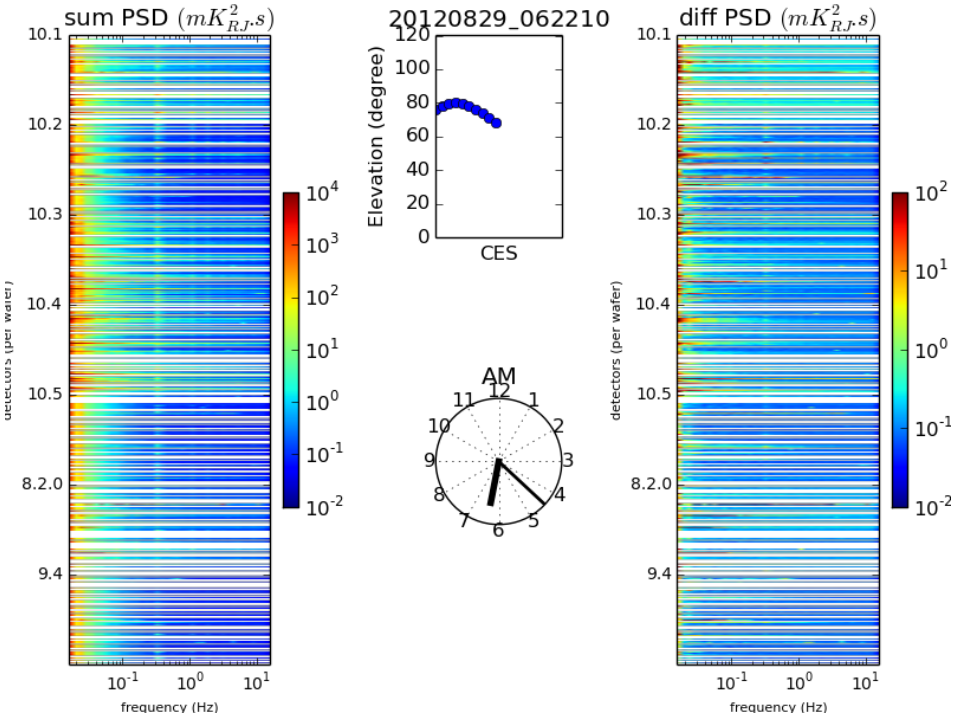

Figure 8.3: Frequency-space waterfall plots for calibrated TOD obtained from intensity timestream (left) and polarization timestream (right) for 15 minutes of data (one CES). The y-axis corresponds to the different pairs of detectors sorted by wafers. White rows are broken pairs of detectors or pairs which have been discarded from the analysis by the data selection. The y-axis corresponds to the frequency (binned). The lower frequencies are dominated by 1/f noise. We can also see correlations among different pairs (frequency lines) such as around 300 mHz. Those lines are mostly scan harmonics. Notice than the colorscale is not the same for both panels. This plot comes from a simple software which displays PSD as well as time and elevation for each observation, in order to have a quick look on the data quality before processing the data.

file per observation, we have a lot of them to produce ($\mathcal{O}(10^4)$). Fortunately, we could trivially parallelized the computation over many processors since two different observations are uncorrelated.

Assuming a constant velocity on the sky of $0.75°/s$, the science band corresponds to roughly a range of multipole $[500, 1500]$, which is the region of the spectrum targeted for the first releases - the lensing B-modes peaking at $\ell \sim 1,000$. For the difference timestream, any power due to correlated sources should decrease in the resulting PSD. Assuming that atmosphere is not (or weakly) polarized, we should remove most of the contribution from the atmosphere. We can clearly see this effect in the PSD of the difference timestream in Fig. 6.20, where the noise contribution in the difference timestream is mostly white.

PSD as a monitor of problems The distribution of the signal in the frequency domain is a good indicator of the quality of the data. The telescope is complex, and its functioning can affect the data. For example, we found excess of signals in the band 9-10 Hz or around 40 Hz, corresponding to telescope vibrations confirmed afterwards by both accelerometer measurements and encoder data. There are also known signals such as signals coming from the MUX boards which generate a 6 mHz tone in many pixels, or the spectral lines from the cryostat mostly at high frequencies, or even the frequencies of scans (motion of the telescope). Such signals are easy to detect since they appear on all the pairs simultaneously. Therefore, we often perform quick overviews of the PSD to detect gross problems during scans and we designed filters to remove periodical ones. In this respect, we also implemented a software which displays PSD for every observations. An example is shown in Fig. 8.3.

8.2.2 Simulating white noise from real data

In practice, we never have white noise in the map. Even if we the detector noise is truly white to start with, the operation of filtering correlates scales:

$$\mathbf{F} = \underbrace{\mathbf{N}^{-1}}_{\text{diagonal}} - \mathbf{N}^{-1} \underbrace{[\mathbf{G}, \mathbf{P}] \begin{bmatrix} \mathbf{G}^T \\ \mathbf{P}^T \end{bmatrix}}_{\text{not diagonal}}. \tag{8.19}$$

However, we want to have a way to quickly perform white noise simulations based on the real data, in order to compare with real data. Let the matrix $\mathbf{M}$ be the pixel-pixel noise correlation matrix for two Q and U Stokes parameter maps (assumed block diagonal). For simplicity in the notation, we only focus on the polarized part, but adding the temperature to the computation is trivial. In our specific case, $\mathbf{M}^{-1}$ is made of $[2 \times 2]$ non-zero blocks which contain the polarization noise weights estimated from the PSD (unique number per observation and pixels are uncorrelated), with each block $\mathbf{M}_p^{-1}$ given by

$$\mathbf{M}_p^{-1} = (\mathbf{A}^t \mathbf{N}^{-1} \mathbf{A})_p = \begin{pmatrix} \sigma^{-2} \sum_{t \in p} \cos^2 2\Theta(t) & \sigma^{-2} \sum_{t \in p} \cos 2\Theta(t) \sin 2\Theta(t) \\ \sigma^{-2} \sum_{t \in p} \cos 2\Theta(t) \sin 2\Theta(t) & \sigma^{-2} \sum_{t \in p} \sin^2 2\Theta(t) \end{pmatrix}_p . \tag{8.20}$$

Intuitively, this covariance matrix gives us the level of noise per pixels (squared) as if it was white noise only. We need first to invert $\mathbf{M}^{-1}$, and perform a Cholesky decomposition on each block to have access to the level of noise per pixel for the Q and U maps:

$$(\mathbf{A}^t \mathbf{N}^{-1} \mathbf{A})_p^{-1/2} = \begin{pmatrix} a_{00} & a_{01} \\ 0 & a_{11} \end{pmatrix}_p . \tag{8.21}$$

Then, we want to perform white noise simulations. The terms a_{00} and a_{11} represent Q and U (white) noise level respectively for a given pixel p, whereas a_{01} represents the correlation between Q and U within the pixel p. For a white noise map, we expect the distribution of pixel values to follow a Gaussian distribution with zero mean and unit variance, meaning no pixel-pixel correlations. So when we simulate noise maps N_Q and N_U , we draw for each map a vector of random numbers $\mathbf{x}$ of size number of pixels from a Gaussian distribution with mean = 0 and rms =1, and we multiply the matrix defined in Eq. 8.21 by this vector:

$$\begin{pmatrix} N_Q \\ N_U \end{pmatrix}_p = (\mathbf{A}^t \mathbf{N}^{-1} \mathbf{A})_p^{-1/2} \, \mathbf{x}_p. \tag{8.22}$$

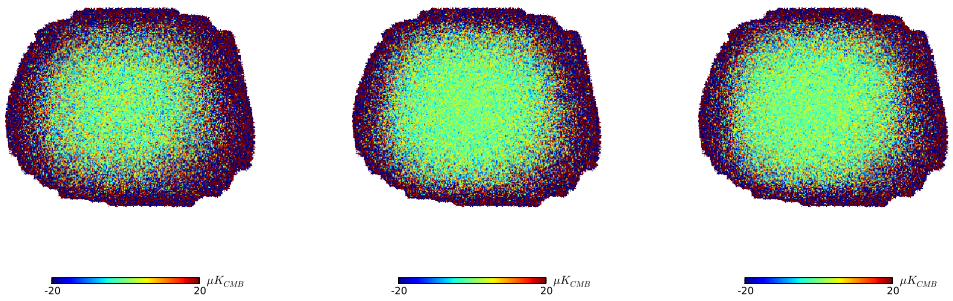

Figure 8.4: Simulated white noise maps N_I, N_Q and N_U based on one of our sky patch (first season only). The raw sensitivity of the instrument is modulated by the distribution of integration time once projected on the sky maps, giving an inhomogeneous distribution of the noise. The center of the patch is observed roughly few ten times more than the edge. Each map contains roughly 55,000 pixels at a resolution of nside=2048 (1.7' resolution).

Simulated white noise maps for I, Q and U based on the RA23 patch (first season only) are shown in Fig. 8.4. We can clearly see the effect of the scanning strategy which makes the noise inhomogeneous as the center of the patch is more observed than the edge.

8.2.3 Correlated noise

White noise is clearly an ideal case, and if we analyze raw observations, without any pre-processing, the timestream noise is likely dominated by correlated noise. We call systematic or correlated noise any noise which affects more than a single detector at a time and thus producing correlations between detectors[8]. The biggest correlated signal for POLARBEAR is the signal coming from the atmosphere. The

[8]Those correlated signals can also have a coherence length in the time direction.

amplitude and correlation of atmospheric fluctuations depend on both the scanning strategy and the properties of the atmosphere at the time of observation, such as the wind direction and speed [Errard *et al.* 2015]. This noise depends on the frequency considered (colored noise, mostly affects the low frequencies) and spatially correlates different timestream detectors. In addition, the functioning of the telescope produces correlated noise. Thermal drifts arise from the fact that all detectors are in the same temperature bath. Mechanical vibrations happen very often, and produce known lines in the PSD of each detectors (scan harmonics). We have also other contamination such as magnetic contamination, electronic noise, and thermal oscillations. Given the fact that those signals are correlated between detectors, their contribution does not average out well[9] as the white noise does, at least for samples acquired within the time scale of the correlation. In addition these effects are arising from strong time dependent effects, but they are not necessarily correlated in map-space. In other words, the features that they can produce in map space are not as strongly localized as the correlated features in the TOD. So we need to perform checks in TOD rather than map-space which makes it more difficult given that the size of the time-domain data set is many order of magnitudes bigger than in map-space.

We can divide the correlated signals into two categories. The first category is almost 3 orders of magnitude higher than the CMB signal in the frequency range of interest, and it contains the atmospheric fluctuations. The second category is made of all other correlated signals, and has been found weaker than the white noise level and the CMB. So only the first category requires a specific treatment as of now[10]. This means that almost any correlation that can be found between detectors is almost surely due to correlated contamination from the atmosphere drift at low frequencies. To get rid of most the atmosphere fluctuations during observations, we subtract linear polynomials for difference (polarization) timestreams, and cubic polynomials for sum (temperature) timestreams. The filtering is done for each subscan (each sweep in azimuth). This is clearly sub-optimal as the level of atmospheric fluctuations is not the same for every subscans. As of now, based on the PSD (see for instance Fig. 6.20), we found that the third order polynomials and the first order polynomials were describing well the low frequency parts of the spectrum. But we could have adapted a specific subtraction for each subscan or more clever method such as a singular value decomposition [Dünner *et al.* 2013]. But our simple method gives somehow good performances to remove most of the correlated noise and it doesn't affect dramatically the runtime of the mapmakers.

The level of correlated signal between detectors is easily seen through a correlation matrix C. Each column and each row of the matrix represents a detector, and each element in the matrix represents the level of correlation between the total

[9] They do not fall as the square root of the integration time.

[10] As observations are done, the relative level between white noise and correlated noise may change, and we will need also a specific treatment for the second category. Dark bolometers are very good probe for correlated noise of the second category.

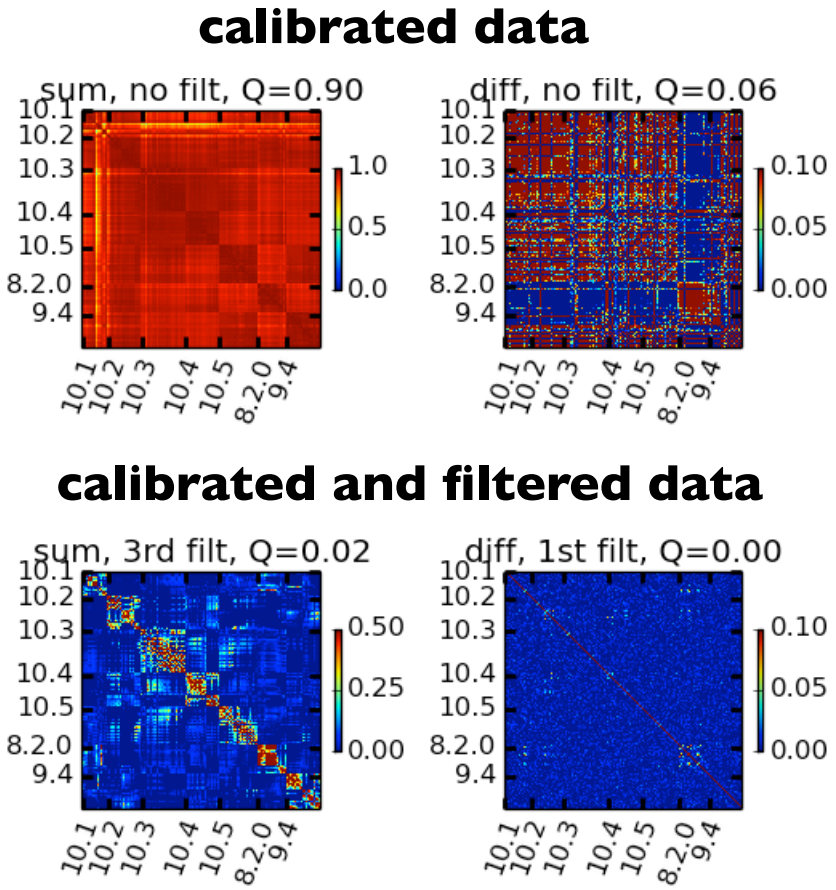

Figure 8.5: Correlation matrices for live detectors in the focal for a CES (15 minute long observation). Matrices have been normalized so that the diagonal elements are equal to one, and detectors are sorted by wafers. The top panels show the correlation matrices using calibrated intensity (left) and polarization (right) timestreams. Both matrices are dominated by long modes which correlate the timestreams of all the detectors. The detectors inside wafers are the most correlated due to their spatial proximity. The bottom panels show the same timestream correlations but after filtering. The decorrelation works well, especially for detectors not belonging to the same wafers. The Q factor drops from $\mathcal{O}(1)$ to $\mathcal{O}(10^{-2})$ in intensity and from $\mathcal{O}(10^{-2})$ to $\mathcal{O}(10^{-4})$ in polarization. Notice that the colorscale is not the same for each panel.

signal[11] of the detectors associated to it. Notice that C is a symmetric matrix. In order to ease the detection of correlation by eyes, the best is to organize detectors as they are put in the focal plane, that is grouped by wafers. In this respect, we

[11]The total signal is made of CMB signal, white noise and correlated noise. In principle for a short period of time, only the noise terms is dominant.

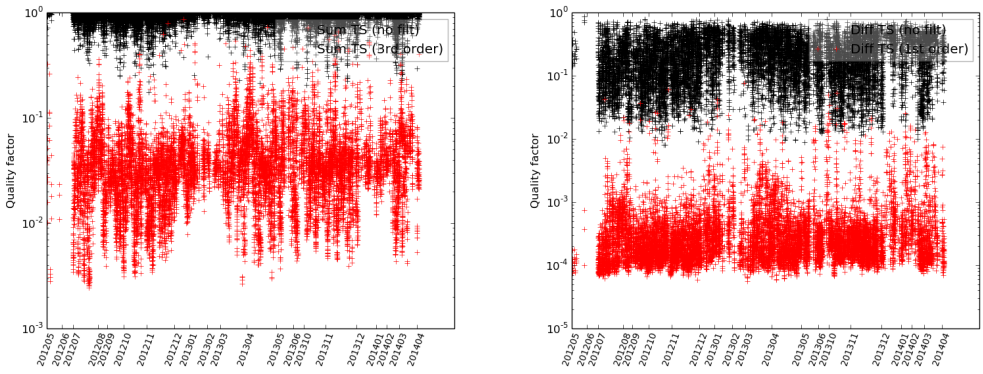

Figure 8.6: Distribution of the quality factor Q for the two first seasons of observations before polynomial filtering (black) and after polynomial filtering (red). Intensity timestreams are shown in the left panel, and polarization timestreams are shown in the right panel. For some observations, the decorrelation doesn't work well. Most of the times, those observations correspond to a moment of very bad weather (PWV $>$ 4 mm) or are affected by ground signals, and they will be removed by the data selection step. Notice that y-axis do not have the same scale on each panel.

highlight better the spatial correlations. In addition, we would like also to assess the level of correlated signal no matter how we organize the detectors inside our matrix Following [Dünner *et al.* 2013], we define a quality factor defined as the mean of the off-diagonal elements squared of the correlation matrix

$$Q = \frac{2}{N(N-1)} \sum_{i>j} C_{ij}^2, \tag{8.23}$$

where C_{ij} is the correlation between the detector timestreams i and j, and N is the number of detector timestreams. Q quantifies the amount of correlation between all detectors in the focal plane. A good timescale to compute Q is a CES (15 minute observation), as atmosphere properties are likely to be rather stable. Such correlation matrices and their quality factor are shown in Fig. 8.5 for a given CES. We also show the effect of the polynomials filtering. We can see that the filters decorrelate well the timestreams detectors, reducing the quality factor by few order of magnitudes[12].

[12]For a fair comparison, it is worth mentioning that the number of degree of freedom is given by $n_{subscan}(n_{poly}+1)n_{det}$, where $n_{subscan}$ is the number of subscans ($\sim 10^2$), n_{poly} is the order of polynomials (0, 1 or 3) and n_{det} is the number of live detectors ($\sim 10^2 - 10^3$).

8.3 Performances of the PCG mapmaker and maps

The choice of a good linear solver is primordial, on the one hand for its speed, but also for its robustness and the core memory which it requires. Therefore, a compromise is to be operated between these stresses.

8.3.1 Algorithm and performances in more details

As described previously, the PCG mapmaker shares the same low-level pre-processing and filtering[13] than the primary mapmaker, but the method to get the map solution is different. We recall that the equation that we are trying to solve is a generalized least-squares equation, given by

$$\left(\mathbf{A}^T\mathbf{F}\mathbf{A}\right)\hat{\mathbf{s}} = \mathbf{A}^T\mathbf{F}\mathbf{d}, \tag{8.24}$$

where $\mathbf{F}$ contains both the effect of the filtering of the timestreams and the noise weights, as defined in Eq. 8.17. In practice, $\mathbf{A}^T\mathbf{F}\mathbf{A}$ is extremely difficult to build and to invert due to the size of the problem. We have few Terabyte data in time-space ($\mathcal{O}(10^8)$ samples after calibration), and we want to make maps with $\mathcal{O}(10^5)$ pixels (the brute force inversion of a matrix scales as n_{pix}^3). So we decided to make use of an iterative method called Preconditioned Conjugate Gradient (PCG) [Golub & Van Loan 2012]. The idea behind the PCG method is to be able to estimate $\mathbf{s}$ without building and inverting explicitly the whole system. In each iteration of the PCG, it is necessary to apply the pixel-pixel covariance matrix $\mathbf{A}^T\mathbf{F}\mathbf{A}$ to the map-domain vector $\hat{\mathbf{s}}_j$ and this can be achieved by using its factors in the following procedure

- Use the pointing matrix, $\mathbf{A}$, to project the map-domain vector $\hat{\mathbf{s}}_j$ at iteration j into the time domain.
- Apply the filtering operator and the inverse noise covariance matrix $\mathbf{N}^{-1}$ to the time-domain vector.
- Use the transpose of the pointing matrix $\mathbf{A}^T$ to map the time-domain vector back into the map domain.

The first and the third steps are quick because the pointing matrix is sparse. The second step is the longest because of the filters (recall that the noise covariance matrix is diagonal). Unfortunately, a standard Conjugate Gradient (CG) method convergence is largely dependent on the condition number of the matrix $\mathbf{A}^T\mathbf{F}\mathbf{A}$. The condition number is the ratio of the smallest and the biggest eigenvalues of the system. The smaller the condition number, the faster the convergence. In the case of POLARBEAR, the condition number for each blocks (pixels) of $\mathbf{A}^T\mathbf{F}\mathbf{A}$ can be huge, especially for pixels which haven't been observed well. So we use a technique

[13] Except that the low-pass filter is not used.

to "precondition" the system before solving it. The idea is rather to solve Eq. 8.24, we solve for

$$\mathbf{P}^{-1}\mathbf{A}^T\mathbf{F}\mathbf{A}\hat{\mathbf{s}} = \mathbf{P}^{-1}\mathbf{A}^T\mathbf{F}\mathbf{d}, \tag{8.25}$$

were $\mathbf{P}$ is a symmetric, positive-definite matrix that approximates $\mathbf{A}^T\mathbf{F}\mathbf{A}$, but is easier to invert. In the case of the PCG mapmaker, we choose $\mathbf{P}$ to be the diagonal of $\mathbf{A}^t\mathbf{N}^{-1}\mathbf{A}$, that is a block diagonal matrix with each block being a full sub-matrix of size [3x3] corresponding to a sky pixel. In principle, the matrix $\mathbf{P}^{-1}\mathbf{A}^T\mathbf{F}\mathbf{A}$ has a smaller condition number than $\mathbf{A}^T\mathbf{F}\mathbf{A}$, and so the convergence is better (*Preconditioned* Conjugate Gradient). In the pipeline, we chose to put a threshold on the condition number equal to 10^3, to avoid to include highly degenerate pixels. We also carefully discard those data from the time domain for consistency.

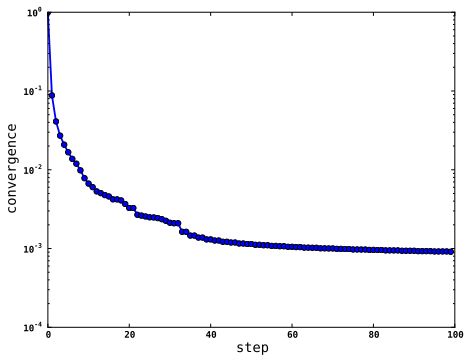

Figure 8.7: Typical trend for the convergence of the PCG for one day of data processed. There is a quick decrease of the convergence in the first steps (<40), and then the convergence reaches a plateau. This plateau is a consequence of long modes which are badly conditioned. In most of the case, the plateau is not overcame, even with few hundreds of steps. Each step takes from few seconds to few minutes, depending on the volume of data to process per day.

Convergence criterion In principle, the PCG method guarantees to reach the solution with numerical precision in a finite number of steps. Unfortunately, due to roundoff errors and very badly conditioned modes, the convergence always reaches a plateau. We define the convergence at step k to be the ratio between the residual at step k and the RHS $\mathbf{b}$:

$$n_k = \frac{|\mathbf{r}_k|}{|\mathbf{b}|}. \tag{8.26}$$

With this definition, the convergence is equal to one at the zeroth step and it decreases as the number of steps increase. Such a convergence for a typical day is shown in Fig. 8.7. We usually reach a convergence of $\mathcal{O}(10^{-3})$, with best performances

around $\mathcal{O}(10^{-4})$. We put a minimum convergence of 10^{-6}, but it is never reached in practice, and we stop the PCG after typically 100 iterations. The behavior of the convergence can be tuned via the parameter β used to update the conjugate direction (see the detail of the algorithm in Appendix A). There exists several form for this parameter in the literature, and we tried different ones. However, we found that in our specific case, there was no improvement to choose one or the other, and we implement the rather standard Polak-Ribière formula [Polak & Ribière 1969]. While in principle the residual cannot grow up, it does sometimes in practice due to numerical precision. To prevent the behavior to start to be meaningless, we implement a *restart* of the algorithm if such a case happens. Typically, this happens when the convergence is in the plateau, and the PCG experiences the nearly singular modes of $\mathbf{A}^T\mathbf{F}\mathbf{A}$. The filtering step also introduce spurious pixel-pixel correlations, and the influence of the filtering for the convergence is detailed in Sec. 8.4.

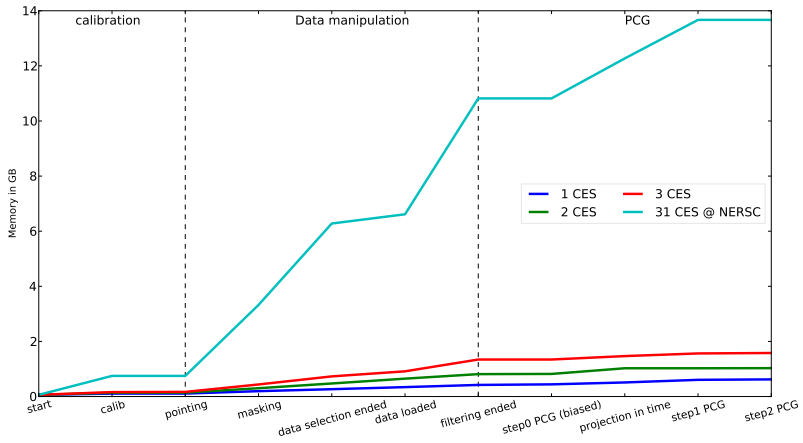

Figure 8.8: Total memory used by one MPI task as the function of the different actions of the PCG mapmaker for the first season data using the first method (see text). The case with 1 CES (blue) stopping at the step 0 of the PCG would roughly correspond to the primary mapmaker. We emphasize the case with 31 CES processed at once (cyan) which is a typical day. We split up the functioning in three categories: calibration, data manipulation and PCG. We stop the x-axis at 2 steps, because the memory remains the same for the steps after.

Memory We process all the data for one day at once. The processing of the data means to store in the memory the timestreams data, but also the pointing of the observations, the masks of the timestreams (to flag bad samples), the noise weights, and the calibration products. We easily reach tens of GB for most of the days as shown in Fig. 8.8. In order to manage such a big amount of memory, we designed two modes of functioning. The first mode is to use the memory of several cores at once. In the supercomputer (Edison machine), approximately 61 GB of memory can

be allocated from within an MPI program using a full node (24 cores). Therefore we use less MPI tasks per node in order to increase the memory available for each task (typically 2-4 cores/node). The drawback of this method is that we have to allocate the full node regardless of how many cores we actually use, and so this is somehow a decrease of "efficiency". The second mode of functioning is still to process the data of each day at once, but inside each task the processing is done wafer-by-wafer, meaning $1/7^{th}$ of the focal plane at each time. By doing so, we decrease the memory by a factor roughly 7, but we have to perform 7 times the PCG[14]. The cross-linking for each pixel is also a bit reduced, but given the huge redundancy even at the level of a wafer, we did not see a reduction of quality in the final map.

Convergence in the map The convergence can be also checked at the level of the map itself. We can compute the rms amplitude of the correction for each steps, in μK/iteration, that is the change in pixel value between subsequent iterations. We expect that the distribution converges towards a zero mean and zero standard deviation at the end of the PCG run. In practice, we reach almost zero mean but never zero standard deviation, but we checked that the last corrections are sufficiently small. This is shown in Fig. 8.9 for pre-whitened intensity and Stokes Q parameter, for 20, 40, 60, 80 and 99 iterations. The change in pixel value for intensity is still large after 99 iterations, due to the poor convergence of the long modes (the residual in each pixel oscillates a lot), but the distributions for Q and U are quickly stable.

8.3.2 Maps for the first season

Table 8.2: The three POLARBEAR patches.

Patch	Raw area	Effective area	White noise level
RA23	46 deg^2	8.6 deg^2	8.3 μK.arcmin
RA12	45 deg^2	9.0 deg^2	12.6 μK.arcmin
LST	42 deg^2	7.2 deg^2	11.0 μK.arcmin

Note. — The raw area is computed by using the same weight to all observed pixels, and zero otherwise. The computation of the effective area includes the effect of the scanning strategy, which makes the core pixels more observed than the ones at the edge. The values for the effective area are slightly different than those reported in Tab. 5.1 based on the maps from the primary mapmaker (biased maps). The differences mainly come from the masks used and the assumptions used to compute them.

Unfortunately at the moment of writing those lines, the maps of the second

[14]Note that the PCG scales linearly with time samples, and in principle we do not loose much in terms of real time. In practice, we observe an increase of time of 20% with respect to the previous method.

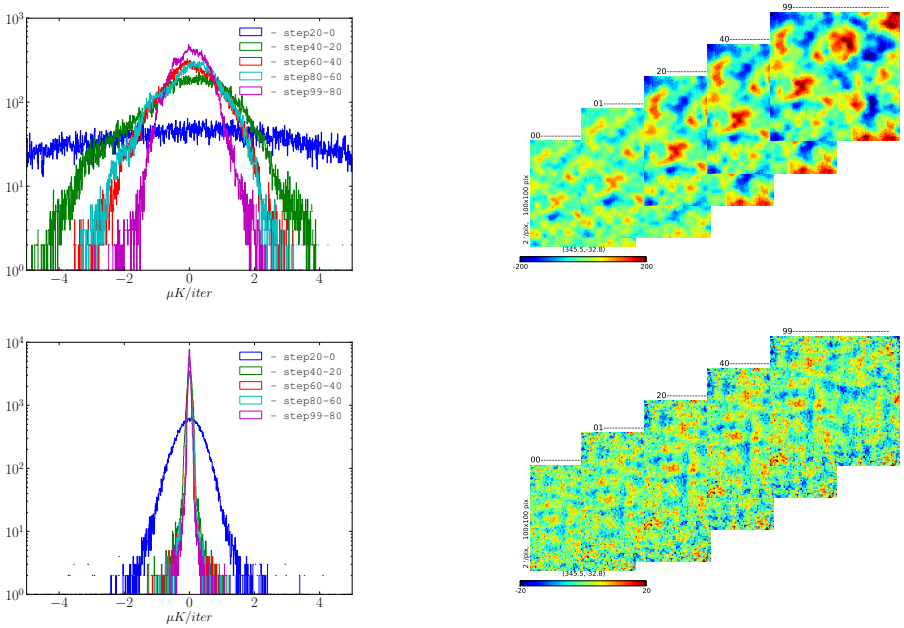

Figure 8.9: Change in pixel value between subsequent iterations for the full intensity map (top left panel) and the full Stokes Q map (bottom left panel). The change are shown for 20, 40, 60, 80 and 99 iterations of the PCG. After roughly 50 iterations, most of the pixels which are still converging are located at the edge of the map (not well seen so badly conditioned). The convergence is also slowed down due to pixel-pixel correlations not properly accounted for. Each map contains roughly $\mathcal{O}(10^4)$ sky pixels. We also show the evolution of the core of the intensity map (top right panel) and Stokes Q map (bottom right panel) for one of the sky patch for 0, 1, 20, 40 and 99 iterations.

season are not yet published. Therefore, I'm only presenting the results concerning the first season. In addition, we only focus on the maps from the PCG mapmaker (unbiased maps). Q and U maps from the primary mapmaker (biased maps) can be found in [POLARBEAR Collaboration 2014c]. The full season co-added maps from the PCG mapmaker of the three sky patches are shown in Fig. 8.10 and 8.10. The approximate raw sky coverage are 46 deg^2, 45 deg^2, and 42 deg^2 for RA23, RA12, and LST respectively. We have a well observed core of about $3° \times 3°$, where we can see the structures from the CMB. Given the relative small size of the sky patches, we see only sub-degree structures. The "griddy" structures for Q and U maps are clearly detected, although the level of noise is still high. At the edges, which are less observed, the noise level is increasing very fast, and we can see long modes (mainly residual from atmosphere). The different characteristics of the patches are summarized in the Tab. 8.2.

We also have point sources clearly detected in intensity within the maps as shown in Fig. 8.12 for LST (the same point sources used for the pointing and

beam calibration, see Sec. 6.3 & 6.6). Those point sources have often a counter part in the PLANCK intensity map at 143 GHz (data from the 2015 release). RA23 and RA12 do not have currently polarized counterparts to point sources detected in intensity. The locations of sources make it also more difficult to identify the polarized counterpart (often close to the edge in the noisy regions). In the LST sky patch, we identified one mildly polarized signal at the location of source detected in intensity. This source (first column in Fig. 8.12) shows a clear spot in the U Stokes parameter, but the Q Stokes doesn't have a clear counter part. This polarized source has been identified by the Australia Telescope 20-GHz (AT20G J043900-452222), in which they report a polarization fraction of 6-8% and a polarization angle from 0-10°. Other catalogs such as the Bright Extra-Galactic AT20G Sources Polarizations Catalog (at20gbspol) report polarization fraction around 3%, which is consistent with what we estimate for this source (although we do not have yet done a clear analysis). For precaution, we apply the same mask of point sources in temperature and in polarization (for the filtering and the power-spectrum estimation).

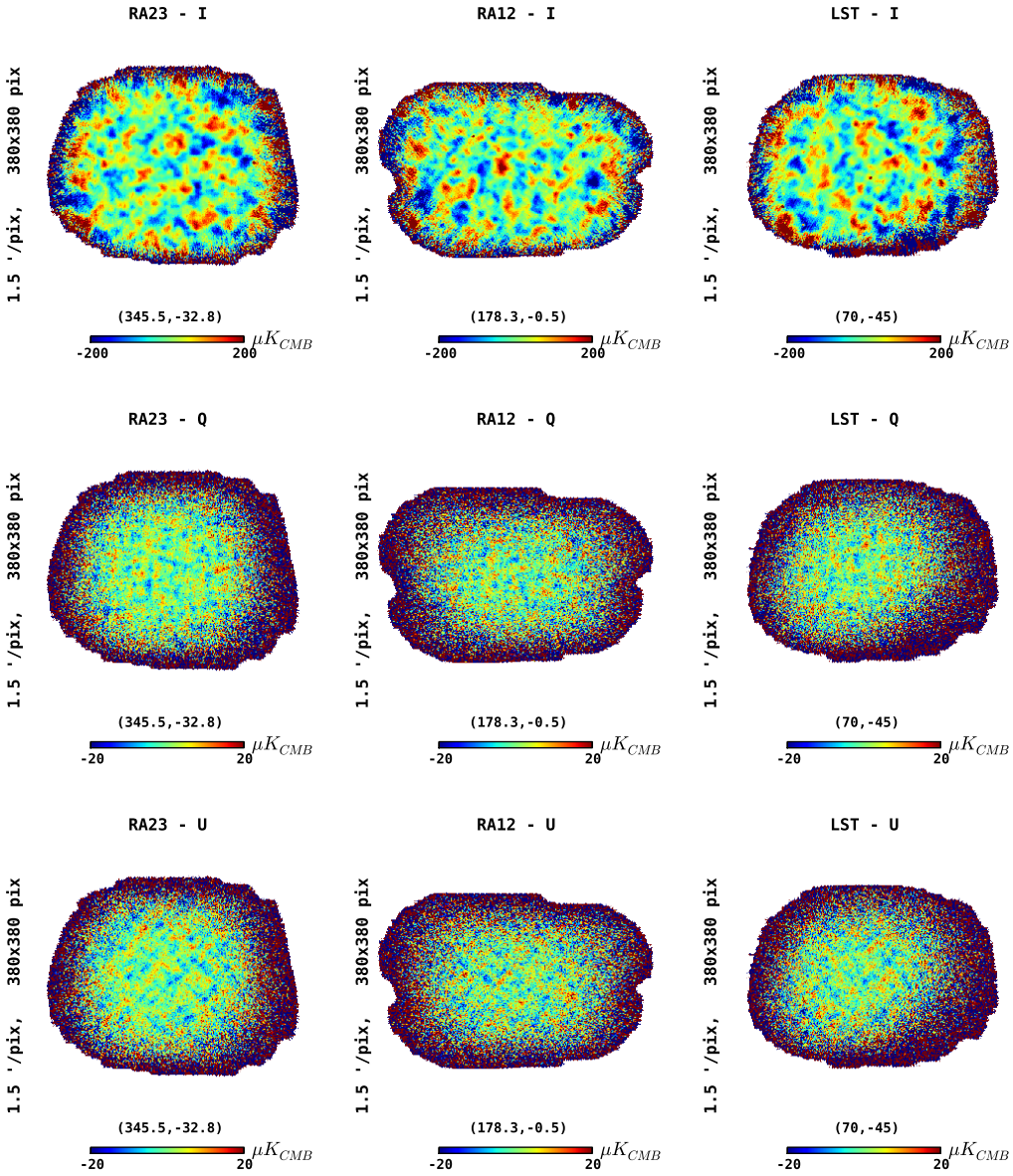

Figure 8.10: First season POLARBEAR maps from the PCG mapmaker. Each column corresponds to one sky patch: RA23, RA12, and LST. Each row correspond to a Stokes parameter: I, Q, and U.

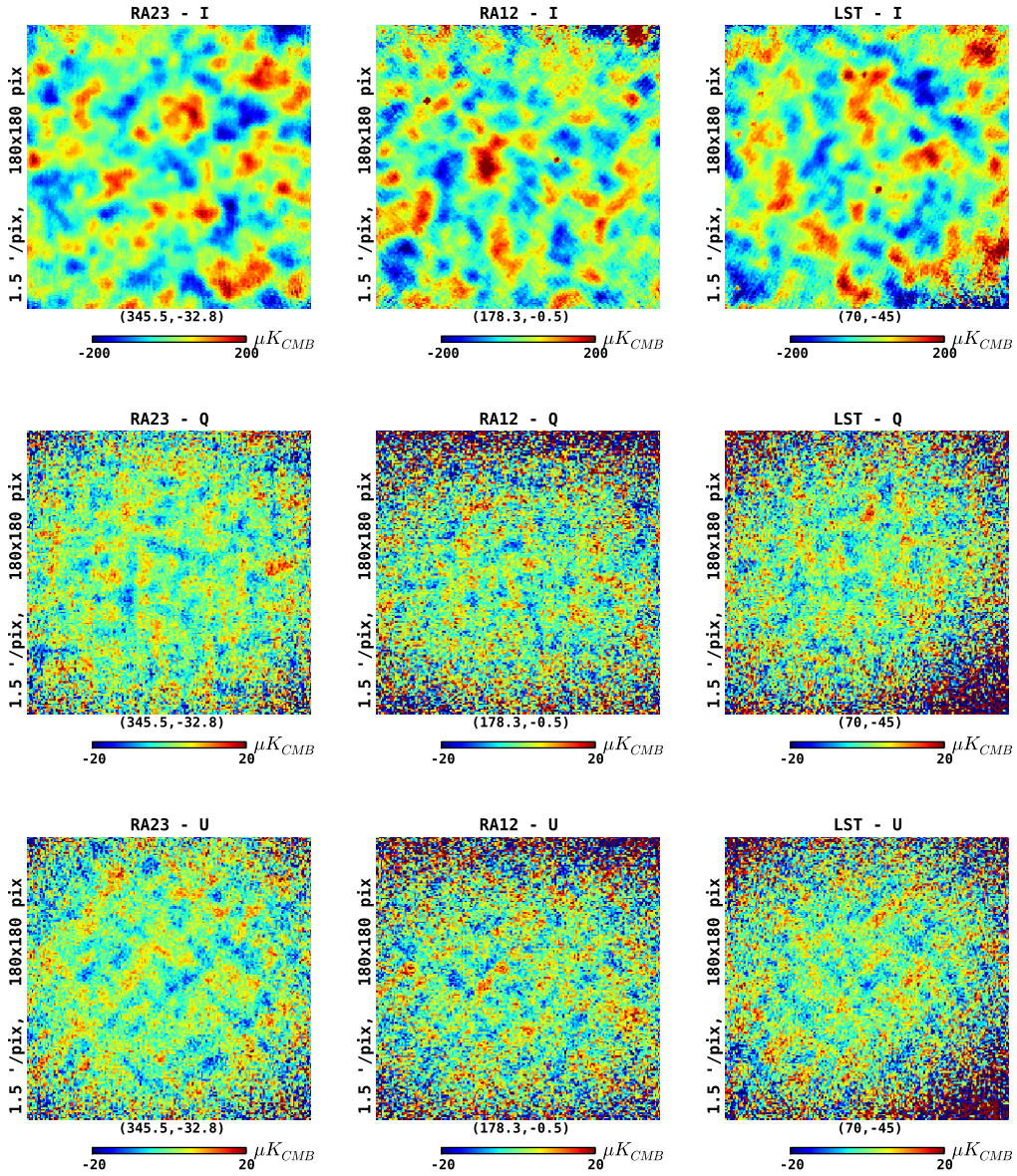

Figure 8.11: Similar plot as in Fig. 8.10, but we apply a zoom over the center region ($4.5° \times 4.5°$) of the first season POLARBEAR maps from the PCG mapmaker.

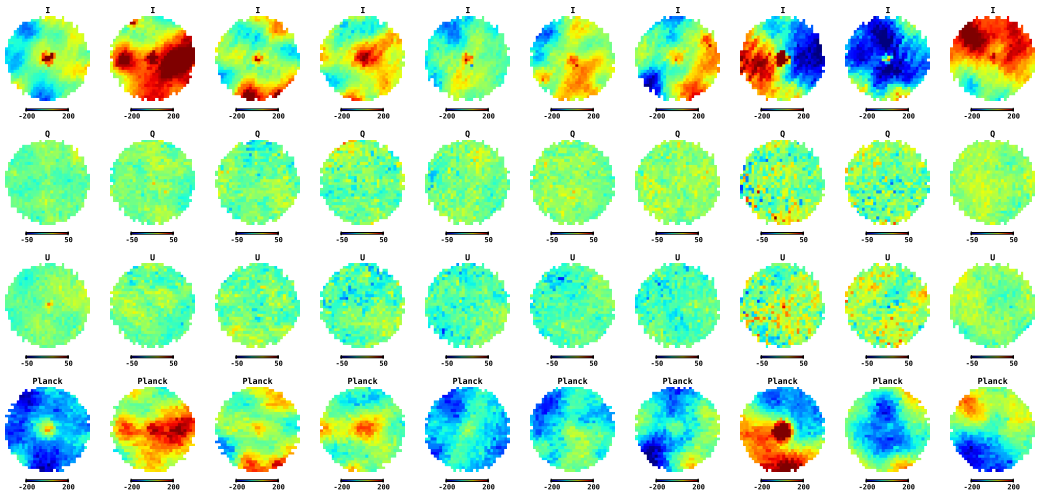

Figure 8.12: Zoom over the 10 identified point sources in intensity in the LST patch (each circle has a diameter of 45 arcminutes). Few of them seem to have a counter part in polarization (second and third row), but for precaution, we apply the same point source mask in intensity and in polarization. The last row shows the same region of the sky in intensity seen by the satellite Planck (2015 release) at 143 GHz.

8.3.3 Noise properties

We want to check the noise properties of our maps, and eventually compare to the white noise case described in Sec. 8.2.2. Let Q_0, Q_1 and U_0, U_1 be subsets of the Q and U coadded maps of the full season such that

$$Q_0 + Q_1 = Q \tag{8.27}$$
$$U_0 + U_1 = U. \tag{8.28}$$

Let Q_n and U_n be estimates of the noise of the Q and U maps from *jackknives*, meaning:

$$\frac{Q_0 - Q_1}{2} = Q_n \tag{8.29}$$
$$\frac{U_0 - U_1}{2} = U_n \tag{8.30}$$

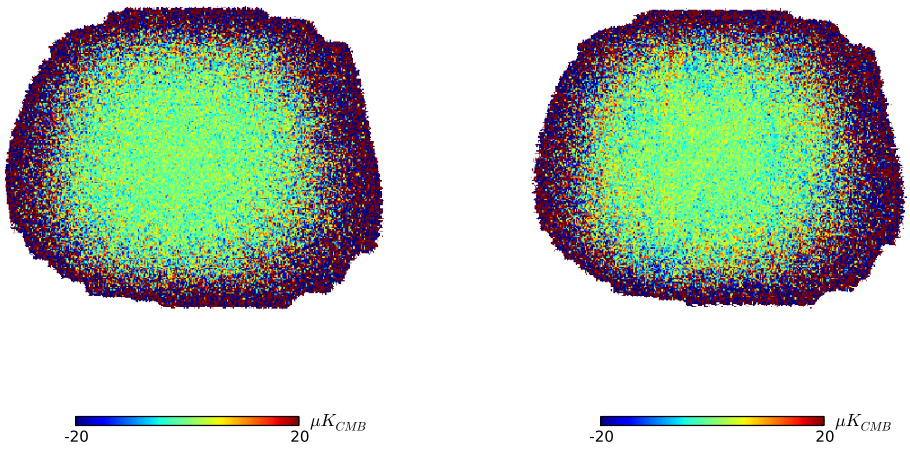

Figure 8.13: Simulated white noise maps N_Q based on one of our sky patch (left) and estimate of the Stokes Q noise, Q_n, in the same patch (right). The estimate of the noise is done by performing a jackknife map from two halves of the first season. Both contains an inhomogeneous distribution of the noise, arising from the scanning strategy of POLARBEAR. The real data map has a small amount of long modes and stripes which arise from a combination of atmospheric fluctuation residual, and incomplete convergence of the PCG due to nearly singular modes of the pixel-pixel covariance matrix (mostly due to filtering). Maps contain about 55,000 pixels, with roughly 1.7' pixel size.

In the ideal case, Q_n and U_n are (inhomogeneous) white noise maps, as described previously. However the reality is more complex. Due to residuals from atmosphere fluctuations, and incomplete convergence of the PCG due to nearly singular modes (mostly due to filtering), the noise maps contain some level of pixel-pixel correlations, as shown in Fig. 8.13. In both maps in this figure, we can see the inhomogeneity of the noise, typical from our scanning strategy, but only the real data exhibit (small!) correlations between pixels. If we would like to describe the properties of the noise maps for real data, we would need a huge multi-dimensional probability distributions, with the number of dimensions equal to the number of pixels in the map considered. So a simple histogram of the pixel values is likely to display significant deviations from the 1-dimensional Gaussian distribution even for the truly Gaussian case [Stompor *et al.* 2001]. Instead, to look at noise properties of the maps, we want to compute $\tilde{Q}_n$ and $\tilde{U}_n$ for a given sky pixel p given by

$$\begin{pmatrix} \tilde{Q}_n \\ \tilde{U}_n \end{pmatrix}_p = \mathbf{M}_p^{-1/2} \begin{pmatrix} Q_n \\ U_n \end{pmatrix}_p , \tag{8.31}$$

where the matrix $\mathbf{M}_p^{-1} = (\mathbf{A}^T \mathbf{N}^{-1} \mathbf{A})_p$ is the inverse covariance matrix (defined in Eq. 8.20) and $\mathbf{M}_p^{-1/2}$ is obtained by performing a Cholesky decomposition[15]. This corresponds to a pre-whitening of the maps, that is a decorrelation of the measurements in the different pixels. Because Q_n and U_n are computed from jackknives, we need to know the combined covariance matrix, given by the individual covariance

[15] Performing one Cholesky decomposition for one sky pixel is fast, but we have $\mathcal{O}(10^4)$ sky pixels for each map. In order to test the method, or to have a quick view on the noise properties, without performing Cholesky decomposition, we could also work with a simplified method. Re-writing the inverse covariance matrix as

$$M_{01}^{-1} = 4 \left[\sum_{i=(0,1)} \begin{pmatrix} a_{00} & a_{01} \\ a_{10} & a_{11} \end{pmatrix}_i^{-1} \right]^{-1} , \tag{8.32}$$

we find the eigenvalues

$$\lambda_{01}^{\pm} = \mathrm{Tr} M_{01}^{-1} \left(\frac{1 \pm \sqrt{1 - 4 \det M_{01}^{-1}}}{2} \right) . \tag{8.33}$$

Then we construct our inverse coupling matrix $\tilde{M}_{01}^{-1}$ for a given pixel by choosing the smallest eigenvalue so that

$$\tilde{M}_{01}^{-1} = \begin{pmatrix} \lambda_{01}^{-} & 0 \\ 0 & \lambda_{01}^{-} \end{pmatrix} , \tag{8.34}$$

and

$$\begin{pmatrix} \tilde{Q} \\ \tilde{U} \end{pmatrix} = \begin{pmatrix} \sqrt{\lambda_{01}^{-}} & 0 \\ 0 & \sqrt{\lambda_{01}^{-}} \end{pmatrix} \begin{pmatrix} Q_n \\ U_n \end{pmatrix} . \tag{8.35}$$

In practice, we found this simplification to give almost the same results as the Cholesky decomposition, because the cross-term a_{10} is very small compared to the diagonal coefficients in most of the case.

matrices of the half maps 0 and 1 as

$$\mathbf{M}_{p,01} = \frac{\mathbf{M}_{p,0} + \mathbf{M}_{p,1}}{4} = \frac{1}{4}\left((\mathbf{A}^T\mathbf{N}^{-1}\mathbf{A})^{-1}_{p,0} + (\mathbf{A}^T\mathbf{N}^{-1}\mathbf{A})^{-1}_{p,1}\right), \tag{8.36}$$

If we estimate correctly the noise correlations, then the components of $\tilde{Q}_n$ and $\tilde{U}_n$ are uncorrelated and their variances are equal to one. In addition, if the noise in the pixel domain is Gaussian then each of the components of $\tilde{Q}_n$ and $\tilde{U}_n$ is randomly drawn from the Gaussian distribution in one dimension with the unit variance. Therefore, by pre-whitening the noise, we reduce our multi-dimensional problem to a one-dimensional one, easier to test. However, if the noise is somehow badly modeled (pixel-pixel correlations), we should start to see deviations to the Gaussian distribution. The results for the first season POLARBEAR maps are shown in Fig. 8.14. We are in good agreement with the Gaussian distribution with unit variance (variance is roughly 1.06 in both cases, for maps with 55,000 pixels). The results to the one-dimensional Kolmogorov-Smirnov test are quite good with a significance of 7.6% and 43% for $\tilde{Q}_n$ and $\tilde{U}_n$ respectively. However, we have very small departures from the Gaussian case in the tails (not shown here). The latter points towards a refining of our model for the noise, by including properly pixel-pixel correlations. We will see later that those long modes are mostly outside our science band ($\ell = 500 - 2100$), and most of the scales of interest are on good agreement with the white noise assumption.

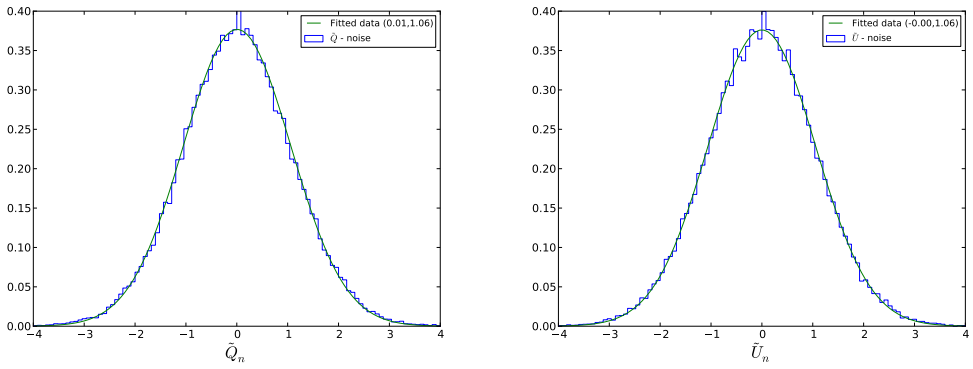

Figure 8.14: Probability distribution functions of the pixel amplitudes for the prewhiten noise maps $\tilde{Q}_n$ (left) and $\tilde{U}_n$ (right) computed as a difference of two maps made from two halves of the first season. Histograms show the results for the real data and smooth green curves the Gaussian curves fitted to best match the actual results. The results compatible from the Gaussian distribution with unit variance, as both probability distribution functions give a variance of the order 1,06 (55,000 pixels). The results to the one-dimensional Kolmogorov-Smirnov test are quite good with a significance of 7.6% and 43% for $\tilde{Q}_n$ and $\tilde{U}_n$ respectively.

8.3.4 Extension of the mapmaker: IGQU model

In order to have a better control of the unwanted scan-synchronous signals in the polarized timestreams (difference of the two bolometers within a pair p), we use a slightly different version data model as the one presented in Eq. 8.1. Let's model $d_{/\!//\perp}$ the two orthogonal timestream data inside a pair as

$$d_{/\!//\perp}(t) = I(t) \pm G(t) \pm Q(t)\cos 2\Theta(t) \pm U(t)\sin 2\Theta(t) + n_{/\!//\perp}(t), \tag{8.37}$$

where G is a map which contains contributions from the polarized timestreams (G vanishes if we sum the timestreams) which are not modulated by the polarization angle Θ (any intensity to polarization leakage for instance)[16]. In the presence of G, the pointing matrix is modified (4 non-zero components entries for each row corresponding to time t), and the pixel inverse covariance matrix in Eq. 8.14 is extended as

$$(\mathbf{A}^T\mathbf{N}^{-1}\mathbf{A})_p = \sum_{t\in p} \begin{pmatrix} \sigma_+^{-2}(t) & 0 & 0 & 0 \\ 0 & \sigma_+^{-2}(t) & \sigma_-^{-2}(t)\cos 2\Theta(t) & \sigma_-^{-2}(t)\sin 2\Theta(t) \\ 0 & \sigma_-^{-2}(t)\cos 2\Theta(t) & \sigma_-^{-2}(t)\cos^2 2\Theta(t) & \sigma_-^{-2}(t)\cos 2\Theta(t)\sin 2\Theta(t) \\ 0 & \sigma_-^{-2}(t)\sin 2\Theta(t) & \sigma_-^{-2}(t)\cos 2\Theta(t)\sin 2\Theta(t) & \sigma_-^{-2}(t)\sin^2 2\Theta(t) \end{pmatrix}_p, \tag{8.38}$$

where the lower [3x3] full block is the polarized part, including G, Q, and U. The preconditioner is also updated accordingly. Correlation of G maps with temperature maps can be used to estimate differential gain leakage or put upper limits on it. No power is detected in any of the TG cross-spectra; the measured leakage value for each pixel type on each wafer is consistent with zero (within the noise). All the maps in this manuscript have been computed using the IGQU model of the data.

8.4 A more detailed study of the filtering and the PCG

We filter the map to remove slow drifts in each telescope scan, and scan-synchronous signals which could contaminate our data (see Sec. 8.1.4 and 8.2.3). All filters have a specific effect on the data, but they also interact between each other. As an example, the effect of the ground template and the effect of the polynomials filtering are not independent if the filters are not orthogonal[17]. On overall, the combinatory between filters is not very big, but it is not straightforward to have a good intuition on the interactions.

[16] Despite the same name, this G has nothing to do with the ground template defined earlier.

[17] Unfortunately, we do not have yet orthogonalized the filters. This is still under study at the moment that I write those lines. We believe that the orthogonalization of filters will bring better results for the convergence of the PCG, and the quality of the results in general.

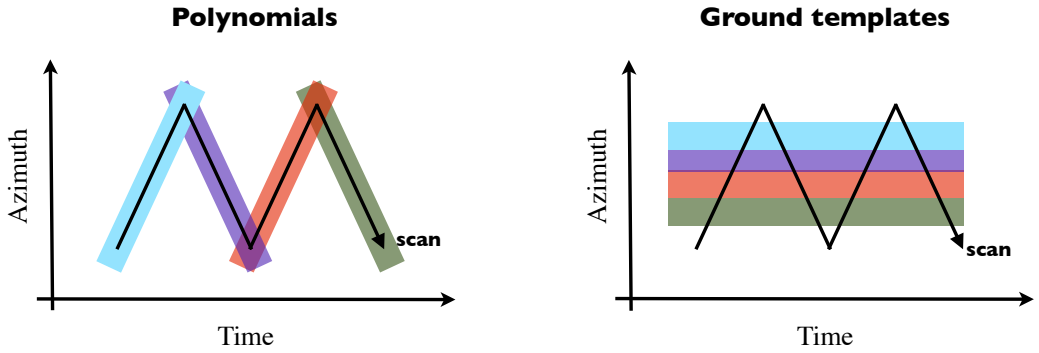

Figure 8.15: Schematic view of the filters. The polynomials filtering is done subscan-by-subscan, that is following the path of the scan, while the ground templates are built at constant azimuths. In the mapmaking, we first subtract the polynomials filters and then we estimate and subtract the ground templates.

The filtering is not performed on the entire timestreams. First of all, the timestreams are not continuous. During scans, packet drops or failures happen. Then, we also cut data which are found to be of not sufficient quality based on our data selection. Those cuts are based on the data quality, which means that the structure of each timestream is different depending on how much data the cuts remove. Finally, we mask the point sources in the timestreams during the filtering, to avoid a leakage of power. This last point is maybe true in the case of the temperature, but can be questioned for the case of the polarized timestreams[18].

8.4.1 Ground template

We would like to build an estimate of the ground signal and remove it from the timestreams. Let's consider a Constant Elevation Scan (CES). During this CES we scan back and forth in azimuth while the CMB field moves across the sky. There are about 15 minutes between the time when a given sky pixel is first scanned to when it is last scanned. In the meantime the sky rotated by $\sim 4°$. By making the hypothesis that the ground signal remains constant over the time of a CES, it is therefore possible to separate the signal on the sky which moves around from the signal from the ground which doesn't, over scales smaller than $\sim 4°$. Within this subset of data, the elevation is constant and so the ground signal estimates or ground templates are constructed as a function of azimuth only. For a CES i, and for a channel j in that CES, we model our timestream data as following:

$$d_{j\in i}(t) = s_{j\in i}(p(t)) + g_{j\in i}(\alpha(t)) + n_{j\in i}(t). \tag{8.39}$$

[18] As far as we know, there is no evidence (or few) in the POLARBEAR patches of strong polarized sources.

$d_{j\in i}(t)$ is the timestream for the channel j in the CES i at the time t. $s_{j\in i}(p(t))$ is the sky signal in the direction $p(t) = (\theta(t), \phi(t))$ on the sky for the channel j in the CES i, and $\mathrm{n}_{j\in i}(t)$ is the noise component [19] for the channel j in the CES i at the time t. Finally $g_{j\in i}(\alpha(t))$ is the ground signal as a function of azimuth $\alpha(t)$ for the channel j in the CES i. For more clarity, we drop the indices and just write the multi-detector multi-observations system as

$$\mathbf{d} = \mathbf{A}\mathbf{s} + \mathbf{G}\mathbf{g} + \mathbf{n}, \tag{8.40}$$

where $\mathbf{A}$ and $\mathbf{G}$ are the pointing matrices for the sky signal and the ground signal respectively. To build the ground templates, we have to remap the time within a CES into the corresponding azimuth[20]. To do so, we have to choose a resolution for the ground signal map. By default we use a ground pixel size $\Delta\alpha$ in azimuth of 0.08° (for comparison, we project the timestream data into maps with a pixel size of approximately 0.028°.). To construct the templates of the ground we simply bin the timestream data in azimuth. For each bolometer and each ground pixel, an estimate of the ground signal is computed as

$$\hat{g}(\alpha) = \frac{1}{\sum_{t\in\Delta\alpha} W(t)} \sum_{t\in\Delta\alpha} d(t), \tag{8.41}$$

where the sum is over all data of a channel in a CES which fall in the azimuth range $\Delta\alpha$. $W(t)$ is the mask applied to the timestream data for the filtering, equal to 1 if the sample is good, 0 otherwise. Given that the size of a subscan (time between two turnarounds, which spans the full range of azimuth) is typically $\mathcal{O}(10^2)$ time samples, the choice of the ground pixel size matters. Too small ground pixel sizes lead to spurious effects during the averaging of the timestreams. On the other hand, a too big ground pixel size is not enough sensitive to the ground variation, and the timestreams will not be correctly cleaned. Fortunately there is a large range of pixel sizes for which the ground maps are equivalent, meaning that the ground signal varies quite smoothly on azimuth. I show in Fig. 8.17 the map of ground signal for different ground pixel sizes.

The constructed ground templates also contain sky signal and noise. The expectation value of the constructed templates is given by:

$$< \hat{g}(\alpha) >= g(\alpha) + \frac{1}{\sum_{t\in\Delta\alpha} W(t)} \Big[\sum_{t\in\Delta\alpha} s(p(t)) + \sum_{t\in\Delta\alpha} n(t) \Big] \tag{8.42}$$

In the limit of highly redundant scan strategy, the term which contains the CMB signal averages to the monopole (total intensity) or zero (polarization). The term of noise averages to zero only in the case of uncorrelated noise. In the case of a realistic scan strategy POLARBEAR these terms are unfortunately non zero, and large scales

[19] In [Brown *et al.* 2009b] they split the noise component into a random part and a correlated part (atmosphere fluctuations). Here, both are in the noise component as we assume that the correlated component has been removed by the polynomials filtering.

[20] Ground templates are built independently for each bolometer.

(CMB and noise) are filtered out when we subtract the ground templates to the timestream data. Finally we construct the timestream data which are (in principle) free of ground signal from the original timestream data as:

$$\mathbf{d}^{\text{clean}} = \mathbf{d} - \mathbf{G}\hat{\mathbf{g}}. \tag{8.43}$$

To give an order of magnitude, for a given CES with somewhat regular cuts, the number of time samples is $\mathcal{O}(10^4)$, the number of ground pixels is $\mathcal{O}(10^2)$ and the number of channels is $\mathcal{O}(10^2)$. The algorithm can be slightly modified to separate left and right going subscans to form two distinct ground templates[21].

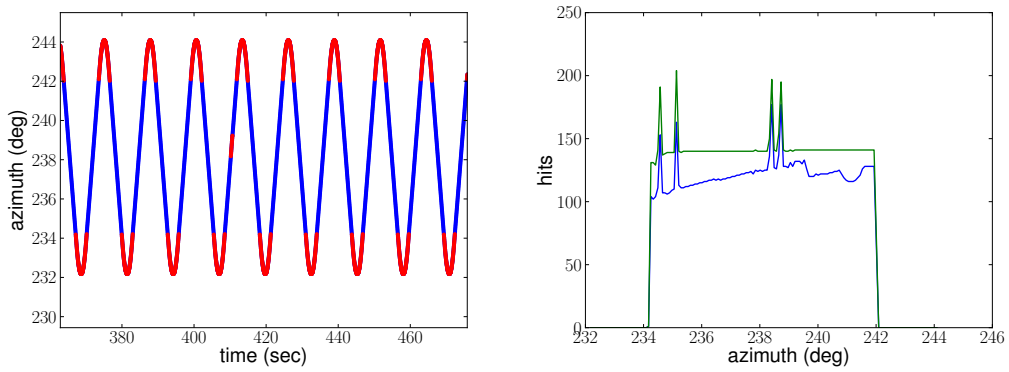

Figure 8.16: *Left*: Azimuth as a function of the time for one CES (the elevation is 69.6°) and for one channel. The range of azimuth is fairly constant over the entire CES (only a fraction of the CES is shown here). The regions in red are the masked regions not used to compute the ground template. They concern mainly data in turnarounds, but one can also see a subscan completely masked because the data were not good ($t \sim 410$ seconds). *Right*: Number of hits each 0.08° azimuth bin received for two particular channels (blue and green). One can see that the number of hits is not the same, and there are spikes which may denote the fact that the size of the pixels for the ground template is not correctly set.

As seen in Eq. 8.42, the ground template subtraction removes part of the CMB signal. Ignoring the ground signal and the noise, one can re-write Eq. 8.42 as:

$$< \hat{g}^{CMB}(\alpha) >= \frac{1}{\sum_{t\in\Delta\alpha} W(t)} \sum_{t\in\Delta\alpha} s(p(t)). \tag{8.44}$$

We know that we should lose some large scales, due to the fact that given the length of observation for a CES, we can only separate scales smaller than $\sim 4°$. Bigger scales are stationary over the time of observation, and are completely degenerated with a ground-like signal. In order to quantify the loss, we scan an input map

[21] In fact, we already used this distinction to process the data of the first and the second releases. This allows to separate specific behaviors specific to only right or only left going scans (vibrations mainly).

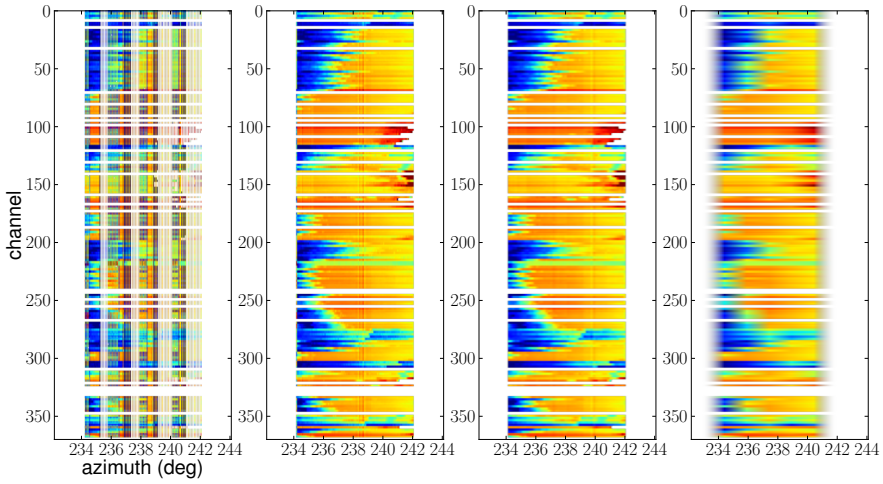

Figure 8.17: Ground signal level per detector for one CES as a function of azimuth for different ground pixel sizes: $\Delta\alpha = 0.04°$, $0.08°$, $0.16°$ and $1.6°$. If the size of the ground pixel is too small, we see vertical stripes due to a bad averaging of the timestreams. For too big pixel size, we can clearly see a smoothing of the structures. White rows are discarded bolometers (data quality). In this figure, the azimuth is between 234° and 242° and elevation at 69.6°.

which contains only a CMB component, and applying only the ground template subtraction (not the polynomials removal). After 100 iterations of the PCG, we look at the output map, and we compare it to the input map (residual=output-input). In Fig. 8.19, we show the residual maps after 100 iterations for all Stokes parameters using the pointing information from an entire day (29 CES). On all residuals for all Stokes parameters by using only the ground template (third row), we can see horizontal stripes, due to the fact that modes that are constant in the direction of sky motion (RA) are by design in the null space of the scan-synchronous signal filter, and therefore can not be solved for by the mapmaker. For the mapmaking, the ground template removal is done on the level of a CES, so even if we come back several time on the same pixel, it is always at the same elevation. Projected on the sky, the ground template bins are at constant declination. One interesting fact is that the residual in the case of the Q Stokes parameter is always bigger with more stripes than the residual in the case of the U Stokes parameter. This could be directly linked to the fact that Q presents structures parallel to the RA axis.

8.4.2 Effects in the map and convergence

We have seen that the PCG doesn't converge to numerical precision, that is we do not obtain the exact solution at the end of the run, as shown in the Fig. 8.18. The filters play a major role in the convergence of the PCG, and we need to understand

their effects. Let's first look at the effect of the filters using a set of simulated signal only input maps (I, Q and U). We use the pointing information from an entire day of data for one patch (29 CES), and we look at the residual maps (output-input) after 100 iterations of the PCG. The effect of the filters is shown in Fig. 8.19. The first row shows the output I, Q and U maps if no filters are used[22]. The other rows correspond to the residual maps for a run of the mapmaking with a particular combination of the filters: only polynomials filtering (second row), only ground templates subtraction (third row), and both filters (fourth row). The residuals in the case of polynomials filtering only are made of long modes, mainly "gradient-like" in the case of the polarization. For the intensity, the residual follows more or less the large-scale structures in the patch (with a minus sign coming from the fact that residual=output-input). We can also see stripes following the scans of the patch at the edge of the patch, which correspond to pixels observed only few times (with bad condition numbers). In the case we use only the ground templates, the residuals are seen as horizontal stripes, due to the fact that modes that are constant in the direction of sky motion (RA) are by design in the null space of the scan synchronous signal filter, and therefore can not be solved for by the mapmaker (see previous section). In the case both filters are used, the residuals are a combination of the two previous residuals. We can easily see the long modes from the polynomials modulated by the stripes from the ground templates. Concerning the amplitude of the residuals, there is a factor $\sim$2 for intensity and $\sim$20 for polarization[23]. The fact that the residuals are not zero doesn't necessarily mean that we do things wrongly or we hardly biased our results. It depends on the nature of the residuals. Given the relative small size of our patches ($\sim 3^\circ \times 3^\circ$), we do not have access to all the modes. Our science band covers the range of multipoles between 500 and 2100. We found that the typical scales of the residuals are much lower than a multipole of 500, therefore poorly biasing our science results. We also tried to see whether those problems of convergence could be bypassed by using a different version of the preconditioner, or by solving the mapmaking equation with more data at once to decrease the condition number of the covariance matrix. We found, in a different analysis which goes beyond the scope of this mapmaking section[24], that there are true singular modes of $\mathbf{A}^T\mathbf{F}\mathbf{A}$, meaning no matter what we try, they are always here. In fact, using the default configuration for the mapmaking (including filters and data selection), each map has two singular modes, and several nearly singular modes (null vectors are induced by the cut pixels and filters).

We also show the results of the filters on the real data, in Fig. 8.20 (the same day as in Fig. 8.18 and 8.19). For a short period of time (one day), the maps are dominated by noise, especially correlated noises from atmospheric fluctuations and ground signals, and so we want to probe the effectiveness of the filters to remove them. Without filtering (top panels), the intensity map is completely dominated by

[22] It is worth mentioning that the PCG converges in one step to numerical precision in this case.

[23] recall that we probe here the effect of the filters on the CMB component only, that is the nature of being unbiased and not the efficiency of the filters to remove spurious signals.

[24] and not done by myself.

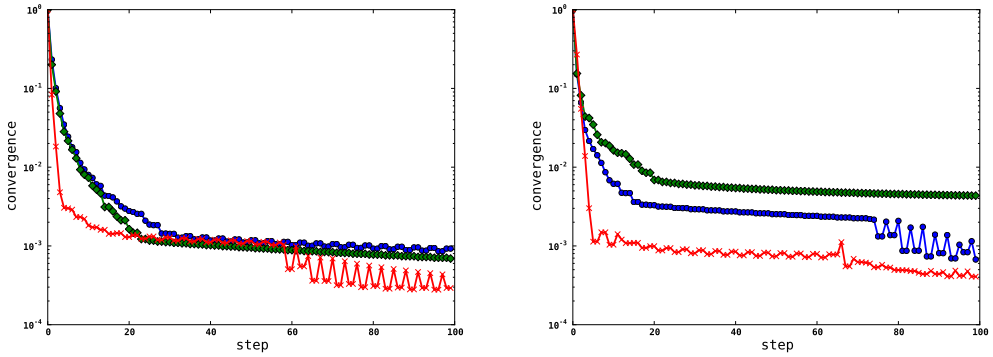

Figure 8.18: Convergence of the PCG by using a simulated input data (CMB only, left) and real data (right) for one day of data (29 CES). In both cases the PCG doesn't converge to numerical precision. In each case, a different combination of filters is used: polynomials filters only (green diamond), ground templates only (red cross), and both filters (blue circle). Although there are some small differences between the different cases, the behavior is always the same: a quick decrease the first tens iterations, and then a plateau. The polynomials filters are the ones which made the convergence of the PCG the slowest.

long modes, and the amplitude is huge ($\mathcal{O}(10^5)$ μK) compared to what we would expect from CMB only ($\mathcal{O}(10^2)$ μK). These long modes are typically arising from atmosphere fluctuations. The Q and U maps are dominated by residuals of atmosphere, one or two orders of magnitude higher than the expected white noise level for such a period of time (one day). It is worth noting that without filters, the PCG converges to numerical precision in one step. If we now try to subtract those long modes, by using polynomials filters (cubic for intensity and linear for polarization), we obtain the panels on the second row. The polynomials filtering works quite well, and for the intensity map we start to see some CMB structures popping out from the noise, especially in the core of the patch where the pixels have been observed the more. The Q and U maps are still strongly contaminated. We have here the typical signature of signals coming from the ground: long modes with a "quadrupolar-like" shape. The maps on the third row are the maps after only ground templates subtraction. Unfortunately, the dominant contribution to the correlated noise being the atmosphere (which is not correlated with the azimuth at different time), the ground templates subtraction alone is not very effective, and we are left with similar maps than int the no filter cases. Finally, with all the filters on (fourth row in the figure), most of the atmosphere fluctuations have been removed, as well as the spurious scan-synchronous signals. The intensity map exhibits clear CMB structures in the core. The Q and U maps still suffer from a small residuals of long modes (which are still here, but dimer, in the final coadded maps, see Fig. 8.13 and 8.10). We are still working on improving the filtering methods in order to remove at best the

signals which could contaminate our data.

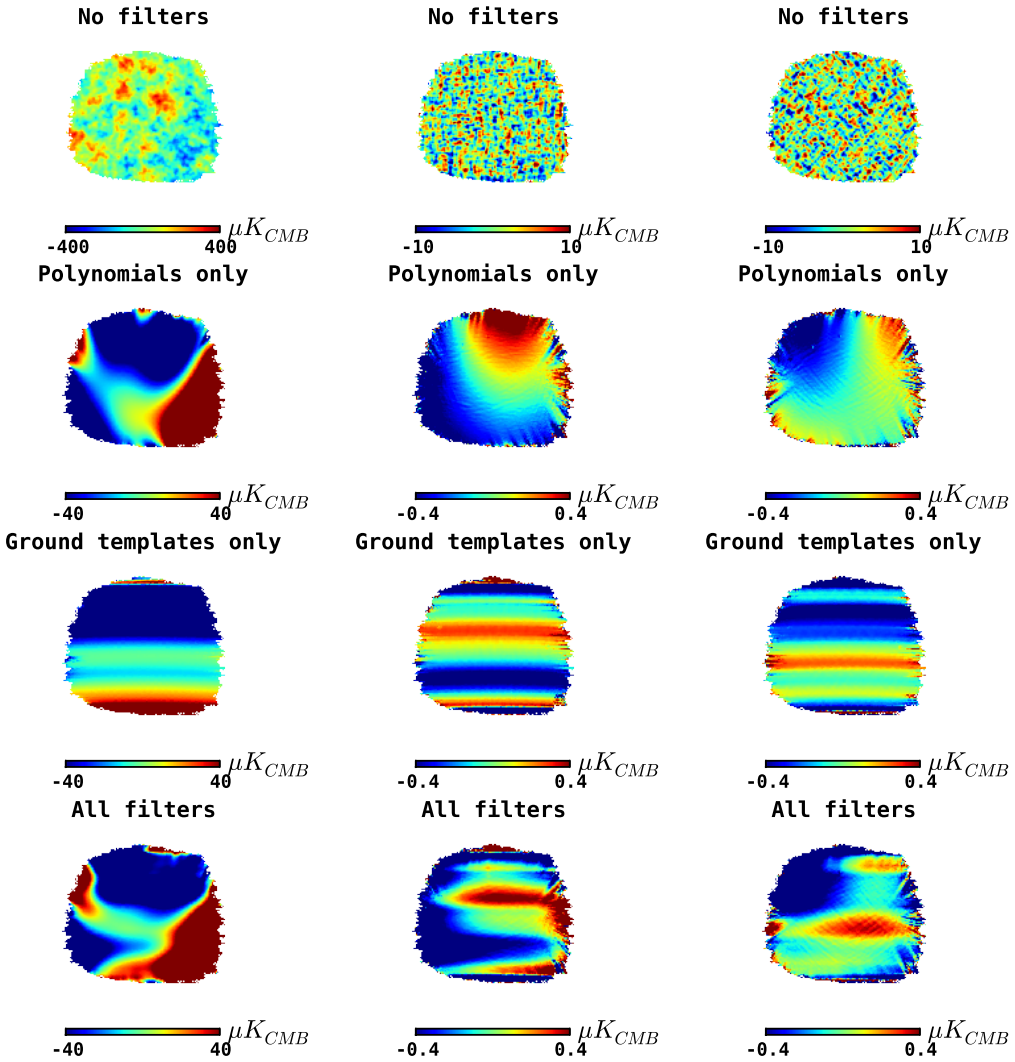

Figure 8.19: Effect of the filters using a set of simulated signal only input maps (I, Q and U) for one day after 100 iterations of the PCG. The first row shows the output I, Q and U maps if no filters are used. The other rows correspond to the residual maps (output-input) for a run of the mapmaking with a particular combination of the filters: only polynomials filtering (second row), only ground templates subtraction (third row), and both filters (fourth row). See text for more explanations.

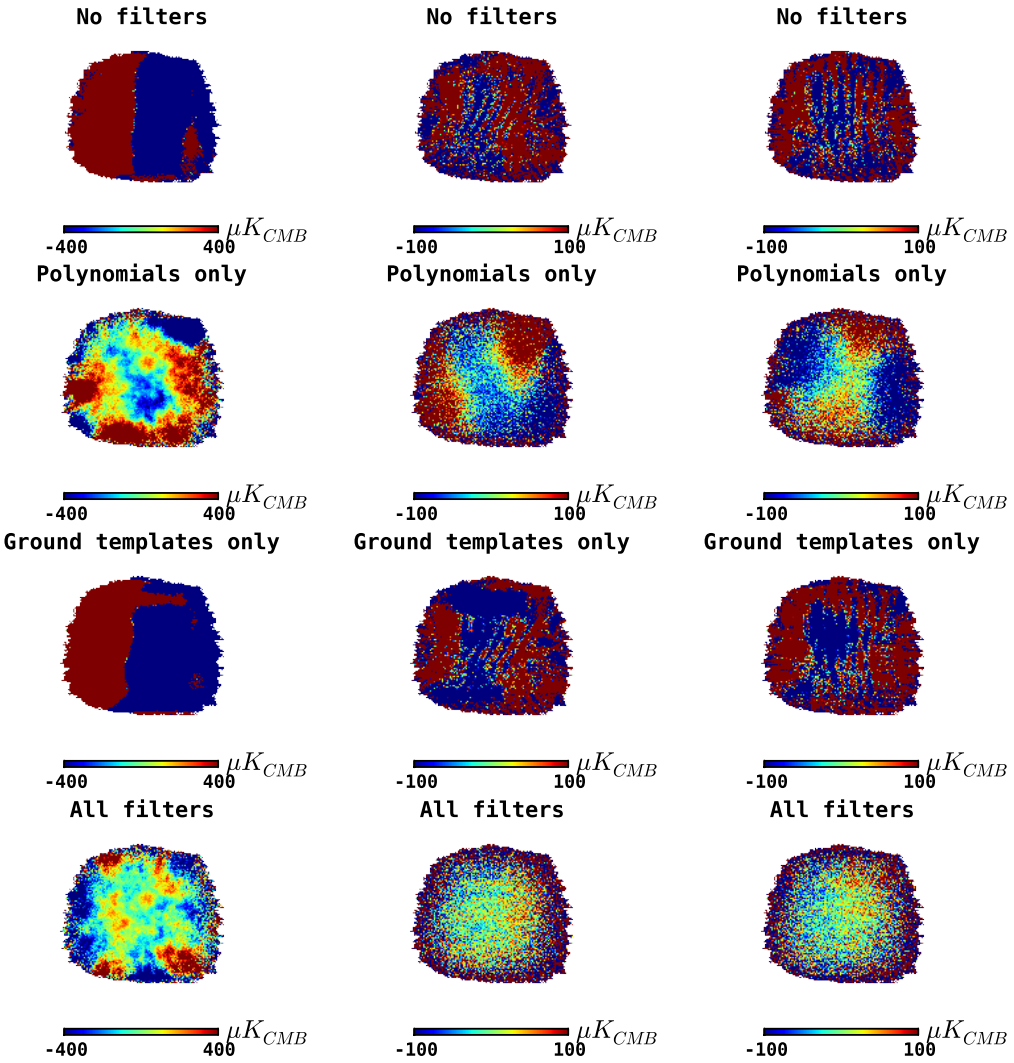

Figure 8.20: Effect of the filters on one day of data (29 CES). We stop the PCG after 100 iterations. Each column is a Stokes parameter (I, Q, and U). The first row shows the output maps without any filtering. The other rows correspond to the output maps for a run of the mapmaking with a particular combination of the filters: only polynomials filtering (second row), only ground templates subtraction (third row), and both filters (fourth row). See text for more explanations.

Chapter 9

Power spectrum estimation

Contents

Once we have the maps of each sky patch, we estimate the angular power-spectra. The geometry of the patches as well as the inhomogeneous sky coverage, and the different transfer functions of the instrument have to be taken into account to have a correct estimation. I was highly involved in the power-spectrum estimation throughout my thesis. More specifically, I focused on the pure powerspectrum reconstruction of the B-mode. I adapted and validated the X²pure code for POLARBEAR, and I maintained a version up-to-date for the collaboration at NERSC. I conducted many tests and proposed optimization procedures, specific to small patches (geometry of the masks, optimal division of data, influence of point sources). I also participated in estimating uncertainties, and in conducting the massive runs of Monte Carlo simulations to validate the estimator.

9.1 Pure pseudospectrum formalism

We already introduced the basics about temperature and polarization power spectra, see Sec. 2.2.1 and 2.3.4. There are several ways to estimate the angular power spectra. In principle, assuming that we know the pixel-pixel correlation matrix, we could use a maximum likelihood formalism, *e.g.* see [Jaffe *et al.* 2003]. In practice, we do not know this matrix in general (at best a diagonal estimate), and the maximum likelihood techniques are computationally expensive requiring $\mathcal{O}(N_{pix}^3)$ time and $\mathcal{O}(N_{pix}^2)$ memory. Given our large number of pixel $N_{pix} \sim 10^5$, we cannot use this technique easily. So in order to estimate the angular power spectra

from the maps, we use rather a pseudospectrum technique [Wandelt *et al.* 2001, Tegmark & de Oliveira-Costa 2001, Hivon *et al.* 2002, Tristram *et al.* 2005]. The idea is to estimate directly the pseudospectrum from the data, and correct in the harmonic domain the different biasing effects such as the mode-mode couplings induced by the small and irregular size of the patch, the beam function, and the pixelization. The pseudospectrum technique is very fast (requiring $\mathcal{O}(N^{3/2})$ time) and it is frequently near-optimal for temperature in practice. The estimation of polarized spectra however suffers from a spurious mixing of E and B modes, called E-to-B leakage, which has to be taken into account carefully to obtain the near optimality of the estimator.

9.1.1 Mode-mixing matrix: the standard case

For temperature and polarization anisotropies, the partial-sky pseudo-multipoles are defined as :

$$\begin{aligned}
\tilde{a}^T_{\ell m} &= \int_{4\pi} W_I \Big(\frac{\Delta T}{T} Y^*_{\ell m}\Big) d\vec{n} \\
\tilde{a}^E_{\ell m} &= -\frac{1}{2}\int_{4\pi} W_P \Big[{}_2P_2Y^*_{\ell m} + {}_{-2}P_{-2}Y^*_{\ell m}\Big] d\vec{n} \\
\tilde{a}^B_{\ell m} &= \frac{i}{2}\int_{4\pi} W_P \Big[{}_2P_2Y^*_{\ell m} - {}_{-2}P_{-2}Y^*_{\ell m}\Big] d\vec{n}
\end{aligned} \tag{9.1}$$

where W_I and W_P are window function applied to the temperature map (intensity) and polarized maps (polarization). In POLARBEAR, we use the same window function W_P for both Q and U maps (or E and B fields). The multipole decompositions on the sphere of the three fields $\Delta T/T$ (spin 0), ${}_{\pm2}P$ (spin ±2) and the window functions are given by [1]:

$$\begin{aligned}
\frac{\Delta T}{T}(\vec{n}) &= \sum_{\ell m} a^T_{\ell m} Y_{\ell m}(\vec{n}) \\
{}_{\pm2}P(\vec{n}) &= (Q \pm iU)(\vec{n}) = -\sum_{\ell m} (a^E_{\ell m} \pm i a^B_{\ell m})\, {}_{\pm2}Y_{\ell m}(\vec{n}) \\
W_{I/P}(\vec{n}) &= \sum_{\ell m} w^{I/P}_{\ell m} Y_{\ell m}(\vec{n})
\end{aligned} \tag{9.2}$$

So using the set of equations in Eq. 9.1 and Eq. 9.2, we obtain

[1] I denote partial-sky *pseudo*-multipoles with a tilde ($\tilde{a}^X$), estimates of the full-sky multipoles with a hat ($\hat{a}^X$), and full-sky multipoles without anything (a^X)

$$
\begin{aligned}
\tilde{a}^{T}_{\ell m} &= \sum_{\ell' m', \ell'' m''} w^{I}_{\ell' m'} a^{T}_{\ell'' m''} \int_{4\pi} Y_{\ell' m'}(\vec{n}) Y_{\ell'' m''}(\vec{n}) Y^{*}_{\ell m}(\vec{n}) d\vec{n} \\
\tilde{a}^{E}_{\ell m} &= \frac{1}{2} \sum_{\ell' m', \ell'' m''} w^{P}_{\ell' m'} \int_{4\pi} \Big(a^{E}_{\ell'' m''} \Big[Y_{\ell' m'}(\vec{n})_2 Y_{\ell'' m''}(\vec{n})_2 Y^{*}_{\ell m}(\vec{n}) + Y_{\ell' m'}(\vec{n})_{-2} Y_{\ell'' m''}(\vec{n})_{-2} Y^{*}_{\ell m}(\vec{n}) \Big] \\
&\qquad + i a^{B}_{\ell'' m''} \Big[Y_{\ell' m'}(\vec{n})_2 Y_{\ell'' m''}(\vec{n})_2 Y^{*}_{\ell m}(\vec{n}) - Y_{\ell' m'}(\vec{n})_{-2} Y_{\ell'' m''}(\vec{n})_{-2} Y^{*}_{\ell m}(\vec{n}) \Big] \Big) d\vec{n} \\
\tilde{a}^{B}_{\ell m} &= \frac{1}{2} \sum_{\ell' m', \ell'' m''} w^{P}_{\ell' m'} \int_{4\pi} \Big(a^{B}_{\ell'' m''} \Big[Y_{\ell' m'}(\vec{n})_2 Y_{\ell'' m''}(\vec{n})_2 Y^{*}_{\ell m}(\vec{n}) + Y_{\ell' m'}(\vec{n})_{-2} Y_{\ell'' m''}(\vec{n})_{-2} Y^{*}_{\ell m}(\vec{n}) \Big] \\
&\qquad - i a^{E}_{\ell'' m''} \Big[Y_{\ell' m'}(\vec{n})_2 Y_{\ell'' m''}(\vec{n})_2 Y^{*}_{\ell m}(\vec{n}) - Y_{\ell' m'}(\vec{n})_{-2} Y_{\ell'' m''}(\vec{n})_{-2} Y^{*}_{\ell m}(\vec{n}) \Big] \Big) d\vec{n}
\end{aligned}
\tag{9.3}
$$

A useful property of the spin-weighted spherical harmonics can be used to ease the computation[2]

$$
\int_{4\pi} {}_s Y_{\ell' m'}(\vec{n}) {}_s Y_{\ell'' m''}(\vec{n}) {}_s Y^{*}_{\ell m}(\vec{n}) d\vec{n} = \sqrt{\frac{(2\ell+1)(2\ell'+1)(2\ell''+1)}{4\pi}} \begin{pmatrix} \ell & \ell' & \ell'' \\ s & s' & s'' \end{pmatrix} \begin{pmatrix} \ell & \ell' & \ell'' \\ m & m' & m'' \end{pmatrix},
\tag{9.4}
$$

where we have introduced the so-called Wigner-3j symbols [Varshalovich *et al.* 1988]. Let's define $J^{(T)}$ and $J^{(\pm)}$ which help to the clarity as

$$
\begin{aligned}
J^{(T)}(\ell, \ell', \ell'') &= \begin{pmatrix} \ell & \ell' & \ell'' \\ 0 & 0 & 0 \end{pmatrix} \\
J^{(\pm)}(\ell, \ell', \ell'') &= \begin{pmatrix} \ell & \ell' & \ell'' \\ -2 & 2 & 0 \end{pmatrix} \pm \begin{pmatrix} \ell & \ell' & \ell'' \\ 2 & -2 & 0 \end{pmatrix}.
\end{aligned}
\tag{9.5}
$$

We recall that if we assume that the temperature and polarization fields are Gaussian and isotropic random fields, then the angular power spectra are given by

$$
\left\langle a^{X}_{\ell m} a^{Y^*}_{\ell' m'} \right\rangle = \left\langle C^{XY}_{\ell} \right\rangle \delta_{\ell, \ell'} \delta_{m, m'},
\tag{9.6}
$$

where X, Y $\in$ (T,E,B) and we can define a pseudo-power spectrum estimator as

$$
\tilde{C}^{XY}_{\ell} = \frac{1}{2\ell+1} \sum_{m=-\ell}^{\ell} \tilde{a}^{X}_{\ell m} \tilde{a}^{Y}_{\ell m}
\tag{9.7}
$$

The couplings due to inhomogeneous coverage of the sky do not mix spectra between them but C^{EE}_{ℓ} and C^{BB}_{ℓ} spectra. If we write the estimates of the true spectra in a vector such as

[2] This is defined as the Gaunt integral.

$$\hat{C}_\ell = \left(\hat{C}_\ell^{TT}, \hat{C}_\ell^{EE}, \hat{C}_\ell^{BB}, \hat{C}_\ell^{TE}, \hat{C}_\ell^{TB}, \hat{C}_\ell^{EB}\right), \tag{9.8}$$

so that the total mode-mode coupling matrix is diagonal by block and could be written as :

$$M_{\ell\ell'} = \begin{pmatrix} M_{\ell\ell'}^{TT,TT} & 0 & 0 & 0 & 0 & 0 \\ 0 & M_{\ell\ell'}^{EE,EE} & M_{\ell\ell'}^{EE,BB} & 0 & 0 & 0 \\ 0 & M_{\ell\ell'}^{BB,EE} & M_{\ell\ell'}^{BB,BB} & 0 & 0 & 0 \\ 0 & 0 & 0 & M_{\ell\ell'}^{TE,TE} & 0 & 0 \\ 0 & 0 & 0 & 0 & M_{\ell\ell'}^{TB,TB} & 0 \\ 0 & 0 & 0 & 0 & 0 & M_{\ell\ell'}^{EB,EB} \end{pmatrix} \tag{9.9}$$

then the effect of an incomplete sky coverage is summarized in the following equation

$$\tilde{C}_\ell = \sum_{\ell'} M_{\ell\ell'} \hat{C}_{\ell'}. \tag{9.10}$$

The non-vanishing[3] mode-mode mixing matrices in the standard formalism are

$$M_{\ell\ell'}^{TT,TT} = \frac{2\ell'+1}{4\pi} \sum_{\ell'' m''} \left| w^I_{\ell'' m''} J^{(T)}(\ell, \ell', \ell'') \right|^2 \tag{9.11}$$

$$M_{\ell\ell'}^{EE,EE} = M_{\ell\ell'}^{BB,BB} = \frac{2\ell'+1}{16\pi} \sum_{\ell'' m''} \left| w^P_{\ell'' m''} J^{(+)}(\ell, \ell', \ell'') \right|^2 \tag{9.12}$$

$$M_{\ell\ell'}^{EE,BB} = M_{\ell\ell'}^{BB,EE} = \frac{2\ell'+1}{16\pi} \sum_{\ell'' m''} \left| w^P_{\ell'' m''} J^{(-)}(\ell, \ell', \ell'') \right|^2 \tag{9.13}$$

$$M_{\ell\ell'}^{EB,EB} = \frac{2\ell'+1}{16\pi} \sum_{\ell'' m''} \left[\left| w^P_{\ell'' m''} J^{(+)}(\ell, \ell', \ell'') \right|^2 - \left| w^P_{\ell'' m''} J^{(-)}(\ell, \ell', \ell'') \right|^2 \right] \tag{9.14}$$

$$M_{\ell\ell'}^{TE,TE} = M_{\ell\ell'}^{TB,TB} = \frac{2\ell'+1}{8\pi} \sum_{\ell'' m''} w^I_{\ell'' m''} w^P_{\ell'' m''} J^{(T)}(\ell, \ell', \ell'') J^{(+)}(\ell, \ell', \ell'') \tag{9.15}$$

We have then to solve the Eq. 9.10 to obtain the estimates of the true spectra. However, because of the non-zero mixing between E and B, the standard pseudo-spectrum estimator suffers from E-to-B leakage, although it is unbiased.

9.1.2 E and B mixing

Applying standard pseudospectrum technique to partial sky maps in the polarization context leads to a mix between E and B modes. In other words, for a noiseless CMB realization containing only E-modes, the estimated B-mode bandpowers are

[3] $J^{(+)}$ vanish for odd values of $(\ell + \ell' + \ell'')$ while $J^{(-)}$ vanish for even values of $(\ell + \ell' + \ell'')$. The vanishing terms involve cross terms such as $J^{(+)}J^{(-)}$.

non-zero[4], and depending on the experimental setup the leakage can completely dominate the B-mode signal at low multipoles. These past years several efforts have been done to treat this effect such as in [Lewis *et al.* 2001, Bunn *et al.* 2003, Smith 2006, Grain *et al.* 2009].

We saw that the space of polarization can be decomposed in two orthogonal subspaces E and B defined through the ${}_{\pm2}Y^{E/B}_{\ell m}$ (see Sec. 2.3.3). However these subspaces are orthogonal only if we consider the full sky[5]. If the polarization field is known on a limited part of the celestial sphere, the reconstruction of E and B modes by projecting the measured polarization on the ${}_{\pm2}Y^{E/B}_{\ell m}$ is "nonpure", meaning that the estimated E or B multipoles receive contributions from both true E and true B modes. It is the so-called E/B leakage. In a ensemble of realizations, the estimated B-modes leaking from E-modes are zero in the mean -due to the fact that pseudo-C_l are unbiased by construction-, but because they are non-zero in each realization, E-mode signal power does contribute to the variance of the B-mode estimators. Therefore, if the power contained in one of the polarization states is much higher than the other, as it is the case for the CMB anisotropies, the errors bars estimated for the mode with lower power are drastically exaggerated due to sample variance of the leaked contribution [Grain *et al.* 2009]. As E-modes are much bigger than B-modes the effect of this variance in the measure of B is enormous. So when using a limited part of the sky, a new subspace has to be taken into account : the subspace containing these ambiguous E/B modes. Let's re-write the polarized component in Eq. 9.2 as

$$\tilde{a}^E_{\ell m} = \sum_{\ell' m'} M^{(+)}_{\ell m,\ell' m'} a^E_{\ell' m'} + i M^{(-)}_{\ell m,\ell' m'} a^B_{\ell' m'} \tag{9.16}$$

$$\tilde{a}^B_{\ell m} = \sum_{\ell' m'} M^{(+)}_{\ell m,\ell' m'} a^B_{\ell' m'} - i M^{(-)}_{\ell m,\ell' m'} a^E_{\ell' m'}. \tag{9.17}$$

The $\mathrm{M}^{(\pm)}$ matrices are kernels, which in general can be all different for E and B, non-vanishing, and non-diagonal in both ℓ and m. In particular for the pseudo-power spectra, we have

$$\begin{pmatrix} \tilde{C}^{EE}_\ell \\ \tilde{C}^{BB}_\ell \end{pmatrix} = \begin{pmatrix} M^{(+)}_{\ell\ell'} & M^{(-)}_{\ell\ell'} \\ M^{(-)}_{\ell\ell'} & M^{(+)}_{\ell\ell'} \end{pmatrix} \begin{pmatrix} \hat{C}^{EE}_{\ell'} \\ \hat{C}^{BB}_{\ell'} \end{pmatrix}.$$

where the kernels $M^{(\pm)}$ correspond to Eq. 9.12 and 9.13, and have been defined as

$$M^{(\pm)}_{\ell\ell'} = \sum_{m'=-\ell'}^{\ell'} \frac{1}{2\ell+1} \sum_{m=-\ell}^{\ell} |M^{(\pm)}_{\ell m,\ell' m'}|^2. \tag{9.18}$$

[4] And vice versa. But the E modes being stronger than the B-modes, we mainly care about the E-to-B leakage.

[5] This is only theoretically. In practice, even if we observe the full sky, we always have to subtract for instance region contaminated by foregrounds or to mask point sources, and so we never have a real full sky.

Therefore, we need to go beyond to avoid this leakage from E to B as soon one has uncomplete sky. The corrections can directly be done in the definition of the ${}_{\pm2}Y_{\ell m}$ and $\tilde{a}^{E/B}_{\ell m}$ with

$$ {}_{\pm2}\tilde{\mathbf{Y}}^{E/B}_{\ell m} = {}_{\pm2}\mathbf{D}^{E/B}(WY_{\ell m}), \tag{9.19}$$

where the W function is zero for non-observed pixel, and non-zero otherwise (we implicitly define the mask by W). We can understand this definition by noticing that applying ${}_2\mathbf{D}^B$ to the polarization field corresponds to a local filtering of the E-modes whereas projecting on the ${}_2\mathbf{Y}^{B\dagger}_{\ell m}$ basis corresponds to a global filtering and so suffers from partial sky effects. Thus, if the window function satisfies the Neumann and Dirichlet conditions, the estimated multipoles are pure and we have a block diagonal mixing matrix, and hence we avoid coupling between E and B-modes :

$$\begin{pmatrix} \tilde{C}^{EE}_{\ell} \\ \tilde{C}^{BB}_{\ell} \end{pmatrix} = \begin{pmatrix} M^{(+)}_{\ell\ell'} & 0 \\ 0 & M^{(+)}_{\ell\ell'} \end{pmatrix} \begin{pmatrix} \hat{C}^{EE}_{\ell'} \\ \hat{C}^{BB}_{\ell'} \end{pmatrix}.$$

In order to remove efficiently the modes which are neither solely E nor B, we have to find a suitably chosen sky apodization W. The corresponding mode-mode mixing matrices within the pure formalism are somewhat similar (but more complex to deduce) to the ones shown in Eq. 9.11-9.15, and their expressions can be found in [Grain *et al.* 2012].

9.2 X^{2}pure and applications for POLARBEAR

To compute our spectra, we use the X^{2}pure software which implements the pure pseudo-spectrum techniques described above and in [Grain *et al.* 2009, Grain *et al.* 2012]. This software is mainly written in C, and is interfaced with few FORTRAN routines. The code makes use of the publicly available software package S^{2}HAT containing MPI-parallel routines permitting quick computation of the pure multipoles. The runs for POLARBEAR are performed mainly at NERSC, on the Hopper machine. The code was already written when I started to work on it in 2012. However all along my thesis I was an active contributor, participating to the development of a specific framework for POLARBEAR, and I was in charge to maintain a version of the code updated and available for collaborators at NERSC (including people from POLARBEAR and EBEX, and independent groups). The code proceeds in 3 steps. First it computes the spin-weighted apodizations given an input spin-0 window. Then it computes the pure mode-mode coupling matrices from the spin-weighted apodizations. Finally it solves the Eq. 9.27 to find the pure estimator. The code is fully parallel (in time and memory), and achieves excellent performances as reported in Tab. 9.1.

9.2.1 Pre-processing for POLARBEAR

The masks that we use to construct our mode-mode mixing matrices are a combination of the estimate of the inverse covariance matrices and analytic windows. On

Table 9.1: Elapsed real time between invocation and termination (in second) of the different steps of the power spectrum computation for a standard Polarbear run on the Hopper machine, using 96 cores.

Step	Cores used	Time (second)
Mask apodizations	1	7
Spin-weighted windows	96	40
Mode-mode mixing matrices	96	400
Pure estimator	96	40

Note. — Only the mask apodization is a separate code from X^{2}pure, written by M. Betoule. To perform Monte Carlo, we pre-compute first the spin-weighted windows and the mode-mode mixing matrices, and only the last step is repeated. A large number of Monte Carlo (∼500) can be performed on thousand cores in less than an hour. The ACML package which provides a full suite of Linear Algebra (LAPACK) routines has been used to perform calculations.

the one hand, the inverse covariance matrix provides an estimate of the noise per pixel, and it is used to weight the contribution of each pixel in the computation of the power spectrum, so that we can naturally incorporate inhomogeneous noise as shown in Fig. 8.13. Unfortunately, we do not include the pixel-pixel correlations, therefore we are not able to weight properly the correlated modes. On the other hand, we use analytic window functions to control the E-to-B leakage arising from the sharp transition at the edges or around masked point sources. The analytics windows are construct from the binary version of the inverse covariance matrix (pixel value is 1 if the pixel has been seen, 0 otherwise), and we apply a function which goes smoothly to zero at the boundaries. Formally speaking, calling δ_p the distance between the $p-th$ observed pixel and the boundary, meaning the smallest angular distance from the considered pixel to the contour of the mask or a hole due to a masked point source, we adopt the C^2-window defined in [Grain *et al.* 2009]

$$W_p = \begin{cases} -\frac{1}{2\pi}\sin(2\pi\frac{\delta_p}{\delta_c}) - \frac{\delta_p}{\delta_c} & \text{if } \delta_p < \delta_c, \\ 1 & \text{if } \delta_p > \delta_c, \end{cases} \tag{9.20}$$

and vanishes outside the mask. δ_c is called the apodization length and we treat it as an adjustable parameter. The choice of δ_c is crucial since we want to treat correctly the E-to-B leakage without degrading the sensitivity. Indeed, a too small apodization length does not take into account sufficiently the spurious effects arising at the irregular boundaries, and a too wide apodization length drastically reduces the effective sky area used to compute the power spectra. For our typical patch size of 3°, we found that $\delta_c = 30$ arcminutes leads to reasonable performances. Those analytics windows are in general not well suited for providing an optimal performance in the presence of low instrumental noise because they assume nothing

about the properties of the data in the map (sky signal). However, they are quick to calculate, do not require any prior knowledge about the sky signals and can fulfill the boundary conditions with high precision. Furthermore in our case, given that the level of noise is still high compared to the targeted signal in polarization, there is no gain to run optimization procedures to get windows adapted to the specific properties of the data, because the procedure naturally converges to the inverse noise weights. So for each pixel p, the spin-0 mask that we use is given by

$$W_p^0 = W_p \times \lambda_p^{min}, \tag{9.21}$$

where λ_p^{min} is the smallest eigenvalue of the estimate of the polarized 2x2 inverse covariance matrix $\left(A^T N^{-1} A\right)_p$. As seen in Eq. 9.19, we need to apply the derivative operator to products of the spherical harmonics times the window functions and perform then integral by parts. So we also define two spin-weighted windows

$$W^1 = \eth W^0 \tag{9.22}$$
$$W^2 = \eth^2 W^0. \tag{9.23}$$

Such windows using the co-added data from one patch are shown in Fig. 9.1. The resulting mode-mode mixing matrices $M_{\ell\ell'}^{(\pm)}$ for the standard case (no specific treatment of E-to-B leakage) and the pure case (E-to-B leakage is minimized) are shown in Fig. 9.2.

The typical size of the patch tells us that the smaller multipole that we can constrain is about $\ell_{min} \sim 180°/3° = 60$. However, this limit is an optimistic estimate coming from simple geometrical consideration. In practice, we start at a much higher multipole because our noise model is not sufficient to weight properly the low multipoles (noise is not really white). There are also a potential contamination from instrumental systematic effects or the effect of the time-domain filters which decrease our ability to constrain the low multipoles. For the first season of observation, our science band was defined between $\ell = 500$ and $\ell = 2100$[6]. In addition, we cannot constrain all the modes within this science band. The finite size of the patch introduces mode-mode correlations with a typical width given by the size of the patch, as seen in the Fig. 9.2. The mode-mode mixing matrix $M_{\ell\ell'}^{(+)}$ for instance is diagonal dominated, with a correlation length of about 100 modes. Therefore we cannot constrain individually modes separated by less than ~ 100. The angular power spectra are reconstructed within bandpowers, labelled b hereafter, with bandwidths $\Delta\ell$. The binned power spectrum is given by $C_b = \sum_\ell P_{b\ell}\, C_\ell$, where the binning operator is defined as

$$P_{b\ell} = \begin{cases} \dfrac{\ell(\ell+1)}{2\pi\Delta\ell} & \text{if } \ell \in b, \\ 0 & \text{if } \ell \notin b, \end{cases} \tag{9.24}$$

[6]The upper mode is driven by our beam size of 3.5 arcminutes. For modes > 2000, the noise start to be exponentially boosted by the deconvolution of the beam function.

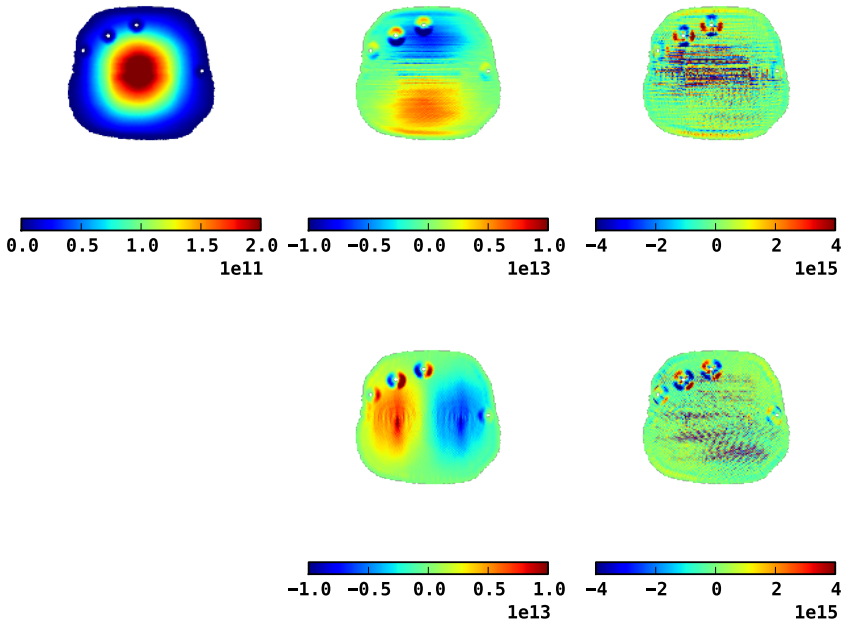

Figure 9.1: W^0 (left), and its derivatives for the sky patch RA23: Re(W^1) (top middle), Im(W^1) (bottom middle), Re(W^2) (top right), Im(W^2) (bottom right). The holes are the masks for the point sources.

with the interpolation operator, $Q_{b\ell}$:

$$Q_{b\ell} = \begin{cases} \dfrac{2\pi}{\ell(\ell+1)} & \text{if } \ell \in b, \\ 0 & \text{if } \ell \notin b. \end{cases} \tag{9.25}$$

For the first season of observation, we were rather conservative, and we chose $\Delta\ell = 400$. In addition to this mode coupling effect, we take into account the beam of the instrument which is represented by a single function B_ℓ of the multipole for all the bolometers (Sec. 6.6). The effect of the pixelization has to be also corrected. The pixels act as a low-pass filter in the harmonic domain, which is represented as a decreasing function p_ℓ of the multipole. All those functions are shown in Fig. 9.3, and are incorporated into the binned mode-mode mixing matrix

$$\tilde{M}_{bb'} = \sum_{\ell \in b} \sum_{\ell' \in b'} P_{b\ell} M_{\ell\ell'} B^2_{\ell'} p^2_{\ell'} Q_{b'\ell'}, \tag{9.26}$$

and the pseudo-spectra and estimate of the true spectra are related by

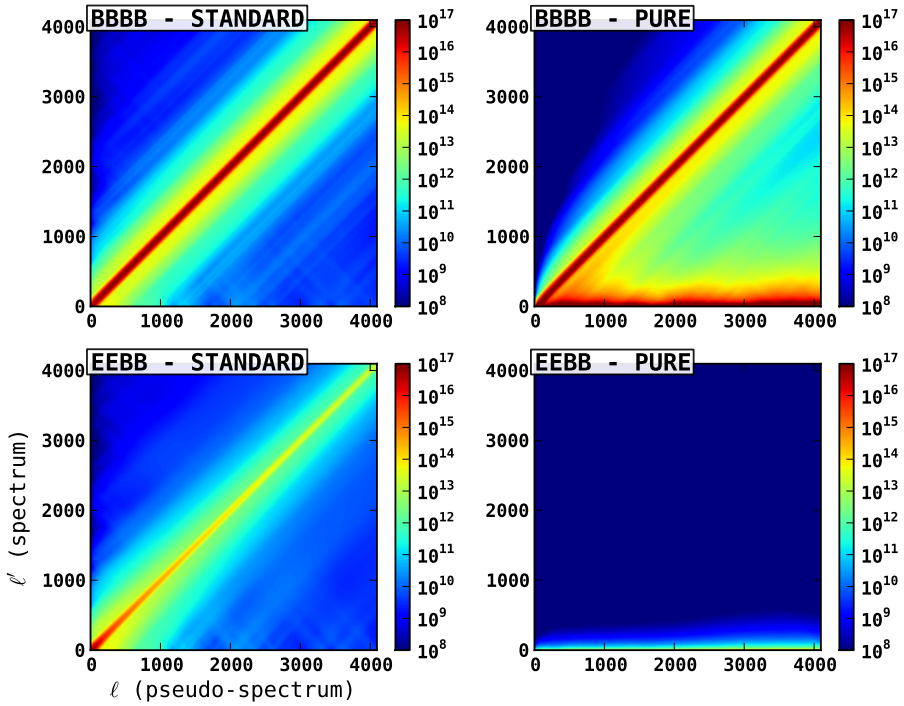

Figure 9.2: Mode-mode mixing matrices for the sky patch RA23 in the case of the standard computation (no specific treatment of E-to-B leakage) and in the case of the pure case (E-to-B leakage is minimized). The first row shows the BBBB ($M^{(+)}_{\ell\ell'}$) component, and the second row shows the cross term EEBB ($M^{(-)}_{\ell\ell'}$). In the case of the standard method, the BBBB component is diagonal, and the cross term is non zero. In the case of the pure-pseudo spectrum method, the BBBB case exhibits a large correlation of low multipoles of the spectrum (horizontal ℓ'), correlated with all multipoles of the pseudo-spectrum (vertical ℓ), while the EEBB component is vanishing. These features are here to ensure that the E-to-B leakage is minimized.

$$\tilde{C}_b = \sum_{b'} \tilde{M}_{bb'} \hat{C}_{b'}. \tag{9.27}$$

The functional dependence of the binned band powers $\hat{C}_b$ on the true high-resolution power spectra is given by the band power window functions $w_{b\ell}$, where

$$\hat{C}_b = \sum_{\ell} w_{b\ell} C_\ell \tag{9.28}$$

$$w_{b\ell} = \sum_{b'\ell'} \tilde{M}^{-1}_{bb'} P_{b'\ell'} M_{\ell'\ell} B^2_\ell p^2_\ell \tag{9.29}$$

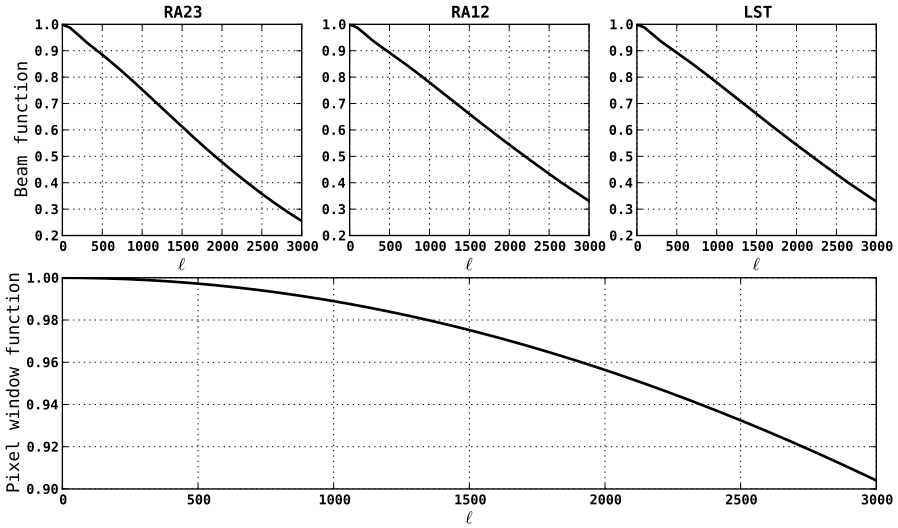

Figure 9.3: The three upper panels are the beam function as a function of the multipole for the three sky patches (RA23, RA12 and LST). The lower panel show the pixel window function from the package HEALPIX for a resolution of nside = 2048.

The resulting band power window function (for the four bins of science band) for TT and BB are shown in Fig. 9.4.

In practice, two small effects are not taken into account in the analysis and they are not corrected by the pure-pseudo spectra formalism. First we expect that some residual E-to-B leakage is present due to the sky discretization. Second, the time-domain filters can generate mixing between E and B modes. While our maps are unbiased, the fact that we do not orthogonalized properly the filters can leave some unwanted pixel-pixel correlations and E-to-B leakage.

9.2.2 Power spectrum uncertainty estimation

If we co-add the data of the full season into a single set of I, Q, U maps, and we compute the pure estimator using Eq. 9.27, the estimator is noise biased. Given the relatively high level of noise compared to the expected B-modes signal, we would like to get rid of the noise component. To do so, we compute "cross-spectra" instead of "auto-spectra", as described for instance in [Tristram *et al.* 2005]. Given two maps a and b[7], we can rewrite equation 9.27 by explicitly separating the signal and the noise contributions

$$\tilde{C}_b^{XY,ab} = \sum_{b'} \tilde{M}_{bb'}^{XYXY,ab} \hat{C}_{b'}^{XY,ab} + N_b^{XY,ab} \tag{9.30}$$

[7] b as a subscript denotes a bin number, while b as a superscript denotes a map.

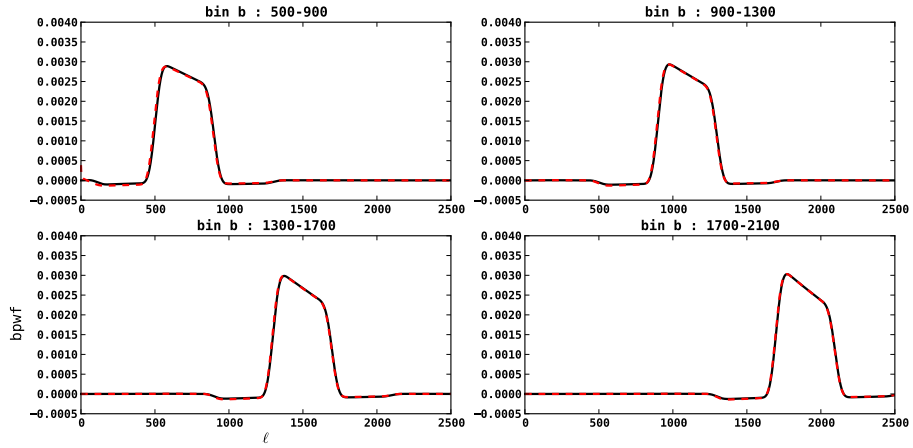

Figure 9.4: Band power window functions $w_{b\ell}$ for TT (dashed red lines) and BB (solid black lines) for the sky patch RA23. The four bins used for the first release of data are shown. The band power window functions describe the transfer function for temperature (TT here) or polarization (BB here) power from a $\ell(\ell+1)C_\ell/(2\pi)$ power spectrum to binned band powers, as described in equation 9.29.

where $X, Y = (T, E, B)$. If the two maps are different, *i.e.* $a \neq b$ and their noise are uncorrelated, we have statically $N_b^{XY,ab} = 0$ (although the noise of each map contributes to the variance of the estimator). As mentioned in the mapmaking section we compute daily maps, so in principle we could perform cross-spectra among all the daily maps ($\mathcal{O}(10^2)$). However, the exact computation of all the "cross mode-mode mixing matrices" ($\tilde{M}_{bb'}^{XYXY,ab}$) becomes extremely time consuming. Instead, we co-add the daily maps into eighth of the full season (correspond to roughly 1.5 months of data) and we perform cross-spectra with the eight sets of maps. From $N = 8$ input maps and for each polarization mode, we can obtain $N(N-1)/2 = 28$ cross-power spectra C_ℓ^{ab} ($a \neq b$) which are unbiased estimates of the angular power spectrum but which are not all independent. Let a, b, c, and d labels for maps, and let's define the cross-correlation matrix $\Xi_{\ell\ell'}^{ab,cd}$ for cross-spectra ab ($a \neq b$) and cd ($c \neq d$) by

$$\Xi_{\ell\ell'}^{ab,cd} = \left\langle \left(\hat{C}_\ell^{ab} - \left\langle \hat{C}_\ell^{ab} \right\rangle\right)\left(\hat{C}_{\ell'}^{cd} - \left\langle \hat{C}_{\ell'}^{cd} \right\rangle\right)^* \right\rangle. \tag{9.31}$$

Using the relation between pseudo-spectrum and spectrum, we can rewrite the cross-correlation matrix as

$$\Xi_{\ell\ell'}^{ab,cd} = [\tilde{M}_{\ell\ell_1}^{ab}]^{-1} \left\langle \left(\tilde{C}_\ell^{ab} - \left\langle \tilde{C}_\ell^{ab} \right\rangle\right)\left(\tilde{C}_{\ell'}^{cd} - \left\langle \tilde{C}_{\ell'}^{cd} \right\rangle\right)^* \right\rangle ([\tilde{M}_{\ell'\ell_2}^{cd}]^{-1})^T \tag{9.32}$$

where $\tilde{M}_{\ell\ell'}^{ab} = M_{\ell\ell'}^{ab} B_{\ell'}^a B_{\ell'}^b p_{\ell'}^a p_{\ell'}^b$. After a quite long calculation detailed in [Efstathiou 2004, Tristram *et al.* 2005, Tristram 2005, Efstathiou 2006], we finally

end up with the expression for the cross-correlation matrix[8] :

$$\Xi^{ab,cd}_{\ell\ell'} = [\tilde{M}^{ab}_{\ell\ell_1}]^{-1}\Big(\frac{\tilde{M}^{(2)}_{\ell_1\ell_2}(W^{ac,bd})\hat{C}^{ac}_{\ell_1}\hat{C}^{bd}_{\ell_2} + \tilde{M}^{(2)}_{\ell_1\ell_2}(W^{ad,bc})\hat{C}^{ad}_{\ell_1}\hat{C}^{bc}_{\ell_2}}{2\ell_2+1}\Big)([\tilde{M}^{cd}_{\ell'\ell_2}]^{-1})^T, \tag{9.33}$$

with $M^{(2)}_{\ell_1\ell_2}(W^{ac,bd})$ defined as :

$$M^{(2)}_{\ell_1\ell_2}(W^{ac,bd}) = (2\ell_2+1)\sum_{\ell_3}\frac{(2\ell_3+1)}{4\pi}W^{ac,bd}_{\ell_3}\begin{pmatrix}\ell_1 & \ell_2 & \ell_3\\ 0 & 0 & 0\end{pmatrix}^2 \tag{9.34}$$

$$W^{ac,bd}_{\ell_3} = \frac{1}{2\ell_3+1}\sum_{m_3} w^{ac}_{\ell_3 m_3} w^{bd*}_{\ell_3 m_3}. \tag{9.35}$$

However the numerical calculation of Eq. 9.33 is prohibitively slow in our case. The MASTER approach [Hivon *et al.* 2002] proposed a simplification under the hypothesis that all the masks have the same sky coverage (almost true in our case, given that each map has roughly 1.5 months of data). Let's first define w_i the $i-th$ moment of the mask W as[9]

$$w_i = \frac{1}{4\pi f_{sky}}\int_{4\pi} d\vec{n} W^i(\vec{n}) \tag{9.37}$$

We want to relate the different moments of the mask to power spectra of the mask. For simplicity of notation, let's drop indices for masks (since it is the same mask for both maps). We can show that :

$$f_{sky}w_2 = \frac{1}{4\pi}\int_{4\pi} d\vec{n} W^2(\vec{n}) = \frac{1}{4\pi}\sum_\ell (2\ell+1)W_\ell \tag{9.38}$$

$$f_{sky}w_4 = \frac{1}{4\pi}\int_{4\pi} d\vec{n} W^4(\vec{n}) = \frac{1}{4\pi}\sum_\ell (2\ell+1)W^{(2)}_\ell \tag{9.39}$$

where $W^{(2)}_\ell$ is the cross spectrum of the product of masks defined in Eq. 9.35. The RHS of equations above can be identified to a simplified version of the mode-mode mixing matrix as defined in 9.34. Given that, the cross-correlation matrix can be written as :

$$\Xi^{ab,cd}_{\ell\ell'} = \frac{1}{\nu(\ell')}\Big(\hat{C}^{ac}_\ell\hat{C}^{bd}_{\ell'} + \hat{C}^{ad}_\ell\hat{C}^{bc}_{\ell'}\Big) \tag{9.40}$$

[8] In practice we work with the binned cross-correlation matrix, and a term $\Delta\ell$ appears in the denominator.

[9] For HEALPIX we have :

$$w_i = \frac{1}{4\pi f_{sky}}\int_{4\pi} d\vec{n} W^i(\vec{n}) \approx \frac{1}{4\pi f_{sky}}\sum_{pixel}\Omega(p)W^i(p) \approx \frac{1}{N_{pix}f_{sky}}\sum_{pixel} W^i(p) \tag{9.36}$$

where $\nu(\ell)$ is a function of the multipole which contains the effect of the inhomogeneous sky coverage (cut-sky and inhomogeneous weights per pixel). We can associate this function to the degrees of freedom of the distribution function χ^2_ℓ of the C_ℓ on the sky. Using previous equations, this function is given by :

$$\nu(\ell) = (2\ell+1) f_{sky} \frac{w_2^2}{w_4} \tag{9.41}$$

where f_{sky} is the sky fraction over which the weighting is non-zero (each pixel has a value one if seen, zero otherwise). In practice we do not work with the mode-by-mode version, and we rather use $\nu(b) = (2\ell_{mid}+1)\Delta\ell f_{sky} w_2^2/w_4$, with ℓ_{mid} being the center of the bin b. Using a gaussian approximation of the likelihood, that is

$$-2\ln\mathcal{L} = \sum_{ij}\Big[(\hat{C}_b^i - C_b)|\Xi^{-1}|_{bb'}^{ij}(\hat{C}_{b'}^j - C_{b'})\Big], \tag{9.42}$$

where i and j are combinations of maps : $i,j = (ab,cd)$ with $a \neq b$ and $c \neq d$, the cross-correlation matrices and error bars are related through[10]

$$\left(\Delta\hat{C}_b\right)^2 = \frac{1}{\sum_{ij}|\Xi^{-1}|_{bb}^{ij}}, \tag{9.45}$$

and the final cross (in terms of all maps for each patch) spectrum is given by :

$$\hat{C}_b = \frac{1}{2}\frac{\sum_{ij}\left[|\Xi^{-1}|_{bb}^{ij}\hat{C}_b^j + \hat{C}_b^i|\Xi^{-1}|_{bb}^{ij}\right]}{\sum_{ij}|\Xi^{-1}|_{bb}^{ij}}. \tag{9.46}$$

This estimator does not contain the noise bias, but its variance does (through auto-spectra of individual maps). The three sky patches are treated independently. We estimate the power-spectra and their uncertainties for all three sky patches using Eq. 9.46 and 9.45, and we combine them into a single power-spectrum using a weighted coaddition:

$$\hat{C}_b^{tot} = \frac{\sum_{p=patch}\hat{C}_b^p/\left(\Delta\hat{C}_b^p\right)^2}{\sum_{p=patch}1/\left(\Delta\hat{C}_b^p\right)^2} \tag{9.47}$$

with variance

[10] For $XX \in TT, EE$, and BB, the uncertainty estimate is

$$\Delta\hat{C}_b^{XX,i} = \sqrt{\frac{2}{\nu(b)}}(\hat{C}_b^{XX,i} + \hat{N}_b^{XX,i}). \tag{9.43}$$

For $XY \in TE, TB$, and EB, the uncertainty estimate is

$$\Delta\hat{C}_b^{XY,i} = \sqrt{\frac{(\hat{C}_b^{XY,i})^2 + (\hat{C}_b^{XX,i} + \hat{N}_b^{XX,i})(\hat{C}_b^{YY,i} + \hat{N}_b^{YY,i})}{\nu(b)}}. \tag{9.44}$$

$$\left(\Delta\hat{C}_b^{tot}\right)^2 = \Big(\sum_{p=patch} 1/\left(\Delta\hat{C}_b^{p}\right)^2\Big)^{-1}. \tag{9.48}$$

In addition, we also take into account uncertainties coming from the beams (including pointing error), and from the gain calibration. This binned uncertainty estimation is validated using full-season Monte Carlo simulations including signal and noise. We chose two noise models on which to test this estimator, a white noise model and a correlated noise mode [Errard *et al.* 2015]. In each case, the spread in the power spectra obtained from the Monte Carlo simulations is consistent with the mean result of the analytic binned uncertainty estimator to 10% (although we do not seem to reproduce correctly all correlations in temperature).

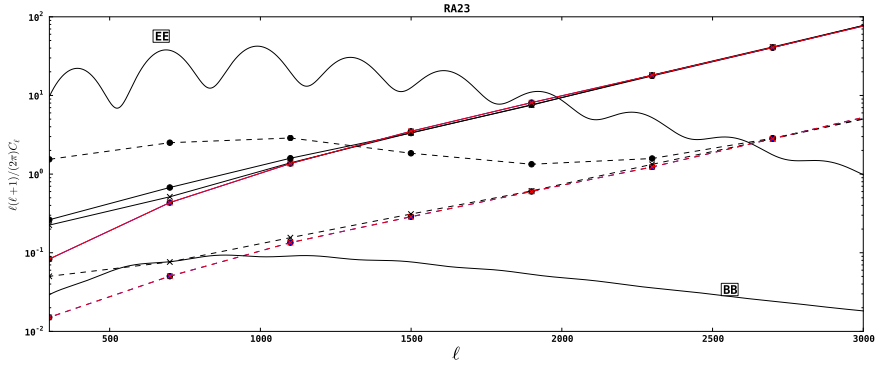

Figure 9.5: Estimate of the noise (solid curve) and estimate of the signal plus noise uncertainty (dashed curve) for EE (circle) and BB (cross) for one sky patch. The mean and the standard deviation from 100 Monte Carlo simulations using white noise (no CMB signal) are overplotted in color (EE in blue, and BB in red). The E-modes are signal dominated in the range $500 < \ell < 2000$, while B-modes are noise-dominated all along the multipole range. The noise has been estimated as the difference between the auto-spectrum of the full season and the cross-spectrum. The difference at low ℓ between real data noise and simulations is mainly due to unmodeled correlations (such as residual signal from atmosphere). Fiducial models for EE and BB based on the WMAP-9 ΛCDM best-fit parameters are overplotted for comparison (thick solid line). The science band is from $\ell = 500$ to $\ell = 2100$.

The Fig. 9.5 displays the results for 100 Monte Carlo simulations using white noise maps for E and B modes compared to the real data. The white noise model adds random spectrally flat noise to the timestream of each detector variance equivalent to that measured from the detectors as described in Sec. 8.2. The simulated timestreams are passed through the whole pipeline (PCG with filtering and power spectrum estimation) and we use the same pointing and detector weighting as the real data, and include signal from a beam-convolved realization of a WMAP-9 ΛCDM power spectrum that includes the effect of gravitational lensing. Given the

size of the whole data set, the amount of time required to run large Monte Carlo simulations is one of the limiting step of the PCG mapmaker ($\sim$ 50,000 CPUh for 100 MC just for the mapmaking step). At the moment of writing, we are still investigating how to obtain more realistic simulations (beyond the white noise) and we are still also trying to boost the performances (speed and memory) of the code.

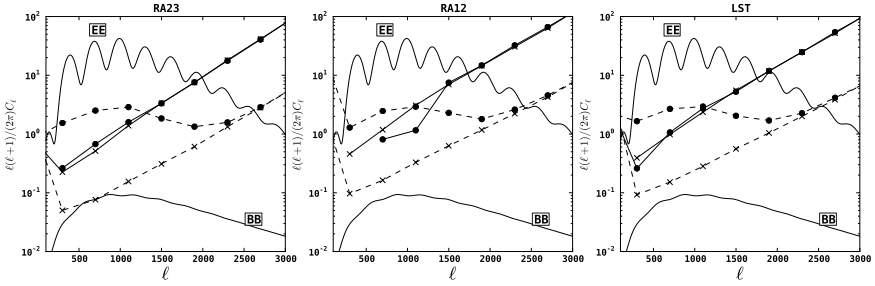

Figure 9.6: Estimate of the noise (solid curve) and estimate of the signal plus noise uncertainty (dashed curve) for EE (circle) and BB (cross). The estimates for the three sky patches are shown from left to right: RA23, RA12, and LST. The E-modes are signal dominated in the range $500 < \ell < 2000$, while B-modes are noise-dominated all along the multipole range. The noise has been estimated as the difference between the auto-spectrum of the full season and the cross-spectrum. Fiducial models for EE and BB based on the WMAP-9 ΛCDM best-fit parameters are overplotted for comparison (thick solid line). The science band is from $\ell = 500$ to $\ell = 2100$.

9.2.3 Application to the maps of the PCG mapmaker

Unfortunately at the moment of writing those lines, the power spectra of the second season are not published, and are even kept blind for us (see Sec. 10.1 about the blindness policy). In the remaining part of this chapter, I will only present the results concerning the first season.

The first release of papers including [POLARBEAR Collaboration 2014c] makes primarily use of the maps coming from the naive mapmaker linked to a flat sky pure pseudospectrum estimator, called hereafter primary pipeline. During this period, the PCG mapmaker, linked to X^2pure and called hereafter the PCG pipeline, was used to cross-check the results from the latter pipeline. One way to check the convergence of the PCG is to look at the evolution of the pseudo-spectra of the full co-added maps for different step of the procedure, as shown in Fig. 9.7 (see also Fig. 8.9) for one sky patch. We find that in the range of multipoles under consideration (500-2100), after 100 iterations, the fractional change of the pseudo-spectra for TT and EE was less than 0.1%, and for BB it the fractional change is less than 3% in the multipole range $[500, 700]$ and then less than 1% for higher multipoles.

The final results of the PCG pipeline are consistent with the results of the

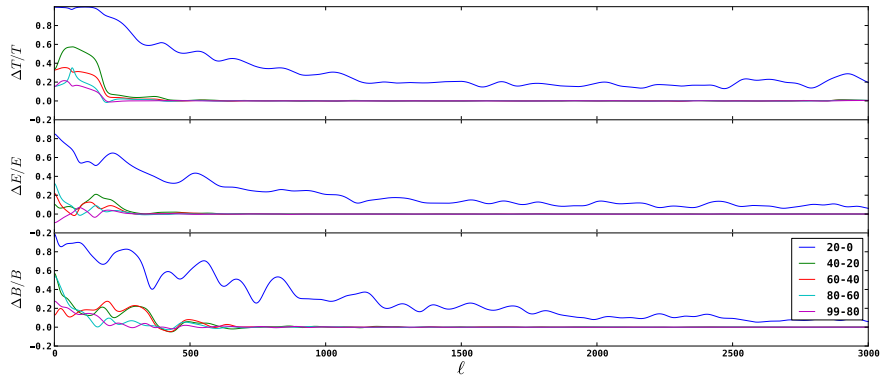

Figure 9.7: The fractional change in the angular pseudospectra for TT (top panel), EE (middle panel), and BB (bottom panel) from maps at subsequent iterations of the PCG mapmaker: 0, 20, 40, 60, 80 and 99 iterations. The largest scales ($<$500) take the longest to converge, and the BB signal generally takes longer to converge than does the temperature or E-modes. The science band is from $\ell = 500$ to $\ell = 2100$.

primary pipeline as shown in Fig. 9.9. Concerning the BB spectrum, we also fit the band powers to a ΛCDM cosmological model with a single A_{BB} amplitude parameter. We find $A_{BB} = 1.24 \pm 0.68(\mathrm{stat})^{+0.04}_{-0.12}(\mathrm{sys}) \pm 0.05(\mathrm{multi})$, where $A_{BB} = 1$ is defined by the WMAP-9 ΛCDM spectrum. With the primary pipeline, we measure an amplitude of $A_{BB} = 1.12 \pm 0.61(\mathrm{stat})^{+0.04}_{-0.12}(\mathrm{sys}) \pm 0.07(\mathrm{multi})$. The difference in the uncertainty related to multiplicative effect between the two pipelines comes from the fact that the PCG pipeline do not use a filter transfer function to de-bias the spectra (see Sec. 10.3 for the detail of uncertainties). We also show the detailed results for the PCG pipeline for all the spectra in Fig. 9.8.

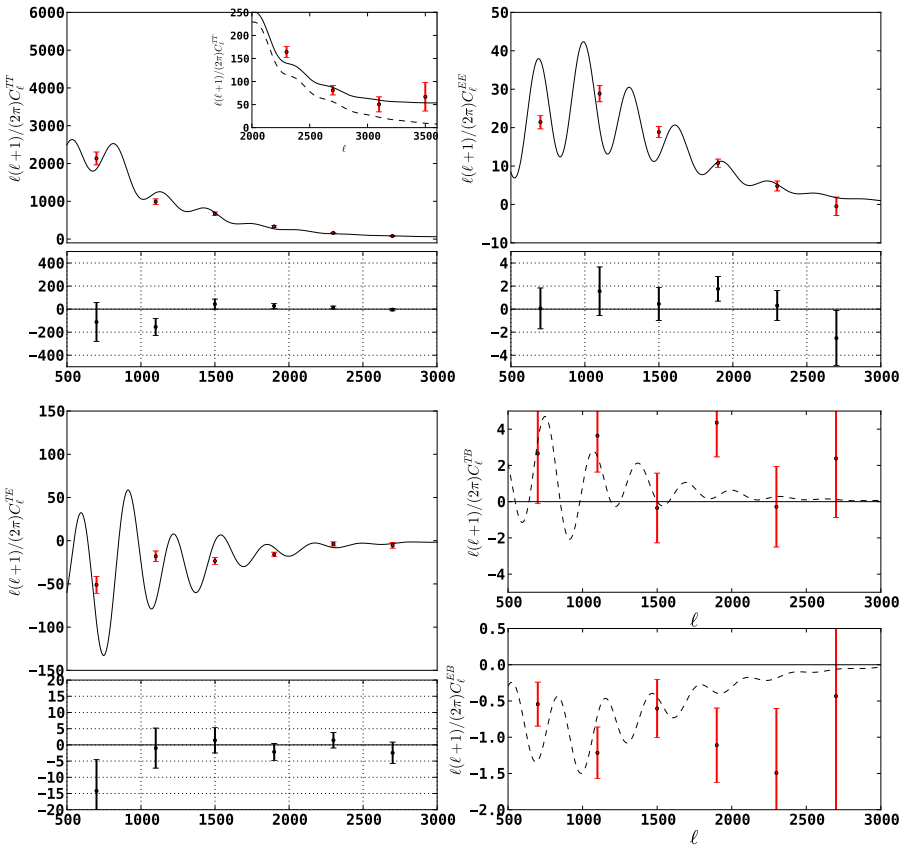

Figure 9.8: First season POLARBEAR power spectra used for calibration and cross-checks from the PCG pipeline. Red dots show the measured band powers, with vertical bars representing the uncertainty due to noise, sample variance, and beam uncertainty (the diagonal of the band power covariance matrix). The black curve is the WMAP-9 ΛCDM theory. The small panels under main spectra shows the deviation with respect to the binned theory (data - theory). The two panels at the bottom right are the TB and EB spectra, with a theoretical TB and EB spectra (dashed curves), expected if the instrument polarization angle calibration is incorrect (fitted to the data, see Sec. 9.3.2). For the TT panel, a zoom is made over the high ℓ part, where a model without foreground (dashed curve) and with foreground (solid curve) are plotted for comparison. The absolute gain correction has been applied to all spectra, but not the polarization angle calibration based on the EB spectrum. The science band is from $\ell = 500$ to $\ell = 2100$.

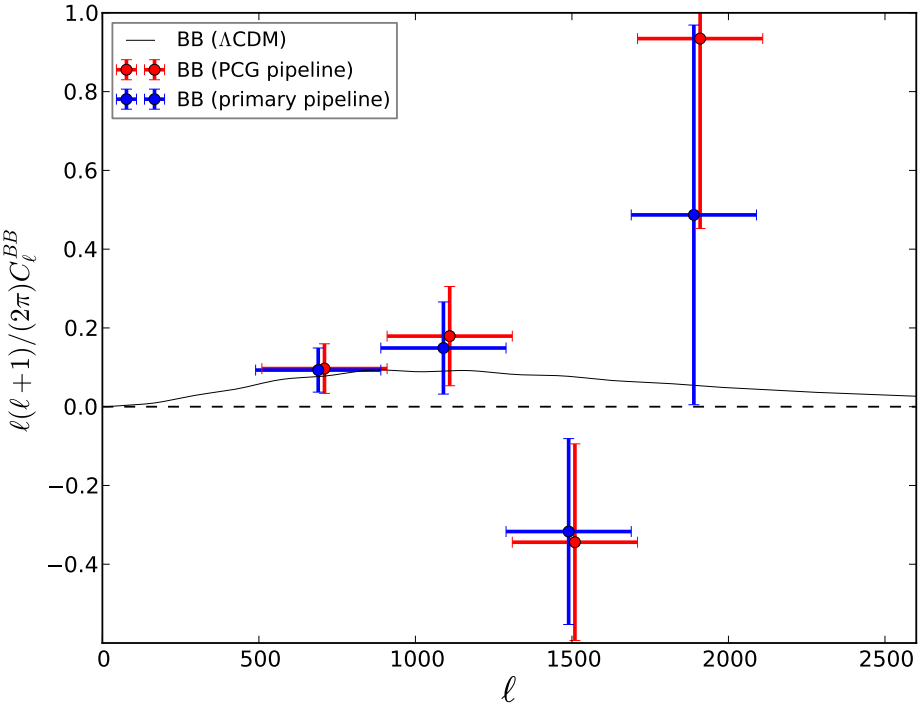

Figure 9.9: Binned BB spectrum measured using data from all three patches ($\sim$ 25deg^2) from the PCG pipeline (red) and the primary pipeline (blue) described in [POLARBEAR Collaboration 2014c]. For clarity, the measurements have been slightly shifted horizontally by $\pm$ 10 multipoles around the center of the bin. A theoretical WMAP-9 ΛCDM high-resolution BB spectrum with $A_{BB} = 1$ is shown. The uncertainty shown for the band powers is the diagonal of the band power covariance matrix, including sample variance, noise variance, beam covariance and gain uncertainty. The two pipelines give results in very good agreement.

9.3 Late calibration using power spectra

In addition to the calibration step described in Chap. 6, we use the estimated power-spectra to further calibrate our results.

9.3.1 Absolute calibration

Although we already applied an absolute and relative gain correction for each pixel in the focal plane (see Sec. 6.5), the global calibration of the whole focal plane can be slightly different from unity. A single estimate of the power spectra $\hat{C}_b^{XY}$ from the three patches is created using the band powers and their covariance matrices from Eq. 9.47. The power spectra are gain-calibrated by fitting the patch-combined TT power spectrum to the WMAP-9 ΛCDM spectrum. We find that the patch-combined and individual patch spectra are consistent with the ΛCDM model (probability-to-exceed $> 20\%$), where the binned uncertainties on each spectra are from sample variance, noise variance, and beam uncertainty.

9.3.2 Polarization angle calibration

As described in Sec. 6.7, Tau A is used to calibrate the relative pixel polarization angles. We use simulations of instrumental systematic effects in Sec. 10 to show that our uncertainty in relative pixel polarization angle, and in all other instrumental systematics, does not contribute significantly to the BB or EB spectra. This allows us to use the EB spectrum as a more precise calibration of instrument polarization angle to search for the signature of gravitational lensing in BB [Keating *et al.* 2013]. Miscalibration of the instrument polarization angle biases the measured BB spectrum and produces non-zero EB and TB spectra. The bias in BB and non-zero EB corresponding to an instrument polarization angle error $\Delta\psi \ll \pi$ are given by

$$C_\ell'^{BB} \simeq 4\Delta\psi^2 C_\ell^{EE}\,, \tag{9.49}$$

$$C_\ell'^{EB} \simeq 2\Delta\psi C_\ell^{EE}\,. \tag{9.50}$$

A cosmic rotation of polarization would produce a non-zero EB that is degenerate with an instrument polarization angle miscalibration. Either signal can be removed by rotating the instrument polarization angle to minimize the best-fit angle as measured by EB and TB. For the first season analysis, we calibrate the instrument polarization angle using the patch-combined EB spectrum, which is more sensitive than TB[11]. We then find consistency between TB and EB, and find that each patch is individually consistent with the single EB-defined instrument polarization angle, which has a statistical uncertainty of 0.20°. Note that this process is expected to minimize the measured BB, as any miscalibration of polarization angle or cosmic rotation of polarization increases the power in BB [Ferte & Grain 2014, Kaufman *et al.* 2014].

[11] We also fitted simultaneously EE, EB, TE, and EB. The resulting angle was consistent with the fit using EB only.

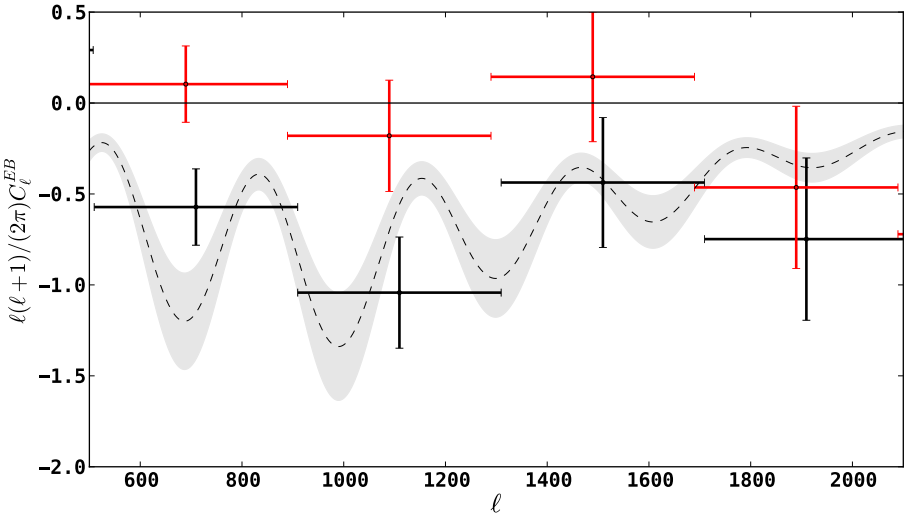

Figure 9.10: Patch-combined EB spectrum from the Tau A-derived polarization (black) and patch-combined EB spectrum after the subtraction of a bias corresponding to an instrument polarization angle error $\Delta\psi = -1.01°$ (red). The expected theoretical EB spectrum (dashed curves) corresponding to a miscalibration of -1.01°± 0.2° is shown (dashed curve with the shaded region). For clarity, the measurements have been slightly shifted horizontally by ± 10 multipoles around the center of the bin. The science band is from $\ell = 500$ to $\ell = 2100$.

The measurements in black in Fig. 9.10 shows the EB power spectrum measured using the Tau A calibration of instrument polarization from the PCG pipeline (PCG mapmaker and X^2pure). This shows that the instrument polarization angle calibrated by EB is different from the Tau A-derived polarization angle by -1.01°; the statistical uncertainty in the global EB-derived instrument polarization angle is 0.20°[12]. Given the uncertainty in the IRAM-measured angle of 0.5°, the POLARBEAR measurement uncertainty estimated in Sec. 6.7 of 0.43°, and the statistical uncertainty of in the EB-derived angle, there is slight tension between the Tau A angle measurement and the EB angle measurement. Recently, the ACTPOL team also reported an inconsistency of 1.0°± 0.5°between their Tau A angle measurement and their EB measurement [Naess *et al.* 2014] (the sign of EB is matter of convention). As of 2015, we still do not understand the reason of this tension. We show in Chap. 10 that Tau A is more than sufficient as a relative calibration between pixel angles, because relative uncertainties across the focal plane are mitigated by averaging of many pixels and sky rotation. The effect of the EB statistical uncertainty on BB is shown in Fig. 10.3, and corresponds to less than 2% contamination of the measured BB signal.

[12]The primary pipeline finds -1.08°± 0.20°.

Chapter 10

Instrumental systematics

Contents

This chapter describes our evaluation of spurious instrumental effects on the BB and EB spectra. The blindness policy adopted in the team forced us to develop several frameworks in order to assess the quality of the data without looking at the final products. I contributed to the null tests effort, especially for the PCG pipeline, but my main contribution in the systematic effect characterization is about the simulations of instrumental effects. Together with G. Fabbian, we implemented a high-resolution simulation pipeline in order to determine the effect of instrument model uncertainties on the maps and the power-spectra. This systematics pipeline is common to both the primary and the PCG pipeline (mapmaker and power-spectrum estimation). Complementary informations and results about this pipeline can be found in [Fabbian 2013].

10.1 Blind analysis

As of 2012 when we started the analysis of the first season of observation, the B-modes were not measured. Both lensing B-modes and primordial B-modes remained theoretical. The difficulty of the B-mode measurement mainly comes from the weakness of the signal. The Polarbear experiment is designed to reach high enough sensitivity to detect it. But such a high sensitivity means that we are also more prone to detect any spurious signals, which were considered until now too weak to matter.

The possibility of data analyzers biasing their result toward their own preconceptions, known as "observer bias", is a form of systematic bias that can affect

the result of an experiment [Klein & Roodman 2005]. Examples of preconceptions include theoretical predictions, the statistical significance that the team expect to obtain, or consistency with previous measurements. Since it is difficult to estimate the effects of observer bias, we employed an analysis methodology designed to minimize its impact.

Therefore we decided to adopt a blind-analysis framework, which is a standard technique to minimize observer bias, frequently employed in particle and nuclear physics, but also recently in cosmology [Araujo *et al.* 2012]. In our framework, no one in the team viewed the measured BB power-spectrum values, the deflection power spectra based on B-modes [POLARBEAR Collaboration 2014a, POLARBEAR Collaboration 2014b], or the corresponding maps, until we eliminated possible sources of observer bias by finalizing calibration, filtering, data selection, data validation and showed that all systematic uncertainties were small[1]. This framework forced us to develop quantitative tools, including null tests and simulations, that convincingly argued for analysis choices and constraints without showing the BB angular power-spectrum, thus removing the possibility that people within the team would be more convinced by an argument or method because of the BB spectrum that it produced. Other power spectra and maps were used as subsidiary information in this work, and they were unblinded in stages during the analysis procedure.

Although we stick to the blindness policy until the last moment, we are not immune to mistakes. After the unblinding the results have to go over a battery of test and pass them all without any changes to the data selection or its characterization.

10.2 Null tests framework

In order to assess the quality of the data, that is to show that the data set is internally consistent and to search for possible systematic contamination in the power-spectra, we partly rely on null tests. In a null test, the full season data set is split into two parts based on configurations associated with possible sources of contamination or miscalibration. Unlike the primary pipeline which produces biased maps, the PCG pipeline can directly work in the map domain to perform null tests as the maps are unbiased (see Sec 7.3 from [POLARBEAR Collaboration 2014c] for the biased approach). However for the PCG pipeline we decided to stick with the harmonic approach developed for the primary pipeline, in order to compare easily the results. Explicitly, a binned null power spectrum is defined by

$$\hat{C}_b^{\rm null} = \hat{C}_b^A + \hat{C}_b^B - 2\hat{C}_b^{AB}, \tag{10.1}$$

$\hat{C}_b^A$ and $\hat{C}_b^B$ are two spectra formed by cross-correlating data in the same fashion as the PCG pipeline, but for only the selected data in A and B (see Sec. 9.2). $\hat{C}_b^{AB}$

[1]The calibration and the data validation is not yet done for the second season of observation. This is the reason why I cannot show the maps and power-spectra of the second season while writing this manuscript.

corresponds to cross-pseudo-power spectra between two data sets. We primarily estimate the EB and BB null binned power spectra. The TT and EE power-spectra have a too high signal-to-noise to be useful in detecting systematics, and TB is too noisy (due to uncertainty from temperature). As stressed previously, we do not have yet the capability in the PCG pipeline to perform large runs of Monte Carlo simulations, so the results of this pipeline are used to support and validate the results from the primary pipeline. In addition, the primary pipeline checks for consistency with the results of 500 Monte Carlo simulations per null test that include signal and white noise.

The null tests are performed for several interesting splits of the data, chosen to be sensitive to various sources of systematic contamination or miscalibration. We also required that the data divisions for different null tests be reasonably independent. The data splits are:

- "First half vs. second half": probes time variation on month-long time-scales. This test is sensitive to systematic changes in the calibration, beams, telescope, and detectors, and effects due to the mid-season addition of absorptive shielding above the primary mirror.

- "Rising vs. setting": checks for systematic bias due to poor sky rotation. This is also sensitive to residual ground signal via the far sidelobe, which for RA23 sees a nearby hill in only the setting scans (see Sec. 8.4).

- "High elevation vs. low elevation": tests for contamination caused by noise or glitches due to the faster telescope motion required at higher elevation.

- "High gain vs. low gain": probes for problems due to linearity or saturation power of the detectors, and checks for miscalibration.

- "Good vs. bad weather": checks for residual problems after the PWV cut (see Sec. 6.8.1 and Chap. 7) is made.

- "Pixel type": each detector wafer is fabricated with pixels at two different polarization orientation angles. We split the data into the two individual types of pixels to check for systematic contamination or miscalibration by different cross-linking, bandwidth, or microfabrication differences.

- "Left-side vs. right-side": checks for optical distortion on one side of the focal plane versus another, or for different map coverage.

- "Left- vs. right-going subscans": probes for residual atmosphere (which is asymmetric in telescope direction due to wind), and for contamination due to vibration, which may be asymmetric in velocity.

- "Moon distance": checks for residual contamination after setting the moon proximity threshold for an observation to be considered for analysis.

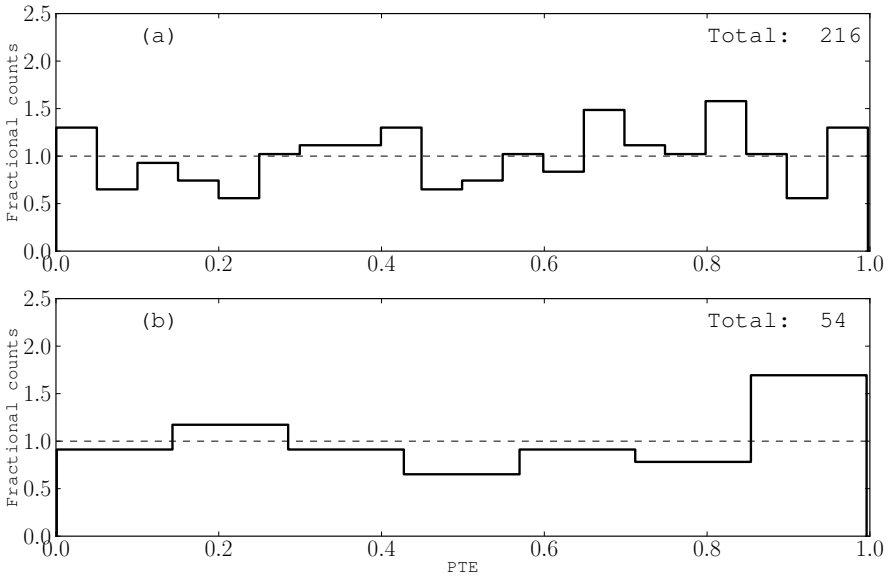

Figure 10.1: Each plot shows a PTE distribution from the null suite of the C_b^{BB} and C_b^{EB} power spectra of the three patches (PCG pipeline). (a) and (b) corresponds to distribution of $\chi^2_{\rm null}(b)$, and $\chi^2_{\rm null}$ by spectrum respectively. Each is consistent with the uniform expectation.

We also established a "Sun distance" null test, but it was highly correlated with the "high gain vs. low gain" test for the LST patch, and also correlated with the "first half vs. second half" test for RA12 and RA23, so we did not include it. For each null power spectrum bin b over $500 < b < 2100$, and for EB and BB separately, we calculate the statistic $\chi^2_{\rm null}(b) \equiv (\hat{C}_b^{\rm null}/\sigma_b)^2$, where σ_b is an analytic estimation of the corresponding standard deviation. Fig. 10.1 shows the probability-to-exceed (PTE) distribution of the $\chi^2_{\rm null}$ by (a) bin, and (b) spectrum for the three patches and for EB and BB. We require that each of these sets of PTEs be consistent with a uniform distribution, as evaluated using a KS test, requiring a p-value (probability of seeing deviation from uniformity greater than that which is observed given the hypothesis of uniformity) greater than 5%. These distributions are consistent with a uniform distribution from zero to one. In addition, those distributions are consistent with the ones from the primary pipeline, see [POLARBEAR Collaboration 2014c]. We found no evidence for systematic contamination or miscalibration based on those null tests in the POLARBEAR data set and analysis.

10.3 Simulations of instrumental effects

We apply three frameworks for the investigation of instrumental bias. We already described in the previous sections the blind analysis and the null test framework and we show that the data set is internally consistent. Special analyses of the data focused on illuminating possible effects of instrumental contamination (beams and crosstalk) are used but it will not be described here (see [POLARBEAR Collaboration 2014c]) as I didn't perform this work. Finally, signal-only simulations used to determine the effect of instrument model uncertainties on the power spectrum are described in this section.

The result of all these analyses is that none of the instrumental effects taken into account produces significant contamination of the POLARBEAR B-mode measurement. The calculated upper bound on the sum of all considered systematic contamination in the BB power-spectrum is shown in Fig. 10.3. To evaluate the effect of this systematic uncertainty on the measurement, these binned upper bound values are conservatively added linearly together with the binned upper bounds on foreground contamination given in the Tab. 4 in [POLARBEAR Collaboration 2014c]. Those values are then subtracted from the measured B-mode power-spectrum, and the significance with which we reject the null hypothesis is calculated using these reduced band powers, combined with their statistical uncertainties. The A_{BB} fit to these reduced band powers sets the lower bound of the reported asymmetric systematic uncertainty on the measured A_{BB} in Chap. 9 and [POLARBEAR Collaboration 2014c].

Table 10.1: First season estimates of the maximum contribution to the B-mode power-spectrum due to instrumental uncertainties that could bias (additively) the B-mode signal as estimated using the simulations described in Sec. 10.3. The linear sum of these effects in each band power is taken as an upper limit on the possible instrumental bias on the measurement. *Note* - † are the effects not included in the simulation pipeline for the first season (therefore not described here). They have been probed separately (special analyses). However they have been included properly in the simulation pipeline for the analysis of the second season of data.

Source of uncertainty	Measurement technique	Maximum spurious $\ell(\ell+1)C_\ell^{BB}/2\pi$ $[10^{-4}\,\mu\mathrm{K}^2]$	Effect on A_{BB}
Boresight pointing	Comparison of pointing models	5.5	0.007
Differential pointing	Planet beammaps	7.1	0.010
Instrument & relative polarization angle	C_ℓ^{EB} statistical uncertainty and Tau A	12	0.014
Pixel-pair relative gain: HWP-independent	Tau A, differential-gain map-making†	2.2	0.002
Pixel-pair relative gain: HWP-dependent	Comparison with elevation nods	9.4	0.010
Pixel-pair relative gain: drift	Compensation versus no compensation	0.41	0.001
Differential beam ellipticity†	Planet beammaps	3.3	0.001
Differential beam size†	Planet beammaps	8.3	0.003
Electrical crosstalk†	Simulation of measured level	1.7	0.002
Total possible bias	bin central ℓ: 700, 1100, 1500, 1900	40, 41, 39, 29	0.050

10.3.1 High-resolution simulation pipeline

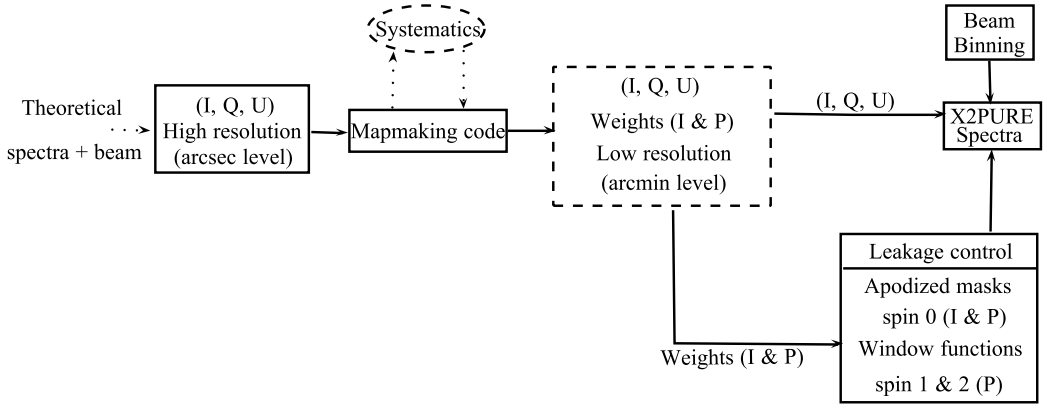

Figure 10.2: Schematic view of the pipeline used to study the impact of the instrumental effects. The systematics are introduced on-the-fly in the timestreams.

All of the instrumental effects (except beam asymmetries and crosstalk) in Tab. 10.1 were analyzed using signal-only simulations from a high-resolution simulation pipeline to highlight the effect of specific instrumental uncertainties. This pipeline is fairly general with respect to the types of systematic errors it can simulate, and is particularly well-suited to effects that involve small deflections in map-space.

$12^\circ \times 12^\circ$ sky maps with 3 arcsecond resolution pixels are created from realizations of the theoretical unlensed ΛCDM spectra multiplied by the symmetric POLARBEAR B_ℓ^2. These realizations contain TT, TE and EE temperature and polarization power, but no BB power. The maps are scanned with the actual POLARBEAR pointing and the instrumental effects in question are injected directly into the timestreams on the fly. I, Q and U maps are then reconstructed at the standard POLARBEAR map resolution. No filtering is included in this process[2]. The power spectra of these maps are then estimated using the X^{2}pure code described in the previous section, which implements the pure-pseudospectrum technique to minimize the effects of the E-to-B leakage due to the cut-sky effects. Finally, the power spectra from each patch are combined into a single power spectrum as for the real data (see Chap. 9). As a result of this framework, any non-zero EB or BB power is spurious, and a measurement of the instrumental systematic effect. This pipeline, which co-adds daily observations and then auto-correlates to measure power spectra, is slightly more sensitive to some systematic errors than the primary pipeline, which cross-correlates data from different days. Of course, instrumental effects could also distort an existing BB power-spectrum, and these effects could be understood using

[2]For the first season, we wanted to keep separated the instrumental effects and the filtering effects. Especially, the latter introduces E-to-B leakage, which overwhelms any signal from the former. However, there could be potentially a correlation term between instrumental effects and filter, which is therefore not probed here. For the analysis of the second season, we include both effects in the simulation, with a specific E-to-B leakage (due to filtering) removal.

the pipeline described above by including B-mode power in the simulated maps. We expect these effects to be small, given the already faint B-mode signal. In the future, these effects will have to be understood to precisely characterize the B-mode power spectrum. Given the statistical uncertainties reported here, we chose not to investigate effects distorting the BB power-spectrum for the analysis of the first season (although we performed some checks, as described in Sec. 10.3.4).

The method outlined above was used to investigate five systematic instrumental effects: uncertainty in instrument polarization angle; uncertainty in relative pixel polarization angles; uncertainty in instrument boresight pointing model; differential pointing between the two bolometers in a pixel; and relative gain calibration uncertainty between the two bolometers in a pixel. All of these instrumental systematic uncertainties have also been described analytically, see *e.g.* [Hu *et al.* 2003, O'Dea *et al.* 2007, Shimon *et al.* 2008, Miller *et al.* 2009, Brown *et al.* 2009a, Su *et al.* 2009]. All five were found to produce spurious BB power well below the statistical uncertainty in the measurement of C_ℓ^{BB}, and EB power substantially smaller than the signal discussed in Sec. 9.3.2. The simulated contamination is shown in Figs. 10.3 and 10.4. The results for $\ell\,(\ell+1)\,C_\ell^{BB}/2\pi$ are enumerated in Tab. 10.1. Each individual simulation is described in more detail below.

10.3.2 Uncertainty in polarization angle

All pixel polarization angles are referenced to the instrument's global reference angle. How this angle maps to the sky is the sum of different contributions, described in equation 6.39. The miscalibration of this angle has been studied analytically by [Keating *et al.* 2013]. Simulations with an incorrect instrument polarization angle were consistent with these analytic results. We simulated 100 realizations of miscalibration of the instrument polarization angle based on estimate described in Sec. 9.3.2, and found that they produced bias in C_ℓ^{EB} and C_ℓ^{BB} expected from the analytical calculation. For the POLARBEAR C_ℓ^{BB} results, the global reference angle was measured using C_ℓ^{EB} with an uncertainty of 0.20° as discussed in Sec. 9.3.2. All of the relative polarization angle uncertainties were simulated 100 times, and in each simulation the instrument angle was measured from C_ℓ^{EB}, with realistic variance in the angle added to the noiseless simulations. In this way, we calibrated the instrument angle for the systematic uncertainty simulations in the same way it is calibrated in the analysis.

10.3.3 Uncertainty in relative pixel polarization angle

The relative polarization angles of each pixel are measured using Tau A, as described in Sec. 6.7.1. We simulate the noise in this measurement with two random components (see Fig. 10.5): one component which is common across the detectors in each wafer (the uncertainty of wafer-averaged polarization angles) and a component that is a pixel-by-pixel random uncertainty within each wafer (the individual pixel

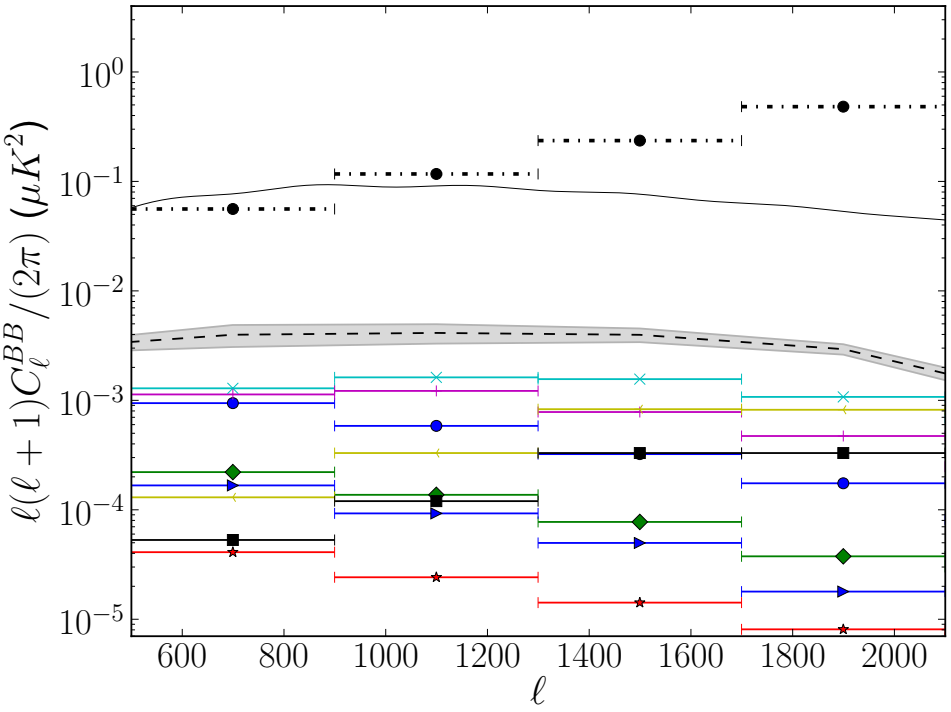

Figure 10.3: Estimated levels or upper bounds on instrumental systematic uncertainties in the C_ℓ^{BB} power spectra for the three CMB patches combined, as described in Sec. 10.3. Both the individual sources of uncertainty (solid color) and the cumulative bias coming from their combination (black dashed) are displayed after the combination of all CMB patches. The grey-shaded region show the 1σ bounds on the cumulative bias limit, after the self-calibration procedure described in Sec. 9.3.2. This is found through Monte Carlo simulations of our observations with the systematics included. The effects included in this analysis were the boresight and differential pointing uncertainty (light blue cross mark), the residual uncertainty in instrument polarization angle after self-calibration (purple plus mark), the differential beamsize and ellipticity (yellow arrow and black square mark respectively), the electrical crosstalk (blue arrow mark), the drift of the gains between two consecutive thermal source calibrator measurements (red star mark), and the HWP-independent and HWP-dependent terms of the relative gain model (green diamond and blue circle mark respectively). Also shown are the theoretical unlensed ΛCDM C_ℓ^{BB} (solid black line) and the binned statistical uncertainties (black bullets with horizontal bars).

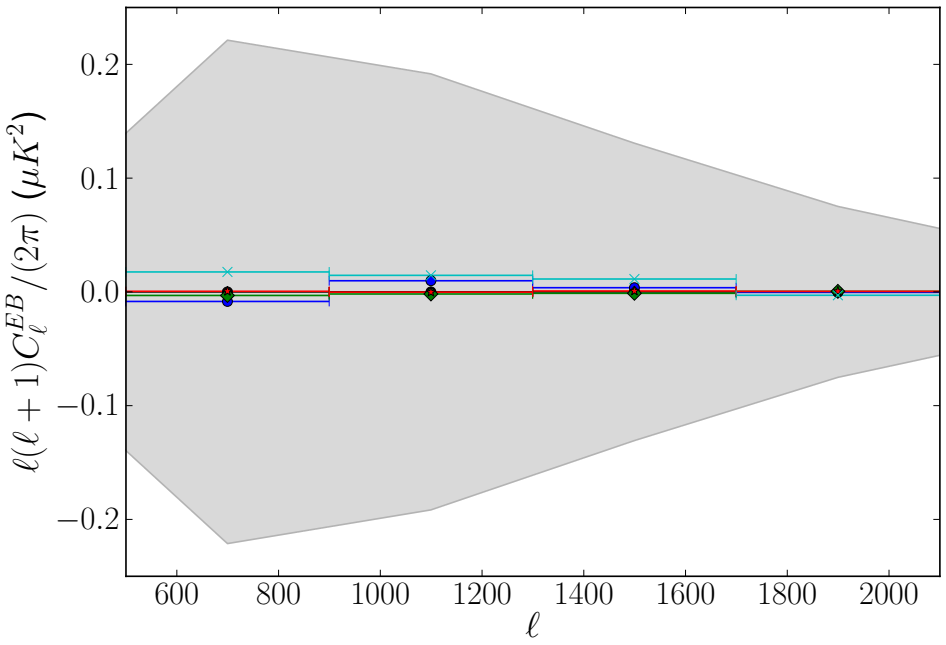

Figure 10.4: Impact of instrumental systematic uncertainties on the C_ℓ^{EB} power spectra for the three CMB patches combined, as described in Sec. 10.3. See Fig. 10.3 for details on the individual sources of uncertainty. The shaded region shows the 1σ boundaries of the uncertainty in the C_ℓ^{EB} self-calibration procedure described in Sec. 9.3.2. Note that all of the systematic uncertainties are much smaller than this statistical uncertainty.

polarization angle uncertainty). The amplitude of each is based on the measurement uncertainty discussed in Sec. 6.7.2. We also include day-to-day variations in the instrument polarization angle at the largest level allowed by measurements of Tau A. Note that we do not expect or see evidence for day-to-day variations, however this treatment accounts for any possible rotation (jitter) of the stepped and fixed HWP. The combined uncertainty in C_ℓ^{EB} and C_ℓ^{BB} due to polarization angle calibration uncertainty, after self-calibration using C_ℓ^{EB}, is shown in Figs.10.3 and 10.4. We found that the global reference angle uncertainty has a somewhat larger contribution to this uncertainty than the relative pixel polarization angle uncertainty. The grey-shaded region in Figs. 10.3 and 10.4 shows the 1σ bounds on the cumulative bias limit for the polarization angles from 100 realizations after the self-calibration procedure.

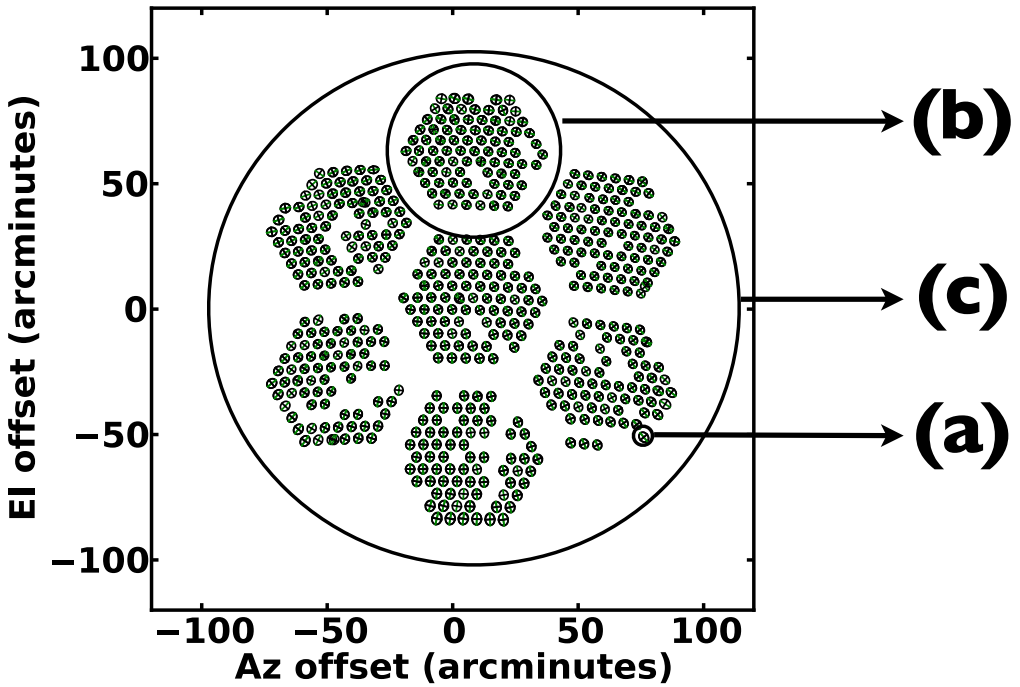

Figure 10.5: Schematic view of the three different contributions used to model the uncertainty in the polarization angles. The uncertainty in relative pixel polarization angle (Sec. 10.3.3) has two random components: a component that is a pixel-by-pixel random uncertainty within each wafer (a) and one component which is common across the detectors in each wafer (b). The uncertainty in polarization angle (Sec. 10.3.2) is a single number across all the detectors (c).

10.3.4 Uncertainty in the reconstructed telescope pointing

The effect of incorrect pointing reconstruction can be evaluated in this simulation pipeline by scanning the noiseless map into timestreams using one pointing model – the scanning pointing model – but then reconstructing the map using a second pointing model – the mapping pointing model. Measuring the spurious C_ℓ^{EB} and C_ℓ^{BB} created by this procedure is a measure of how different the pointing models are, referenced to power spectrum space. The different models are built from planets observations, Tau A observations, radio source observations, or a combination of them.

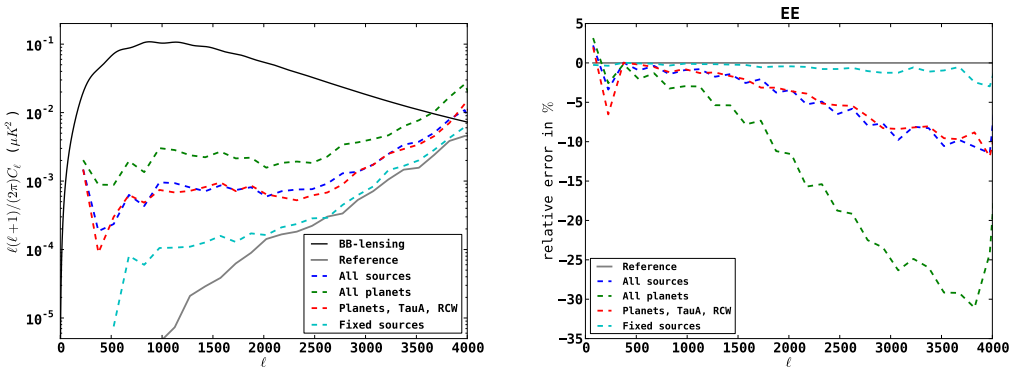

Figure 10.6: *Left:* Systematic bias on B-modes introduced by a pointing model misestimation. *Right:* Relative error between the recovered E-modes and the input E-modes for various pointing model misestimations. In all the cases, the scanning pointing model is the model of reference, but the mapping pointing model is changed. We can see the smoothing introduced by a pointing model misestimation. This level of systematic error in pointing model would have been responsible for more beam-smearing than was observed in the POLARBEAR maps and spectra.

The covariance matrix of the five parameters in the pointing model describes the constraints that the pointing data have put on the model parameters. For the pointing model to be precise enough, inaccuracies in these parameters within the space of this covariance matrix must be acceptable. 100 realizations of the pointing model within the parameter covariance matrix were generated and used as the mapping pointing model in the simulation. The mean of the spurious signal created in these simulations was found to be negligible compared to the systematic uncertainty in the pointing model described in the next paragraph.

Systematic differences in pointing reconstruction were noticed depending on the sources used to create the pointing model. To ensure that these differences were unimportant in this measurement of C_ℓ^{BB}, simulations were done with each of these systematically different pointing models used as the mapping pointing model. The largest spurious C_ℓ^{BB} and C_ℓ^{EB} found in these simulations is shown in Figs. 10.3 and 10.4. This level of systematic error in pointing model would have been responsible

for more beam-smearing than was observed in the POLARBEAR maps (as described in Sec. 6.6 and Fig. 10.6), but the spurious C_ℓ^{EB} and C_ℓ^{BB} are still small compared to the statistical uncertainties in the measurement. While sufficiently accurate for the measurement of C_ℓ^{BB}reported here, in the future, we plan to establish a more precise and consistent pointing model for POLARBEAR through more detailed pointing calibration observations.

10.3.5 Differential pointing between two pixel-pair bolometers

The differential pointing between two detectors in a pixel is measured from observations of planets. It is estimated independently for each HWP position. The mean differential pointing magnitude is 5 arcseconds (from planet measurements). This is one of the most important instrumental systematic effects because it creates spurious polarization proportional to the derivative of the CMB intensity.

Data averaged over different angles between the sky polarization and the differential pointing vector act to average out the effect of differential pointing. This averaging out is provided by sky rotation as the CMB patch rises and sets, and HWP rotation from one angle to another [Miller *et al.* 2009]. The simulations show that a majority of this leakage-mitigation provided by the POLARBEAR observation strategy has occurred after several days of observation. The Fig. 10.7 shows the spurious C_ℓ^{BB} signals created by the differential pointing from 1/4 to 17 days of observation of RA23, and how the mitigation takes place. Figs. 10.3 and 10.4 show the spurious C_ℓ^{BB} and C_ℓ^{EB} signals created by the differential pointing in an entire season for the three patches combined.

10.3.6 Uncertainty in pixel-pair relative gain

Miscalibrations of relative bolometer gains in a pixel pair will "leak" temperature signal into Q or U. A systematic miscalibration between two bolometers does not necessarily lead to a significant systematic bias in polarization maps.

The relative gain model we use has a term motivated by the polarization of the thermal calibration source which depends on the angle of the HWP, and a term motivated by variations in detector properties which has no HWP dependence. Uncertainty in either of these terms can lead to leakage of temperature into polarization. We evaluate our uncertainty in the term that changes with HWP position by comparing two different gain models with an independent determination of this term, as described in more detail below. We evaluate uncertainty in the term that does not change when the HWP rotates in two ways: via a comparison of different gain models with separate measurements of this HWP-independent term, and also via differential gain map-making described in [POLARBEAR Collaboration 2014c].

The simulation pipeline described above is used to compare relative gain models. In each case, a simulated map with no B-modes is "observed," producing timestreams using the gain model under question, and then reconstructed using the standard analysis gain model. The level of resulting C_ℓ^{BB} quantifies the difference in these

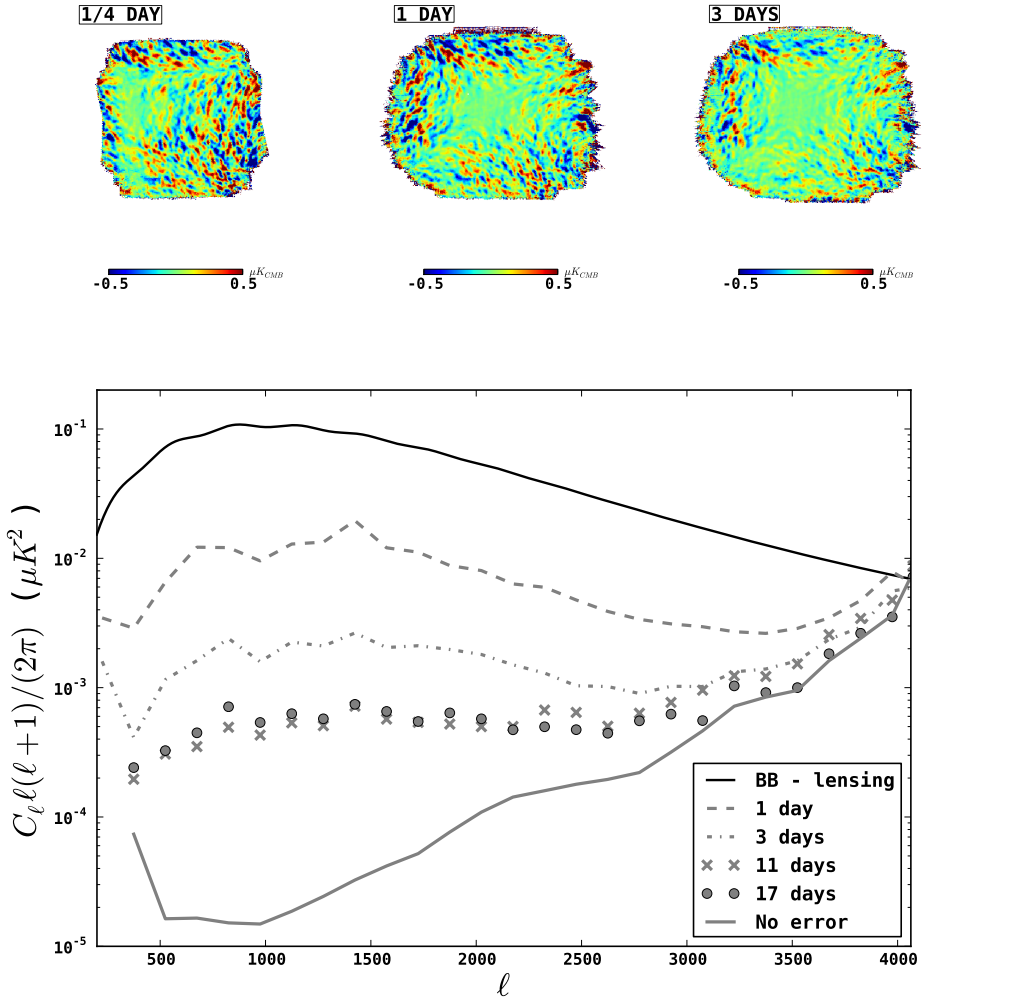

Figure 10.7: Evolution of the differential pointing effect over time as simulated by the pipeline. Residual Stokes Q maps (input-output) are shown for 1/4, 1, and 3 days of observations. We can see that after one day of observation, the patch has almost its definitive geometry and we almost keep observing the same area the next days. In principle, the averaging out provided by sky rotation should stop after one day, but because we do not span all the possible orientations every day (mainly due to data cuts), few days are required to see a saturation of the effect. In addition, the HWP provides further mitigation of the effect (15 possible positions, one per day). The plot on the bottom shows the differential pointing effect in the harmonic domain for 1, 3, 11 and 17 days of observations. In all the cases, the input B-mode spectrum has been set to zero. For comparison, the residual without differential pointing error is shown (pixelization effect), as well as the theoretical lensing B-modes.

gain models in power spectrum space.

As explained in Sec. 6.7.1, each pixel's polarization angle relative to the instrument frame is measured using Tau A. This fit also returns a single value for the average relative gain miscalibration over the course of the year, which we use to independently determine our non-HWP dependent gain model term. The difference between this measurement and the measurement by planets that is used to calibrate the pixel-pair relative gain was analyzed with the simulation pipeline. The resulting C_ℓ^{BB} bias is shown in Fig. 10.3 and enumerated in Tab. 10.1.

Elevation nods can also be used to establish the relative gain between detectors. We use this technique to determine our HWP-dependent relative gain model term and compare to the planet-derived term with the same simulation process. We find the difference to be small, as shown in Figs. 10.3 and 10.4 and Tab. 10.1.

Our normal procedure to correct for gain drift over the duration of a scan is to interpolate our gains between measurements of the thermal calibration source taken at the beginning and end of hour-long observation periods. In order to understand the impact of potential errors in this interpolation, we constructed a set of gains based only on the measurements taken at the beginning of every hour and thus use no interpolation. We find the impact, evaluated through a simulation comparing these two models, to be negligible as shown in Tab. 10.1. All four probes of the relative gain model described here show that the uncertainty in the POLARBEAR relative gain model is small compared to the statistical uncertainty in C_ℓ^{BB}. We perform a further systematic check on all sources of differential gain via a cross-correlation of temperature maps with B-mode maps, described in [POLARBEAR Collaboration 2014c], and find consistency with zero leakage to within this test's statistical power.

Chapter 11

Results from the first campaign of observation

Contents

11.1 2012-2015: fast evolution of the field

11.1.1 Recent constraints on weak gravitational lensing of the CMB

In the section 3.7, we presented the status of the field concerning the weak gravitational lensing as of 2012. From 2012, there has been the publication of an important number of observational constraints on CMB lensing using different techniques: cross-correlations with infrared-selected galaxies [Bleem *et al.* 2012, Planck Collaboration 2014d], high-redshift submillimeter galaxies [Bianchini *et al.* 2014], quasars [Sherwin *et al.* 2012, Planck Collaboration 2014d, Geach *et al.* 2013], gamma-rays [Fornengo *et al.* 2014], the cosmic shear from optical galaxies [Hand *et al.* 2013], galaxy clusters emitting in the X-ray [Planck Collaboration 2014d] and via the Sunyaev-Zel'dovich effect [Hill & Spergel 2014].

Among all different tracers, one of the most used recently is the Cosmic Infrared Background (CIB). Recent studies have measured the cross-correlation of the flux of the CIB and CMB temperature lensing [Holder *et al.* 2013, Planck Collaboration 2014e]. As far as polarization is concerned, a non-zero cross-correlation of the flux of the CIB and CMB polarization lensing has been mea-

sured by several teams [Hanson *et al.* 2013, POLARBEAR Collaboration 2014a, van Engelen *et al.* 2014], as shown in Fig. 11.1.

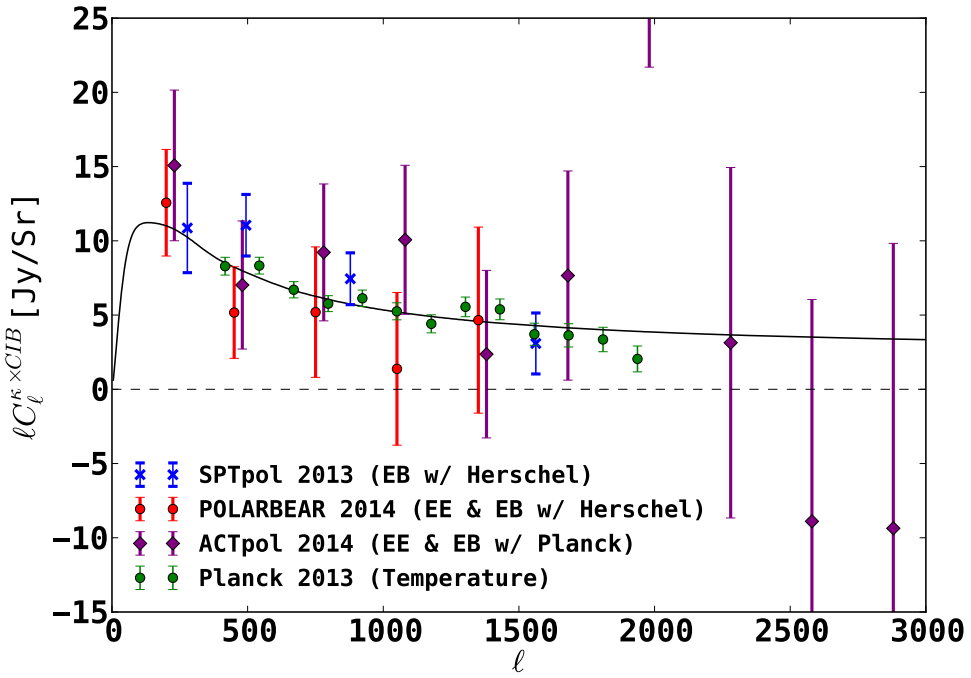

Figure 11.1: Lensing reconstruction from polarization data cross-correlated with the CIB (three-point function): SPTpol [Hanson *et al.* 2013] (EB only, in blue), Polarbear [POLARBEAR Collaboration 2014a] (EE and EB estimators combined, in red), ACTpol [van Engelen *et al.* 2014] (EE and EB estimators combined, in purple). For comparison, the Planck 2013 results using temperature data is shown. A color correction to normalize everything at 545GHz has been applied because the results for SPTpol and Polarbear use flux maps from Herschel at 500μm, whereas ACTpol and Planck results use Planck CIB maps at 545GHz. Polarbear and ACTpol use the same binning scheme, and in order to have a better visualization, the ACTpol data have been shifted horizontally (+50). The significances for polarization data are of the order of 5σ. I would like to thank A. van Engelen and D. Hanson for data.

Since the first measurement of the CMB lensing potential power spectrum from the CMB temperature data [Das *et al.* 2011], there have been several other measurements using temperature data by different experiments such as SPT [van Engelen *et al.* 2012] or the satellite Planck [Planck Collaboration 2014d]. The first measurements using polarization data have been made very recently by Polarbear [POLARBEAR Collaboration 2014b], SPTpol [Story *et al.* 2014], and Planck [Planck Collaboration 2015e] thanks to the development of large arrays of

powerful detectors enabling to reach very low instrumental noise levels and powerful data analysis tools to deal with those huge and complex data sets. Such measurements of the CMB lensing potential power-spectrum are shown in Fig. 11.2 and 11.3.

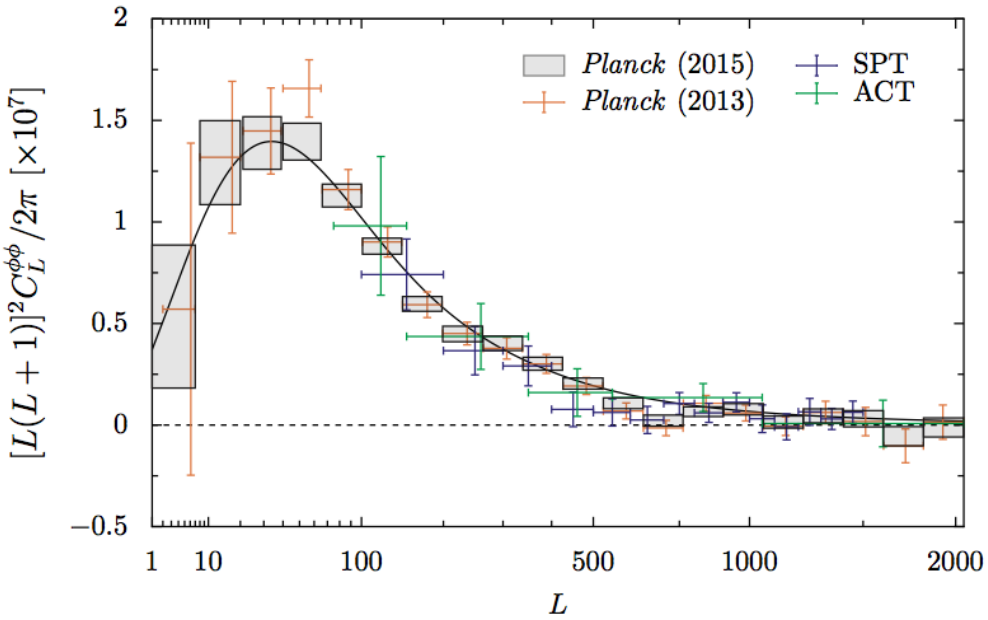

Figure 11.2: Planck 2015 full-mission and Planck 2013 nominal-mission minimum-variance lensing potential power spectrum measurements [Planck Collaboration 2015e, Planck Collaboration 2014d]), as well as those previously reported for temperature by SPT [van Engelen *et al.* 2012], and ACT [Das *et al.* 2014]. Figures taken from [Planck Collaboration 2015e].

11.1.2 Recent constraints on CMB polarization

After the first successful measurements of the E-modes polarization and the T-E cross-correlation described in Sec. 2.5, there have been several high signal-to-noise ratio measurements published in the course of 2014: Polarbear [POLARBEAR Collaboration 2014c], SPTpol [Crites *et al.* 2014], ACTpol [Naess *et al.* 2014], and Planck [Planck Collaboration 2015d]. The quest for the B-modes is however just starting. The first constraint on CMB B-modes was put in 2013 by SPTpol with an indirect detection of B-modes by combining E-mode polarization measured with estimates of the lensing potential from a Herschel-SPIRE map of the cosmic infrared background [Hanson *et al.* 2013]. By comparing the resulting template for the lensing B-mode signal to their measured B-modes, they found a non-zero correlation of 7.7σ. Shortly after, the Polarbear experiment puts out results on i) the cross-correlation of the flux of the CIB (from Herschel) and their

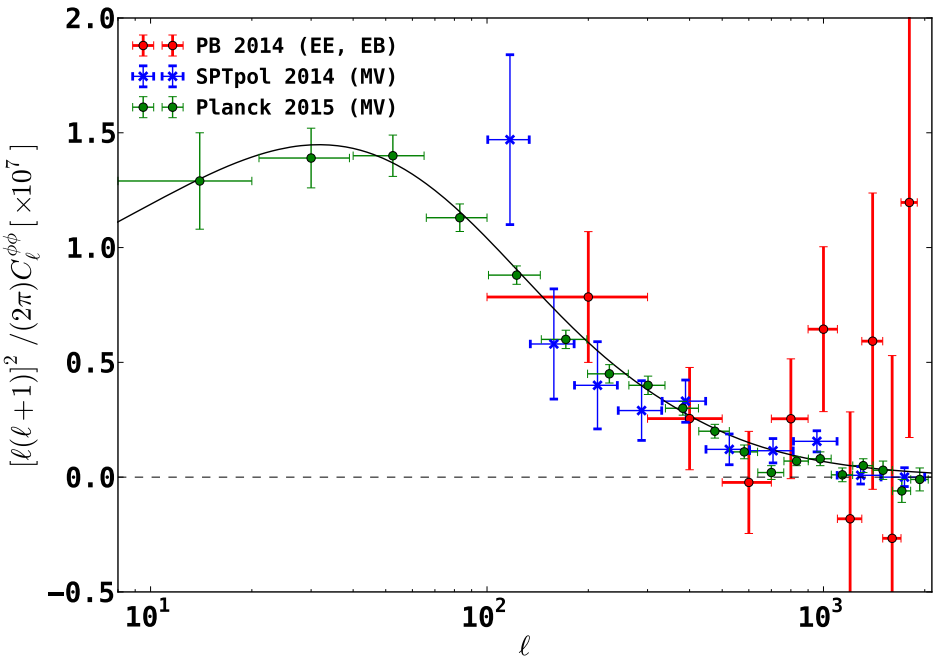

Figure 11.3: CMB lensing potential power-spectrum measurements (as in Fig. 11.2) using polarization data: POLARBEAR [POLARBEAR Collaboration 2014b] (only EE and EB estimators used, in red), SPTPOL [Story *et al.* 2014] (minimum-variance, in blue), PLANCK [Planck Collaboration 2015e] (minimum-variance, in green). As of now, the reconstruction of the lensing potential is still dominated by the temperature data, as the signal-to-noise ratio is much higher. The first measurements using polarization have been published very recently and they are expected very soon to surpass the ones in temperature as soon as experiments will reach very low instrumental noise levels. The black solid line shows the PLANCK+Lens+WP+highL best-fit ΛCDM model.

CMB polarization lensing, leading to evidence of (lensing) B-modes with a significance around 2.3σ [POLARBEAR Collaboration 2014a] and ii) the first detection of the CMB lensing potential power spectrum using the four-point function with polarization data only, rejecting the absence of polarization lensing at a significance of 4.2σ [POLARBEAR Collaboration 2014b].

Few months later, POLARBEAR announced the first direct measurement of the CMB B-mode polarization power-spectrum [POLARBEAR Collaboration 2014c]. This measurement has been done at sub-degree scales (lensing B-modes domination). Since then, ACTPOL [Naess *et al.* 2014] and SPTPOL [Keisler *et al.* 2015] released also their sub-degree B-modes power-spectrum measurements, summarized in Fig. 11.5. Concerning primordial B-modes, the BICEP2 experiment claimed a detection of B-mode polarization at degree angular scales

early 2014 [BICEP2 Collaboration 2014] (one week after POLARBEAR announcement!), but the PLANCK satellite shortly after rejected their conclusions [Planck Collaboration 2014g], pointing out that the level of polarized dust emission (at 353 GHz) was sufficient to explain the 150 GHz excess observed by BICEP2, although with relatively low signal-to-noise. This rejection has been confirmed by a joint analysis of the PLANCK and BICEP2 data sets [Ade *et al.* 2015]. Regardless of the interpretation of the excess B-mode signal, the joint analysis also reported a 7σ detection of lensing B-modes at degree scale, the tightest direct constraint so far. As of now, the quest for precision measurements of the lensing B-modes starts, and the existence of primordial B-modes is still to be proven. Both will continue to drive the main efforts in the CMB community for the upcoming years.

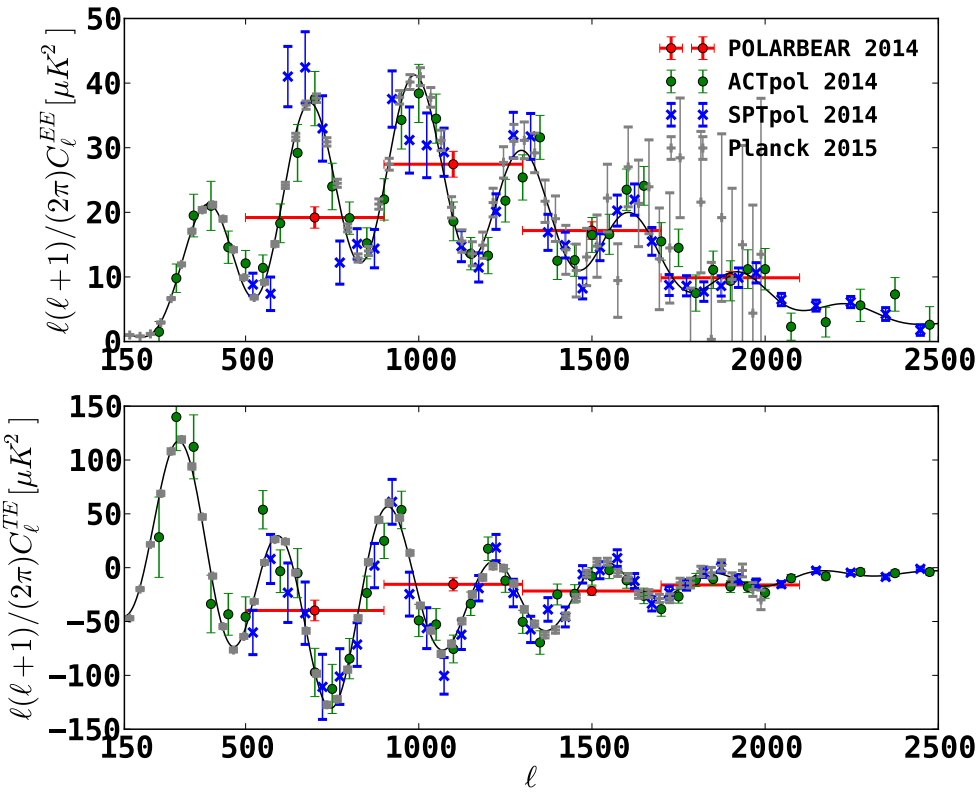

Figure 11.4: Recent measurements of EE and TE angular power spectra from small-scale experiments: POLARBEAR (PCG pipeline, red), ACTPOL [Naess *et al.* 2014] (green), SPTPOL [Keisler *et al.* 2015] (blue). The PLANCK 2015 results are also shown (grey). The black solid line shows the PLANCK+Lens+WP+highL best-fit ΛCDM model.

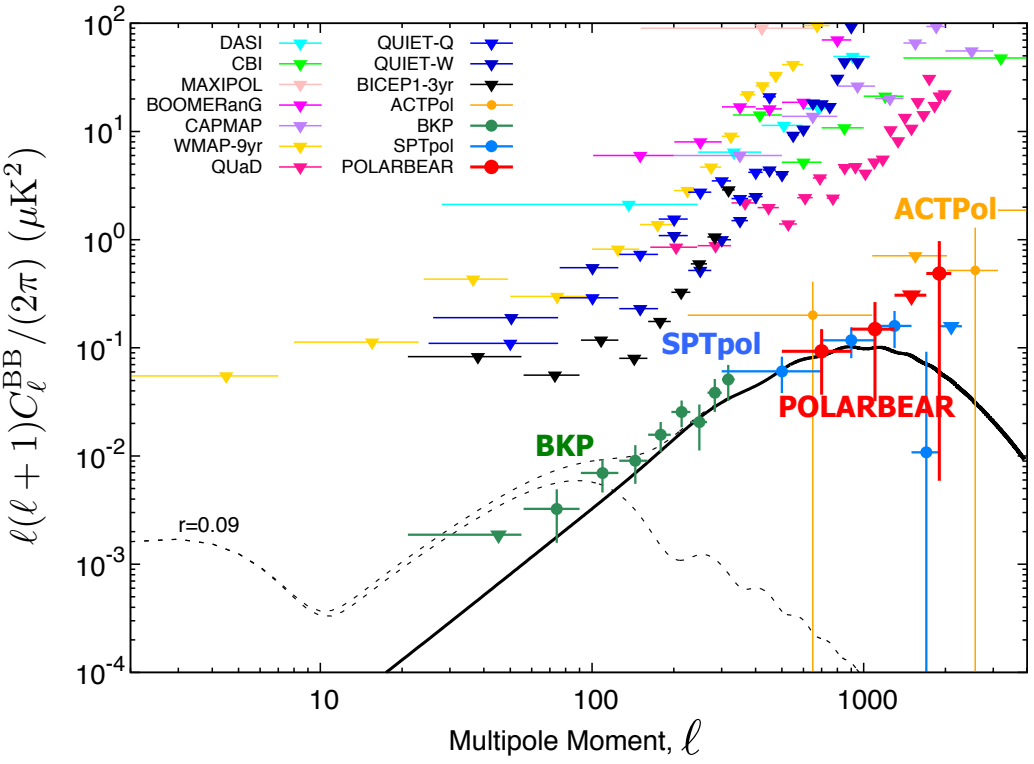

Figure 11.5: Constraints on CMB B-modes from many CMB experiments as of June 2015. Measurements from POLARBEAR [POLARBEAR Collaboration 2014c], SPTPOL [Keisler *et al.* 2015], and ACTPOL [Naess *et al.* 2014] are highlighted. They first focus on the part of the spectrum dominated by the lensing B-modes (small scales), and will progressively go down to larger scales. The major challenges when reaching small multipoles from the ground will be foreground contamination, atmosphere contamination, and to have access to a large portion of sky (after cuts). The results of the joint analysis between PLANCK and BICEP2 [Ade *et al.* 2015] (BKP) is also shown. All results with high significance have been announced between the previous year and now. Courtesy: Yuji Chinone.

11.2 Evidence for Gravitational Lensing of the CMB Polarization from Cross-correlation with the CIB

This section is a summary of the results published by the POLARBEAR Collaboration in [POLARBEAR Collaboration 2014a].

At frequencies higher than 300 GHz, the Cosmic Infrared Background (CIB) is the dominant extragalactic signal. It is composed of redshifted thermal radiation from UV-heated dust, enshrouding young stars. The CIB contains much of the energy from processes involved in structure formation [Planck Collaboration 2014e].

The CIB around CMB frequencies (submillimeter and millimeter) has a flux distribution that peaks around a redshift of $z \sim 1.5 - 2$ [Viero *et al.* 2009, Béthermin *et al.* 2013]. High correlation between the CMB lensing and CIB fields was found, with a maximal correlation coefficient of $\sim 80\%$ observed at a CIB wavelength of approximately $\sim 500\mu$m.

In this paper, we measure the gravitational lensing of CMB polarization by cross-correlating CMB polarization lensing convergence κ from POLARBEAR with maps of the cosmic infrared background from HERSCHEL. The purpose of this work is threefold: first, to measure the gravitational lensing of polarization and the lensing B-mode polarization and test that the data agree with the prediction of the standard ΛCDM cosmological model; second, to support the concurrent direct detection of the polarized lensing deflection power spectrum by POLARBEAR with an independent measurement of polarized lensing via the robust cross-correlation channel; third (and probably most importantly), to demonstrate the new, promising technique of polarization lensing reconstruction in practice. Recently, a similar cross-correlation result was published by the SPTPOL collaboration [Hanson *et al.* 2013]. This work differs in some aspects (for example, our lensing maps have higher signal-to-noise per mode on a smaller area), but it essentially confirms the SPTPOL results. This is a non-trivial check of a challenging observation, using an independent experiment with potentially different systematic errors (e.g., due to differences in map depth, scan strategy, observing location or experiment design).

We use the observations of HERSCHEL H-ATLAS survey at 500 μm as an estimate of the CIB emission in the RA23 and RA12 regions[1] and the convergence extracted from POLARBEAR maps in the same fields. We use POLARBEAR data from the first season of observation. The POLARBEAR maps come from the primary pipeline (biased maps), and the cut-sky and filter effects are corrected in the harmonic domain[2].

As described in Chap. 3, gravitational lensing by large-scale structure results in a remapping of the CMB photons by the lensing deflection field $\mathbf{d}$ (called $\boldsymbol{\alpha}$ in Chap. 3) – typically few arcminutes in magnitude – which points from the direction in which a CMB photon is received to the direction in which it was originally emitted. Lensing converts E modes into B modes and thus induces a correlation between the lensing B modes and E modes; similar correlations are also introduced between formerly independent pairs of E polarization modes. The optimal polarized quadratic estimators for lensing (described in Sec. 3.5) make use of these changes in the statistical properties of the CMB sky, and estimate lensing by measuring the characteristic lensing-induced correlation between different polarized Fourier modes. In this work, we focus only on the so-called EB and EE estimators which are given by:

$$\hat{\kappa}_{EB}(\mathbf{L}) = \int \frac{\mathrm{d}^2\mathbf{l}}{(2\pi)^2} g^{EB}(\mathbf{L},\mathbf{l}) E(\mathbf{l}) B(\mathbf{L}-\mathbf{l}) \tag{11.1}$$

[1] HERSCHEL maps and LST do not overlap.

[2] We left for future work the estimation of the CMB polarization lensing convergence κ using unbiased maps from the PCG pipeline.

$$\hat{\kappa}_{EE}(\mathbf{L}) = \int \frac{\mathrm{d}^2\mathbf{l}}{(2\pi)^2} g^{EE}(\mathbf{L},\mathbf{l}) E(\mathbf{l}) E(\mathbf{L}-\mathbf{l}) \tag{11.2}$$

where g is a function chosen as in [Hu & Okamoto 2002] to normalize and optimize the estimator, and κ is the lensing convergence, defined from the lensing deflection field $\mathbf{d}$ by $\kappa = -\nabla \cdot \mathbf{d}/2$. In the estimators, we only use scales $500 \leq \ell \leq 2700$ in the polarization maps.

Using these estimators, we calculate a noisy map of the lensing convergence field κ which can be correlated with the HERSCHEL submillimeter background maps. The correlation with the EB reconstruction channel in all the patches provides evidence at 2.3σ level of the presence of lensing generated B-modes. The combination of the EE and EB channels in all the patches provides a 4σ measurement of polarized lensing (see Figs. 11.6 & 11.1). We also perform different tests to estimate the effects of potential sources of systematic error (astrophysical and instrumental) on the polarization lensing – CIB cross-correlation. The data were analyzed using a blind analysis framework (see Sec. 10.1) and checked for spurious systematic contamination using null tests (see Sec. 10.2) and specific combinations of the data (curl and swap-field null-tests). No evidence of contamination was found.

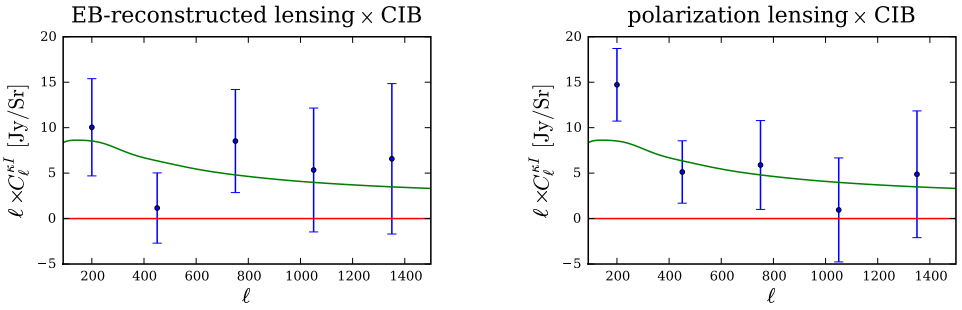

Figure 11.6: Cross-power spectra of CMB polarization lensing and the 500μm HERSCHEL CIB flux. *Left panel*: the cross power of EB-reconstructed lensing with the HERSCHEL maps; constructed from the EB estimator applied to both POLARBEAR maps, this result corresponds to 2.3σ evidence for lensing B-modes. *Right panel*: the minimum variance combination of all polarization lensing measurements cross-correlated with the HERSCHEL maps; this result corresponds to 4σ evidence for gravitational lensing of CMB polarization. The fiducial theory curve for the lensing – CIB cross-spectrum [Holder *et al.* 2013] is also shown (Note that it slightly differs from the one in Fig. 11.1, which is based on the PLANCK 2013 best-fit).

11.3 Measurement of the CMB Polarization Lensing Power Spectrum with the POLARBEAR experiment

This section is a summary of the results published by the POLARBEAR Collaboration in [POLARBEAR Collaboration 2014b].

A companion paper to this one has shown the evidence of the CMB lensing – Cosmic Infrared Background cross-correlation results using POLARBEAR data [POLARBEAR Collaboration 2014a], finding good agreement with the SPTPOL measurements [Hanson *et al.* 2013]. This cross-correlation is immune to several instrumental systematic effects but the cosmological interpretation of this measurement requires assumptions about the relation of sub-mm galaxies to the underlying mass distribution [Abazajian *et al.* 2013]. In this work, we present the first direct evidence for gravitational lensing of the polarized CMB using first season data from the POLARBEAR experiment. The calibration and data selection of those data is described in Chaps. 6 & 7. The maps are computed from the primary pipeline (biased maps), and the cut-sky and filter effects are corrected in the harmonic domain[3].

The gravitational lensing of large-scale structure on CMB changes the statistical properties of the primordial CMB signal. Lensing in fact acts as a convolution in harmonic domain and correlates different Fourier modes which are otherwise independent as discussed in Chap. 3. This off-diagonal non-Gaussian feature can be exploited to reconstruct the underlying deflection field $\mathbf{d}$ (called $\boldsymbol{\alpha}$ in Chap. 3) from the observed CMB. Quadratic estimators take advantage of this feature to measure CMB lensing. The channels chosen for the reconstruction are the so-called EE and EB channels. The power-spectrum of these estimators are given by

$$\langle d_\alpha(\mathbf{L}) d^*_\beta(\mathbf{L}')\rangle = (2\pi)^2\delta(\mathbf{L}-\mathbf{L}')(C_L^{dd} + N^{(0)}_{\alpha\beta}(L) + \text{higher-order terms}). \quad (11.3)$$

Here, C_L^{dd} is the deflection power spectrum and $N^{(0)}_{\alpha\beta}$ is the lensing reconstruction noise, α and β are chosen from $\{EE, EB\}$, however we do not use $\alpha = \beta = EE$ as our focus is on the direct probe of CMB lensing represented by the conversion of E-to-B patterns. The BB estimator also probes B-modes, but it does not make a substantial contribution to the deflection power spectrum [Hu & Okamoto 2002], so it is not used in this work. The estimator is affected by the presence of the so-called lensing Gaussian bias term $N^{(0)}_{\alpha\beta}$, which is the disconnected part in the four-point correlation, and by higher order biases that depend on the lensing field itself. Though higher order terms are found to be negligible, the $N^{(0)}_{\alpha\beta}$ has to be subtracted as often it is larger than the deflection field power spectrum. We create 500 simulated lensed and unlensed maps to estimate the Gaussian bias and establish the lensing transfer function. In addition, the data were analyzed using a blind analysis framework (see Sec. 10.1) and checked for spurious systematic contamination using null tests

[3] We left for future work the estimation of the power spectrum of the lensing deflection field using maps from the PCG pipeline.

(see Sec. 10.2), simulations, and specific combinations of data (curl and swap-field null-tests). No evidence of contamination was found. The rejection of the hypothesis of no lensing on CMB polarization has a significance of 4.2σ combining statistical and systematic errors in quadrature. We note however that since the lensing reconstruction exploits peculiar off-diagonal correlation, it is less sensitive to systematics than standard CMB analysis. The $\langle$EEEB$\rangle$ channel used alone provides an evidence of lensing generated B-modes at 3.2σ level. If we include the presence of lensing in our data set, the measured lensing amplitude is consistent at 2σ level with ΛCDM predictions (see Figs. 11.7 and 11.3).

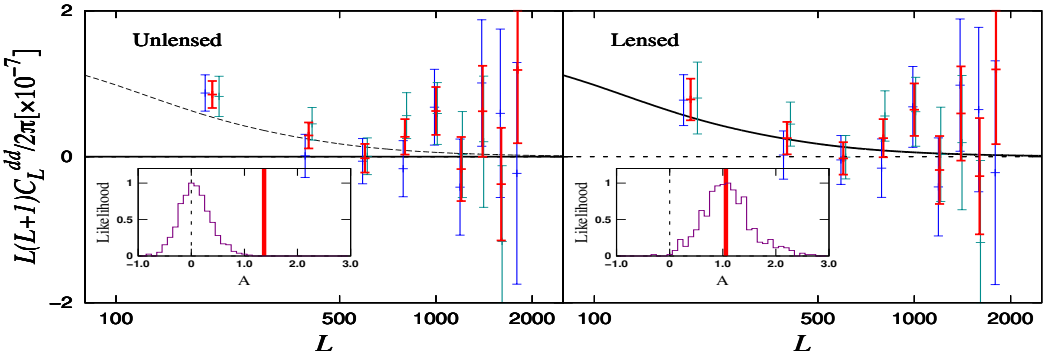

Figure 11.7: Polarization lensing power spectra co-added from the three patches and two estimators (in red). The lensing signal predicted by the ΛCDM model is shown in black dashed curve and solid curve in the left and right panel respectively. The reconstructed lensing potential from $\langle$EEEB$\rangle$ and $\langle$EBEB$\rangle$ is shown in blue and green respectively. *Left* A 4.2σ rejection of the null hypothesis of no lensing. *Right*: The same data, assuming the existence of gravitational lensing to calculate error bars, including sample variance and including the covariance between the two reconstruction channels $\langle$EEEB$\rangle$ and $\langle$EBEB$\rangle$. The histograms of the expected amplitudes of $\mathcal{A}$ from 500 unlensed and lensed simulations are shown in the inset boxes.

11.4 A Measurement of the CMB *B*-Mode Polarization Power Spectrum at Sub-Degree Scales with POLARBEAR

This manuscript describes in details the alternative pipeline (PCG pipeline) used to support and to validate the results from the primary pipeline described in [POLARBEAR Collaboration 2014c]. The calibration, data selection and instrumental systematics characterization parts (see Chaps. 6, 7, & 10) are shared between the two pipelines, but the mapmaking and power-spectrum steps adopt different approaches to the data. However, as shown in this work the results of the PCG pipeline are consistent with the results of the primary pipeline, with a mea-

surement of the CMB's B-mode angular power spectrum, C_ℓ^{BB}, over the multipole range $500 < \ell < 2100$ with a significance about 2σ.

We previously presented evidence for gravitational lensing of the CMB in POLARBEAR data using the non-Gaussianity imprinted in the CMB by large-scale structure [POLARBEAR Collaboration 2014a, POLARBEAR Collaboration 2014b]. We can calculate the combined significance with which those measurements of non-Gaussian B-modes and the C_ℓ^{BB} measurements reported here reject the hypothesis that there are no CMB lensing B-modes. In this null hypothesis, the signals are uncorrelated (when using a realization-dependent lensing bias subtraction to calculate the deflection field), so a simple quadrature sum of the rejection significance is appropriate. This calculation results in a rejection of the hypothesis that there are no lensing B-modes with 4.7σ confidence for a normal distribution.

Chapter 12

Forecasts for ongoing and future CMB experiments

Contents

Though the impact of the E-to-B leakage on the variance of the B-mode power spectrum is generally acknowledged, it is rarely included in projecting performance of planned CMB experiments or instrumental concepts from the point of view of their setting constraints on the tensor-to-scalar ratio, r. Instead, the major body of work (see [Caligiuri & Kosowsky 2014, Wu *et al.* 2014] for some recent examples) in this area is based on simplified mode-counting arguments (see, however e.g., [Smith & Zaldarriaga 2007, Stivoli *et al.* 2010] for some exceptions). This stemmed mostly from the practical reasons, as the impact of the leakage is neither calculable analytically nor analysis method independent.

In this chapter, I first describe a minimum variance quadratic estimator in the case of azimuthally symmetric patches which can be used to estimate efficiently parameters. I implemented the algebra in a massively-parallel code, nicknamed fiSher2HAT for Fisher using Scalable Spherical Harmonic Transforms (S^2HAT). Then, in collaboration with A. Ferté, J. Grain, and R. Stompor, we presented a more systematic study of the impact of the presence of the leakage on the performance forecasts of CMB B-mode experiments, by comparing results from the pure pseudospectrum method, the minimum variance quadratic estimator, and the naïve mode counting method.

12.1 Minimum variance quadratic estimator in the case of azimuthally symmetric patches

12.1.1 Fisher matrix formalism

Translating the uncertainties on the B-mode angular power spectrum reconstruction into error bars on the measured tensor-to-scalar ratio, σ_r, can be done using a Fisher matrix formalism. Consider the error bars that could be incurred by using a minimum variance quadratic estimator [Tegmark 1997b, Tegmark & de Oliveira-Costa 2001]. The estimator is defined as follows:

$$\widehat{C}_\ell^{BB} = \frac{1}{2}\sum_{\ell'} \mathbf{F}^{-1}{}_{\ell\ell'} \left\{ \mathrm{Tr}\left[\mathbf{m}^\dagger \left(\mathbf{C}^{-1} \frac{\partial \mathbf{C}}{\partial C_{\ell'}^{BB}} \mathbf{C}^{-1} \right) \mathbf{m} \right] - \tilde{N}_{\ell'} \right\}. \tag{12.1}$$

In the above, $\mathbf{C} = \left\langle \mathbf{m}\mathbf{m}^\dagger \right\rangle$ is the covariance matrix of the maps of the Stokes parameter, and $\mathbf{m}$ is the column vector composed of noisy (I, Q, U). The quantity $\tilde{N}_{\ell'}$ stands for the noise debias. Finally, $\mathbf{F}$ is the Fisher information matrix given by:

$$\mathbf{F}_{\ell\ell'} = \frac{1}{2}\mathrm{Tr}\left[\frac{\partial \mathbf{C}}{\partial C_\ell^{BB}} \mathbf{C}^{-1} \frac{\partial \mathbf{C}}{\partial C_{\ell'}^{BB}} \mathbf{C}^{-1} \right]. \tag{12.2}$$

It is then shown that the covariance of the above estimator is given by the inverse of the Fisher matrix, i.e. $\mathrm{Cov}\left(\widehat{C}_\ell^{BB}, \widehat{C}_{\ell'}^{BB}\right) = \mathbf{F}^{-1}{}_{\ell\ell'}$. We remind that this estimator is precisely built to be the quadratic estimator with the lowest variance.

If the B-mode power spectrum is indeed estimated for each multipole, ℓ (for a discussion on the binning, see the section 12.2), this directly gives the following expression for the error bars expected on r:

$$(\sigma_r)^{-2} = F_{rr} = \frac{1}{2}\mathrm{Tr}\left[\frac{\partial \tilde{\mathbf{C}}}{\partial r} \tilde{\mathbf{C}}^{-1} \frac{\partial \tilde{\mathbf{C}}}{\partial r} \tilde{\mathbf{C}}^{-1} \right], \tag{12.3}$$

with $\tilde{\mathbf{C}}$ the same covariance matrix *but* assuming that only C_ℓ^{BB} does depend on r, in line with our approach consisting in constraining the tensor-to-scalar ratio from the B-mode's measurements only[1]. In practice, the exact computation of such a Fisher matrix for current and future CMB experiments is impossible. Indeed, the brute force inversion of the covariance matrix of the maps of the Stokes parameter $\mathbf{C}$ is a $\mathcal{O}(N_{pix}^3)$ operations, where N_{pix} is the number of pixel $N_{pix} \sim 10^6$ times the number of Stokes parameters.

12.1.2 Fisher analysis with azimuthal symmetry

In the case of azimuthally symmetric patches, the numerical computation of such Fisher matrices (either $\mathbf{F}_{\ell\ell'}$ or F_{rr}), can be performed in a reasonable time using the expression found in the appendix F of Ref. [Smith 2006], and by using the S^{2}HAT

[1] More generally, all spectra (TT, EE, BB, TE) have a dependency on r.

package to perform spherical harmonic transforms [Szydlarski *et al.* 2014]. In this section, we therefore work with a specific mock survey which is a spherical cap of radius R. The covariance matrix of the maps of the Stokes parameter $\mathbf{C}$ can be written as the sum of the signal $\mathbf{S}$ and the noise $\mathbf{N}$. If we take the Fourier transform in the azimuthal coordinate ϕ, the covariance matrices $\mathbf{S}$ and $\mathbf{N}$ become block diagonal in the azimuthal number m and so their computation and the inversion become affordable (however, while $\mathbf{N}$ is diagonal in the coordinate θ, $\mathbf{S}$ is still dense in θ). Consider uncorrelated noise between pixels and isotropic in each pixels but not necessarily homogeneous, we can write the noise part of the covariance as

$$\left\langle n_Q(p) n_Q(p') \right\rangle = \left\langle n_U(p) n_U(p') \right\rangle = \eta(\theta)^2 \delta^{(2)}(p - p'), \tag{12.4}$$

where $\eta(\theta)$ is the noise profile in the θ direction and p, p' are pixels ($p = (\theta, \phi)$). For homogeneous noise, $\eta(\theta) = \eta$ a constant with units μK.arcmin. If the noise is inhomogeneous, we can take for example

$$\eta(\theta) = \eta' \Big(\frac{R}{R - \cos R} \Big) \sin\theta, \tag{12.5}$$

where R is the radius of our spherical cap. For convenience, let's change variable from {Q,U} to $\Pi^{\pm} = (\mathrm{Q} \pm i\mathrm{U})$. Taking the Fourier transform in the azimuthal coordinate ϕ, we obtain

$$\tilde{\Pi}^{\pm}_m(\theta) = \int_0^{2\pi} d\phi [Q \pm iU](\theta, \phi) e^{im\phi}. \tag{12.6}$$

The noise part of the covariance then reads

$$\left\langle \tilde{\Pi}^{+*}_m(\theta) \tilde{\Pi}^{+}_{m'}(\theta') \right\rangle = \left\langle \tilde{\Pi}^{-*}_m(\theta) \tilde{\Pi}^{-}_{m'}(\theta') \right\rangle = 4\pi \frac{\eta(\theta)^2}{\sin(\theta)} \delta(\theta - \theta') \delta_{mm'}, \tag{12.7}$$

which is diagonal in both m and θ. The change of variable makes the signal part of the covariance diagonal in m, but it is still dense in θ:

$$\left\langle \begin{pmatrix} \tilde{\Pi}^{+*}_m(\theta) \\ \tilde{\Pi}^{-*}_m(\theta) \end{pmatrix} \left(\tilde{\Pi}^{+}_{m'}(\theta') \tilde{\Pi}^{-}_{m'}(\theta') \right) \right\rangle = 4\pi^2 \delta_{mm'} \times$$
$$\sum_\ell \begin{pmatrix} (C^{EE}_\ell + C^{BB}_\ell) {}_{-2}Y_{lm}(\theta, 0) {}_{-2}Y_{lm}(\theta', 0) & (C^{EE}_\ell - C^{BB}_\ell) {}_{-2}Y_{lm}(\theta, 0) {}_{2}Y_{lm}(\theta', 0) \\ (C^{EE}_\ell - C^{BB}_\ell) {}_{2}Y_{lm}(\theta, 0) {}_{-2}Y_{lm}(\theta', 0) & (C^{EE}_\ell + C^{BB}_\ell) {}_{2}Y_{lm}(\theta, 0) {}_{2}Y_{lm}(\theta', 0) \end{pmatrix}. \tag{12.8}$$

C^{EE}_ℓ and C^{BB}_ℓ are the fiducial angular power spectra used (we assume that only C^{BB}_ℓ depends on the tensor-to-scalar ratio). Due to the azimuthal symmetry, we can notice that there is a spin symmetry, *i.e.* the signal covariance matrix remains the same under the change ${}_{\pm 2}Y_{lm}(\theta, 0) \to {}_{\mp 2}Y_{lm}(\theta, 0)$. We also assume that the angular resolution is given by an azimuthally symmetric, gaussian beam with a width σ_b so that the signal covariance matrix is given by

$$\left\langle \begin{pmatrix} \tilde{\Pi}^{+*}_m(\theta) \\ \tilde{\Pi}^{-*}_m(\theta) \end{pmatrix} \left(\tilde{\Pi}^{+}_{m'}(\theta')\tilde{\Pi}^{-}_{m'}(\theta')\right) \right\rangle = 4\pi^2\delta_{mm'} \times$$
$$\sum_\ell \begin{pmatrix} C^+_\ell \, {}_{-2}Y_{lm}(\theta,0)\,{}_{-2}Y_{lm}(\theta',0) & C^-_\ell \, {}_{-2}Y_{lm}(\theta,0)\,{}_{2}Y_{lm}(\theta',0) \\ C^-_\ell \, {}_{2}Y_{lm}(\theta,0)\,{}_{-2}Y_{lm}(\theta',0) & C^+_\ell \, {}_{2}Y_{lm}(\theta,0)\,{}_{2}Y_{lm}(\theta',0) \end{pmatrix} \tag{12.9}$$

with

$$C^\pm_\ell = (C^{EE}_\ell \pm C^{BB}_\ell) e^{-\ell(\ell+1)\sigma_b^2}. \tag{12.10}$$

Now let's consider discrete computation. We replace the continuous coordinate θ by a set of N_θ equally spaced values $\{\theta_i\}_{i=0,..,N_\theta}$, with a constant spacing $\Delta\theta$. We use an ECP pixelization scheme [Crittenden & Turok 1998], and the ${}_{\pm2}Y_{lm}$ that we use are defined in such a way that they are not orthogonal on the sphere. We need to take into account a normalization factor $W(\theta)$ which carries the resolution element information, which is the ring in the case of azimuthal symmetry (in Healpix scheme for instance the resolution element is the pixel and all pixels have equal area, but this is not the case in the ECP pixelization). The weights are explicitly added in the definition of $\Pi^\pm$

$$\Pi^\pm(\theta_i,\phi_j) = \sqrt{W(\theta_i)}(Q \pm iU)(\theta_i,\phi_j) \tag{12.11}$$

where $W(\theta_i)$ is the area of the i^{th} ring, meaning $W(\theta_i) \approx 2\pi\Delta\theta\sin(\theta_i)$ in the ECP scheme. Changing variable from pixels to rings, the equation 12.4 then reads

$$\left\langle n_Q(\theta_i,0)n_Q(\theta_j,0)\right\rangle = \left\langle n_U(\theta_i,0)n_U(\theta_j,0)\right\rangle = \eta(\theta_i)^2\frac{\delta(\theta_i-\theta_j)}{W(\theta_i)}, \tag{12.12}$$

and the Eq. 12.6 becomes

$$\tilde{\Pi}^\pm_m(\theta_i) = \int_0^{2\pi} d\phi\sqrt{W(\theta_i)}[Q+iU](\theta_i,\phi)e^{im\phi}. \tag{12.13}$$

The noise covariance elements of the previous discretized variables are then given by

$$\begin{aligned}\left\langle \tilde{\Pi}^{\pm*}_m(\theta_i)\tilde{\Pi}^{\pm}_{m'}(\theta_j)\right\rangle &= 4\pi^2\sqrt{W(\theta_i)}\sqrt{W(\theta_j)}\Big(\left\langle n_Q(\theta_i,0)n_Q(\theta_j,0)\right\rangle + \left\langle n_U(\theta_i,0)n_U(\theta_j,0)\right\rangle\Big)\delta_{mm'} \\ &= 4\pi^2\sqrt{W(\theta_i)}\sqrt{W(\theta_j)}\Big(2\eta(\theta_i)^2\frac{\delta(\theta_i-\theta_j)}{W(\theta_i)}\Big)\delta_{mm'} \\ &= 8\pi^2\eta(\theta_i)^2\delta(\theta_i-\theta_j)\delta_{mm'} \end{aligned} \tag{12.14}$$

So the full $[2N_\theta \times 2N_\theta]$ noise covariance is then given by

$$\mathbf{N}^{(m)} = 8\pi^2 \begin{pmatrix} \eta(\theta_i)^2\delta_{ij} & 0 \\ 0 & \eta(\theta_i)^2\delta_{ij} \end{pmatrix} \delta_{mm'} \tag{12.15}$$

By using 12.13, we can also construct the $[2N_\theta \times 2N_\theta]$ signal covariance

$$\mathbf{S}^{(m)} = 4\pi^2\delta_{mm'}\times \sum_{\ell=max(2,m)}^{\ell_{max}} \begin{pmatrix} C_\ell^+ A(\theta_i,\theta_j)_{-2}Y_{lm}(\theta_i,0)_{-2}Y_{lm}(\theta_j,0) & C_\ell^- A(\theta_i,\theta_j)_{-2}Y_{lm}(\theta_i,0)_2Y_{lm}(\theta_j,0) \\ C_\ell^- A(\theta_i,\theta_j)_2Y_{lm}(\theta_i,0)_{-2}Y_{lm}(\theta_j,0) & C_\ell^+ A(\theta_i,\theta_j)_2Y_{lm}(\theta_i,0)_2Y_{lm}(\theta_j,0) \end{pmatrix} \tag{12.16}$$

where $A(\theta_i,\theta_j) = \sqrt{W(\theta_i)}\sqrt{W(\theta_j)}$. The Fisher matrix is then given by summing over m and tracing over θ :

$$\mathbf{F}_{\ell\ell'} = \frac{1}{2}\sum_{m=-m_{max}}^{m_{max}} \mathrm{Tr}\big(\mathbf{S}_\ell^{(m)}(\mathbf{S}^{(m)}+\mathbf{N})^{-1}\mathbf{S}_{\ell'}^{(m)}(\mathbf{S}^{(m)}+\mathbf{N})^{-1}\big) \tag{12.17}$$

$$= \frac{1}{2}\mathrm{Tr}\big(\mathbf{S}_\ell^{(0)}(\mathbf{S}^{(0)}+\mathbf{N})^{-1}\mathbf{S}_{\ell'}^{(0)}(\mathbf{S}^{(0)}+\mathbf{N})^{-1}\big) \tag{12.18}$$

$$+ \sum_{m=1}^{m_{max}} \mathrm{Tr}\big(\mathbf{S}_\ell^{(m)}(\mathbf{S}^{(m)}+\mathbf{N})^{-1}\mathbf{S}_{\ell'}^{(m)}(\mathbf{S}^{(m)}+\mathbf{N})^{-1}\big). \tag{12.19}$$

In the expression above, $\mathbf{S}_\ell^{(m)}$ is the signal covariance matrix associated to each flat bandpower in BB (derivative of the signal covariance matrix $\mathbf{S}^{(m)}$ with respect to C_ℓ^{BB}). Then the value for the error bars expected on r, $(\sigma_r)^{-2} = F_{rr}$, is computed using derivatives of C_ℓ^{BB} over r. Exploiting the azimuthal symmetry of both signal and noise in the survey allows to decrease the computational cost of the Fisher matrix element. In the standard case, for brute force calculation it requires $\mathcal{O}(N_{pix}^3)$ to be evaluated, but in this calculation, evaluating the spin harmonics by recursion in ℓ makes the computational cost as $\mathcal{O}(N_\theta^3 m_{max})$, where N_θ is the number of rings actually used.

I implemented the method described here (minimum variance quadratic estimator in the case of azimuthally symmetric patches) in a massively parallel C code, nicknamed FISHER2HAT for Fisher using Scalable Spherical Harmonic Transforms (S^{2}HAT). The algorithmic description of this code is given in Appendix B. With the current implementation, on the Hopper machine at NERSC, a case assuming 10% of the sky (N_θ(fullsky) = 1024, $N_\theta(10\%) = 210$) with $\ell_{max} = 512$ is done in $\sim$20 minutes using 384 cores[2].

A comparison of the best r achievable at 2σ between this method and the naïve mode counting[3] (or so-called f_{sky} formula) is shown in Fig. 12.1. We always start from the North pole ($\theta = 0$) and we play with the aperture by setting θ_{max} ($\theta_{max} = \pi$ at the South pole). In this configuration, the parameter f_{sky} used in the standard

[2]If we assume a map with $N_{pix} = N_\theta^2$ pixels, the speed-up of this method over the brute force is in principle given by $\mathcal{O}(N_\theta^3/m_{max})$.

[3]The naïve mode counting is essentially used as a benchmark as such an evaluation of the statistical error bars on the B-mode reconstruction underestimates the error bars coming from any numerical methods to be applied to the data.

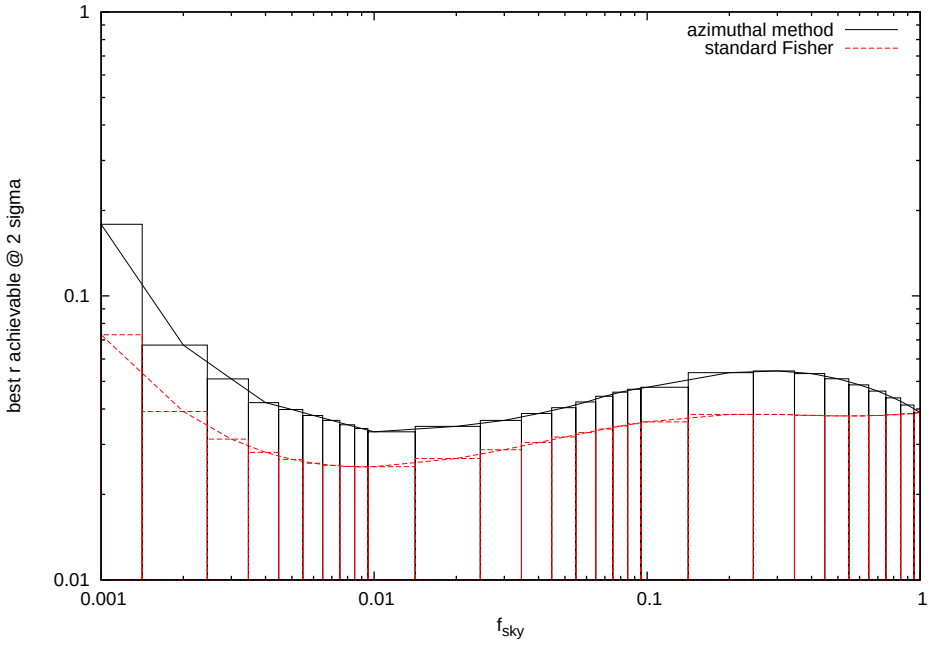

Figure 12.1: Limits on detectability on the parameter r with respect to the sky coverage by solving the equation $r = n\sqrt{(F_{rr})^{-1}}$ for $n = 2$. In other words, it is the best r achievable at 2σ for a given sky coverage. The black points show the results from the azimuthal method and the red ones from the simple f_{sky} formula as given by Eq. 12.21. The boxes represent intervals. The noise level in the full sky coverage is 80 μK.arcmin and then scale as noise$/\sqrt{f_{sky}} = cst$. The highest multipole is $l_{max} = 256$ and the resolution is $N_\theta = 512$.

Fisher approximation and the parameter θ_{max} used in the azimuthal method are related by

$$f_{sky} = \frac{1}{2}(1 - \cos\theta_{max}). \tag{12.20}$$

In the case of the naïve mode counting expression, the covariance on r is approximated by:

$$F_{rr} = \sum_{\ell=2}^{l_{max}} \frac{(2\ell+1)f_{sky}}{2}\left[C_\ell^{BB} + \eta^2 e^{\ell(\ell+1)\sigma_b^2}\right]^{-2}\left(\frac{\partial C_\ell^{BB}}{\partial r}\right)\left(\frac{\partial C_\ell^{BB}}{\partial r}\right) \tag{12.21}$$

where $C_\ell^{BB} = C_\ell^{BB,prim}(r) + C_\ell^{BB,lensed}$. In the case of full sky coverage, the azimuthal method and the mode-counting expression give the same values for r. How-

ever as soon as we decrease the sky coverage the methods show some differences. As clearly shown in Fig. 12.1, there exists a value of the sky coverage, which minimizes the best r achievable at 2σ (maximizes the signal-to-noise ratio). This optimal value of f_{sky} was already observed in [Jaffe *et al.* 2000], using only the mode-counting expression for the statistical error bars on the B-mode estimation though. We found that such an optimal value also exists using the minimum variance quadratic estimator (and more generally also for the pure pseudo-C_ℓ estimator even if this is less pronounced, see next section for more details). In the Fig. 12.2, we show the best achievable r at 2σ if we include explicitly the r dependency for the EE angular power spectrum in addition to BB. The contribution from EE to the total is weak, bringing at most 8% better constraints on the detectability of r with respect to the case with only BB power spectrum (for large sky coverage).

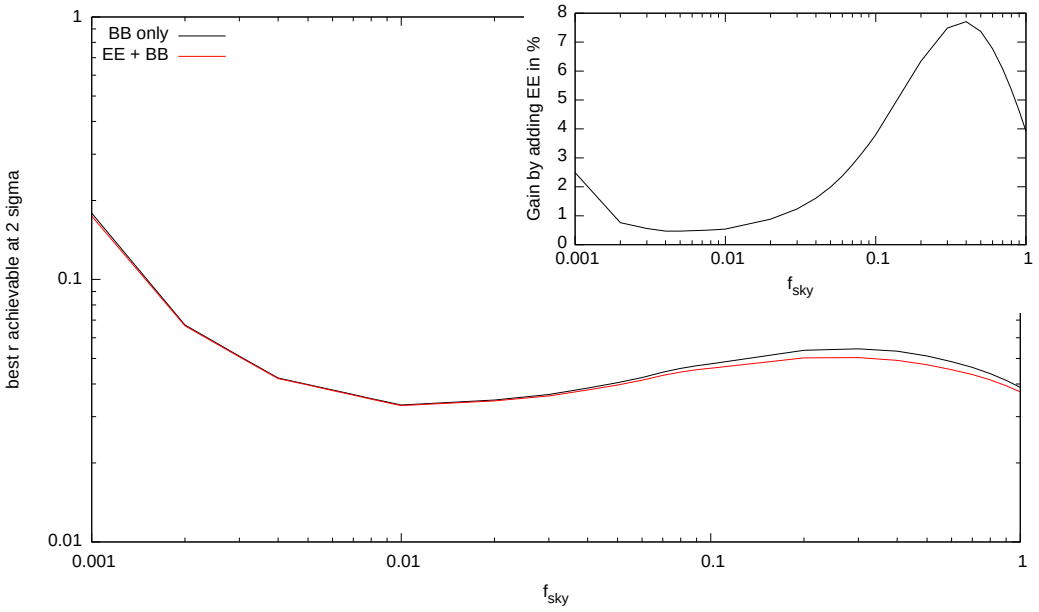

Figure 12.2: The best r achievable at 2σ computed by the azimuthal method for different sky coverages. *Black :* Computed only by using the r dependency of the BB power spectrum. *Red :* Computed by assuming that both EE and BB angular power-spectra depends on r. Only the high sky coverages are affected by adding information from the EE spectrum, but the contribution is not very significant : the gain is at best 8%, for high sky coverages. This simulation has been done for a level of noise of 80 μK.arcmin in the full sky coverage (noise scales then as noise$/\sqrt{f_{sky}} = cst$).

We note that this way of estimating the uncertainties on the power spectrum reconstruction is also relevant for maximum-likelihood approaches (it makes optimal power spectrum estimation affordable), see e.g. Ref. [Bond *et al.* 1998], assuming that we use surveys in which both the sky coverage and noise are azimuthally sym-

metric. Such surveys therefore permit benchmark comparisons between pseudo-C_ℓ estimators and optimal, likelihood-based methods, for survey sizes which are large enough that comparison would normally be infeasible as mentioned in [Smith 2006]. This was investigated recently in [Ferté *et al.* 2015], and this work is described in the Sec. 12.2.

12.2 Detecting the tensor-to-scalar ratio with the pure pseudospectrum reconstruction of B-mode

This section is based on the work (submitted to Physical Review D) in [Ferté *et al.* 2015]. In this paper, we investigate how the tensor-to-scalar ratio quantifying the amplitude of primordial gravity waves, can be constrained using the pure pseudospectrum estimation of the B-modes of CMB anisotropies (see [Smith 2006, Grain *et al.* 2009] and Sec. 9.1 for details about the pure pseudospectrum method). We also include comparisons with the minimum variance quadratic estimator described in the Sec. 12.1. We consider realistic experimental setups, including ground-based and/or balloon-borne experiments, as well as a potential satellite mission. So far, the efficiency of the pure pseudospectrum methods has been considered from the perspective of the reconstruction of the angular power spectrum only, but rarely included in projecting performance of planned CMB experiments or instrumental concepts from the point of view of their setting constraints on the tensor-to-scalar ratio. Instead, the major body of work in this area is based on simplified mode-counting arguments. The objective of this work is to fill this gap and present a more systematic study of the impact of the presence of the leakage on the performance forecasts of CMB B-mode experiments.

In the following, I summarize the main results of the paper. For more details, see [Ferté *et al.* 2015].

12.2.1 Measuring the tensor-to-scalar ratio for idealized small-scale experiment

We consider first the case of small-scale experiments in an idealized way. The observed part of the celestial sphere is assumed to be azimuthally symmetric. We work with spherical caps, with sky coverages ranging from 0.5% to 10%. The noise is an homogeneous, white noise, and its level is fixed at $n_P(1\%) = 5.75\mu$K.arcmin for $f_{\rm sky} = 1\%$ (a typical level for ongoing small-scale experiments). For a fixed sensitivity and a fixed time of observation, the noise level (in μK.arcmin) scales as:

$$n_P(f_{\rm sky}) = \sqrt{\frac{f_{\rm sky}[\%]}{1\%}} \times n_P(1\%). \tag{12.22}$$

The instrumental noise reprojected on the sky thus varies from 4.1μK.arcmin to 18μK.arcmin for an observed fraction of the sky of 0.5% and 10%, respectively. Finally, the angular resolution is given by an azimuthally symmetric, gaussian beam with a width of 8 arcminutes.

Our chosen bandpowers for reconstructing C_ℓ^{BB} are the following. The first bin starts at $\ell = 20$ and we use a constant bandwidth, $\Delta\ell = 40$. Our last bin extends up to $\ell = 1020$. In addition, for the experimental cases under consideration, we use beamwidths up to 8 arcminutes, corresponding to a cut-off of $\ell \sim 1300$.

We subsequently investigate the signal-to-noise ratio, $(\mathrm{S/N})_r = r/\sigma_r$, as a function of the sky coverage, for four values of the tensor-to-scalar ratio: $r = 0.07,\ 0.1,\ 0.15$ and 0.2. We remind that the the error bars on r are derived from the Fisher matrix *via*:

$$(\sigma_r)^{-2} = F_{rr} = \sum_{b,b'} \left(\frac{\partial \mathcal{C}_b^{BB}}{\partial r}\right) \left(\mathbf{\Sigma}^{-1}\right)_{bb'} \left(\frac{\partial \mathcal{C}_{b'}^{BB}}{\partial r}\right). \tag{12.23}$$

In the above, $\mathbf{\Sigma}_{bb'} = \mathrm{Cov}\left(\widehat{\mathcal{C}}_b^{BB}, \widehat{\mathcal{C}}_{b'}^{BB}\right)$, which stands for the covariance matrix of the reconstructed, binned angular power spectrum of the B-mode. (Note that $\widehat{C}_\ell^{BB}$ denotes the *estimator* of the angular power spectrum, C_ℓ^{BB}.) All the challenge here is to find a way to estimate $\mathbf{\Sigma}_{bb'}$. In this respect we investigated the performances of three different methods. First, we rely on a naïve mode-counting expression (or so-called f_{sky}-formula). In this case, the covariance on $\widehat{C}_\ell^{BB}$ is approximated by:

$$\mathrm{Cov}\left(\widehat{C}_\ell^{BB}, \widehat{C}_{\ell'}^{BB}\right) = \frac{2\delta_{\ell,\ell'}}{(2\ell+1)f_{\mathrm{sky}}} \left(C_\ell^{BB} + \frac{N_\ell(f_{\mathrm{sky}})}{B_\ell^2}\right)^2, \tag{12.24}$$

with N_ℓ the noise power spectrum, B_ℓ the beam of the telescope, and, f_{sky} the portion of the celestial sphere, which is observed (or kept in the analysis). The noise power spectrum scales linearly with the sky coverage. The covariance matrix for the binned power spectrum is thus given by:

$$\mathbf{\Sigma}_{bb'}^{\mathrm{naive}} = \left[\sum_{\ell\in b} (P_{b\ell})^2 \times \mathrm{Cov}\left(\widehat{C}_\ell^{BB}, \widehat{C}_\ell^{BB}\right)\right] \delta_{b,b'}, \tag{12.25}$$

where $P_{b\ell}$ is the binning operator defined in 9.24. This simple method is essentially used as a benchmark as such an evaluation of the statistical error bars on the B-mode reconstruction underestimates the error bars coming from any numerical methods to be applied to the data.

Second we consider the error bars that could be incurred by using the minimum variance quadratic estimator (QML) defined in the previous section (recall that the patches are azimuthally symmetric). On can show that the covariance matrix for the binned power spectrum is given by

$$\mathbf{\Sigma}_{bb'}^{\mathrm{QML}} = [\tilde{\mathbf{F}}^{-1}]_{bb_1} \left[P_{b_1\ell_1}\ \mathbf{F}_{\ell_1\ell_1'}\ P_{b_1'\ell_1'}\right] [(\tilde{\mathbf{F}}^{-1})^\dagger]_{b_1'b'}, \tag{12.26}$$

where summations over repeated indices (i.e. b_1, b_1' and ℓ_1, ℓ_1') is implicitly assumed, and $\dagger$ means the transpose operation. The Fisher matrix $\mathbf{F}$ is defined in 12.2, and

$$\tilde{\mathbf{F}}_{bb'} = \sum_{\ell\in b} \sum_{\ell'\in b'} P_{b\ell} F_{\ell\ell'} B_{\ell'}^2 Q_{b'\ell'}, \tag{12.27}$$

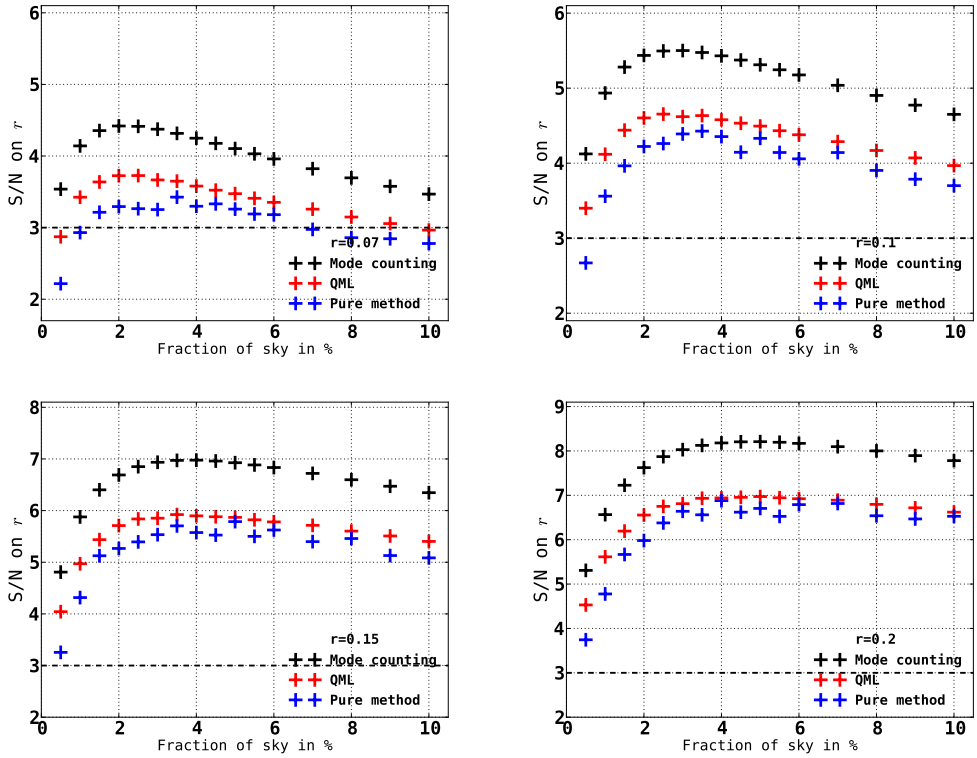

Figure 12.3: Signal-to-noise ratio for the estimation of r from B-mode polarization data shown as a function of the sky coverage. The uncertainties are computed using three different approaches: mode-counting (black crosses), minimum variance quadratic estimator (red crosses) and pure pseudospectrum estimator (blue crosses). Each panel corresponds to a different fiducial value of the tensor-to-scalar ratio, $r = 0.07,\ 0.1,\ 0.15$ and 0.2 from left to right and top to bottom.

where $Q_{b\ell}$ is the interpolation operator defined in Eq. 9.25.

Third, we make use of the X^{2}PURE code and Monte-Carlo simulations to estimate the covariance matrix expected for the pure pseudospectrum approach. In practice, the power spectrum is estimated within bandpower and the covariance matrix reconstructed from the MC simulations is directly $\mathbf{\Sigma}_{bb'}^{\rm pure}$. We ran 500 MC simulations for each value of r and each sky fraction.

Our numerical results on the signal-to-noise ratio for r are gathered in Fig. 12.3, showing $({\rm S/N})_r$ as a function of the sky coverage. Each panel corresponds to a given value of the tensor-to-scalar ratio, $r = 0.07,\ 0.1,\ 0.15$, and, 0.2 (from left to right, and top to bottom). For each panel, the black, red, and blue crosses correspond to the signal-to-noise ratio derived by using the mode-counting, the minimum variance quadratic estimator, and, the pure pseudo-C_ℓ estimator, respectively. The horizontal, dashed line marks a 3σ detection. The sky fraction varies from 0.5% to 10%, what is wide enough to sample the maximal values of the signal-to-noise ratio.

As already pointed out in [Jaffe *et al.* 2000] and highlighted in Fig. 12.3, the trade-off between sampling variance and noise variance translates into the fact that for a given value of r (and a given experimental configurations, i.e. sensitivity and time of observation), there exists a value of f_{sky} which maximizes the signal-to-noise ratio. We note that the signal-to-noise ratio keeps decreasing for $f_{\rm sky} > 10\%$. This is because for the level of noise and values of r here considered, the uncertainties on the reconstructed B-mode are noise dominated at all scales for $f_{\rm sky} > 10\%$. Similarly, the $({\rm S/N})_r$ keeps decreasing for $f_{\rm sky} < 0.5\%$, because the uncertainties on angular scales greater than a degree are dominated by the sampling variance for such low values of the sky fraction. As expected from the error bars on the reconstructed B-mode, the highest and lowest $({\rm S/N})_r$'s are respectively obtained from the mode-counting estimation, and the pure pseudospectrum estimator, while the $({\rm S/N})_r$ from the minimum variance quadratic estimator lies between those two. This is the case for all the values of the tensor-to-scalar ratio we consider. At the peak, the signal-to-noise ratio from the pure pseudospectrum estimation of the C_ℓ^{BB} is $\sim$15% ($r = 0.2$) to $\sim$20% ($r = 0.07$) smaller than the signal-to-noise ratio derived from the optimistic mode-counting. This means that the statistical significance on the measurement of r by using the optimistic mode-counting is overestimated by a factor ~ 1.25 as compared to the more realistic case of the pure pseudoreconstruction of the B-mode. Similarly, the $({\rm S/N})_r$ from the pure pseudospectrum estimator is $\sim$1.5% ($r = 0.2$) to $\sim$8% ($r = 0.07$) smaller than the signal-to-noise ratio derived from the minimum variance, quadratic estimator. Using the minimum variance, quadratic estimator to estimate the B-mode, as compared to the use of the pure pseudospectrum, thus translates into a gain in the statistical significance on the measurement of r, of a factor 1.01 to 1.08. This gain appears rather small but is larger for smaller values of the tensor-to-scalar ratio.

For the two specific cases of the mode-counting uncertainties and the minimum variance, quadratic estimator, we note that an explicit reconstruction of the power spectrum is not mandatory to derive the $({\rm S/N})_r$ in the Fisher formalism. One can indeed directly plugged in Eq. (12.23) the formulas (12.25) or (12.26). This allows for a study of the impact of binning on the signal-to-noise ratio, letting the bandwidth to vary from $\Delta\ell = 1$ (i.e. no binning) to $\Delta\ell = 40$ (i.e. the binning imposed by the use of the pseudospectrum estimator in this analysis).

The impact of binning is illustrated in Fig. 12.4 showing the signal-to-noise ratio on $r = 0.1$ as a function of the sky coverage. The overall effect of increasing the width of the bandpower is to lower the signal-to-noise ratio. The decrease is however more pronounced for the case of the minimum variance, quadratic estimator than for the mode-counting estimation of the error bars on the reconstructed B-mode. This is due to the fact that correlations between multipoles (or bandpowers) are accounted for in the minimum variance, quadratic estimator, while those are supposed to be systematically vanishing for the mode-counting estimation of the covariance matrix. This additional piece of information contained in the correlations is therefore partially lost by averaging over bandpowers. We also checked that artificially imposing those off-diagonal correlations to be zero lowered the signal-to-

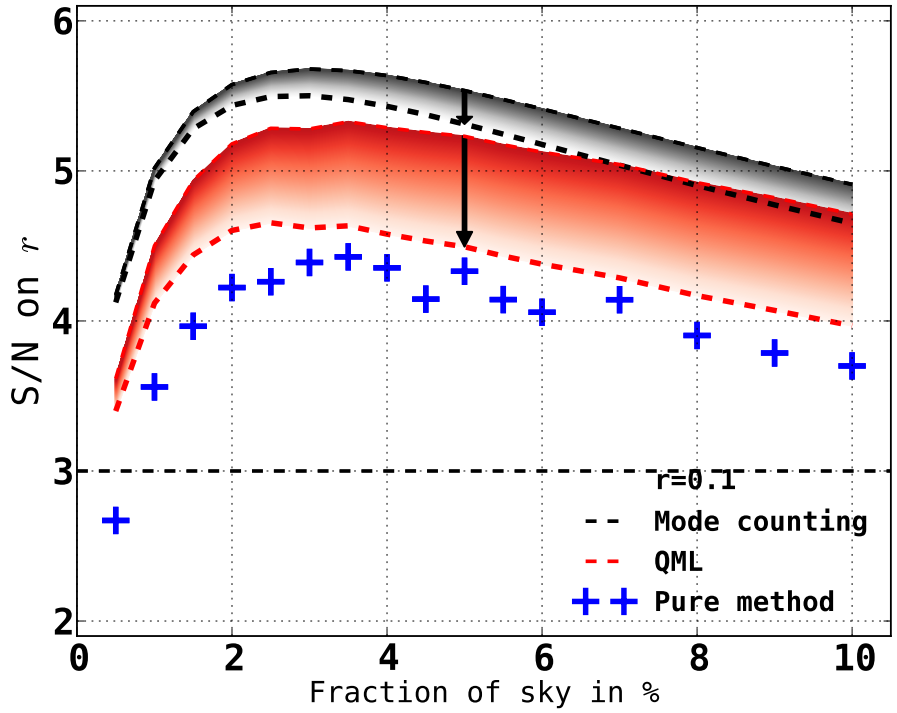

Figure 12.4: Signal-to-noise ratio for $r = 0.1$ as a function of the observed sky fraction, derived for three methods used to estimate the uncertainties on the B-mode reconstruction: mode-counting (black area), minimum variance quadratic estimator (red area), and, pure pseudospectrum estimator (blue crosses). For the two first methods, we let the bandwidth of the bins to vary from $\Delta\ell = 1$ (highest $(\mathrm{S/N})_r$) to $\Delta\ell = 40$ (lowest $(\mathrm{S/N})_r$). For the specific case of the pure pseudospectrum estimator, the reconstruction of the C_ℓ^{BB} requires to use the bandwidth $\Delta\ell = 40$ (we remind that the range of multipoles used to compute the signal-to-noise ratio is $20 \leq \ell \leq 1020$).

noise ratio in the minimum variance method, although we note that once the bins are sufficiently wide the effect of the binwidth on the $(S/N)_r$ should be weak.

12.2.2 Measuring the tensor-to-scalar ratio: selected realistic examples

In a second time, we focus on more realistic experimental cases. A spherical cap is ideal because it leads to the smallest amount of leakages for a given sky fraction since its contour has the smallest perimeter for that given sky fraction (the issue of leakages is strongly related to the detailed shape of the contours of the kept-in-the-analysis portion of the sky, as pointed by e.g. [Grain *et al.* 2009] in the Fig. 20), but it does not correspond to usual scanning strategy. Therefore, we consider three archetypal cases, which capture the main characteristics of ongoing, or being-deployed, small-scale experiments (ground-based or balloon-borne, covering ∼1% of the sky), a possible upgrade of those ground-based experiments to an array covering a rather large fraction of the sky (∼50% but keeping ∼ 36% for the analysis)[4], and, a possible satellite mission covering the entire celestial sphere (but keeping only ∼71% of the sky).

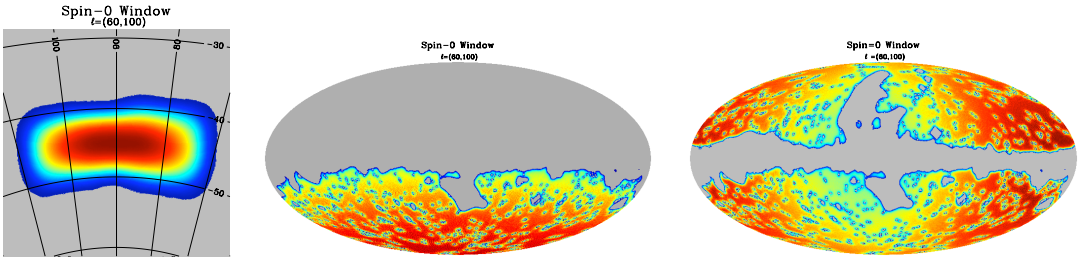

Figure 12.5: Spin-0 (scalar) component of the optimized sky apodization for a small-scale experiment covering ∼1% of the sky with inhomogeneous noise (left panel), for a possible array of ground-based telescope covering ∼36% of the sky with homogeneous noise (middle panel), and, for a possible satellite mission covering ∼71% of the sky with homogeneous noise (right panel). This sky apodization is optimized for a bandpower ranging from $\ell = 60$ to $\ell = 100$ and for a value of the tensor-to-scalar ratio $r = 0.05$.

The computation of the signal-to-noise ratio on the tensor-to-scalar ratio is done by using the same Fisher matrix formalism as employed in the previous section, however we now add the largest angular scales, from $\ell = 2$ to $\ell = 20$ gathered in one single bandpower, in the summation in Eq. 12.23. The results on the signal-to-noise ratio for r ranging from 0.001 to 0.2 are shown in Fig. 12.6. From a

[4]We note that this sky coverage is just the restriction to the galactic south hemisphere of the kept-in-the-analysis portion of the sky for a satellite mission as defined below. In reality, an array of telescopes is more likely to cover the ecliptic south hemisphere. However, from the point of view of the leakage, one or the other are equivalent (large sky areas with complicated shapes).

qualitative viewpoint, the signal-to-noise ratios computed in the framework of the mode-counting expression are always higher compared to the signal-to-noise ratios assuming the pure pseudospectrum reconstruction of B-mode (this is obviously expected from the fact that the mode-counting approach is an idealized and *underestimated* computation of the uncertainties). We observe that the overestimation using the mode-counting expression (as compared to the more realistic pure pseudospectrum reconstruction of C_ℓ^{BB}) is less marked for higher values of r. This behavior is common to the three experimental configurations here-considered, though there are differences from a quantitative viewpoint. The reason is that for low values of r, most of the information comes from the largest scales, which is precisely at those large scales that the underestimation of the B-mode reconstruction using the mode-counting formulæ is more marked. We also stress that in the case of mode-counting approach, the leakages are ignored. On the contrary, the pure pseudospectrum approach consistently includes them but corrects them in the analysis. This explains why the mode counting approach overestimates the signal-to-noise ratio on r.

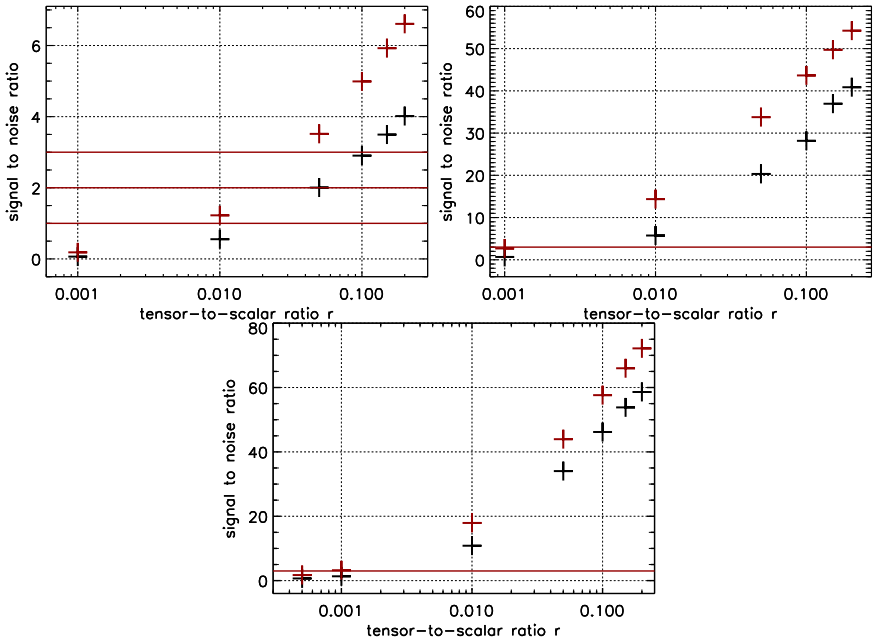

Figure 12.6: Signal-to-noise ratio for the detection of r using pure pseudospectrum reconstruction for a potential small-scale experiment ($f_{\rm sky} = 1\%$ and inhomogeneous noise at an average level of 5.75μK-arcminute) in the top left panel, an array of telescope ($f_{\rm sky} = 36\%$ and homogeneous noise at 1μK-arcminute) in the top right panel, and, a satellite mission ($f_{\rm sky} = 71\%$ and homogeneous noise at 2.2μK-arcminute) in the bottom panel. Red crosses assume the mode-counting expression for the error bars on the reconstructed C_ℓ^B and black crosses assume the pure pseudospectrum error estimated using Monte-Carlo simulations.

Adding the smallest scales (from $\ell = 2$ to $\ell = 20$) is relevant for the case of an

array of telescopes, and the case of a satellite mission. The impact of the first bin on the measurement of r is shown in Fig. 12.7 (note that we use the binned covariance for both the mode-counting and the pure pseudospectrum reconstruction of C_ℓ^{BB}). We define the relative decrease as

$$\delta = \left| \frac{(\mathrm{S/N})_r^{(\ell>20)} - (\mathrm{S/N})_r}{(\mathrm{S/N})_r} \right|, \tag{12.28}$$

with $(\mathrm{S/N})_r$ the signal-to-noise on r accounting for *all* the angular scales, and $(\mathrm{S/N})_r^{(\ell>20)}$ the signal-to-noise ratio obtained by *discarding* the first bandpower. This relative decrease can alternatively be interpreted as the relative contribution from the first bin to the signal-to-noise on r since:

$$\delta = \left| \frac{(\mathrm{S/N})_r^{(\ell<20)}}{(\mathrm{S/N})_r} \right|, \tag{12.29}$$

with $(\mathrm{S/N})_r^{(\ell<20)}$ the signal-to-noise ratio on r that would be obtained by using the first bandpower *only*. Removing the first bins can be viewed as the worst case scenario where the foreground contamination could not be removed at all on the largest scale, meaning that the information from the reionization peak is no more taken into account in the computation of the signal-to-noise ratio. This study shows

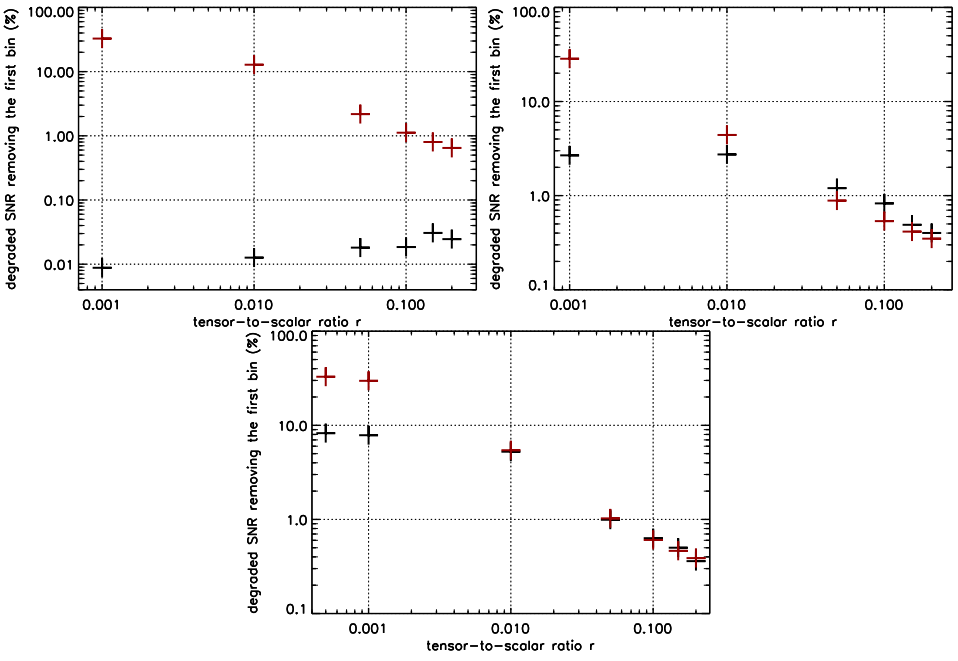

Figure 12.7: Relative decrease of the signal-to-noise ratio (in percent) if the information from the reionization peak (i.e. the first bin) is discarded from the analysis. The top left, top right and bottom panels are for the small-scale experiment, an array of telescopes and a satellite mission, respectively.

Table 12.1: The minimal accessible value r with *at least* a 3σ statistical significance, regarding the experimental setups and the estimation of the variance on the B-mode reconstruction.

	Small-scale exp.	Telescopes array	Satellite mission
Mode-counting:			
Case A	$r \gtrsim 0.038$	$r \gtrsim 0.0011$	$r \gtrsim 0.0009$
Case B	$r \gtrsim 0.04$	$r \gtrsim 0.0016$	$r \gtrsim 0.0013$
Pure pseudo-C_ℓ :			
Case A	$r \gtrsim 0.11$	$r \gtrsim 0.0051$	$r \gtrsim 0.0026$
Case B	$r \gtrsim 0.11$	$r \gtrsim 0.0053$	$r \gtrsim 0.0028$

Note. — The *case A* means that all the bins are used. The *case B* means that the information from the reionization peak (i.e. the first bin from $\ell = 2$ to $\ell = 20$) has been removed. The results in this table are obtained by linearly interpolating the computed $(\mathrm{S/N})_r$ on our grid of values of r.

the relative importance of the reionization peak. The case of a small-scale experiment is poorly affected by the removal of the first bin using the pure peudospectrum reconstruction of C_ℓ^B, the relative decrease of the signal-to-noise ratio on r being systematically smaller than 0.1%. For the case of an array of telescopes, the relative decrease ranges from 0.4% for $r = 0.2$ to roughly 3% for $r = 0.001$. Finally, in the case of a satellite mission, the relative decrease varies from 0.35% for $r = 0.2$ to 9% for $r = 0.0005$.

Thus considering the realistic forecasts performed thanks to the pure estimation of the B-mode power spectrum, we conclude that a satellite mission would give access to the largest range of r, with a minimal r value of 2.6×10^{-3}. A typical small scale experiment is indeed expected to reach only r higher than 0.1 at 3σ (note that $r = 0.05$ is detectable at 2σ). Between these two cases lies the one of an array of telescopes, which warrants a detection of the tensor-to-scalar ratio if it is higher than 5.1×10^{-3}. As a result, each studied experiments widens the accessible range of the tensor-to-scalar ratio r. In terms of minimal detectable vlaue of r, one gains about a factor 20 from small-scale experiments to an array of telescopes, and about a factor 2 between the latter and a satellite mission.

Conclusion

CMB investigations have been and continue to be a very active and exciting area of research, which has excellent potential to impact profoundly our understanding of cosmology and fundamental physics in its broadest sense, providing a new and unique window on the physics of both the early Universe and the growth of its large-scale structure.

In this thesis, I have presented my contribution to the data analysis of a ground-based CMB B-modes experiment, POLARBEAR. Notably, I have gained unique experience in all stages of data analysis of the CMB data sets, from the low-level processing of raw data to sophisticated techniques for statistically robust and numerically efficient estimation of the sky maps and their statistical properties. I have successfully applied all this expertise in the analysis of the first year of the POLARBEAR data as published in 3 papers by the collaboration. Those results include the first measurement of the CMB's B-mode angular power spectrum, C_ℓ^{BB}, over the multipole range $500 < \ell < 2100$ with a significance about 2σ [POLARBEAR Collaboration 2014c]. We also measure the gravitational lensing of CMB polarization by cross-correlating CMB polarization lensing convergence κ from POLARBEAR with maps of the cosmic infrared background from HERSCHEL [POLARBEAR Collaboration 2014a], and present the first direct evidence for gravitational lensing of the polarized CMB using first season data from the POLARBEAR experiment [POLARBEAR Collaboration 2014b].

In chapter 6, I have detailed the parts of the calibration process which I was responsible for or involved in. The calibration is a long and complex task, which requires the in-depth knowledge of the instrument. While I only had a small contribution to the calibration for the first release, mostly learning from experienced observers, I was highly involved in the calibration throughout the second release by coordinating the overall effort. In this thesis I have presented an end-to-end procedure to use consistently observations of planets in combination with external relative measurements to find the conversion from ADC counts to physical temperature units. I specifically focused on Saturn accounting for the impact from its rings in the analysis. Then from an already existing thermal-response calibration pipeline, I implemented an automated and parallelized fast pipeline which take into account results from planet observations to perform an absolute and relative calibration of pair of detectors, and correct for unwanted polarized response of each detector arising from the ground-based calibrator. Although I was not directly involved in the calibration of the instrument effective beam nor the polarization angle, I followed closely on the development of the models and the characterization of the observations by providing the inputs and feedback from the studies I led. In the context of the polarization angle calibration, I also proposed an alternative model, which may be of interest for the future work. Finally the

atmosphere correction and the pixel differencing technique were already in place when I started to work on, but I participated in the characterization of their performances from real data.

Once data are calibrated, we clean them from any instrumental or environmental contamination as described in chapter 7. It required a good understanding of the data properties and particularities of all possible pathologies. While I mostly learned from more experienced collaborators during the first season, I again took over the leadership for the second season. In particular, I redefined the data selection criteria for the second release. One of the limitations when I took over this task was the slowness of the pipeline which applies the data selection. Therefore I developed automated and parallelized pipelines to speed-up this step and to back up all the details which go through each particular run in order to compare easily different versions of data cuts.

In chapter 8, I have described the estimation of the sky maps from the cleaned and calibrated Time Ordered Data. I was an active contributor of the primary mapmaker, and a co-leader of the alternate pipeline (PCG mapmaker, entirely implemented by the APC team during my thesis). All along my thesis I optimized the performance, implemented routines, tested and used the pipelines almost daily. Part of my time was also devoted to check the consistency of both mapmakers, by running regularly test cases and implementing new features from one pipeline to the other when needed. I also worked actively on the estimation of the noise and its characterization. A special attention has been made to the correlated noise (from atmosphere and scan-synchronous signals) and its removal: time-domain visualization tools, jackknives, time-domain filtering, specific model of data (IGQU).

I was highly involved in the power-spectrum estimation throughout my thesis, and I have detailed an existing formalism and the way I applied it on POLARBEAR data on chapter 9. More specifically, I focused on the pure powerspectrum reconstruction of the B-mode, to minimize the so-called E-to-B leakage as on an incomplete sky coverage the E-mode signal is unavoidably mislabeled as B-modes and *vice-versa*. I adapted the X^2pure code for the alternate pipeline of POLARBEAR, and I maintained a version up-to-date for the collaboration at NERSC. I conducted numerous tests and proposed optimization procedures specific to small patches (geometry of the masks, optimal division of data, influence of point sources), in order to obtain the lowest uncertainties. I have also participated in conducting the massive runs of Monte Carlo simulations to validate the estimator. I have finally showed the consistency between the primary pipeline and the PCG pipeline concerning the B-modes measurement.

In chapter 10 I described the three frameworks applied for the investigation of instrumental biases. I contributed to the null tests effort, especially for the PCG pipeline, but my main contribution in the systematic effect characterization was

about the simulations of instrumental effects. I co-led the implementation and the use of a high-resolution simulation pipeline in order to determine the effect of instrument model uncertainties on the maps and the power-spectra. I have investigated several effects: global polarization angle miscalibration, uncertainty in relative pixel polarization angle, uncertainty in the reconstructed telescope pointing, differential pointing between two pixel-pair bolometers, and uncertainty in pixel-pair relative gain. The result of all these analyses is that none of the instrumental effects taken into account produce significant contamination of the POLARBEAR B-mode measurement.

In chapter 11, I described the latest results from the field, with a special focus on polarization. I have also showed POLARBEAR results along with the latest results from major ongoing experiments, namely ACTPOL, BICEP2, SPTPOL, and PLANCK. I have also summarized the first three science results of POLARBEAR.

As of now, I am co-leading and finalizing the analysis of the second season of observations (including a re-analysis of the first season), and the analysis of the third season just started. In addition, the POLARBEAR program will be upgraded very quickly with two forthcoming reincarnations of the current instrument, which are referred to as POLARBEAR-2 and SIMONS ARRAY. Their anticipated data sets alone will be already extremely powerful in constraining the cosmology. They will be however even more impressive, when co-analyzed with other data sets, including data from galaxy surveys, *e.g.*, for studying gravitational lensing effects, but also the PLANCK public data set with unique insights it will offer into the physics of the galactic emissions, which unavoidably contaminate the measured CMB signals.

In the last chapter, and in the context of those next generation CMB B-mode experiments, I presented a more systematic study of the impact of the presence of the leakage on the performance forecasts of CMB B-mode experiments, by comparing results from the pure pseudospectrum method, the minimum variance quadratic estimator, and the naïve mode counting method as described in [Ferté *et al.* 2015]. I have also described how the minimum variance quadratic estimator in the case of azimuthally symmetric patches can be used to estimate efficiently parameters. I have developed a massively-parallel code, nicknamed FISHER2HAT, to implement this idea. This code is fairly general, and it is not limited to the tensor-to-scalar ratio r.

During my thesis, I also had the chance to work on other topics, not described in this thesis, and not published yet. I would like to mention the work in collaboration with G. Fabbian and R. Stompor on the development of a bandlimited interpolation algorithm capable of preserving the bandlimit properties of the signal while reducing at the same time the computational cost. Our technique capitalizes on state-of-the-art approaches developed in the context of so-called Fast Multipole Methods. This interpolation technique should result in significant speed-ups in computation of spin-

weighted spherical harmonics on irregular grids of points as, for instance, required in CMB lensing simulations and promises to supersedes any of the methods used to date, enabling massive Monte Carlo simulations and opening the doors to new investigations, which where hitherto either limited in scope or outrightly impossible due the numerical workload they implied.

Appendix A

Mapmaking: PCG algorithm

Algorithm 1: PCG

COMMENT : *Each processor has the data for one day of observation.*

- *Inverse covariance:* $\boldsymbol{M}=\boldsymbol{A}^T\boldsymbol{F}\boldsymbol{A}$
- *RHS:* $\boldsymbol{b}=\boldsymbol{A}^T\boldsymbol{F}\boldsymbol{d}$
- *Trial solution:* $\boldsymbol{x}_0=\boldsymbol{0}$
- *Residual:* $\boldsymbol{r}_0 = \boldsymbol{b} - \boldsymbol{M}\boldsymbol{x}_0$
- *Apply preconditioner:* $\boldsymbol{z}_0=\boldsymbol{P}^{-1}\boldsymbol{r}_0$
- *Convergence:* $n_0 = \frac{|\boldsymbol{r}_0|}{|\boldsymbol{b}|}$
- *Initialize:* $\boldsymbol{p}_0 = \boldsymbol{z}_0$
- *Initialize: restart = False*
- *Define stop:* n_{min}

for k in 0,...,n_{iter} **do**

- *Apply inverse covariance matrix:* $\boldsymbol{M}\boldsymbol{p}_k$
- *Compute step:* $\alpha_k = \frac{\boldsymbol{r}_k^T\boldsymbol{z}_k}{\boldsymbol{p}_k^T\boldsymbol{M}\boldsymbol{p}_k}$
- *Move:* $\boldsymbol{x}_{k+1} = \boldsymbol{x}_k + \alpha_k\boldsymbol{p}_k$
- *New residual:* $\boldsymbol{r}_{k+1} = \boldsymbol{r}_k - \alpha_k\boldsymbol{M}\boldsymbol{p}_k$
- *New convergence:* $n_{k+1} = \frac{|\boldsymbol{r}_{k+1}|}{|\boldsymbol{b}|}$

if $n_{k+1} < n_{min}$ **then**

- *Solution is* $\boldsymbol{x}_{k+1}$
- *exit*

end if

if $k > 1$ and $n_{k+1} \geq n_k$ and not restart **then**

- $p_k = z_k$
- *restart = True*

else

- *restart = False*
- *Apply preconditioner:* $\boldsymbol{z}_{k+1}=\boldsymbol{P}^{-1}\boldsymbol{r}_{k+1}$
- *Polak-Ribière formula:* $\beta_k = \frac{\boldsymbol{z}_{k+1}^T(\boldsymbol{r}_{k+1} - \boldsymbol{r}_k)}{\boldsymbol{z}_k^T\boldsymbol{r}_k}$
- *Update the conjugate direction:* $\boldsymbol{p}_{k+1} = \boldsymbol{z}_{k+1} + \beta_k\boldsymbol{p}_k$

end if

end for k

Appendix B

fiSher2HAT: algorithm

The main code to compute the Fisher matrix is presented as Algorithm 1. The code we discuss here uses the binned C_ℓ as the parameters. However there is also the possibility of taking the parameters as the cosmological parameters that enter into the power-spectrum, as the tensor-to-scalar ratio r.

Algorithm 1 Fisher computation. Main part.

COMMENT : *Each MPI process executes a part of the m loop.*
for m in 0,..., m_{max} **do**
  - *Compute $P_{\ell m}$ using* $\mathrm{S}^2\mathrm{HAT}$ *library (fixed m, ℓ in max(2,m),..,ℓ_{max})*
  for ℓ in max(2,m),..., ℓ_{max} **do**
    - *Compute $\mathbf{S}^{(m)}$, $\mathbf{S}_\ell^{(m)}$ and $\mathbf{N}^{(m)}$*
    - *Compute Fisher elements*
  end for ℓ
  - *Update Fisher matrix*
end for m

This algorithm is made of 3 sub-algorithms plus P_{lm} computation describing the computation of the key elements. For the computation of the signal and the noise covariance matrices, we loop over the number of iso-latitude rings of the full sky map covering the Northern hemisphere (plus equatorial ring if present) and pick only observed ones. Due to this special implementation (loop over m plus ring description), the number of computed (*ie* non-zero value) Legendre polynomials P_{lm} is reduce to $N_{obs}(\ell_{max} + 1 - m)$, where N_{obs} is the number of iso-latitude rings of the full sky map observed either in the Northern hemisphere or in the Southern hemisphere (plus equatorial ring if present).

Algorithm 1.1 $\mathbf{S}^{(m)}$ computation

COMMENT : *Computation for a given m.*
for every ring r **do**
  for ℓ in max(2,m),...,ℓ_{max} **do**
    - *Compute $\mathbf{S}^{(m)}$ using Eq. [12.16]*
  end for ℓ
end for r

Algorithm 1.2 $\mathbf{S}_\ell^{(m)}$ computation

COMMENT : *Computation for a given m.*
for every ring r **do**
  for ℓ in max(2,m),...,ℓ_{max} **do**
    - *Compute* $\mathbf{S}_\ell^{(m)}$ *from derivatives of Eq. [12.16]*
  end for ℓ
end for r

Algorithm 1.3 Fisher element computation

COMMENT : *Computation for a given m.*
- *Compute* $(\mathbf{S}^{(m)} + \mathbf{N})^{-1}$ *using a Singular Value Decomposition*
for ℓ in max(2,m),...,l_{max} **do**
  - *Compute* $(\mathbf{S}^{(m)} + \mathbf{N})^{-1}\mathbf{S}_\ell^{(m)}$
end for ℓ

The code is parallelized in the way that each MPI process carries a range of m values, and the data distribution over the processors is determined by taking into account map parameters such as pixelization scheme and fraction of the observed sky, and the maximum value of ℓ (or m here). Concerning the factorization and inversion routines used in the Algorithm 1.3, I had some trouble in using Cholesky decomposition in the noiseless (or low noise) case (only $\mathbf{S}^{(m)}$ contributing). Indeed, this matrix is supposed to be positive definite, but due to numerical precision, some of its eigenvalues are very close to zero but negative, which makes the decomposition failed. Therefore a singular value decomposition is performed instead. The code also carries cut-sky analysis by choosing upper and lower observed rings. Exploiting the azimuthal symmetry of both signal and noise in the survey allows to decrease the computational cost of the Fisher matrix element. In the standard case, for brute force calculation it requires $\mathcal{O}(N_{pix}^3)$ to be evaluated, but in our calculation, evaluating the spin harmonics by recursion in ℓ makes the computational cost as $\mathcal{O}(N_\theta^3 m_{max})$, where N_θ is the number of rings.

Bibliography

[Abazajian *et al.* 2013] KN Abazajian, JE Carlstrom and AT Lee. *Neutrino Physics from the Cosmic Microwave Background and Large Scale Structure.* arXiv preprint arXiv:1309.5383, 2013. (Cited on page 223.)

[Acquaviva & Baccigalupi 2006] Viviana Acquaviva and Carlo Baccigalupi. *Dark energy records in lensed cosmic microwave background.* Physical Review D, vol. 74, no. 10, page 103510, 2006. (Cited on pages 72 and 73.)

[Ade *et al.* 2015] Peter AR Ade, N Aghanim, Z Ahmed, RW Aikin, KD Alexander, M Arnaud, J Aumont, C Baccigalupi, AJ Banday, D Barkats*et al. Joint Analysis of BICEP 2/Keck Array and Planck Data.* Physical review letters, vol. 114, no. 10, page 101301, 2015. (Cited on pages 25, 49, 75, 79, 219 and 220.)

[Albrecht & Magueijo 1999] Andreas Albrecht and Joao Magueijo. *Time varying speed of light as a solution to cosmological puzzles.* Physical Review D, vol. 59, no. 4, page 043516, 1999. (Cited on page 18.)

[Alpher & Herman 1948] Ralph A Alpher and Robert Herman. *Evolution of the Universe.* Nature, vol. 162, pages 774–775, 1948. (Cited on page 13.)

[Anderes & Paul 2012] Ethan Anderes and Debashis Paul. *Shrinking the quadratic estimator of weak lensing.* Physical Review D, vol. 85, no. 10, page 103003, 2012. (Cited on page 70.)

[Anderes 2013] Ethan Anderes. *Decomposing CMB lensing power with simulation.* Physical Review D, vol. 88, no. 8, page 083517, 2013. (Cited on page 71.)

[Araujo *et al.* 2012] D Araujo, C Bischoff, A Brizius, I Buder, Y Chinone, K Cleary, RN Dumoulin, A Kusaka, R Monsalve, SK Næss*et al. Second season QUIET observations: Measurements of the cosmic microwave background polarization power spectrum at 95 GHz.* The Astrophysical Journal, vol. 760, no. 2, page 145, 2012. (Cited on page 200.)

[Arnold *et al.* 2010] K Arnold, PAR Ade, AE Anthony, F Aubin, D Boettger, J Borrill, C Cantalupo, MA Dobbs, J Errard, D Flanigan*et al. The POLARBEAR CMB polarization experiment.* In SPIE Astronomical Telescopes+ Instrumentation, pages 77411E–77411E. International Society for Optics and Photonics, 2010. (Cited on pages 85 and 96.)

[Audren *et al.* 2013] Benjamin Audren, Julien Lesgourgues, Karim Benabed and Simon Prunet. *Conservative constraints on early cosmology with MONTE PYTHON.* Journal of Cosmology and Astroparticle Physics, vol. 2013, no. 02, page 001, 2013. (Cited on page 53.)

[Aumont *et al.* 2010] J Aumont, L Conversi, C Thum, H Wiesemeyer, E Falgarone, JF Macías-Pérez, F Piacentini, E Pointecouteau, N Ponthieu, JL Puget*et al. Measurement of the Crab nebula polarization at 90 GHz as a calibrator for CMB experiments.* Astronomy & Astrophysics, vol. 514, page A70, 2010. (Cited on pages 119 and 121.)

[Balbi *et al.* 2000] A Balbi, P Ade, J Bock, J Borrill, A Boscaleri, P De Bernardis, PG Ferreira, S Hanany, V Hristov, AH Jaffe*et al. Constraints on cosmological parameters from MAXIMA-1.* The Astrophysical Journal Letters, vol. 545, no. 1, page L1, 2000. (Cited on page 9.)

[Barron *et al.* 2014] D Barron, PAR Ade, Y Akiba, C Aleman, K Arnold, A Bender, J Borrill, S Chapman, Y Chinone, A Cukierman*et al. Development and characterization of the readout system for POLARBEAR-2.* In SPIE Astronomical Telescopes+ Instrumentation, pages 915335–915335. International Society for Optics and Photonics, 2014. (Cited on page 81.)

[Bartelmann & Schneider 2001] Matthias Bartelmann and Peter Schneider. *Weak gravitational lensing.* Physics Reports, vol. 340, no. 4, pages 291–472, 2001. (Cited on pages 60 and 65.)

[Bartlett 2001] James G Bartlett. *The cosmic microwave background: from the spectrum to the anisotropies.* New Astronomy Reviews, vol. 45, no. 4, pages 283–292, 2001. (Cited on page 14.)

[Basak *et al.* 2009] Soumen Basak, Simon Prunet and Karim Benabed. *Simulating weak lensing of CMB maps.* Astronomy & Astrophysics, vol. 508, no. 1, pages 53–62, 2009. (Cited on page 69.)

[Baumann 2009] Daniel Baumann. *TASI lectures on inflation.* arXiv preprint arXiv:0907.5424, 2009. (Cited on pages 18 and 23.)

[Bennett *et al.* 1992] CL Bennett, GF Smoot, G Hinshaw, EL Wright, A Kogut, G De Amici, SS Meyer, R Weiss, DT Wilkinson, S Gulkis*et al. Preliminary separation of galactic and cosmic microwave emission for the COBE Differential Microwave Radiometer.* The Astrophysical Journal, vol. 396, pages L7–L12, 1992. (Cited on page 78.)

[Bennett *et al.* 1996] CL Bennett, AJ Banday, KM Gorski, G Hinshaw, P Jackson, P Keegstra, A Kogut, George F Smoot, DT Wilkinson and EL Wright. *Four-year COBE DMR cosmic microwave background observations: maps and basic results.* The Astrophysical Journal Letters, vol. 464, no. 1, page L1, 1996. (Cited on page 29.)

[Bennett *et al.* 2013] CL Bennett, D Larson, JL Weiland, N Jarosik, G Hinshaw, N Odegard, KM Smith, RS Hill, B Gold, M Halpern*et al. Nine-year Wilkinson Microwave Anisotropy Probe (WMAP) observations: final maps and results.* The Astrophysical Journal Supplement Series, vol. 208, no. 2, page 20, 2013. (Cited on pages 29 and 78.)

[Benoit *et al.* 2003] Alain Benoit, P Ade, A Amblard, R Ansari, E Aubourg, S Bargot, JG Bartlett, J-Ph Bernard, RS Bhatia, A Blanchard*et al. The cosmic microwave background anisotropy power spectrum measured by Archeops.* Astronomy & Astrophysics, vol. 399, no. 3, pages L19–L23, 2003. (Cited on page 56.)

[Béthermin *et al.* 2013] Matthieu Béthermin, Lingyu Wang, Olivier Doré, Guilaine Lagache, Mark Sargent, Emanuele Daddi, Morgane Cousin and Hervé Aussel. *The redshift evolution of the distribution of star formation among dark matter halos as seen in the infrared.* Astronomy & Astrophysics, vol. 557, page A66, 2013. (Cited on page 221.)

[Bianchini *et al.* 2014] F Bianchini, P Bielewicz, A Lapi, J Gonzalez-Nuevo, C Baccigalupi, G de Zotti, L Danese, N Bourne, A Cooray, L Dunne*et al. Cross-correlation between the CMB lensing potential measured by Planck and high-z sub-mm galaxies detected by the Herschel-ATLAS survey.* arXiv preprint arXiv:1410.4502, 2014. (Cited on page 215.)

[BICEP2 Collaboration 2014] 2014 BICEP2 Collaboration. *Detection of B-mode polarization at degree angular scales by BICEP2.* Physical Review Letters, vol. 112, no. 24, page 241101, 2014. (Cited on pages 79 and 219.)

[Blanchard & Schneider 1987] A Blanchard and J Schneider. *Gravitational lensing effect on the fluctuations of the cosmic background radiation.* Astronomy and Astrophysics, vol. 184, pages 1–6, 1987. (Cited on page 59.)

[Blas *et al.* 2011] Diego Blas, Julien Lesgourgues and Thomas Tram. *The cosmic linear anisotropy solving system (CLASS). part II: approximation schemes.* Journal of Cosmology and Astroparticle Physics, vol. 2011, no. 07, page 034, 2011. (Cited on pages 53 and 63.)

[Bleem *et al.* 2012] LE Bleem, A van Engelen, GP Holder, KA Aird, R Armstrong, MLN Ashby, MR Becker, BA Benson, T Biesiadzinski, M Brodwin*et al. A Measurement of the Correlation of Galaxy Surveys with CMB Lensing Convergence Maps from the South Pole Telescope.* The Astrophysical Journal Letters, vol. 753, no. 1, page L9, 2012. (Cited on page 215.)

[Bond & Efstathiou 1984] J Richard Bond and George Efstathiou. *Cosmic background radiation anisotropies in universes dominated by nonbaryonic dark matter.* Astrophys. J, vol. 285, pages L45–L48, 1984. (Cited on page 28.)

[Bond *et al.* 1980] J Richard Bond, George Efstathiou and Joseph Silk. *Massive neutrinos and the large-scale structure of the universe.* Physical Review Letters, vol. 45, no. 24, 1980. (Cited on pages 59 and 72.)

[Bond *et al.* 1998] JR Bond, Andrew H Jaffe and L Knox. *Estimating the power spectrum of the cosmic microwave background.* Physical Review D, vol. 57, no. 4, page 2117, 1998. (Cited on page 233.)

[Bonifacio & Molaro 1997] Piercarlo Bonifacio and Paolo Molaro. *The Primordial lithium abundance.* Monthly Notices of the Royal Astronomical Society, vol. 285, no. 4, pages 847–861, 1997. (Cited on page 11.)

[Borrill 1999] Julian Borrill. *The challenge of data analysis for future CMB observations.* arXiv preprint astro-ph/9903204, 1999. (Cited on page 140.)

[Brandt *et al.* 1994] WN Brandt, CR Lawrence, ACS Readhead, JN Pakianathan and TM Fiola. *Separation of foreground radiation from cosmic microwave background anisotropy using multifrequency measurements.* The Astrophysical Journal, vol. 424, pages 1–21, 1994. (Cited on page 78.)

[Brown *et al.* 2009a] Michael L Brown, Anthony Challinor, Chris E North, Bradley R Johnson, Daniel O'Dea and David Sutton. *Impact of modulation on CMB B-mode polarization experiments.* Monthly Notices of the Royal Astronomical Society, vol. 397, no. 2, pages 634–656, 2009. (Cited on page 206.)

[Brown *et al.* 2009b] ML Brown, P Ade, J Bock, M Bowden, G Cahill, PG Castro, S Church, T Culverhouse, RB Friedman, K Ganga*et al.* *Improved measurements of the temperature and polarization of the cosmic microwave background from quad.* The Astrophysical Journal, vol. 705, no. 1, page 978, 2009. (Cited on page 169.)

[Bunn *et al.* 2003] Emory F Bunn, Matias Zaldarriaga, Max Tegmark and Angelica de Oliveira-Costa. *E/B decomposition of finite pixelized CMB maps.* Physical Review D, vol. 67, no. 2, page 023501, 2003. (Cited on pages 44, 46 and 181.)

[Bunn 2002] Emory F Bunn. *Detectability of microwave background polarization.* Physical Review D, vol. 65, no. 4, page 043003, 2002. (Cited on page 44.)

[Burles & Tytler 1998] Scott Burles and David Tytler. *The Deuterium abundance toward Q1937–1009.* The Astrophysical Journal, vol. 499, no. 2, page 699, 1998. (Cited on page 11.)

[Burles *et al.* 2001a] Scott Burles, Kenneth M. Nollett and Michael S. Turner. *Big Bang Nucleosynthesis Predictions for Precision Cosmology.* The Astrophysical Journal Letters, vol. 552, no. 1, page L1, 2001. (Cited on page 10.)

[Burles *et al.* 2001b] Scott Burles, Kenneth M Nollett and Michael S Turner. *What is the big-bang-nucleosynthesis prediction for the baryon density and how reliable is it?* Physical Review D, vol. 63, no. 6, page 063512, 2001. (Cited on page 10.)

[Busca *et al.* 2013] N. G. Busca, T. Delubac, J. Rich, S. Bailey, A. Font-Ribera, D. Kirkby, J.-M. Le Goff, M. M. Pieri, A. Slosar*et al.* *Baryon acoustic oscillations in the Lyα forest of BOSS quasars.* Astronomy & Astrophysics, vol. 552, page A96, apr 2013. (Cited on page 57.)

[Cabella & Kamionkowski 2004] Paolo Cabella and Marc Kamionkowski. *Theory of cosmic microwave background polarization.* arXiv preprint astro-ph/0403392, 2004. (Cited on pages 48 and 50.)

[Calabrese *et al.* 2015] Matteo Calabrese, Carmelita Carbone, Giulio Fabbian, Marco Baldi and Carlo Baccigalupi. *Multiple lensing of the cosmic microwave background anisotropies.* Journal of Cosmology and Astroparticle Physics, vol. 2015, no. 03, page 049, 2015. (Cited on page 61.)

[Caligiuri & Kosowsky 2014] Jerod Caligiuri and Arthur Kosowsky. *Inflationary Tensor Perturbations after BICEP2.* Physical review letters, vol. 112, no. 19, page 191302, 2014. (Cited on page 227.)

[Cartan 1923] Élie Cartan. *Sur les variétés à connexion affine et la théorie de la relativité généralisée (première partie).* In Annales Scientifiques de l'Ecole Normale Supérieure, volume 40, pages 325–412. Société mathématique de France, 1923. (Cited on page 3.)

[Cartan 1924] Elie Cartan. *Sur les variétés à connexion affine, et la théorie de la relativité généralisée (première partie)(Suite).* In Annales Scientifiques de l'Ecole Normale Supérieure, volume 41, pages 1–25. Société mathématique de France, 1924. (Cited on page 3.)

[Cartan 1925] Elie Cartan. *Sur les variétés à connexion affine, et la théorie de la relativité généralisée (deuxième partie).* In Annales Scientifiques de l'École Normale Supérieure, volume 42, pages 17–88. Société mathématique de France, 1925. (Cited on page 3.)

[Cayon *et al.* 1993] Laura Cayon, Enrique Martinez-Gonzalez and Jose L Sanz. *Gravitational lensing and the cosmic microwave background.* The Astrophysical Journal, vol. 403, pages 471–475, 1993. (Cited on page 59.)

[Challinor & Chon 2002] Anthony Challinor and Gayoung Chon. *Geometry of weak lensing of CMB polarization.* Physical Review D, vol. 66, no. 12, page 127301, 2002. (Cited on page 64.)

[Chatterjee & Mazumdar 2015] Arindam Chatterjee and Anupam Mazumdar. *Bound on largest r lesssim 0.1 from sub-Planckian excursions of inflaton.* Journal of Cosmology and Astroparticle Physics, vol. 2015, no. 01, page 031, 2015. (Cited on page 26.)

[Cheng *et al.* 1993] ES Cheng, DA Cottingham, DJ Fixsen, CA Inman, MS Kowitt, SS Meyer, LA Page, JL Puchalla and RF Silverberg. *A measurement of the medium-scale anisotropy in the cosmic microwave background radiation.* arXiv preprint astro-ph/9305022, 1993. (Cited on page 54.)

[Chiang *et al.* 2010] H Cynthia Chiang, Peter AR Ade, Denis Barkats, John O Battle, Evan M Bierman, JJ Bock, C Darren Dowell, Lionel Duband, Eric F Hivon, William L Holzapfel*et al. Measurement of cosmic microwave background polarization power spectra from two years of BICEP data.* The Astrophysical Journal, vol. 711, no. 2, page 1123, 2010. (Cited on pages 38 and 56.)

[Christensen *et al.* 2001] Nelson Christensen, Renate Meyer, Lloyd Knox and Ben Luey. *Bayesian methods for cosmological parameter estimation from cosmic microwave background measurements.* Classical and Quantum Gravity, vol. 18, no. 14, page 2677, 2001. (Cited on page 53.)

[Coble *et al.* 1997] Kimberly Coble, Scott Dodelson and Joshua A Frieman. *Dynamical Λ models of structure formation.* Physical Review D, vol. 55, no. 4, page 1851, 1997. (Cited on page 74.)

[Cole & Efstathiou 1989] Shaun Cole and G Efstathiou. *Gravitational lensing of fluctuations in the microwave background radiation.* Monthly Notices of the Royal Astronomical Society, vol. 239, no. 1, pages 195–200, 1989. (Cited on page 59.)

[Contaldi *et al.* 2008] Carlo R Contaldi, Joao Magueijo and Lee Smolin. *Anomalous cosmic-microwave-background polarization and gravitational chirality.* Physical review letters, vol. 101, no. 14, page 141101, 2008. (Cited on page 47.)

[Crites *et al.* 2014] AT Crites, JW Henning, PAR Ade, KA Aird, JE Austermann, JA Beall, AN Bender, BA Benson, LE Bleem, JE Carstrom*et al. Measurements of E-Mode Polarization and Temperature-E-Mode Correlation in the Cosmic Microwave Background from 100 Square Degrees of SPTpol Data.* arXiv preprint arXiv:1411.1042, 2014. (Cited on page 217.)

[Crittenden & Turok 1998] Robert G Crittenden and Neil G Turok. *Exactly azimuthal pixelizations of the sky.* arXiv preprint astro-ph/9806374, 1998. (Cited on pages 30 and 230.)

[Danese & De Zotti 1982] L Danese and G De Zotti. *Double Compton process and the spectrum of the microwave background.* Astronomy and Astrophysics, vol. 107, pages 39–42, 1982. (Cited on page 14.)

[Das *et al.* 2011] Sudeep Das, Blake D Sherwin, Paula Aguirre, John W Appel, J Richard Bond, C Sofia Carvalho, Mark J Devlin, Joanna Dunkley, Rolando Dünner, Thomas Essinger-Hileman*et al.* *Detection of the power spectrum of cosmic microwave background lensing by the atacama cosmology telescope.* Physical Review Letters, vol. 107, no. 2, page 021301, 2011. (Cited on pages 71, 74 and 216.)

[Das *et al.* 2014] Sudeep Das, Thibaut Louis, Michael R Nolta, Graeme E Addison, Elia S Battistelli, J Richard Bond, Erminia Calabrese, Devin Crichton, Mark J Devlin, Simon Dicker*et al.* *The Atacama Cosmology Telescope: temperature and gravitational lensing power spectrum measurements from three seasons of data.* Journal of Cosmology and Astroparticle Physics, vol. 2014, no. 04, page 014, 2014. (Cited on page 217.)

[De Bernardis *et al.* 1994] P De Bernardis, E Aquilini, A Boscaleri, M De Petris, G D'Andreta, M Gervasi, E Kreysa, L Martinis, S Masi, P Palumbo*et al.* *Degree-scale observations of cosmic microwave background anisotropies.* The Astrophysical Journal, vol. 422, pages L33–L36, 1994. (Cited on page 54.)

[de Bernardis *et al.* 2000] Pea de Bernardis, PAR Ade, JJ Bock, JR Bond, J Borrill, A Boscaleri, K Coble, BP Crill, G De Gasperis, PC Farese*et al.* *A flat Universe from high-resolution maps of the cosmic microwave background radiation.* Nature, vol. 404, no. 6781, pages 955–959, 2000. (Cited on pages 9 and 54.)

[de Pater & Dickel 1991] Imke de Pater and John R Dickel. *Multifrequency radio observations of Saturn at ring inclination angles between 5 and 26 degrees.* Icarus, vol. 94, no. 2, pages 474–492, 1991. (Cited on page 106.)

[De Sitter 1917] Willem De Sitter. *On the curvature of space.* In Proc. Kon. Ned. Akad. Wet, volume 20, pages 229–243, 1917. (Cited on page 6.)

[De Zotti *et al.* 1999] G De Zotti*et al.* *AIP Conf. Proc. 476, 204.* arXiv preprint astro-ph/9902103, 1999. (Cited on page 77.)

[Devlin *et al.* 1994] MJ Devlin, AC Clapp, JO Gundersen, CA Hagmann, VV Hristov, AE Lange, MA Lim, PM Lubin, PD Mauskopf, PR Meinhold*et al.* *Measurements of anisotropy in the cosmic microwave background radiation at 0.5 deg angular scales near the star Gamma Ursae Minoris.* The Astrophysical Journal, vol. 430, pages L1–L4, 1994. (Cited on page 54.)

[Dicke *et al.* 1965] R. H. Dicke, P. J. E. Peebles, P. G. Roll and D. T. Wilkinson. *Cosmic Black-Body Radiation.* apj, vol. 142, pages 414–419, July 1965. (Cited on page 13.)

[Dickinson *et al.* 2003] C Dickinson, RD Davies and RJ Davis. *Towards a free–free template for CMB foregrounds.* Monthly Notices of the Royal Astronomical Society, vol. 341, no. 2, pages 369–384, 2003. (Cited on page 78.)

[Dodelson & Stebbins 1994] Scott Dodelson and Albert Stebbins. *Analysis of small-scale microwave background radiation anisotropy in the presence of foreground contamination.* The Astrophysical Journal, vol. 433, pages 440–453, 1994. (Cited on page 78.)

[Doroshkevich *et al.* 2005] AG Doroshkevich, PD Naselsky, Oleg V Verkhodanov, DI Novikov, VI Turchaninov, ID Novikov, PR Christensen and L-Y Chiang. *Gauss–Legendre sky pixelization (GLESP) for CMB maps.* International Journal of Modern Physics D, vol. 14, no. 02, pages 275–290, 2005. (Cited on page 30.)

[Dowling *et al.* 1987] TE Dowling, DO Muhleman and GL Berge. *Aperture synthesis observations of Saturn and its rings at 2.7-mm wavelength.* Icarus, vol. 70, no. 3, pages 506–516, 1987. (Cited on page 102.)

[Dragovan *et al.* 1994] M Dragovan, JE Ruhl, G Novak, SR Platt, B Crone, R Pernic and JB Peterson. *Anisotropy in the microwave sky at intermediate angular scales.* The Astrophysical Journal, vol. 427, pages L67–L70, 1994. (Cited on page 54.)

[Draine & Lazarian 1998] BT Draine and A Lazarian. *Diffuse galactic emission from spinning dust grains.* The Astrophysical Journal Letters, vol. 494, no. 1, page L19, 1998. (Cited on page 78.)

[Dunn *et al.* 2002] David E Dunn, Lawrence A Molnar and John D Fix. *More microwave observations of Saturn: Modeling the ring with a Monte Carlo radiative transfer code.* Icarus, vol. 160, no. 1, pages 132–160, 2002. (Cited on pages 102 and 103.)

[Dunn *et al.* 2005] David E Dunn, Imke de Pater, Melvyn Wright, Michiel R Hogerheijde and Lawrence A Molnar. *High-quality BIMA-OVRO images of Saturn and its rings at 1.3 and 3 millimeters.* The Astronomical Journal, vol. 129, no. 2, page 1109, 2005. (Cited on page 106.)

[Dünner *et al.* 2013] Rolando Dünner, Matthew Hasselfield, Tobias A Marriage, Jon Sievers, Viviana Acquaviva, Graeme E Addison, Peter AR Ade, Paula Aguirre, Mandana Amiri, John William Appel*et al. The Atacama Cosmology Telescope: data characterization and mapmaking.* The Astrophysical Journal, vol. 762, no. 1, page 10, 2013. (Cited on pages 152 and 154.)

[Durrer *et al.* 2002] Ruth Durrer, Martin Kunz and Alessandro Melchiorri. *Cosmic structure formation with topological defects.* Physics Reports, vol. 364, no. 1, pages 1–81, 2002. (Cited on page 44.)

[Efstathiou 2004] G Efstathiou. *Myths and truths concerning estimation of power spectra: the case for a hybrid estimator.* Monthly Notices of the Royal Astronomical Society, vol. 349, no. 2, pages 603–626, 2004. (Cited on page 188.)

[Efstathiou 2006] G Efstathiou. *Hybrid estimation of cosmic microwave background polarization power spectra.* Monthly Notices of the Royal Astronomical Society, vol. 370, no. 1, pages 343–362, 2006. (Cited on page 188.)

[Eisenstein *et al.* 2005] Daniel J Eisenstein, Idit Zehavi, David W Hogg, Roman Scoccimarro, Michael R Blanton, Robert C Nichol, Ryan Scranton, Hee-Jong Seo, Max Tegmark, Zheng Zheng*et al. Detection of the baryon acoustic peak in the large-scale correlation function of SDSS luminous red galaxies.* The Astrophysical Journal, vol. 633, no. 2, page 560, 2005. (Cited on pages 28 and 57.)

[Errard *et al.* 2015] J Errard, PAR Ade, Y Akiba, K Arnold, M Atlas, C Baccigalupi, D Barron, D Boettger, J Borrill, S Chapman*et al. Atmospheric contamination for CMB ground-based observations.* arXiv preprint arXiv:1501.07911, 2015. (Cited on pages 152 and 191.)

[Errard 2012] Josquin Errard. *La chasse aux modes-B du fond diffus cosmologique dans la jungle des contaminations systématiques.* PhD thesis, Université Paris-Diderot-Paris VII, 2012. (Cited on pages 8 and 85.)

[Fabbian & Stompor 2013] Giulio Fabbian and Radek Stompor. *High-precision simulations of the weak lensing effect on cosmic microwave background polarization.* Astronomy & Astrophysics, vol. 556, page A109, 2013. (Cited on pages 65, 66 and 69.)

[Fabbian 2013] Giulio Fabbian. *Modeling and Measuring the Weak Lensing of CMB Polarization in Current and Future Ground-based Experiments*. PhD thesis, 2013. (Cited on pages 40 and 199.)

[Farese *et al.* 2004] Philip C Farese, Giorgio Dall'Oglio, Joshua O Gundersen, Brian G Keating, Slade Klawikowski, Lloyd Knox, Alan Levy, Philip M Lubin, Chris W O'Dell, Alan Peel*et al. Compass: An upper limit on cosmic microwave background polarization at an angular scale of 20'*. The Astrophysical Journal, vol. 610, no. 2, page 625, 2004. (Cited on page 119.)

[Ferreira & Jaffe 2000] Pedro G Ferreira and Andrew H Jaffe. *Simultaneous estimation of noise and signal in cosmic microwave background experiments*. Monthly Notices of the Royal Astronomical Society, vol. 312, no. 1, pages 89–102, 2000. (Cited on page 142.)

[Ferte & Grain 2014] A Ferte and J Grain. *Detecting chiral gravity with the pure pseudospectrum reconstruction of the cosmic microwave background polarized anisotropies*. Physical Review D, vol. 89, no. 10, page 103516, 2014. (Cited on pages 47 and 196.)

[Ferté *et al.* 2015] A Ferté, J Peloton, J Grain and R Stompor. *Detecting the tensor-to-scalar ratio with the pure pseudospectrum reconstruction of B-mode*. arXiv preprint arXiv:1506.06409, 2015. (Cited on pages 234 and 247.)

[Ferté 2014] Agnès Ferté. *Statistics of the CMB polarised anisotropies: unveiling the primordial universe*. PhD thesis, Paris 11, 2014. (Cited on page 47.)

[Fornengo *et al.* 2014] Nicolao Fornengo, Laurence Perotto, Marco Regis and Stefano Camera. *Evidence of cross-correlation between the CMB lensing and the gamma-ray sky*. arXiv preprint arXiv:1410.4997, 2014. (Cited on page 215.)

[Fowler *et al.* 2010] JW Fowler, Viviana Acquaviva, PAR Ade, P Aguirre, M Amiri, JW Appel, LF Barrientos, ES Battistelli, JR Bond, B Brown*et al. The Atacama Cosmology Telescope: A Measurement of the 600< ℓ < 8000 Cosmic Microwave Background Power Spectrum at 148 GHz*. The Astrophysical Journal, vol. 722, no. 2, page 1148, 2010. (Cited on page 56.)

[Gamov 1946] G. Gamov. *Expanding universe and the origin of elements*. Physical Review, vol. 70, page 572, 1946. (Cited on page 10.)

[Gamow 1948] George Gamow. *The evolution of the universe*. Nature, vol. 162, no. 4122, pages 680–682, 1948. (Cited on page 13.)

[Geach *et al.* 2013] JE Geach, RC Hickox, LE Bleem, M Brodwin, GP Holder, KA Aird, BA Benson, S Bhattacharya, JE Carlstrom, CL Chang*et al. A direct measurement of the linear bias of mid-infrared-selected quasars at z 1 using cosmic microwave background lensing*. The Astrophysical Journal Letters, vol. 776, no. 2, page L41, 2013. (Cited on page 215.)

[Goldberg & Spergel 1998] David M Goldberg and David N Spergel. *The Microwave Background Bispectrum, Paper II: A Probe of the Low Redshift Universe*. arXiv preprint astro-ph/9811251, 1998. (Cited on page 74.)

[Golub & Van Loan 2012] Gene H Golub and Charles F Van Loan. Matrix computations, volume 3. JHU Press, 2012. (Cited on page 155.)

[Gorski *et al.* 2005] Krzysztof M Gorski, Eric Hivon, AJ Banday, Benjamin D Wandelt, Frode K Hansen, Mstvos Reinecke and Matthia Bartelmann. *HEALPix: a framework for high-resolution discretization and fast analysis of data distributed on the sphere.* The Astrophysical Journal, vol. 622, no. 2, page 759, 2005. (Cited on pages 30 and 147.)

[Grain *et al.* 2009] J Grain, M Tristram and R Stompor. *Polarized CMB power spectrum estimation using the pure pseudo-cross-spectrum approach.* Physical Review D, vol. 79, no. 12, page 123515, 2009. (Cited on pages 44, 45, 181, 182, 183, 234 and 239.)

[Grain *et al.* 2012] Julien Grain, Matthieu Tristram and Radek Stompor. *CMB E B and T B cross-spectrum estimation via pseudospectrum techniques.* Physical Review D, vol. 86, no. 7, page 076005, 2012. (Cited on page 182.)

[Grossman 1990] A. W. Grossman. *PhD thesis.* Caltech, 1990. (Cited on page 106.)

[Guilloux 2008] Frédéric Guilloux. *Analyse harmonique et Estimation spectrale sur la Sphère. Applications à l'étude du Fond diffus cosmologique.* PhD thesis, Université Paris-Diderot-Paris VII, 2008. (Cited on page 29.)

[Gunn & Peterson 1965] James E Gunn and Bruce A Peterson. *On the Density of Neutral Hydrogen in Intergalactic Space.* The Astrophysical Journal, vol. 142, pages 1633–1641, 1965. (Cited on page 36.)

[Gutierrez de La Cruz *et al.* 1995] CM Gutierrez de La Cruz, RD Davies, R Rebolo, RA Watson, S Hancock and AN Lasenby. *Dual-frequency mapping with the Tenerife cosmic microwave background experiments.* The Astrophysical Journal, vol. 442, pages 10–22, 1995. (Cited on page 54.)

[Guzik *et al.* 2000] Jacek Guzik, Uroš Seljak and Matias Zaldarriaga. *Lensing effect on polarization in the microwave background: Extracting the convergence power spectrum.* Physical Review D, vol. 62, no. 4, page 043517, 2000. (Cited on page 69.)

[Halverson *et al.* 2002] NW Halverson, EM Leitch, C Pryke, J Kovac, JE Carlstrom, WL Holzapfel, M Dragovan, JK Cartwright, BS Mason, S Padin*et al. Degree angular scale interferometer first results: a measurement of the cosmic microwave background angular power spectrum.* The Astrophysical Journal, vol. 568, no. 1, page 38, 2002. (Cited on page 56.)

[Hanany *et al.* 2000] Shaul Hanany, P Ade, A Balbi, J Bock, J Borrill, A Boscaleri, P De Bernardis, PG Ferreira, VV Hristov, AH Jaffe*et al. MAXIMA-1: a measurement of the cosmic microwave background anisotropy on angular scales of 10'-5.* The Astrophysical Journal Letters, vol. 545, no. 1, page L5, 2000. (Cited on page 56.)

[Hand *et al.* 2013] Nick Hand, Alexie Leauthaud, Sudeep Das, Blake D Sherwin, Graeme E Addison, J Richard Bond, Erminia Calabrese, Aldée Charbonnier, Mark J Devlin, Joanna Dunkley*et al. First measurement of the cross-correlation of CMB lensing and galaxy lensing.* arXiv preprint arXiv:1311.6200, 2013. (Cited on page 215.)

[Hanson *et al.* 2009a] Duncan Hanson, Graca Rocha and Krzysztof Górski. *Lensing reconstruction from Planck sky maps: inhomogeneous noise.* Monthly Notices of the Royal Astronomical Society, vol. 400, no. 4, pages 2169–2173, 2009. (Cited on page 72.)

[Hanson *et al.* 2009b] Duncan Hanson, Kendrick M Smith, Anthony Challinor and Michele Liguori. *CMB lensing and primordial non-Gaussianity.* Physical Review D, vol. 80, no. 8, page 083004, 2009. (Cited on page 65.)

[Hanson *et al.* 2010] Duncan Hanson, Anthony Challinor and Antony Lewis. *Weak lensing of the CMB.* General Relativity and Gravitation, vol. 42, no. 9, pages 2197–2218, 2010. (Cited on page 61.)

[Hanson *et al.* 2011] Duncan Hanson, Anthony Challinor, George Efstathiou and Pawel Bielewicz. *CMB temperature lensing power reconstruction.* Physical Review D, vol. 83, no. 4, page 043005, 2011. (Cited on page 71.)

[Hanson *et al.* 2013] D Hanson, S Hoover, A Crites, PAR Ade, KA Aird, JE Austermann, JA Beall, AN Bender, BA Benson, LE Bleem*et al. Detection of B-mode polarization in the cosmic microwave background with data from the south pole telescope.* Physical Review Letters, vol. 111, no. 14, page 141301, 2013. (Cited on pages 38, 216, 217, 221 and 223.)

[Hasselfield *et al.* 2013] Matthew Hasselfield, Kavilan Moodley, J Richard Bond, Sudeep Das, Mark J Devlin, Joanna Dunkley, Rolando Dünner, Joseph W Fowler, Patricio Gallardo, Megan B Gralla*et al. The Atacama Cosmology Telescope: Beam Measurements and the Microwave Brightness Temperatures of Uranus and Saturn.* The Astrophysical Journal Supplement Series, vol. 209, no. 1, page 17, 2013. (Cited on pages 102, 104, 105 and 106.)

[Heavens 2009] Alan Heavens. *Statistical techniques in cosmology.* arXiv preprint arXiv:0906.0664, 2009. (Cited on page 53.)

[Hill & Spergel 2014] J Colin Hill and David N Spergel. *Detection of thermal SZ-CMB lensing cross-correlation in Planck nominal mission data.* Journal of Cosmology and Astroparticle Physics, vol. 2014, no. 02, page 030, 2014. (Cited on page 215.)

[Hirata & Seljak 2003] Christopher M Hirata and Uroš Seljak. *Reconstruction of lensing from the cosmic microwave background polarization.* Physical Review D, vol. 68, no. 8, page 083002, 2003. (Cited on page 69.)

[Hirata *et al.* 2008] Christopher M Hirata, Shirley Ho, Nikhil Padmanabhan, Uroš Seljak and Neta A Bahcall. *Correlation of CMB with large-scale structure. II. Weak lensing.* Physical Review D, vol. 78, no. 4, page 043520, 2008. (Cited on page 74.)

[Hivon *et al.* 2002] Eric Hivon, Krzysztof M Górski, C Barth Netterfield, Brendan P Crill, Simon Prunet and Frode Hansen. *MASTER of the cosmic microwave background anisotropy power spectrum: A fast method for statistical analysis of large and complex cosmic microwave background data sets.* The Astrophysical Journal, vol. 567, no. 1, page 2, 2002. (Cited on pages 148, 178 and 189.)

[Holder *et al.* 2013] GP Holder, MP Viero, O Zahn, KA Aird, BA Benson, S Bhattacharya, LE Bleem, J Bock, M Brodwin, JE Carlstrom*et al. A CMB lensing mass map and its correlation with the cosmic infrared background.* arXiv preprint arXiv:1303.5048, 2013. (Cited on pages 215 and 222.)

[Hu & Dodelson 2002] Wayne Hu and Scott Dodelson. *COSMIC MICROWAVE BACKGROUND ANISOTROPIES.* Annu. Rev. Astron. Astrophys, vol. 40, pages 171–216, 2002. (Cited on pages 31, 33 and 56.)

[Hu & Okamoto 2002] Wayne Hu and Takemi Okamoto. *Mass reconstruction with cosmic microwave background polarization.* The Astrophysical Journal, vol. 574, no. 2, page 566, 2002. (Cited on pages 69, 70, 222 and 223.)

[Hu & Sugiyama 1995] Wayne Hu and Naoshi Sugiyama. *Toward understanding CMB anisotropies and their implications.* Physical Review D, vol. 51, no. 6, page 2599, 1995. (Cited on page 34.)

[Hu *et al.* 1997] W Hu, N Sugiyama and J Silk. *The physics of microwave background anisotropies.* Nature, vol. 386, no. 6620, pages 37–43, 1997. (Cited on page 35.)

[Hu *et al.* 2003] Wayne Hu, Matthew M Hedman and Matias Zaldarriaga. *Benchmark parameters for CMB polarization experiments.* Physical Review D, vol. 67, no. 4, page 043004, 2003. (Cited on page 206.)

[Hu 2000] Wayne Hu. *Weak lensing of the CMB: A harmonic approach.* Physical Review D, vol. 62, no. 4, page 043007, 2000. (Cited on pages 62, 64 and 66.)

[Hu 2001] Wayne Hu. *Mapping the dark matter through the cosmic microwave background damping tail.* The Astrophysical Journal Letters, vol. 557, no. 2, page L79, 2001. (Cited on pages 70 and 72.)

[Hu 2005] Wayne Hu. *Crossing the phantom divide: Dark energy internal degrees of freedom.* Physical Review D, vol. 71, no. 4, page 047301, 2005. (Cited on page 72.)

[Hubble 1929] Edwin Hubble. *A relation between distance and radial velocity among extragalactic nebulae.* Proceedings of the National Academy of Sciences, vol. 15, no. 3, pages 168–173, 1929. (Cited on pages 3 and 4.)

[Izotov & Thuan 1998] Yuri I Izotov and Trinh X Thuan. *The primordial abundance of 4He revisited.* The Astrophysical Journal, vol. 500, no. 1, page 188, 1998. (Cited on page 11.)

[Jaffe *et al.* 2000] Andrew H Jaffe, Marc Kamionkowski and Limin Wang. *Polarization pursuers' guide.* Physical Review D, vol. 61, no. 8, page 083501, 2000. (Cited on pages 233 and 237.)

[Jaffe *et al.* 2003] Andrew H Jaffe, JR Bond, PG Ferreira and LE Knox. *CMB likelihood functions for beginners and experts.* arXiv preprint astro-ph/0306506, 2003. (Cited on page 177.)

[Kamionkowski *et al.* 1997a] Marc Kamionkowski, Arthur Kosowsky and Albert Stebbins. *A probe of primordial gravity waves and vorticity.* Physical Review Letters, vol. 78, no. 11, page 2058, 1997. (Cited on page 43.)

[Kamionkowski *et al.* 1997b] Marc Kamionkowski, Arthur Kosowsky and Albert Stebbins. *Statistics of cosmic microwave background polarization.* Physical Review D, vol. 55, no. 12, page 7368, 1997. (Cited on page 42.)

[Kaufman *et al.* 2014] Jonathan Kaufman, Brian Keating and Brad Johnson. *Precision tests of parity violation over cosmological distances.* arXiv preprint arXiv:1409.8242, 2014. (Cited on page 196.)

[Keating *et al.* 2013] Brian G Keating, Meir Shimon and Amit PS Yadav. *Self-calibration of cosmic microwave background polarization experiments.* The Astrophysical Journal Letters, vol. 762, no. 2, page L23, 2013. (Cited on pages 196 and 206.)

[Keisler *et al.* 2015] R Keisler, S Hoover, N Harrington, JW Henning, PAR Ade, KA Aird, JE Austermann, JA Beall, AN Bender, BA Benson*et al. Measurements of Sub-degree B-mode Polarization in the Cosmic Microwave Background from 100 Square Degrees of SPTpol Data.* arXiv preprint arXiv:1503.02315, 2015. (Cited on pages 218, 219 and 220.)

[Kermish *et al.* 2012] Zigmund D Kermish, Peter Ade, Aubra Anthony, Kam Arnold, Darcy Barron, David Boettger, Julian Borrill, Scott Chapman, Yuji Chinone, Matt A Dobbs*et al.* *The POLARBEAR experiment.* In SPIE Astronomical Telescopes+ Instrumentation, pages 84521C–84521C. International Society for Optics and Photonics, 2012. (Cited on pages 85 and 88.)

[Kesden *et al.* 2002] Michael Kesden, Asantha Cooray and Marc Kamionkowski. *Separation of gravitational-wave and cosmic-shear contributions to cosmic microwave background polarization.* Physical Review Letters, vol. 89, no. 1, page 011304, 2002. (Cited on page 75.)

[Kesden *et al.* 2003] Michael Kesden, Asantha Cooray and Marc Kamionkowski. *Lensing reconstruction with CMB temperature and polarization.* Physical Review D, vol. 67, no. 12, page 123507, 2003. (Cited on page 71.)

[Klein & Roodman 2005] Joshua R Klein and Aaron Roodman. *Blind analysis in nuclear and particle physics.* Annu. Rev. Nucl. Part. Sci., vol. 55, pages 141–163, 2005. (Cited on page 200.)

[Knox & Song 2002] Lloyd Knox and Yong-Seon Song. *Limit on the Detectability of the Energy Scale of Inflation.* Physical Review Letters, vol. 89, no. 1, page 011303, 2002. (Cited on page 75.)

[Kogut *et al.* 2007] A Kogut, J Dunkley, CL Bennett, O Doré, B Gold, M Halpern, G Hinshaw, N Jarosik, E Komatsu, MR Nolta*et al.* *Three-year Wilkinson microwave anisotropy probe (WMAP) observations: foreground polarization.* The Astrophysical Journal, vol. 665, no. 1, page 355, 2007. (Cited on page 78.)

[Kolb & Turner 1990] Edward W Kolb and Michael Stanley Turner. *The early universe.* Front. Phys., Vol. 69,, vol. 1, 1990. (Cited on page 10.)

[Komatsu *et al.* 2011] Eiichiro Komatsu, KM Smith, J Dunkley, CL Bennett, B Gold, G Hinshaw, N Jarosik, D Larson, MR Nolta, L Page*et al.* *Seven-year Wilkinson microwave anisotropy probe (WMAP) observations: cosmological interpretation.* The Astrophysical Journal Supplement Series, vol. 192, no. 2, page 18, 2011. (Cited on page 43.)

[Kosowsky 1996] A Kosowsky. *Cosmic microwave background polarization.* Annals of Physics (New York), vol. 246, no. 1, 1996. (Cited on pages 42 and 43.)

[Kovac *et al.* 2002] John Michael Kovac, EM Leitch, C Pryke, JE Carlstrom, NW Halverson and WL Holzapfel. *Detection of polarization in the cosmic microwave background using DASI.* Nature, vol. 420, no. 6917, pages 772–787, 2002. (Cited on pages 38, 56 and 79.)

[Langlois 2005] David Langlois. *Inflation, quantum fluctuations and cosmological perturbations.* In Particle Physics and Cosmology: The Interface, pages 235–278. Springer, 2005. (Cited on page 22.)

[Lavaux & Wandelt 2010] Guilhem Lavaux and Benjamin D Wandelt. *Fast and optimal cosmic microwave background lensing using statistical interpolation on the sphere.* The Astrophysical Journal Supplement Series, vol. 191, no. 1, page 32, 2010. (Cited on page 69.)

[Lesgourgues & Pastor 2006] Julien Lesgourgues and Sergio Pastor. *Massive neutrinos and cosmology.* Physics Reports, vol. 429, no. 6, pages 307–379, 2006. (Cited on pages 72 and 73.)

[Lewis & Bridle 2002] Antony Lewis and Sarah Bridle. *Cosmological parameters from CMB and other data: A Monte Carlo approach.* Physical Review D, vol. 66, no. 10, page 103511, 2002. (Cited on page 53.)

[Lewis & Challinor 2006] Antony Lewis and Anthony Challinor. *Weak gravitational lensing of the CMB.* Physics Reports, vol. 429, no. 1, pages 1–65, 2006. (Cited on pages 60, 61, 63, 64, 69 and 75.)

[Lewis *et al.* 2000] Antony Lewis, Anthony Challinor and Anthony Lasenby. *Efficient computation of cosmic microwave background anisotropies in closed Friedmann-Robertson-Walker models.* The Astrophysical Journal, vol. 538, no. 2, page 473, 2000. (Cited on pages 34, 53 and 63.)

[Lewis *et al.* 2001] Antony Lewis, Anthony Challinor and Neil Turok. *Analysis of CMB polarization on an incomplete sky.* Physical Review D, vol. 65, no. 2, page 023505, 2001. (Cited on pages 44 and 181.)

[Lewis 2005] Antony Lewis. *Lensed CMB simulation and parameter estimation.* Physical Review D, vol. 71, no. 8, page 083008, 2005. (Cited on page 69.)

[Linde *et al.* 2005] Andrei Linde, Viatcheslav Mukhanov and Misao Sasaki. *Post-inflationary behaviour of adiabatic perturbations and the tensor-to-scalar ratio.* Journal of Cosmology and Astroparticle Physics, vol. 2005, no. 10, page 002, 2005. (Cited on page 49.)

[Lueker *et al.* 2010] Martin Lueker, CL Reichardt, KK Schaffer, O Zahn, PAR Ade, KA Aird, BA Benson, LE Bleem, JE Carlstrom, CL Chang*et al.* *Measurements of secondary cosmic microwave background anisotropies with the South Pole Telescope.* The Astrophysical Journal, vol. 719, no. 2, page 1045, 2010. (Cited on page 56.)

[Lyth 1997] David H Lyth. *What would we learn by detecting a gravitational wave signal in the cosmic microwave background anisotropy?* Physical Review Letters, vol. 78, no. 10, page 1861, 1997. (Cited on page 26.)

[M.A. Holdaway 1997] Juan R. Pardo M.A. Holdaway. *MMA Memo 187: Modeling of the Submillimeter Opacity on Chajnantor.* `http://legacy.nrao.edu/alma/memos/html-memos/alma187/memo187.html`, 1997. [Online; accessed 22-April-2015]. (Cited on page 126.)

[Magueijo & Benincasa 2011] Joao Magueijo and Dionigi MT Benincasa. *Chiral vacuum fluctuations in quantum gravity.* Physical review letters, vol. 106, no. 12, page 121302, 2011. (Cited on page 47.)

[Mangum 2001] JG Mangum. *'A Telescope Pointing Algorithm for ALMA'.* Rapport technique, ALMA memo 366, 2001. (Cited on page 96.)

[Marouf *et al.* 1983] Essam A Marouf, G Leonard Tyler, Howard A Zebker, Richard A Simpson and Von R Eshleman. *Particle size distributions in Saturn's rings from Voyager 1 radio occultation.* Icarus, vol. 54, no. 2, pages 189–211, 1983. (Cited on page 102.)

[Martin *et al.* 2014] Jérôme Martin, Christophe Ringeval and Vincent Vennin. *Encyclopædia Inflationaris.* Physics of the Dark Universe, vol. 5, pages 75–235, 2014. (Cited on page 18.)

[Mather *et al.* 1990] John C Mather, ES Cheng, RE Eplee Jr, RB Isaacman, SS Meyer, RA Shafer, R Weiss, EL Wright, CL Bennett, NW Boggess*et al. A preliminary measurement of the cosmic microwave background spectrum by the Cosmic Background Explorer (COBE) satellite.* The Astrophysical Journal, vol. 354, pages L37–L40, 1990. (Cited on pages 2, 12, 13 and 54.)

[Mather *et al.* 1994] John C Mather, ES Cheng, DA Cottingham, RE Eplee Jr, DJ Fixsen, T Hewagama, RB Isaacman, KA Jensen, SS Meyer, PD Noerdlinger*et al. Measurement of the cosmic microwave background spectrum by the COBE FIRAS instrument.* The Astrophysical Journal, vol. 420, pages 439–444, 1994. (Cited on pages 13 and 29.)

[McKellar 1941] Andrew McKellar. *Molecular lines from the lowest states of diatomic molecules composed of atoms probably present in interstellar space.* Publications of the Dominion Astrophysical Observatory Victoria, vol. 7, page 251, 1941. (Cited on page 13.)

[Miller *et al.* 2009] NJ Miller, M Shimon and BG Keating. *CMB beam systematics: Impact on lensing parameter estimation.* Physical Review D, vol. 79, no. 6, page 063008, 2009. (Cited on pages 206 and 211.)

[Moss & Pogosian 2014] Adam Moss and Levon Pogosian. *Did BICEP2 see vector modes? First B-mode constraints on cosmic defects.* Physical review letters, vol. 112, no. 17, page 171302, 2014. (Cited on page 44.)

[Mukhanov 2005] Viatcheslav Mukhanov. Physical foundations of cosmology. Cambridge university press, 2005. (Cited on pages 2, 12, 16 and 46.)

[Murphy *et al.* 2010] Tara Murphy, Elaine M Sadler, Ronald D Ekers, Marcella Massardi, Paul J Hancock, Elizabeth Mahony, Roberto Ricci, Sarah Burke-Spolaor, Mark Calabretta, Rajan Chhetri*et al. The Australia Telescope 20 GHz survey: the source catalogue.* Monthly Notices of the Royal Astronomical Society, vol. 402, no. 4, pages 2403–2423, 2010. (Cited on page 97.)

[Myers *et al.* 2008] MJ Myers, K Arnold, P Ade, G Engargiola, W Holzapfel, AT Lee, X Meng, R O'Brient, PL Richards, H Spieler*et al. Antenna-coupled bolometer arrays for measurement of the cosmic microwave background polarization.* Journal of Low Temperature Physics, vol. 151, no. 1-2, pages 464–470, 2008. (Cited on page 87.)

[Naess *et al.* 2014] Sigurd Naess, Matthew Hasselfield, Jeff McMahon, Michael D Niemack, Graeme E Addison, Peter AR Ade, Rupert Allison, Mandana Amiri, Nick Battaglia, James A Beall*et al. The Atacama Cosmology Telescope: CMB polarization at 200$<$ ℓ $<$ 9000.* Journal of Cosmology and Astroparticle Physics, vol. 2014, no. 10, page 007, 2014. (Cited on pages 38, 197, 217, 218, 219 and 220.)

[Netterfield *et al.* 1997] C Barth Netterfield, MJ Devlin, NORMAN Jarosik, Lyman Page and Ed J Wollack. *A measurement of the angular power spectrum of the anisotropy in the cosmic microwave background.* The Astrophysical Journal, vol. 474, no. 1, page 47, 1997. (Cited on page 54.)

[Newman & Penrose 1962] Ezra Newman and Roger Penrose. *An approach to gravitational radiation by a method of spin coefficients.* Journal of Mathematical Physics, vol. 3, no. 3, pages 566–578, 1962. (Cited on page 45.)

[Nollett & Burles 2000] Kenneth M Nollett and Scott Burles. *Estimating reaction rates and uncertainties for primordial nucleosynthesis.* Physical Review D, vol. 61, no. 12, page 123505, 2000. (Cited on page 11.)

[O'Dea *et al.* 2007] Daniel O'Dea, Anthony Challinor and Bradley R Johnson. *Systematic errors in cosmic microwave background polarization measurements.* Monthly Notices of the Royal Astronomical Society, vol. 376, no. 4, pages 1767–1783, 2007. (Cited on page 206.)

[Okamoto & Hu 2003] Takemi Okamoto and Wayne Hu. *Cosmic microwave background lensing reconstruction on the full sky.* Physical Review D, vol. 67, no. 8, page 083002, 2003. (Cited on page 69.)

[Olive *et al.* 1997] Keith A Olive, Gary Steigman and Evan D Skillman. *The primordial abundance of 4He: an update.* The Astrophysical Journal, vol. 483, no. 2, page 788, 1997. (Cited on page 11.)

[Pacholczyk 1970] Andrzej G Pacholczyk. *Radio astrophysics.* 1970. (Cited on page 78.)

[Page *et al.* 2007] L Page, G Hinshaw, E Komatsu, MR Nolta, DN Spergel, CL Bennett, C Barnes, R Bean, O Doré, J Dunkley*et al.* *Three-year Wilkinson microwave anisotropy probe (WMAP) observations: Polarization analysis.* The Astrophysical Journal Supplement Series, vol. 170, no. 2, page 335, 2007. (Cited on page 78.)

[Pardo *et al.* 2001] Juan R Pardo, José Cernicharo and Eugene Serabyn. *Atmospheric transmission at microwaves (ATM): an improved model for millimeter/submillimeter applications.* Antennas and Propagation, IEEE Transactions on, vol. 49, no. 12, pages 1683–1694, 2001. (Cited on pages 126 and 127.)

[Pearson *et al.* 2014] Ruth Pearson, Blake Sherwin and Antony Lewis. *CMB lensing reconstruction using cut sky polarization maps and pure B modes.* Physical Review D, vol. 90, no. 2, page 023539, 2014. (Cited on page 72.)

[Peebles & Dicke 1968] PJE Peebles and RH Dicke. *Origin of the globular star clusters.* The Astrophysical Journal, vol. 154, page 891, 1968. (Cited on page 28.)

[Peebles & Yu 1970] Philip JE Peebles and JT Yu. *Primeval adiabatic perturbation in an expanding universe.* The Astrophysical Journal, vol. 162, page 815, 1970. (Cited on page 28.)

[Penzias & Wilson 1965] A. A. Penzias and R. W. Wilson. *A Measurement of Excess Antenna Temperature at 4080 Mc/s.* apj, vol. 142, pages 419–421, July 1965. (Cited on pages 13 and 54.)

[Perlmutter *et al.* 1999] Saul Perlmutter, G Aldering, G Goldhaber, RA Knop, P Nugent, PG Castro, S Deustua, S Fabbro, A Goobar, DE Groom*et al.* *Measurements of* Ω *and* Λ *from 42 high-redshift supernovae.* The Astrophysical Journal, vol. 517, no. 2, page 565, 1999. (Cited on pages 9 and 57.)

[Piccirillo & Calisse 1993] Lucio Piccirillo and Paolo Calisse. *Measurements of cosmic background radiation anisotropy at intermediate angular scale.* The Astrophysical Journal, vol. 411, pages 529–533, 1993. (Cited on page 54.)

[Planck Collaboration 2014a] I Planck Collaboration. *Planck 2013 results. I. Overview of products and scientific results.* Astronomy & Astrophysics, vol. 571, page A1, 2014. (Cited on pages 29 and 56.)

[Planck Collaboration 2014b] XV Planck Collaboration. *Planck 2013 results. XV. CMB power spectra and likelihood.* Astronomy & Astrophysics, vol. 571, page A15, 2014. (Cited on page 38.)

[Planck Collaboration 2014c] XVI Planck Collaboration. *Planck 2013 results. XVI. Cosmological parameters.* Astronomy & Astrophysics, vol. 571, page A16, 2014. (Cited on page 53.)

[Planck Collaboration 2014d] XVII Planck Collaboration. *Planck 2013 results. XVII. Gravitational lensing by large-scale structure.* Astronomy & Astrophysics, vol. 571, page A17, 2014. (Cited on pages 71, 215, 216 and 217.)

[Planck Collaboration 2014e] XVIII Planck Collaboration. *Planck 2013 results. XVIII. The gravitational lensing-infrared background correlation.* Astronomy & Astrophysics, vol. 571, page A18, 2014. (Cited on pages 215 and 220.)

[Planck Collaboration 2014f] XXVI Planck Collaboration. *Planck 2013 results. XXVI. Background geometry and topology of the Universe.* Astronomy & Astrophysics, vol. 571, page A26, 2014. (Cited on page 6.)

[Planck Collaboration 2014g] XXX Planck Collaboration. *Planck intermediate results. XXX. The angular power spectrum of polarized dust emission at intermediate and high Galactic latitudes.* arXiv preprint arXiv:1409.5738, 2014. (Cited on pages 79, 80 and 219.)

[Planck Collaboration 2015a] I Planck Collaboration. *Planck 2015 results. I. Overview of products and scientific results.* arXiv preprint arXiv:1502.01582, 2015. (Cited on page 38.)

[Planck Collaboration 2015b] IX Planck Collaboration. *Planck 2015 results. IX. Diffuse component separation: CMB maps. 2015*, 2015. (Cited on page 78.)

[Planck Collaboration 2015c] X Planck Collaboration. *Planck 2015 results. X. Diffuse component separation: Foreground maps. 2015.* A&A, submitted, arXiv, vol. 1502, 2015. (Cited on pages 77, 78 and 79.)

[Planck Collaboration 2015d] XIII Planck Collaboration. *Planck 2015 results. XIII. Cosmological parameters. 2015*, 2015. (Cited on pages 5, 9, 54, 55, 72 and 217.)

[Planck Collaboration 2015e] XV Planck Collaboration. *Planck 2015 results. XV. Gravitational lensing.* arXiv preprint arXiv:1502.01591, 2015. (Cited on pages 216, 217 and 218.)

[Planck Collaboration 2015f] XVIII Planck Collaboration. *results. XVIII. Background geometry and topology of the Universe. 2015*, 2015. (Cited on page 6.)

[Planck Collaboration 2015g] XX Planck Collaboration. *Planck 2015 results. XX.* Constraints on inflation, 2015. (Cited on page 21.)

[Planck Collaboration 2015h] XXII Planck Collaboration. *Planck 2015 results. XXII. A map of the thermal Sunyaev-Zeldovich effect*, 2015. (Cited on pages 36 and 78.)

[Planck Collaboration 2015i] XXIV Planck Collaboration. *Planck 2015 results. XXIV. Cosmology from Sunyaev-Zeldovich cluster counts. 2015*, 2015. (Cited on page 36.)

[Polak & Ribière 1969] Elijah Polak and Gerard Ribière. *Note sur la convergence de méthodes de directions conjuguées.* ESAIM: Mathematical Modelling and Numerical Analysis-Modélisation Mathématique et Analyse Numérique, vol. 3, no. R1, pages 35–43, 1969. (Cited on page 157.)

[POLARBEAR Collaboration 2014a] a POLARBEAR Collaboration. *Evidence for gravitational lensing of the cosmic microwave background polarization from cross-correlation with the cosmic infrared background.* Physical review letters, vol. 112, no. 13, page 131302, 2014. (Cited on pages 85, 200, 216, 218, 220, 223, 225 and 245.)

[POLARBEAR Collaboration 2014b] b POLARBEAR Collaboration. *Measurement of the cosmic microwave background polarization lensing power spectrum with the Polarbear experiment.* Physical review letters, vol. 113, no. 2, page 021301, 2014. (Cited on pages 85, 200, 216, 218, 223, 225 and 245.)

[POLARBEAR Collaboration 2014c] c POLARBEAR Collaboration. *A measurement of the cosmic microwave background B-mode polarization power spectrum at sub-degree scales with POLARBEAR.* The Astrophysical Journal, vol. 794, no. 2, page 171, 2014. (Cited on pages 38, 79, 85, 97, 118, 119, 124, 159, 192, 195, 200, 202, 203, 211, 213, 217, 218, 220, 224 and 245.)

[Polnarev 1985] AG Polnarev. *Polarization and anisotropy induced in the microwave background by cosmological gravitational waves.* Soviet Astronomy, vol. 29, pages 607–613, 1985. (Cited on page 44.)

[Ponthieu *et al.* 2005] N Ponthieu, JF Macías-Pérez, M Tristram, P Ade, A Amblard, R Ansari, J Aumont, É Aubourg, Alain Benoit, J-Ph Bernard*et al. Temperature and polarization angular power spectra of Galactic dust radiation at 353 GHz as measured by Archeops.* Astronomy & Astrophysics, vol. 444, no. 1, pages 327–336, 2005. (Cited on page 78.)

[Poulet *et al.* 2000] François Poulet, Bruno Sicardy, Philip D Nicholson, Erich Karkoschka and John Caldwell. *Saturn's ring-plane crossings of August and November 1995: A model for the new F-ring objects.* Icarus, vol. 144, no. 1, pages 135–148, 2000. (Cited on page 102.)

[QUaD Collaboration 2008] 2008 QUaD Collaboration. *First season QUaD CMB temperature and polarization power spectra.* The Astrophysical Journal, vol. 674, no. 1, page 22, 2008. (Cited on pages 38 and 56.)

[Quiet Collaboration 2011] 2011 Quiet Collaboration. *First season QUIET observations: Measurements of CMB polarization power spectra at 43 GHz in the multipole range* $25 \leq \ell \leq 475$. Astrophys. J, vol. 741, page 1110, 2011. (Cited on pages 38 and 56.)

[Rees & Sciama 1968] Martin J Rees and Dennis William Sciama. *Large-scale density inhomogeneities in the Universe.* Nature, vol. 217, pages 511–516, 1968. (Cited on page 35.)

[Riess *et al.* 1998] Adam G Riess, Alexei V Filippenko, Peter Challis, Alejandro Clocchiatti, Alan Diercks, Peter M Garnavich, Ron L Gilliland, Craig J Hogan, Saurabh Jha, Robert P Kirshner*et al. Observational evidence from supernovae for an accelerating universe and a cosmological constant.* The Astronomical Journal, vol. 116, no. 3, page 1009, 1998. (Cited on pages 9 and 57.)

[Sachs & Wolfe 1967] Rainer K Sachs and Arthur M Wolfe. *Perturbations of a cosmological model and angular variations of the microwave background.* The Astrophysical Journal, vol. 147, page 73, 1967. (Cited on page 33.)

[Sakharov 1967] Andrei D Sakharov. *VIOLATION OF CP INVARIANCE, C ASYMMETRY, AND BARYON ASYMMETRY OF THE UNIVERSE.* JETP Lett.(USSR)(Engl. Transl.), 5: 24-7 (Jan. 1, 1967)., 1967. (Cited on page 13.)

[Schäfer *et al.* 2012] Björn Malte Schäfer, Alessandra Grassi, Mischa Gerstenlauer and Christian T Byrnes. *A weak lensing view on primordial non-Gaussianities.* Monthly Notices of the Royal Astronomical Society, vol. 421, no. 1, pages 797–807, 2012. (Cited on page 62.)

[Schloerb *et al.* 1979] F Peter Schloerb, Duane O Muhleman and Glenn L Berge. *Interferometric observations of Saturn and its rings at a wavelength of 3 3.71 cm.* Icarus, vol. 39, no. 2, pages 214–231, 1979. (Cited on page 102.)

[Schmidt *et al.* 1998] Brian P Schmidt, Nicholas B Suntzeff, MARK M Phillips, Robert A Schommer, Alejandro Clocchiatti, Robert P Kirshner, Peter Garnavich, Peter Challis, BRUNO Leibundgut, J Spyromilio*et al. The high-Z supernova search: measuring cosmic deceleration and global curvature of the universe using type Ia supernovae.* The Astrophysical Journal, vol. 507, no. 1, page 46, 1998. (Cited on page 57.)

[Seljak & Hirata 2004] Uroš Seljak and Christopher M Hirata. *Gravitational lensing as a contaminant of the gravity wave signal in the CMB.* Physical Review D, vol. 69, no. 4, page 043005, 2004. (Cited on page 75.)

[Seljak & Zaldarriaga 1996] Uros Seljak and Matias Zaldarriaga. *A Line-of-Sight Integration Approach to Cosmic Microwave Background Anisotropies.* The Astrophysical Journal, vol. 469, page 437, 1996. (Cited on page 34.)

[Seljak & Zaldarriaga 1997] Uros Seljak and Matias Zaldarriaga. *Signature of gravity waves in the polarization of the microwave background.* Physical Review Letters, vol. 78, no. 11, page 2054, 1997. (Cited on page 35.)

[Seljak & Zaldarriaga 1999] Uroš Seljak and Matias Zaldarriaga. *Direct signature of an evolving gravitational potential from the cosmic microwave background.* Physical Review D, vol. 60, no. 4, page 043504, 1999. (Cited on page 74.)

[Sherwin & Schmittfull 2015] Blake D Sherwin and Marcel Schmittfull. *Delensing the CMB with the Cosmic Infrared Background.* arXiv preprint arXiv:1502.05356, 2015. (Cited on pages 75 and 76.)

[Sherwin *et al.* 2012] Blake D Sherwin, Sudeep Das, Amir Hajian, Graeme Addison, J Richard Bond, Devin Crichton, Mark J Devlin, Joanna Dunkley, Megan B Gralla, Mark Halpern*et al. The Atacama Cosmology Telescope: Cross-correlation of cosmic microwave background lensing and quasars.* Physical Review D, vol. 86, no. 8, page 083006, 2012. (Cited on page 215.)

[Shimon *et al.* 2008] Meir Shimon, Brian Keating, Nicolas Ponthieu and Eric Hivon. *CMB polarization systematics due to beam asymmetry: Impact on inflationary science.* Physical Review D, vol. 77, no. 8, page 083003, 2008. (Cited on page 206.)

[Silk 1968] Joseph Silk. *Cosmic black-body radiation and galaxy formation.* The Astrophysical Journal, vol. 151, page 459, 1968. (Cited on page 34.)

[Simard *et al.* 2014] Gabrielle Simard, Duncan Hanson and Gil Holder. *Prospects for Delensing the Cosmic Microwave Background for Studying Inflation.* arXiv preprint arXiv:1410.0691, 2014. (Cited on page 75.)

[Smecher *et al.* 2012] Graeme Smecher, François Aubin, Eric Bissonnette, Matt Dobbs, Peter Hyland and Kevin MacDermid. *A biasing and demodulation system for kilopixel tes bolometer arrays.* Instrumentation and Measurement, IEEE Transactions on, vol. 61, no. 1, pages 251–260, 2012. (Cited on page 88.)

[Smith & Zaldarriaga 2007] Kendrick M Smith and Matias Zaldarriaga. *General solution to the E- B mixing problem.* Physical Review D, vol. 76, no. 4, page 043001, 2007. (Cited on page 227.)

[Smith *et al.* 2007] Kendrick M Smith, Oliver Zahn and Olivier Dore. *Detection of gravitational lensing in the cosmic microwave background.* Physical Review D, vol. 76, no. 4, page 043510, 2007. (Cited on page 74.)

[Smith *et al.* 2012] Kendrick M Smith, Duncan Hanson, Marilena LoVerde, Christopher M Hirata and Oliver Zahn. *Delensing CMB polarization with external datasets.* Journal of Cosmology and Astroparticle Physics, vol. 2012, no. 06, page 014, 2012. (Cited on page 75.)

[Smith 2006] Kendrick M Smith. *Pseudo-C_ℓ estimators which do not mix E and B modes.* Physical Review D, vol. 74, no. 8, page 083002, 2006. (Cited on pages 181, 228 and 234.)

[Smoot *et al.* 1992] George F Smoot, CL Bennett, A Kogut, EL Wright, J Aymon, NW Boggess, ES Cheng, G De Amici, S Gulkis, MG Hauser*et al. Structure in the COBE differential microwave radiometer first-year maps.* The Astrophysical Journal, vol. 396, pages L1–L5, 1992. (Cited on pages 28 and 54.)

[Stivoli *et al.* 2010] Federico Stivoli, J Grain, Samuel M Leach, M Tristram, Carlo Baccigalupi and Radek Stompor. *Maximum likelihood, parametric component separation and CMB B-mode detection in suborbital experiments.* Monthly Notices of the Royal Astronomical Society, vol. 408, no. 4, pages 2319–2335, 2010. (Cited on page 227.)

[Stompor & Efstathiou 1999] R Stompor and G Efstathiou. *Gravitational lensing of cosmic microwave background anisotropies and cosmological parameter estimation.* Monthly Notices of the Royal Astronomical Society, vol. 302, no. 4, pages 735–747, 1999. (Cited on pages 35 and 59.)

[Stompor *et al.* 2001] Radek Stompor, Amedeo Balbi, Julian D Borrill, Pedro G Ferreira, Shaul Hanany, Andrew H Jaffe, Adrian T Lee, Sang Oh, Bahman Rabii, Paul L Richards*et al. Making maps of the cosmic microwave background: The MAXIMA example.* Physical Review D, vol. 65, no. 2, page 022003, 2001. (Cited on pages 140, 148 and 165.)

[Stompor 1994] R Stompor. *Numerical analysis of the cosmic microwave background anisotropies within framework of linearized gravitational instability model.* Astronomy and Astrophysics, vol. 287, pages 693–712, 1994. (Cited on pages 33 and 34.)

[Story *et al.* 2014] KT Story, D Hanson, PAR Ade, KA Aird, JE Austermann, JA Beall, AN Bender, BA Benson, LE Bleem, JE Carlstrom*et al. A Measurement of the Cosmic Microwave Background Gravitational Lensing Potential from 100 Square Degrees of SPTpol Data.* arXiv preprint arXiv:1412.4760, 2014. (Cited on pages 216 and 218.)

[Su *et al.* 2009] Meng Su, Amit PS Yadav and Matias Zaldarriaga. *Impact of instrumental systematic contamination on the lensing mass reconstruction using the CMB polarization.* Physical Review D, vol. 79, no. 12, page 123002, 2009. (Cited on page 206.)

[Sunyaev & Zeldovich 1970] Rashid A Sunyaev and Ya B Zeldovich. *Small-scale fluctuations of relic radiation.* Astrophysics and Space Science, vol. 7, no. 1, pages 3–19, 1970. (Cited on page 36.)

[Szydlarski *et al.* 2014] Mikolaj Szydlarski, Pierre Esterie, Joel Falcou, Laura Grigori and Radek Stompor. *Parallel spherical harmonic transforms on heterogeneous architectures (graphics processing units/multi-core CPUs)*. Concurrency and Computation: Practice and Experience, vol. 26, no. 3, pages 683–711, 2014. (Cited on pages 30 and 229.)

[Tegmark & de Oliveira-Costa 2001] M. Tegmark and A. de Oliveira-Costa. *How to measure CMB polarization power spectra without losing information.* Physical Review D, vol. 64, no. 6, page 063001, 2001. (Cited on pages 178 and 228.)

[Tegmark *et al.* 2000] Max Tegmark, Daniel J Eisenstein, Wayne Hu and Angelica de Oliveira-Costa. *Foregrounds and forecasts for the cosmic microwave background.* The Astrophysical Journal, vol. 530, no. 1, page 133, 2000. (Cited on page 78.)

[Tegmark 1997a] Max Tegmark. *How to make maps from cosmic microwave background data without losing information.* The Astrophysical Journal Letters, vol. 480, no. 2, page L87, 1997. (Cited on page 142.)

[Tegmark 1997b] Max Tegmark. *How to measure CMB power spectra without losing information.* Physical Review D, vol. 55, no. 10, page 5895, 1997. (Cited on page 228.)

[Tristram *et al.* 2005] M. Tristram, JF Macías-Pérez, C. Renault and D. Santos. *XSPECT, estimation of the angular power spectrum by computing cross-power spectra with analytical error bars.* Monthly Notices of the Royal Astronomical Society, vol. 358, no. 3, pages 833–842, 2005. (Cited on pages 178, 187 and 188.)

[Tristram 2005] Matthieu Tristram. *De Archeops à Planck, analyse des anisotropies du fond diffus cosmologique.* PhD thesis, Université Joseph-Fourier-Grenoble I, 2005. (Cited on page 188.)

[Ulich 1981] BL Ulich. *Millimeter-wavelength continuum calibration sources.* The Astronomical Journal, vol. 86, pages 1619–1626, 1981. (Cited on page 106.)

[van Engelen *et al.* 2012] A van Engelen, R Keisler, O Zahn, KA Aird, BA Benson, LE Bleem, JE Carlstrom, CL Chang, HM Cho, TM Crawford*et al. A measurement of gravitational lensing of the microwave background using South Pole Telescope data.* The Astrophysical Journal, vol. 756, no. 2, page 142, 2012. (Cited on pages 71, 216 and 217.)

[van Engelen *et al.* 2014] Alexander van Engelen, Blake D Sherwin, Neelima Sehgal, Graeme E Addison, Rupert Allison, Nick Battaglia, Francesco de Bernardis, Erminia Calabrese, Kevin Coughlin, Devin Crichton*et al. The Atacama Cosmology Telescope: Lensing of CMB Temperature and Polarization Derived from Cosmic Infrared Background Cross-Correlation.* arXiv preprint arXiv:1412.0626, 2014. (Cited on page 216.)

[Varshalovich *et al.* 1988] Dmitriĭ Aleksandrovich Varshalovich, AN Moskalev and VK Khersonskii. Quantum theory of angular momentum. World Scientific, 1988. (Cited on page 179.)

[Verde 2010] Licia Verde. *Statistical methods in cosmology.* In Lectures on Cosmology, pages 147–177. Springer, 2010. (Cited on page 53.)

[Viero *et al.* 2009] Marco P Viero, Peter AR Ade, James J Bock, Edward L Chapin, Mark J Devlin, Matthew Griffin, Joshua O Gundersen, Mark Halpern, Peter C Hargrave, David H Hughes*et al. BLAST: Correlations in the Cosmic Far-Infrared Background*

at 250, 350, and 500 μm Reveal Clustering of Star-forming Galaxies. The Astrophysical Journal, vol. 707, no. 2, page 1766, 2009. (Cited on page 221.)

[Wandelt *et al.* 2001] Benjamin D Wandelt, Eric Hivon and Krzysztof M Gorski. *Cosmic microwave background anisotropy power spectrum statistics for high precision cosmology.* Physical Review D, vol. 64, no. 8, page 083003, 2001. (Cited on page 178.)

[Weiland *et al.* 2011] JL Weiland, N Odegard, RS Hill, E Wollack, G Hinshaw, MR Greason, N Jarosik, L Page, CL Bennett, J Dunkley*et al. Seven-year wilkinson microwave anisotropy probe (wmap) observations: Planets and celestial calibration sources.* The Astrophysical Journal Supplement Series, vol. 192, no. 2, page 19, 2011. (Cited on pages 102, 105, 106 and 119.)

[Wiesemeyer *et al.* 2011] H Wiesemeyer, C Thum, D Morris, J Aumont and C Rosset. *A sensitive upper limit to the circular polarization of the Crab nebula at λ3 mm.* Astronomy & Astrophysics, vol. 528, page A11, 2011. (Cited on page 123.)

[Wilks 1938] Samuel S Wilks. *The large-sample distribution of the likelihood ratio for testing composite hypotheses.* The Annals of Mathematical Statistics, vol. 9, no. 1, pages 60–62, 1938. (Cited on page 53.)

[Wittman *et al.* 2000] David M Wittman, J Anthony Tyson, David Kirkman, Ian Dell'Antonio and Gary Bernstein. *Detection of weak gravitational lensing distortions of distant galaxies by cosmic dark matter at large scales.* Nature, vol. 405, no. 6783, pages 143–148, 2000. (Cited on page 57.)

[Wrobel *et al.* 1998] JM Wrobel, AR Patnaik, IWA Browne and PN Wilkinson. *A Catalog of 2118 Compact Radio Sources in the Northern Sky.* In Bulletin of the American Astronomical Society, volume 30, page 1308, 1998. (Cited on page 97.)

[Wu *et al.* 2014] WLK Wu, J Errard, C Dvorkin, CL Kuo, AT Lee, P McDonald, A Slosar and O Zahn. *A guide to designing future ground-based cosmic microwave background experiments.* The Astrophysical Journal, vol. 788, no. 2, page 138, 2014. (Cited on page 227.)

[Zahn *et al.* 2005] Oliver Zahn, Matias Zaldarriaga, Lars Hernquist and Matthew McQuinn. *The influence of nonuniform reionization on the CMB.* The Astrophysical Journal, vol. 630, no. 2, page 657, 2005. (Cited on page 36.)

[Zahn *et al.* 2012] O Zahn, CL Reichardt, L Shaw, A Lidz, KA Aird, BA Benson, LE Bleem, JE Carlstrom, CL Chang, HM Cho*et al. Cosmic microwave background constraints on the duration and timing of reionization from the South Pole Telescope.* The Astrophysical Journal, vol. 756, no. 1, page 65, 2012. (Cited on page 36.)

[Zaldarriaga & Seljak 1997] Matias Zaldarriaga and Uroš Seljak. *All-sky analysis of polarization in the microwave background.* Physical Review D, vol. 55, no. 4, page 1830, 1997. (Cited on page 42.)

[Zaldarriaga & Seljak 1999] Matias Zaldarriaga and Uroš Seljak. *Reconstructing projected matter density power spectrum from cosmic microwave background.* Physical Review D, vol. 59, no. 12, page 123507, 1999. (Cited on page 69.)

[Zeldovich & Sunyaev 1969] Ya B Zeldovich and RA Sunyaev. *The interaction of matter and radiation in a hot-model universe.* Astrophysics and Space Science, vol. 4, no. 3, pages 301–316, 1969. (Cited on page 36.)

[Zemcov *et al.* 2010] M Zemcov, Peter Ade, James Bock, Melanie Bowden, Michael L Brown, Gary Cahill, Patricia G Castro, Sarah Church, Thomas Culverhouse, Robert B Friedman*et al. Characterization of the Millimeter-Wave Polarization of Centaurus A with QUaD.* The Astrophysical Journal, vol. 710, no. 2, page 1541, 2010. (Cited on page 119.)